Polyol-mediated Synthesis of Chalcogenide Nanoparticles for Thin-film Solar Cells

Zur Erlangung des akademischen Grades eines

DOKTORS DER NATURWISSENSCHAFTEN

(Dr. rer. nat.)

Fakultät für Chemie und Biowissenschaften

Karlsruher Institut für Technologie (KIT) - Universitätsbereich

genehmigte

DISSERTATION

VON

M.Sc. Hailong Dong

aus

Liaoning, China

Dekan: Prof. Dr. Peter Roesky
Referent: Prof. Dr. Claus Feldmann
Korreferent: Prof. Dr. Uli Lemmer
Tag der mündlichen Prüfung: 14.02.2014

Zusammenfassung

Der Energiemangel, verursacht durch den immer größer werdenden Energieverbrauch, ist eine Herausforderung, welcher sich die Menschheit in diesem Jahrhundert stellen muss. Dünnschicht-Solarzellen als eine der Photovoltaik Technologien wandelt Sonnenenergie direkt in Elektrizität um. Das Ziel dieser Arbeit ist die Synthese und Charakterisierung chalcogenidhaltiger Nanopartikel für druckfähige Dünnschicht-Solarzellen. Zu diesem Zweck wurde eine polyolvermittelte Synthese und ein sogenanntes "hot-injection" Verfahren verwendet. Die Herstellung und Erprobung der Dünnschicht-Solarzellen in dieser Arbeit wurde von unseren Kooperationspartner am ZSW in Stuttgart durchgeführt.

Direkt nach der Synthese sind die Cu_2Se und In_2Se_3 Nanopartikeln amorph und besitzen einen durchschnittliche Partikelgröße von etwa 17 nm beziehungsweise 20 nm. Die Tinten von Cu_2Se und In_2Se_3 in Isopropanol sind stabil und zeigen einen niedrigen Agglomerationsgrad. Nach Mischen dieser beiden Tinten in einem angemessenen Verhältnis wurde die daraus resultierenden Tinte per Rackeln auf einem mit Molybdän bedeckten Kalk-Natron-Glas aufgetragen. Die CISe Dünnschicht-Solarzellen mit einer Energieumwandlungseffizienz von 1-2 % wurden durch Selenisierung oder einen Lasertemperprozess von Prekursorschichten erreicht.

Cu_2ZnSnS_4 (Kesterit) Nanopartikel (CZTS) mit einem Partikeldurchmesser von 10-20 nm wurden hergestellt. Direkt nach der Synthese sind die CZTS Nanopartikel kristallin und besitzen einen durchschnittliche Zusammensetzung von $Cu_{1.35}Zn_{1.11}SnS_{3.96}$ (kupferarm, zink-/zinn- und schwefelreich) und eine direkte Bandlücke von 1,37 eV. In einem ersten Versuch wurden Dünnschicht-Solarzellen nach der Umwandlung der nach der Synthese erhaltenen CZTS Nanopartikel zu kristallinem $Cu_2ZnSn(S,Se)_4$ (CZTSSe) mittels Gasphasen Selenisierung hergestellt. Die Umwandlung führte zu einer Bildung von dichten Schichten aufgrund einer Volumenerhöhung, einer Verringerung der interpartikulären Oberflächen und Defekte und führt zu einer Verkleinerung der Bandlücke auf 1,14 eV. Die Dünnschicht-Solarzelle mit den besten Testergebnissen hat eine Leerlaufspannung von 247,3 mV, eine Kurzschlussstromdichte von 21,3 mA cm^{-2}, einen Füllfaktor von 41,1 % und eine Leistungsumwandlungseffizienz von 2,2 %.

Des Weiteren wurden Selen Nanopartikel mit einem Durchmesser von 85-410 nm durch eine Reduktion von Seleniger Säure mit Hydrazin dargestellt. Die direkt synthetisierten Partikel aus rotem, amorphem Selen (*a-Se*) zeigen weder eine Phasen- noch eine kolloidale Stabilität. Demzufolge sind derartige Se Partikel als Ausgangsstoff für Schichtabscheidung bei der Herstellung von CISe Dünnschicht-Solarzellen ungeeignet. Um diese Einschränkung zu überwinden, wurden in dieser Arbeit Se@CuSe core@shell Nanopartikeln vorgestellt. Die

Phasenumwandlung von *a*-Se zu *t*-Se wurde dabei zu Temperaturen über 100 ℃ verschoben. Überraschenderweise bleibt bei der Phasenumwandlung die sphärische Forme der Nanopartikel erhalten. Die Zusammensetzung und Struktur der Se@CuSe core@shell Nanopartikel wurden mittels REM/RTEM, XRD, FT-IR Spektroskopie und line-scan EDX bestimmt. In einer Konzeptstudie wurden die Se@CuSe Kern@Schale Partikel, welche mit CuSe als schützende Schicht bedeckt sind, um die Phasenumwandlungstemperatur zu erhöhen und colloidale Stabilität zu verbessern, als Se Quelle für die Herstellung von CISe Dünnschicht-Solarzellen eingesetzt und führten bereits zu Wirkungsgraden von bis zu 3 %.

Desweiteren wurden Tellurium Nanostäbchen mit einem Durchmesser von 10-20 nm und einer Länge von 25-55 nm durch Reduktion von Tellursäure mit Hydrazin synthetisiert. Obwohl bei 0 ℃ dargestellt, sind die frisch synthetisierten Te Nanostäbchen kristallin. Für Seitenverhältnisse kleiner fünf, wird eine geringe Kolloid- und Formstabilität erhalten. Die Nanostäbchen agglomerieren und wachsen bei Lagerung und/oder bei einer leichten Temperatursteigerung wie z. B. bei Rühren oder Zentrifugieren schnell zusammen. Um die Kolloid- und Formstabilität zu verbessern wird ein dünne Beschichtung aus Bi_2Te_3 durch die Zugabe von $C_{18}H_{15}Bi$ nach dem ersten Syntheseschritt aufgebracht. Als Ergebnis erhält man Te@Bi_2Te_3 Kern@Schale Nanostäbchen. Die Zusammensetzung und Strukturen wurde mit REM, HRTEM, HAADF-STEM, XRD, FT-IR Spectroskopie und line-scan EDX belegt.

Zusätzlich der Materialien für die Herstellung von chalkogenhaltigen Dünnschichten wurden reine und dotierte Zink Glykerolate (Zn(gly)) in plättchenartige Morphologie dargestellt. Diese Plättchen haben einen Durchmesser von 5-15 μm und eine Dicke von 100-500 nm. Durch Kalzinieren bei 500-600 ℃, reagiert das nach der Synthese erhaltene, reine Zn(gly) zu ZnO unter Erhalt der plättchenartigen Morphologie. Der Verlust des sterisch anspruchsvollen (gly)-Liganden geht einher mit einer körnigen Substruktur der Zinkplättchen, welche nun eine große Anzahl Poren aufweisen. Durch kontrollierte thermische Zersetzung konnte die Porösität der ZnO-Plättchen auf eine spezifische Oberfläche von 5 bis 15 $m^2\ g^{-1}$ eingestellt werden. Zusätzlich konnten, in Abhängigkeit verschiedener Dotierungen, diverse Morphologien und Substrukturen von dotierten ZnO mittels moderater thermischer Zersetzung der korrespondierenden dotierten Zn(gly) Materialien erhalten werden.

Schließlich wurde die Photoluminiszenz von erhitzten Polyolen durch blaue Emission unter UV Anregung nachgewiesen. Verschiedene Polyole und Metallsalze wurden in dieser Arbeit untersucht. Alle erhitzten Polyolproben weisen Vielfarbenemissionen in Abhängigkeit von der angeregten Wellenlänge und relativ hohe Quantenausbeuten (>20 %) auf. Bei Erhitzen mit Seltenerd Terbiumcholrid und Fluorescin als Leuchtstoff wirkt das erhitzende Polyol als ein Verstärker, das die Lumineszenzeigenschaft der so erhaltenen Probe erhöht.

Abstract

Energy scarcity due to the rapid growth of energy demand is one of the severe issues that human being has to face in this century. Thin-film solar cells as one of the photovoltaic technologies convert solar radiation directly into electricity. The aim of this thesis is to synthesize and characterize chalcogenide nanoparticles for printable thin-film solar cells. For this purpose, polyol-mediated syntheses and hot-injection techniques were applied. The manufacturing and testing of thin-film solar cells in this thesis were done by our cooperative partners from ZSW in Stuttgart (Germany).

The as-prepared Cu_2Se and In_2Se_3 nanoparticles were amorphous and exhibited the average particle sizes of about 17 nm and 20 nm in diameter, respectively. The inks of Cu_2Se and In_2Se_3 in isopropanol were stable, containing a low degree of agglomerations. After mixing these two inks in an appropriate ratio, the resulting mixture ink was deposited on molybdenum covered soda-lime-glass substrate via doctor-blade coating. The CISe thin-film solar cells with conversion efficiencies of 1-2 % have been achieved by selenization or laser annealing of the precursor layers.

Cu_2ZnSnS_4 (kesterite) nanoparticles (CZTS) with a particle diameter of 10-20 nm were prepared. The as-prepared CZTS nanoparticles were crystalline and exhibited an overall composition of $Cu_{1.35}Zn_{1.11}SnS_{3.96}$ (Cu-poor, Zn-/Sn- and sulfur-rich) and a direct band gap of 1.37 eV. As a first test, thin-film solar cells were manufactured after conversion of the as-prepared CZTS nanoparticles to crystalline $Cu_2ZnSn(S,Se)_4$ (CZTSSe) via gas-phase selenization. The conversion supported the formation of a dense layer due to the volume increase, reduced the interparticulate surfaces and defects, and led to a reduction of the band gap to 1.14 eV. The thin-film solar cell with the best results showed an open-circuit voltage of 247.3 mV, a short-circuit current density of $21.3 \, mA \, cm^{-2}$, a fill factor of 41.1 % and a power-conversion efficiency of 2.2 %.

Moreover, selenium nanoparticles with diameters of 85-410 nm were prepared via hydrazine-driven reduction of selenious acid. The as-prepared red amorphous selenium (*a*-Se) particles were neither phase stable nor colloidally stable. As a consequence, such Se particles were not suitable for layer deposition and as a Se precursor to manufacture CISe thin-film solar cells. To overcome this restriction, Se@CuSe core@shell nanoparticles are presented in this work. The phase transition from *a*-Se to *t*-Se was shifted to temperatures higher than 100 ℃. Surprisingly, the spherical shape of the nanoparticles was retained even after phase transition. Composition and structure of the Se@CuSe core@shell nanoparticles were characterized by SEM/STEM, XRD, FT-IR spectroscopy and line-scan EDX. As a conceptual study, the newly formed Se@CuSe core@shell nanostructure with CuSe acting as a protecting layer to increase the phase-transition temperature and to

improve the colloidal stability was used as a Se precursor for manufacturing of CISe thin-film solar cells and already led to conversion efficiencies up to 3 %.

Furthermore, tellurium nanorods with a diameter of 10-20 nm and a length of 25-55 nm were synthesized by hydrazine-driven reduction of telluric acid. Although obtained at 0 ℃, the as-prepared Te nanorods were crystalline. For aspect ratios lower than 5, the colloid and shape stability of the nanorods turned out low. The nanorods agglomerated and merged rapidly during storage and/or due to gentle heating (e.g., stirring, centrifugation). In order to increase the colloid and shape stability, a thin capping of Bi_2Te_3 was therefore established by addition of $C_{18}H_{15}Bi$ after the first step of the synthesis. As a result, Te@Bi_2Te_3 core@shell nanorods were obtained. Composition and structure were validated by SEM, HRTEM, HAADF-STEM, FT-IR spectroscopy, XRD, and line-scan EDX.

In addition to the materials for manufacturing chalcogenide thin-film layers, pure and doped zinc glycerolates (Zn(gly)) with platelet-like morphology were prepared. These platelets exhibited diameters of 5-15 μm and a thickness of 100-500 nm. Via the calcination at 500-600 ℃, the as-prepared pure Zn(gly) was reacted to ZnO with the platelet-like morphology maintained. The loss of the spacious (gly)-ligand was accompanied by a granulated sub-structure of the ZnO platelets that now exhibited lots of pores. By controlled thermal decompositmion, moreover, the porosity of the granulated ZnO platelets was adjusted with the specific surface areas of 5-18 $m^2 g^{-1}$. Moreover, depending on different dopants, various morphologies and sub-structures of doped ZnO were obtained via moderate thermal decomposition of corresponding doped Zn(gly)s.

Finally, the photoluminescence of heated polyol was confirmed by showing blue emission under UV excitation. Different types of polyols and metal salts were studied in this work. All heated polyol samples showed multicolor emissions with a dependence on the excitation wavelengths and relatively high quantum yields (>20 %). When heating with rare-earth terbium chloride and fluorescein fluorophor, the heated polyols behaved as an enhancer, which increased the luminescent properties of the resulting samples.

Table of Contents

1 Introduction

Energy scarcity is one of the severe issues that human being has to face in this century due to the rapid growth of energy demand. In the last two hundred years, the world primary energy consumption has explosively increased and in 2012 it reached 12,476.6 Mtoe (Million tonnes oil equivalent), which is equal to 16.65 TW y (terawatt year).[1] A major part of electric power is currently produced by burning fossil fuels (oil, natural gas and coal). Fossil fuels were still dominating energy resources with a market share of 86.9 % in 2012.[1] However, fossil fuels will not be the answer to the current and future fast growing energy demand for two reasons: a) their limited reserves and b) their adverse effects on the climate change due to the significant greenhouse gas emission from exhaust. Consequently, many organizations in the world have been looking for alternatives to fossil fuels which are renewable, environment friendly and low-cost.

Nuclear energy, having the potential to meet a large part of world electricity demand, was once discussed as the major candidate for replacing the fossil fuels, due to its minimal greenhouse gas emission across the whole fuel cycle, reliable and predictable supplies of cheap electricity. In 2008, 13.5 % of world electricity production was from nuclear power plants in 31 countries.[2] After the Fukushima nuclear disaster caused by earthquake and tsunami in March 2011 in Japan, the terrible catastrophe has triggered global questions and oppositions to nuclear technology until now. The world nuclear output decreased by 6.9 % in 2012, which was the largest decline on record for the second consecutive year. In 2012, nuclear energy accounted for only 4.5 % of global energy consumption, the smallest share since 1984. In addition to the most important safety issue, nuclear energy still arouses much controversy because the nuclear fuel, uranium, is radioactive, limited and not renewable. The nuclear waste needs professional handling and has to be carefully stored and disposed.

The development of new energy resources, which are really sustainable, is essential prerequisite to meet the increasing requirement for electrical energy and simultaneously stabilize anthropogenic CO_2 emission. In 2012, renewable energy amounted to 2.4 % of the world's energy consumption, up from 0.8 % in 2002; renewable energy in electricity generation accounted for a record 4.7 % of the world's electricity generation.[1] The renewable energy resources nowadays mainly include wind, biomass, water (hydro energy) and solar energy.

■ Wind energy: It is a fast growing renewable technology, however, it can be utilized only in regions where there is appropriate amount of wind — too little or too much is ineffective. Its limited potential can't fulfill the world energy requirement for the next 40 years along, but as additional option it is a good choice.[3, 4] In 2012, wind energy increased by 18.1 %, contributing more than half of renewable energy generation growth.[1]

- Biomass energy: It is a very inefficient renewable energy and requires large land areas and water resources to produce a sufficient amount of biomass. The bioelectrical processes generate greenhouse gases, which will not benefit the stabilization of CO_2.
- Hydro energy: It is an attractive renewable resource but requires specific geologic formations and has nearly no room to make further contribution to the fast increasing energy demand. It often causes adverse impacts to the local and neighboring environment.
- Solar energy: It is the most promising and fastest growing renewable resource. The sun is the primary source of energy for most biological processes on earth and provides the earth's surface with annual 120,000 TW y solar energy.[5] In other words, the energy generated from one hour solar radiation is equal to the world's energy consumption in an entire year. A practical terrestrial global solar energy potential is about 600 TW y. Solar energy is so far the only renewable resource, which has sufficient terrestrial energy potential to meet a 10-20 TW y carbon-free energy constraint in 2050.[3-5] Solar power generation increased significantly by 86.3 % in 2011 and 58 % in 2012 but from a small base.[1, 6] Despite its advantages as a clean renewable energy resource, there are some disadvantages of solar energy, which prevent it from becoming widely used. The main disadvantage is the high upfront costs of buying and installing the equipment, which varies greatly, depending on different types, number and location of the solar equipment. For the purpose of working efficiently, solar equipments require reliable quantities of sunshine, which means not everywhere on earth it is suitable to use solar equipments. During the night, they are also unable to function due to lack of solar radiation. In spite of the negative aspects mentioned above, many governments, organizations, scientists and activists devote great efforts to make the system more affordable and efficient. Developments in battery technology have made storing the electricity generated by solar equipments cheaper and easier. Some solar energy systems can connect to the electricity grid and allow owners to sell or store "green" electricity to power companies or use electricity at night and on cloudy days. In order to encourage the use of solar energy, many governments subsidize solar energy production and offer tax deductions to individuals, who purchase solar equipments.

Methods of solar energy conversion can be generally classified into two categories: a) photothermal and b) photovoltaic (PV). The photothermal system converts sunlight first into thermal energy that can be used directly or further converted into electricity. The photovoltaic system converts solar radiation directly into electricity. Since 2000, photovoltaic (PV) has already become one of the fastest growing industries worldwide with annual growth rates between 40 % and 90 %, the total PV production increased almost by two orders of magnitude.[7] Among all the PV technologies, wafer-based silicon solar cells had around 85 % market shares in 2011 and are still predominating today. However, their energy-conversion efficiencies have not been

increased significantly in recent years and the potential for cost reduction of wafer-based silicon solar cells is also limited. Thus, scientific research and commercial interests have concurrently begun to focus on thin-film solar cells for the following reasons: higher potential for cost reduction, monolithic integration of cells, fewer processing steps and a higher degree of automation compared to silicon-wafer based technologies, but most important: flexible devices.[8-10]

In all kinds of thin-film solar cells, the family of copper chalcogenides, such as $Cu(In,Ga)S_2$/$Cu(In,Ga)Se_2$ (CIGS/CIGSe: copper indium gallium sulfide/selenide) $CuInS_2$/$CuInSe_2$ (CIS/CISe: copper indium sulfide/selenide), Cu_2ZnSnS_4/$Cu_2ZnSnSe_4$ (CZTS/CZTSe: copper zinc tin sulfide/selenide) has so far demonstrated the highest conversion efficiency for thin-film solar cells both in the laboratory and in mass production.[11, 12] The most recent world record of CIGSe thin-film solar cells with a measured cell area of 0.5 cm^2 achieved a conversion efficiency of 20.3 %, which was reported by ZSW in Stuttgart (Germany), utilizing high-vacuum co-evaporation techniques.[13] This record efficiency is comparable to the best multicrystalline silicon solar cell with 20.4 % efficiency.[12, 14] In contrast to the indirect band-gap of silicon, copper chalcogenide compounds are direct band-gap semiconductors with relatively high light absorption coefficients ($> 10^4$ cm^{-1}), which are ideal for the manufacturing of thin-film solar cells with a layer thickness of 1-2 μm for the active absorber material.[11, 12, 15-17]

The aim of this thesis is polyol-mediated syntheses of chalcogenide nanoparticles for printable thin-film solar cells. Thus, the syntheses of the binary (Cu_2Se and In_2Se_3) and the quaternary (CZTS) chalcogenide nanoparticles by polyol-mediated method and hot-injection technique are going to be introduced. Colloidally and phase stable Se@CuSe core@shell nanoparticles and Te@Bi_2Te_3 core@shell nanorods as new Se and Te sources for printable chalcogenide thin-film solar cells will be synthesized and characterized. In order to test our synthesized nanoparticles, thin-film solar cells are manufactured by our cooperative partners from ZSW in Stuttgart. The behaviors and efficiencies of assembled thin-film solar cells will be briefly discussed. Finally, to further understand the nature of polyols and polyol-mediated synthesis, the polyol photoluminescence will be investigated in this work.

2 Experimental Section

2.1 General Procedures

Evacuation and Inert Gas Apparatus

In order to handle air/moisture sensitive precursors, reactions and products, a standard Schlenk line and glovebox techniques were applied. The Schlenk line (Figure 2.1), a combined evacuation/inert gas apparatus, consisted of an evacuation line for vacuumizing all connected devices and an inert gas line for introducing argon gas (Argon 4.8, from AIR LIQUIDE, Paris, France). Before being introduced into the inert gas line, argon was conveyed through a series of drying towers containing silica gel, potassium hydroxide, molecular sieve (4 Å), and phosphorus pentoxide to further remove impurities such as water or carbon dioxide. Vacuum ($p < 10^{-3}$ mbar) was produced by a rotary vane vacuum pump and the pressure was measured with a manometer from VACUUBRAND (Wertheim, Germany). A cold trap, cooled with liquid nitrogen, was designed between the vacuum pump and the evacuation line to prevent flow of any volatiles into the pump. All air/moisture sensitive chemicals were to weight and decanted in an argon protected glove box from BRAUN (Munich, Germany).
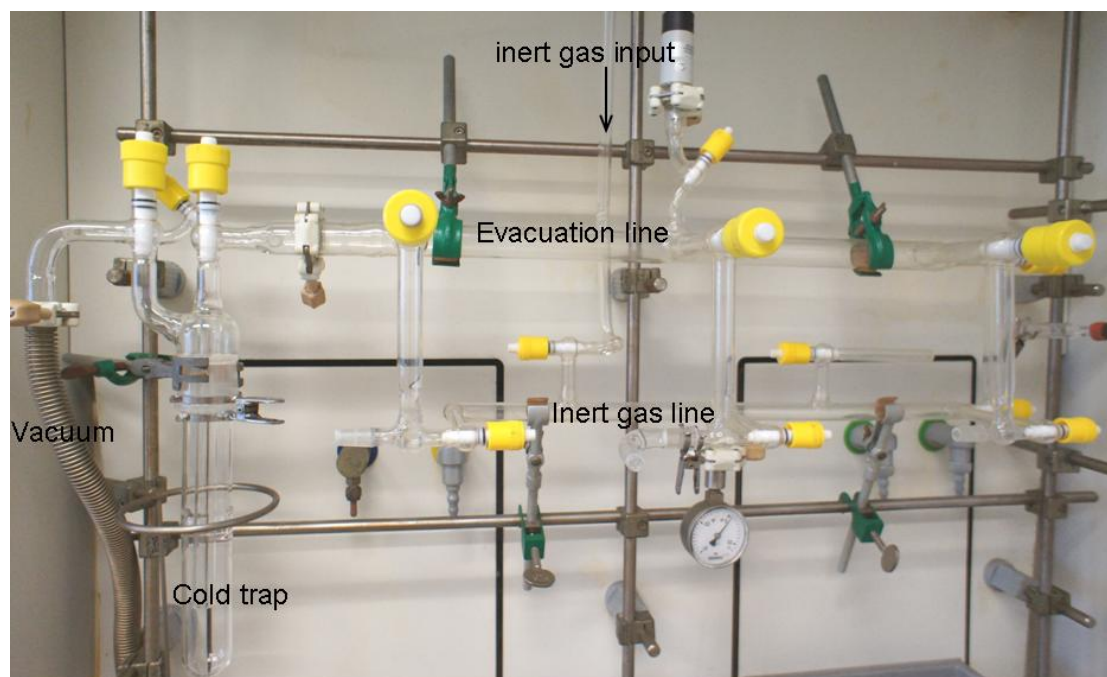
Figure 2.1: Schlenk line.

Washing Process

The as-prepared samples had to be purified by a washing process before further analytical characterization and practical use. Firstly, the as-prepared samples were diluted with suitable washing solvents (ethanol, isopropanol, demineralized water) in

centrifuge tubes from THERMO SCIENTIFIC (New York, USA). The homogenous mixtures were separated in a laboratory centrifuge (3K30 from SIGMA, Osterode am Harz, Germany) for 10-30 minutes at 10,000-23,000 rpm. After decanting the supernatants, the resulting solids were redispersed in fresh washing solvents using an ultrasonic bath (RK 100 H from BANDELIN ELETRONIC, Berlin, Germany). The washing process was repeated at least three times.

2.2 Polyol-mediated Synthesis

Polyols are multivalent high-boiling alcohols containing multiple hydroxyl groups. Ethylenglycol (EG), diethylenglycol (DEG) and glycerol are typical polyols for laboratory use (Figure 2.2). Comparing with standard solvents such as acetone, ethanol and water, polyols are known for relatively high dielectric constants and high boiling points (Table 2.1). Due to their comparably high dielectric constants, polyols can serve as good solvents and have sufficient solubility for dissolving many inorganic compounds/salts. The boiling points, which are much higher compared to water, allow polyol-mediated synthesis in a wide temperature range. Nucleation and growth of particles can even be performed near the boiling points of the polyols. In general, the higher the reaction temperature is, the shorter the reaction time needs, the better crystallinity of the product will be obtained, which is often preliminary to material properties such as color, magnetism, electrical conductivity and luminescence.
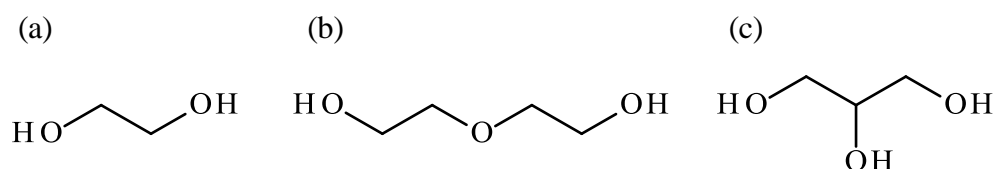
Figure 2.2: Skeletal formulas of typical polyols: a) Ethylene glycol; b) Diethylene glycol; c) Glycerol.

Table 2.1: Dielectric constants and boiling points of typical polyols and solvents.[18]

	Typical polyols			Typical solvents		
	DEG	EG	Glycerol	Acetone	Ethanol	Water
Dielectric constant (25 ℃) / $AsV^{-1}m^{-1}$	31.8	37.7	42.5	20.7	24.6	78.4
Boiling point / ℃		248	197	290	56	78	100

In addition, polyols as chelating agents are able to coordinate multidentately to the particles' surface (Figure 2.3) and act as weak surfactants, which can be removed under certain experimental conditions.[19] As a result, the particle growth is limited and the colloidal stability of particles is increased, which suppresses particle agglomeration. Stable suspensions can then be obtained without additional stabilizers.
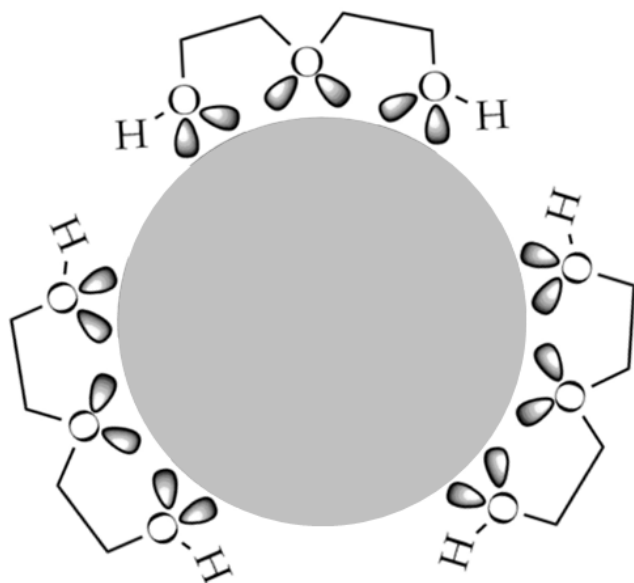
Figure 2.3: Schematic illustration of a nanoparticle stabilized with DEG.

Furthermore, polyols are well known as reducing agents. In fact, the polyol-mediated synthesis was originally developed by Fievet *et al*. for the synthesis of metal particles such as Pd, Cu, Co and Ni, in which the polyol acts as both the solvent and the reducing agent.[20, 21]

Polyol-mediated synthesis is the synthesis using polyols as solvents and taking advantage of the polyol properties mentioned before. This kind of synthetic strategy has been proven to be a promising preparative approach to synthesize 20-300 nm spherical metal oxide particles, which have a low degree of agglomeration, a monodisperse size distribution and enable a homogenous arrangement in thin films or as coatings.[22, 23] The nanoscale metal oxide particles can be easily synthesized by heating suitable metal precursors and a defined amount of water in polyols. Beside metals and metal oxides, metal sulfides and phosphates can also be synthesized in similar procedures, only substituting a concentrated solution of $(NH_2)_2CS$ or $(NH_4)H_2PO_4$ for pure water.[24-26] In principle, polyol-mediated synthesis is comparably easy to perform and suitable for large-scale production.

2.3 Hot-injection Technique

Over the last 40 years, the synthesis of nanoparticles has been developed enormously, not only for fundamental scientific research, but also for novel technological applications. Mechanistic studies have shown that monodisperse nanoparticles are facilely obtained, if the nucleation and growth processes are separated.[27, 28] The hot-injection technique has been widely used to synthesize monodisperse nanocrystals of metal chalcogenides,[29, 30] transition metals,[31, 32] in organic solutions. It involves the rapid injection of a room-temperature precursor solution (cold solution) into another hot surfactant solution, resulting in the instantaneous formation of nuclei

which is called "burst-nucleation". As a synthetic strategy, "burst-nucleation" is often referred to as the separation of nucleation and growth.[27, 33, 34] Due to a sudden drop in monomer concentration and temperature, the formation of additional nuclei is prevented. A suspension of monodisperse nuclei with considerable amounts of precursors is formed and then these nuclei start to grow into mature nanocrystals at a lower temperature. Further increasing temperature of the suspension during the growth process leads to slow growth of the existing nuclei because of the low monomer concentration.

In this work, the hot-injection technique and polyol-mediated synthesis were applied to produce monodisperse nanoparticles for thin-film solar cells. Diethylene glycol (DEG) was chosen as both the solvent and surfactant, since it has been proven to be an excellent synthesis medium.[35, 36] All the precursors were entirely dissolved before hot-injection by continuously stirring, which also kept the heating homogeneous. The omnipresent DEG molecules slowed down the growth rate by chelating the surface of nanoparticles, thus forming a steric barrier for reactant. Due to a high boiling point of DEG (246 ℃), high reaction temperature (180-200 ℃) could be applied to produce crystalline nanoparticles.

2.4 Chemicals

All chemicals in this work were used as received and presented in Table 2.2.

Table 2.2: The applied chemicals in this work.

Chemical	Empirical formula	Purity	Supplier
Diethylene glycol	$C_4H_{10}O_3$	99 %	Alfa Aesar
Isopropanol	C_3H_7OH	98 %	Seulberger
Ethanol	C_2H_5OH	98 %	Seulberger
Glycerol	$C_3H_8O_3$	99+ %	Acros Organics
Magnesium chloride hexahydrate	$MgCl_2\ 6H_2O$	98+ %	Alfa Aesar
Sodium chloride	NaCl	99+ %	Sigma-Aldrich
Potassium chloride	KCl	99+ %	Sigma-Aldrich
Zinc acetate dihydrate	$Zn(CH_3COO)_2\ H_2O$	99 %	Acros Organics
Zinc chloride	$ZnCl_2$	97 %	Alfa Aesar
Copper(II) chloride	$CuCl_2$	98+ %	Alfa Aesar
Copper(II) acetate	$Cu(CH_3COO)_2$	98 %	Sigma-Aldrich
Tin(II) chloride	$SnCl_2$	98+ %	Sigma-Aldrich
Indium(III) chloride	$InCl_3$	99.99 %	ABCR
Telluric acid dihydrate	$H_2TeO_4\ 2H_2O$	99+ %	Alfa Aesar
Sodium sulfide	Na_2S	tech.	Alfa Aesar

Sodium selenide	Na_2Se	99.8 %	Alfa Aesar
Selenious acid	H_2SeO_3	98 %	Sigma-Aldrich
Hydrazine monohydrate	$N_2H_4 \cdot H_2O$	98 %	Sigma-Aldrich
Terbium(III) chloride hexahydrate	$TbCl_3 \cdot 6H_2O$	99.9 %	Sigma-Aldrich
Bismuth(III) chlorid,	$BiCl_3$	99.99 %	ABCR
Triphenylbismuth	$C_{18}H_{15}Bi$	99 %	ABCR
2,2'-thiodiethanethiol	$C_4H_{10}S_3$	90+ %	Alfa Aesar
Polyvinylpyrrolidone (PVP, $M_w = 40000$)	$(C_6H_9NO)_n$	tech.	Sigma-Aldrich
Polyethylene glycol (PEG, $M_w = 400$)	$H(OCH_2CH_2)_nOH$	tech.	Alfa Aesar
Polyethylene glycol (PEG, $M_w = 2000$)	$H(OCH_2CH_2)_nOH$	tech.	Sigma-Aldrich
Fluorescein	$C_{20}H_{12}O_5$	tech.	Sigma-Aldrich

3 Analytical Methods

3.1 X-ray Powder Diffraction (XRD)

X-ray powder diffraction is the most commonly used X-ray diffraction technique for qualitative identification of crystalline phases and unit-cell parameters. The obtained diffraction pattern can be used to determine the crystal structure by comparing it with a database of known substances.[37, 38] The essential components of a typical X-ray powder diffractometer in a material analysis laboratory are 1) an X-ray source generated from a sealed X-ray tube, 2) monochromators, slits and filters, 3) an X-ray detector, 4) a goniometer, which provides precise mechanical motions of the sample, 5) other electronics.

X-ray Sources
X-rays are electromagnetic radiations with a wavelength in the range of 0.01 to 10 nm, corresponding to frequencies in the range of 3×10^{16} to 3×10^{19} Hz. The wavelengths of X-rays are shorter than those of UV light and longer than those of gamma rays. A conventional X-ray tube is a vacuum tube diode with tungsten filament as the cathode and a metal target (e.g., copper, cobalt, molybdenum) as the anode. Electrons are first emitted thermionically from the tungsten filament, and then are accelerated through a high voltage (40-60 kV), finally they bombard the anode metal target. During this process, bremsstrahlung and characteristic X-rays are emitted together. The output spectrum includes a continuous spectrum of X-rays due to bremsstrahlung and additional sharp peaks at certain energies (Figure 3.1). The sharp peaks are characteristic X-rays associated with the atoms in the anode metal target.
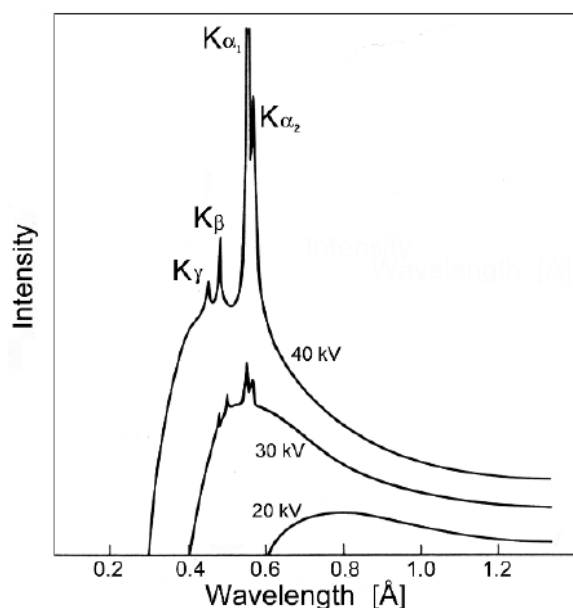
Figure 3.1: Intensity spectrum of an X-ray tube with silver anode.[38]

Bremsstrahlung is continuous radiation caused by deceleration of an incident electron when deflected by an atomic nucleus. The lost kinetic energy of the electron converts into an X-ray photon due to energy conservation. The X-ray can exhibit energy as high as the full kinetic energy of the incident electron, E_0 (equal to its charge, e, times its accelerating voltage, V). Then the "Duane-Hunt rule" for the shortest X-ray wavelength from the anode can be obtained, λ_{min}:

$$\frac{hc}{eV} = \lambda_{min}[\mathring{A}] = \frac{12.3984}{E_0[keV]} \tag{3.1}$$

where h is the Planck's constant, c is the speed of light, V is the accelerating voltage, e is the charge of the electron.

In Figure 3.1, the cutoffs present the values of three λ_{min} at three different accelerating voltages (0.31 Å for 40 kV, 0.41 Å for 30 kV and 0.62 Å for 20 kV). Bremsstrahlung becomes more intense and shifts toward lower wavelengths as the energy of the accelerated electrons is increased.

In addition to the bremsstrahlung, characteristic X-rays with intense discrete energies are also emitted, as depicted in Figure 3.1. The energies are determined by the differences in the binding energies of the electrons of the atom from the anode metal target. When a material is bombarded with high-energy electrons, the inner-shell electrons of target atoms are ejected and the resulting electron holes are then occupied by electrons from outer shells. Because the electron in each shell has its specific binding energy, electron transition from outer to inner shell leads to emission of specific energy as characteristic X-radiations. One of the most popular anode material for monochromatic radiation is copper and the radiation used is Cu-K$_{\alpha 1}$. On the one hand, the required accelerating voltage for maximizing the ratio of characteristic Cu-K$_{\alpha 1}$ intensity to bremsstrahlung intensity is moderate (e.g. around 35 keV for copper, but around 100 keV for silver); on the other hand copper has high thermal conductivity. The Cu-K$_{\alpha 1}$ radiation has a wavelength of 1.54 Å and originates from the transition of copper electron to the innermost "K" shell (1s orbital) from a 2p orbital of the "L" shell.
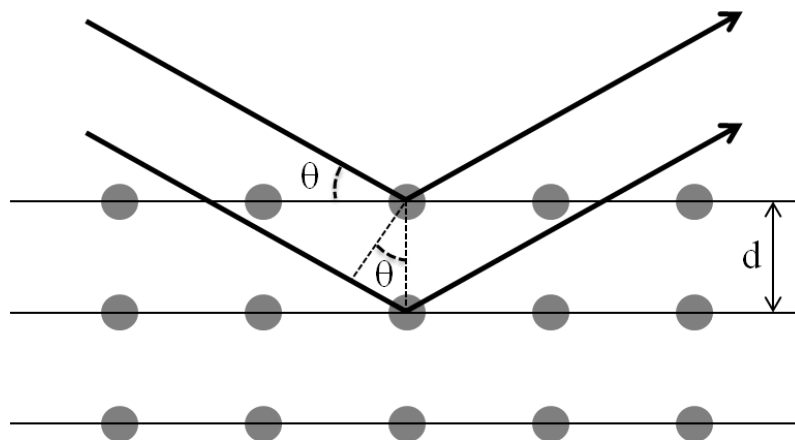
Figure 3.2: Scattering of X-radiation at lattice planes according to Bragg's law.

When monochromatized X-radiation is incident on a periodic structure of lattice

planes (Figure 3.2), it is scattered by the electrons of the lattice atoms. Depending on the incident angle θ (the angle between the incident radiation and the scattering planes) and the lattice plane distance d (the distance between the lattice planes), Constructive or destructive interference occurs between the scattered electromagnetic waves. Constructive interference can be observed, only if Bragg's equation is fulfilled.

$$2dsin\theta = n\lambda \tag{3.2}$$

where d is the lattice plane distance, θ is the incident angle, n is an integer, λ is the wavelength of the incident radiation.

The path length difference that is given by $2dsin\theta$ between two constructive interfering waves has to equal to an integer multiple of the incident wavelength. Constructive interference results in the superimposition of scattered waves to generate Bragg peaks with high intensities that can be detected. Destructive interference, on the other hand, is the overlapping of scattered waves with different phases which subtract from each other and causes low intensity signals.

Monochromators, Slits and Filters

Since only one of the characteristic X-radiations (usually the radiation $K_{\alpha1}$ is used) should be applied in the diffraction analyses, bremsstrahlung and other characteristic X-radiations such as $K_{\alpha2}$ or K_{β} are removed by a monochromator together with slits located in the beam path between the anode and the powder sample. In general, a single crystal of graphite or germanium is used as monochromator. Sometimes, it is useful to install a thin foil of absorbing material as a filter along the incident beam. This filter is helpful to suppress the K_{β}-radiation.

X-ray Detectors

Diffraction patterns are recorded by an X-ray detector, which generates a digital signal when it absorbs an X-ray photon. The ideal detector should produce a digital signal for every incident X-ray. The produced signal should have a net charge proportional to the energy of the X-radiation. This point is less critical for X-ray diffraction but very important for energy-dispersive spectroscopy (EDS) in an electron microscope. The amplitude of the signals should keep steady with time and not vary with the incident X-ray flux. Charge-coupled-device (CCD), one of the position-sensitive detectors (PSD), has been used in most high performance X-ray diffractometers. It detects X-rays at many angles simultaneously, reduces data acquisition time and improves counting statistics.

The resulting diffraction pattern is plotted as intensity versus 2θ angle. The diffraction peaks are directly related to the atomic distances. By comparing the positions and intensities of the peaks in the observed XRD pattern with a known pattern of peaks from an XRD database, the crystalline structure or phase of the material can be identified. A database of diffraction patterns for more than one hundred thousand inorganic and organic materials is maintained by the International Center for Diffraction Data (ICDD). For each material the data include the interplanar spacings (*d*) for all observed diffraction peaks, relative intensities and *hkl* indexing.

In this work, X-ray powder diffraction was carried out with a STADI-P diffractometer (STOE & CIE, Darmstadt, Germany) using Ge-monochromatized Cu-K$_{\alpha1}$ radiation with Debey-Scherrer geometry. The resulting diffraction patterns were evaluated with the program Win-XPOW by comparison with ICDD database. Samples were prepared by dispersing the powder on a piece of adhesive tape. Data were collected within an angle interval of -69°≤ 2θ ≤ 69°.

3.2 Electron Microscopy

Electron microscopes are widely used in scientific research for observation and characterization of materials on a nanometer to micrometer scale.[39] Great progress in natural science has been achieved by the development of electron microscopy techniques. Electron microscopes can provide information about the topography (surface features), morphology (shape and size), composition (component elements and relative content) and crystal structure (atom arrangement).

According to the Abbe's equation developed by Ernst Abbe in 1873, the resolution of a traditional optical microscope is limited by the wavelength of visible light (400-750 nm).[40]

$$d = \frac{0.61\lambda}{n sin\theta} \tag{3.3}$$

where d is the resolution, λ is the wavelength of imaging radiation, n is the refractive index of the medium between object and lens, θ is the semi-angle between object and aperture.

In order to obtain very high resolution (very small d) in atomic scale, electron microscopes were invented and developed by using a focused electron beam to image the object instead of light. According to the principles of classical physics and the quantum theory, moving particles have wave-like properties and their wavelengths can be calculated by the de Broglie equation.

$$\lambda = \frac{h}{m_e v} \tag{3.4}$$

where λ is the wavelength of particle, h is the Planck's constant, m_e is the mass of the particle, v is the velocity of the particle.

Compared to the wavelength of visible light (400-750 nm), the wavelength of an electron beam can be in the range of nanometer to Angstrom (0.1-1 nm), making the resolution of an electron microscope at least 100 times higher than an optical microscope. As an example, the theoretical resolution of an electron microscope with an accelerating voltage of 50 kV is about 0.05 nm.[39]

In principle, an electron microscope works quite similar to an optical microscope. A stream of electrons is generated thermionically from a very sharp tungsten tip in ultra-high vacuum and accelerated through a high voltage. Before high-energy electrons hit the specimen, they are confined and focused by electromagnetic condenser lenses and metal apertures. The whole chamber is under high vacuum to

minimize the scattering with particles left in the chamber. The specimen is bombarded by the electron beam and the interaction starts to generate special signals, which can be detected and transformed into an image.

When an electron beam hits the specimen, most incident electrons interact with specimen atoms and are scattered either elastically or inelastically, the residual electrons pass through the specimen without interaction as transmitted electrons. For elastic scattering, only the electron trajectory changes, the kinetic energy and the velocity remain constant. For inelastic scattering, electron energy is lost or transferred through interaction with electrons of atoms in the specimen. Inelastic scattering results in several types of signals, which can be used for imaging, qualitative and semi-quantitative analyses of the target specimen (Figure 3.3). Typical signals used for imaging include secondary electrons (SE), backscattered electrons (BSE), cathode luminescence (CL) and Auger electrons (AE). Characteristic X-rays are utilized for qualitative and semi-quantitative analyses of specimen compositions.

There are mainly two types of electron microscopy: transmission electron microscopy (TEM) and scanning electron microscopy (SEM). In general, both equipments have their energy dispersive X-ray detector (EDX), with which the emitted characteristic X-rays can be analyzed. The signals labeled above the specimen in Figure 3.3 are applied in SEM for thick or bulk specimens, the signals below the specimen are used in TEM for thin or nano-scaled specimens.
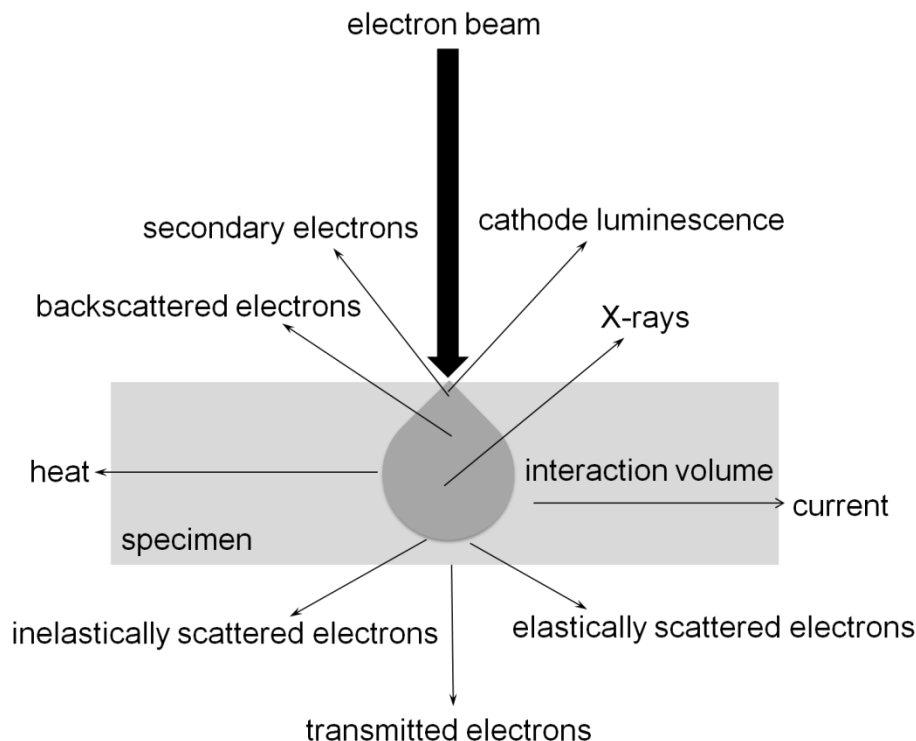
Figure 3.3: Interaction processes between an electron beam and a specimen.

3.2.1 Transmission Electron Microscopy (TEM)

A TEM is one of the typical electron microscopes, which applies transmitted electrons and scattered electrons for imaging.[38, 39, 41] In a transmission electron microscope, electrons are typically accelerated by a voltage of 100 to 300 kV, focused by two electromagnetic condenser lenses and pass through a condenser aperture before they hit the specimen. The geometry of a TEM is shown in Figure 3.4. Specimens have to be well prepared in advance. To avoid complete absorption of electrons, the thickness of specimens should be less than several hundred nanometers. Thereafter, transmitted and scattered electrons pass through an objective lens, an intermediate lens and an projector lens; finally they reach a fluorescent screen that shows the magnified image of the specimen. The image can be studied directly through the binocular or photographed with a CCD camera. A series of pumps are used to achieve an ultra high vacuum, since electrons are easily deflected by gas molecules.
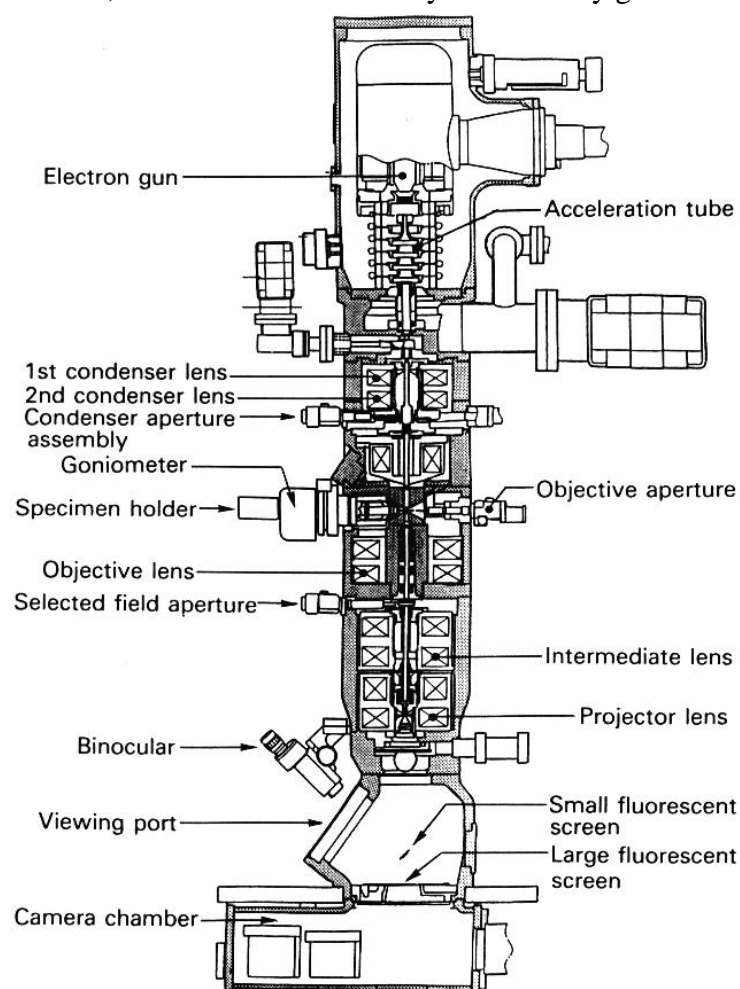
Figure 3.4: Schematic view of a transmission electron microscope.[38]

In a conventional TEM mode, sub-nanometer resolution can be achieved. It includes bright-field (BF) and dark-field (DF) imaging modes. In bright-field imaging mode, transmitted electrons contribute to the image. The image contrast arises from

scattering and absorption of transmitted electrons by specimen atoms. Thicker regions or regions with higher atomic numbers appear darker than other regions, due to stronger scattering and absorption of transmitted electrons. In dark-field imaging mode, transmitted electrons are excluded and only scattered electrons contribute to the image. Therefore, DF mode provides relatively low resolution imaging but with a sharp contrast, which can be used to indicate different crystal orientations, grain boundaries and defects.

In a high-resolution TEM (HRTEM) mode, due to the technique of "phase-contrast imaging" (the phase of scattered electron wave is preserved and interferes constructively or destructively with the phase of a transmitted electron wave), errors are reduced and more interferences are corrected. Therefore, images of atom columns can be directly observed. In HRTEM, it is possible to achieve a resolution of 2 Å.

In a scanning transmission electron microscopy (STEM) mode, a focused electron beam is moved in a television-style raster pattern across the specimen. During the raster scan, various data from the specimen are collected, such as X-rays, secondary electrons and backscattered electrons. At the same time, transmitted electrons are also detected with a mobile detector. When the STEM is combined with a high-angle annular dark-field (HAADF) detector, it is possible to obtain images with atomic resolution where the contrast is directly related to the atomic number (Z). That is why HAADF imaging is also called Z-contrast imaging.

When an electron beam hits a crystalline specimen, Bragg diffractions are expected, since high-energy electrons have wave-like properties. In diffraction mode, electrons can be focused more easily than X-rays, thus diffraction patterns can be measured from a selected microscopic area, making diffraction measurements possible on selected single microcrystals. By analyzing selected area electron diffraction (SAED) patterns, crystallographic data, such as the crystal lattice symmetry and lattice parameters, can be determined with high precision.

Transmission electron microscopes used in this work were conducted with an aberration corrected FEI Titan[3] 80-300 at 300 kV and a Philips CM 200 FEG/ST at 200 kV. TEM samples were prepared by evaporating water-based suspensions on an amorphous carbon (Lacey-) film coated copper grid. The TEM images presented in the thesis were taken by Dr. R. Popescu in the research group of Prof. Dr. D. Gerthsen, Laboratorium für Elektronenmikroskopie, Karlsruhe Institute of Technology (KIT).

3.2.2 Scanning Electron Microscopy (SEM)

A SEM as another major electron microscope has similar components like TEM, such as an electron gun, condenser lenses and a vacuum system (Figure 3.5). However, the ways in which the images are produced and magnified are entirely different.[39, 42] SEM mainly uses secondary and backscattered electrons for imaging. The

magnification of the image involves no lenses and depends only on the ratio between a raster length on the screen and a raster length on the specimen. TEM gives information about the internal structures of thin specimens, while SEM is used to study the surface or near surface regions of the specimens, so the thickness of specimens is not as critical as that for TEM measurements.

In a SEM, the electrons are accelerated to the required energy between 1 keV and 30 keV (100-300 keV for TEM) and focused to an electron beam with a diameter of 2-10 nm by condenser lenses. The focused electron beam scans specimens in a television-style raster pattern and interacts with specimen atoms as described before. The signals, such as secondary electrons and backscattered electrons, combined with locations where the signals are generated, generate the SEM images of scanned areas on a computer screen.
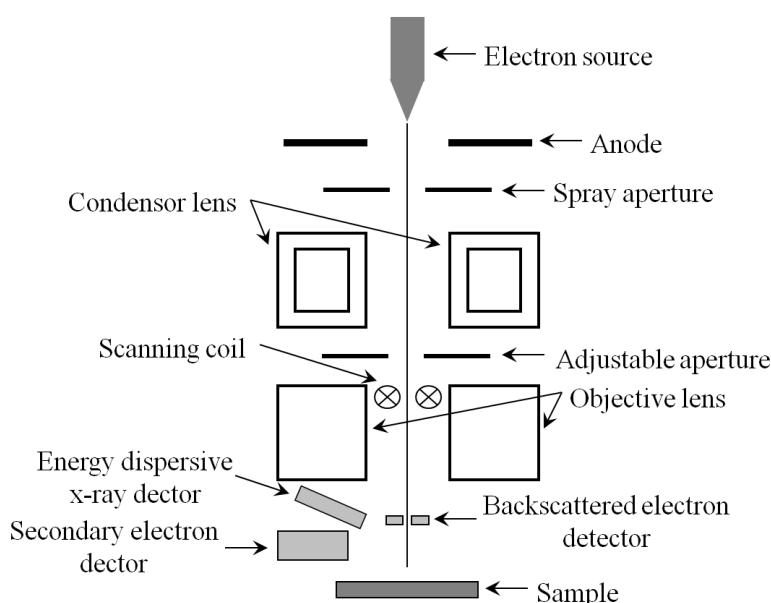
Figure 3.5: Schematic representation of a scanning electron microscope.

The spatial resolution of a SEM depends on the size of the electron spot. In a state-of-art SEM, a field-emission (FE) gun is used to produce sharp electron beams with high current and coherency. Although the electron beam is further confined and focused by condenser lenses, it still interacts with a much larger volume from several hundred nanometers up to micrometers below the specimen surface (known as interaction volume). Because the signals of secondary electrons or backscattered electrons are generated from the upper part of the interaction volume, the resolution of SEM will be not high enough to reach atomic scale, as compared to TEM. The highest resolution of a state-of-art SEM is typically 1-20 nm, depending on the individual equipment, the sample preparation and properties of the specimen.

The electron yield is defined as the number of secondary and backscattered electrons emitted from a specimen when hit by one incident electron. In general, the electron yield is less than unity, which means there are more electrons hitting a specimen than

leaving it, if the specimen is not conductive, negative charges are built up, later the incident electrons are repelled and deviated from their original path, finally lead to the distortions of images. In order to prevent charging effects, nonconductive specimens such as ceramics, polymers and biological materials are usually coated with a thin (2-3 nm) conducting layer of gold or carbon by sputter coating.

In this work, SEM measurements were performed on a Supra 40 VP microscope with a field-emission cathode from ZEISS (Oberkochen, Germany), using an acceleration voltage of 5-20 kV and a working distance of 3-5 mm to analyze the size, the size distribution and the shape of nanoparticles. The Everhart-Thornley detector, VPSE (variable pressure second electron) detector and in-lens detector as secondary electron detectors, a Robinson detector as the BSE detector and a STEM detector were used in the SEM. Statistical analyses were performed based on the software package Scandium 5.0 from Soft Imaging Systems (Münster, Germany) and ImageJ developed by Wayne Rasband (Bethesda, USA). All the samples were prepared by evaporating a single drop of the specimen suspension in demineralised water / ethanol / isopropanol on silicon wafers at room temperature in air. The silicon wafers were then fixed on aluminum sample carriers from PLANO (Wetzlar, Germany) using conductive silver adhesive.

The thin-film morphology of precursor layers, selenized layers and completed solar cells were studied with a XL30 SFEG Sirion from FEI Company (Hillsboro, USA), using a 5 kV acceleration voltage and working distances of 5.9, 4.3 and 3.4 mm. All SEM images of thin-film layers were taken by Dr. E. Ahlswede and his colleagues at the Zentrum für Sonnenenergie- und Wasserstoffforschung (ZSW) in Stuttgart (Germany).

3.2.3 Energy Dispersive X-ray Analysis (EDX)

Energy dispersive X-ray (EDX) analysis is a technique used to determine energy spectra of X-radiations so as to identify elemental compositions of specimens.[38, 39, 41] It is usually performed by a TEM or a SEM equipped with an EDX detector. During an EDX analysis, the specimen is bombarded with a high-energy electron beam and X-radiations are generated by inelastic scattering. When the bombarding electrons knock out electrons of specimen atoms from inner shells, the vacant positions are eventually occupied by higher-energy outer shell electrons, the energy difference between the transition levels is released as X-rays. The specific energy of the released X-ray is characteristic for the energy levels of each element, which can be used to identify the elements present in the specimen. However, in EDX analyses, only elements with atomic numbers equal to or larger than boron can be detected.

The EDX can be used not only for qualitative analysis, but also for quantitative analysis if suitable calibration is performed. By measuring how many X-rays of any type are released per second, it should provide information about how much of the

element is present. However, due to inevitable differences between specimen and calibration standard, considering instrumental and specimen requirements for quantitative analysis, the accuracy of quantitative EDX analysis is relatively low.

In this work, the EDX analysis was performed with a Supra 40 VP SEM from ZEISS equipped with an EDX detector from AMETEC (Berwyn, USA). The applied accelerating voltage was 20-30 kV and the working distance was ~8.5 mm. Dry powder samples for EDX characterization were first pressed to pellets and then fixed on conductive carbon adhesive tapes adhered on aluminum carriers, both from PLANO (Wetzlar, Germany).

3.3 Spectroscopy

Spectroscopy is the study of interaction between matter (i.e., molecules, atoms, nuclei) and radiated energy (i.e. electromagnetic radiation).[43-45] Spectroscopic data are usually represented by spectra that plot the response of interest as a function of wavelength or frequency. Types of spectroscopy can be classified by the different interactions between matter and radiated energy (Table 3.1), which include:

I)   **Absorption:** Absorption occurs when the incident electromagnetic radiation is taken up by the matter and the energy is transformed into the internal energy of the absorber. Different wavelengths of electromagnetic radiation can be absorbed by different matter of species such as atoms and molecules. In general, absorption is evaluated by measuring the amount of radiation that is transmitted through the specimen. This type of spectroscopy typically involves infrared (IR) spectroscopy and ultraviolet-visible (UV-Vis) spectroscopy.

II)   **Emission:** Emission is a process during which electrons at higher-energy states convert to lower ones through the emission of photons, resulting in the production of electromagnetic radiations, such as X-rays, UV-Vis or radio waves. The high-energy electrons are usually excited by an external source of energy such as electromagnetic radiation of higher energy (in case of fluorescence spectroscopy) or flame (in case of atomic emission spectroscopy, AES).

Table 3.1: Information of commonly used spectroscopic techniques, electromagnetic radiation involved, interactions and components of specimen investigated.

Technique	Radiation	Interaction	Components investigated
IR spectroscopy	Infrared	Absorption	Molecular rotations and vibrations, bonds between atoms
UV-Vis spectroscopy	Ultraviolet-visible	Absorption	Electrons, their excitations
Fluorescence spectroscopy	Ultraviolet-visible	Emission	Electrons, their excitations
NMR spectroscopy	Radio wave	Absorption	Nuclei
AES	Ultraviolet-visible	Emission	Atoms

In this work, Fourier transform infrared (FT-IR) spectroscopy, UV-Vis spectroscopy and fluorescence spectroscopy were applied.

3.3.1 Fourier Transform Infrared (FT-IR) Spectroscopy

Infrared (IR) refers to the electromagnetic radiation between visible and microwave regions, having a wavelength of about 780 nm-300 μm. IR is commonly subdivided into three regions: near, mid, and far IR. The mid IR region (3-30 μm) is of greatest practical use in IR spectroscopy.

IR spectroscopy applies infrared radiations to determine the functional groups in organic molecules.[46, 47] When a specimen, which can be solid, liquid or gaseous, is exposed to infrared radiations, different kinds of vibrations of molecules or molecular fragments are excited by interacting dipole moments with infrared radiations. Specific radiant energy or specific wavelength is absorbed, if it matches the energy of a specific molecular vibration. Instead of wavelength, wavenumber $\tilde{v}$ in cm^{-1} as the x-axis is currently preferred in plotting an IR spectrum. Wavenumber, the inverse of the wavelength, is defined as the number of wave cycles in one centimeter. It is proportional to the absorbed energy as described in following equation:

$$\Delta E = hv = h\frac{c}{\lambda} = hc\tilde{v} \tag{3.5}$$

where ΔE is the absorbed energy, h is the Planck's constant, v is the frequency, c is the speed of light, λ is the wavelength, $\tilde{v}$ is the wavenumber.

The transmittance (T), defined as the ratio between the intensity of transmitted radiation (I) and the intensity of incident radiation (I_0), is usually plotted as the y-axis. Sometimes, it can be expressed alternatively as the absorbance (A), which is the logarithm of the reciprocal of the transmittance.

$$A = log_{10}\left(\frac{1}{T}\right) = log_{10}\left(\frac{I_0}{I}\right) \tag{3.6}$$

where A is the absorbance, T is the transmittance, I is the intensity of transmitted radiation, I_0 is the intensity of incident radiation.

By comparing the intensity and wavenumbers of the peaks in IR spectra with a database, specific functional groups and the corresponding vibration modes can be identified.

There are mainly two different types of molecular vibrations, stretching and bending. A stretching vibration can either be symmetric or asymmetric, during which the bond length changes (Figure 3.6). For a bending vibration, the bond angle is changed whereas the bond length remains unchanged. Bending vibration can be subdivided into bending in-plane (rocking and scissoring) and bending out-of-plane (twisting and wagging).

The main type of modern commercial IR spectroscopy is FT-IR spectroscopy, which is able to measure all the infrared frequencies "simultaneously" by using an

interferometer rather than "individually" as in the original dispersive type of infrared instruments. Other advantages of FT-IR spectroscopy include no external calibration, easy handling, short measurement time but high sensitivity and greater optical throughput.

asymmetrical stretching   symmetrical stretching

bending in-plane: rocking   bending in-plane: scissoring

bending out-of-plane: twisting   bending out-of-plane: wagging
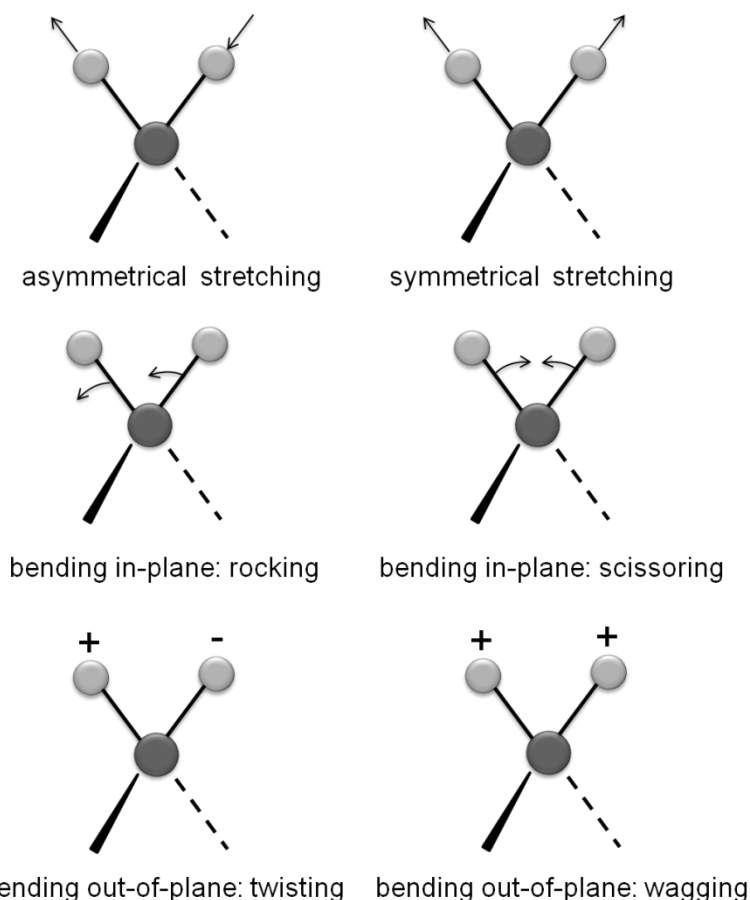
Figure 3.6: Stretching and bending vibrations for a CH_2 group.

In this work, FT-IR spectra were recorded by a Vertex 70 FT-IR spectrometer from BRUKER OPTICS (Ettlingen, Germany), which applied a Globar (a silicon carbide rod) as the radiation source and a pyroelectric detector. The transmittance was measured in a wavenumber range of 4000-400 cm^{-1}. The specimen was measured in KBr pellet. For this purpose, 400 mg dry KBr were carefully pestled with 1 mg specimen and pressed to a thin pellet with pressing tools.

3.3.2 Ultraviolet-Visible (UV-Vis) Spectroscopy

Ultraviolet-visible (UV-Vis) light refers to electromagnetic radiations between X-ray and infrared region, having a wavelength interval of 10-750 nm. Like IR spectroscopy, UV-Vis spectroscopy is also an absorption spectroscopy, which applies the UV-Vis radiation to identify different types of electronic transitions in a specimen.[43, 45, 48] Various types of electronic transitions include:

a) Transition of electrons in high energy orbitals of one atom (e.g., d-d or f-f transitions);

b) Transition of electrons in a molecule from the Highest Occupied Molecular Orbital (HOMO) to the Lowest Unoccupied Molecular Orbital (LUMO), which is known as the excited state or anti-bonding state;

c) Transition of electrons in a complex compound between the ligands and the central atoms (charge transfer transitions);

d) Transition of electrons in semiconducting solids from the valence band to the conduction band.

For the electron transition from the valence band to the conduction band, the energy difference is referred to as the band gap energy (E_g). Only in semiconductors, the band gap energy is low enough for electron transitions. For semiconducting materials, there are generally two types of band gaps: a) the direct band gap, for which the momentum of electrons and holes is the same in both the conduction and the valence bands; b) the indirect band gap, for which the electron transition must pass through an intermediate state and transfer momentum to the crystal lattice. In order to obtain the relation between E_g and the optical absorption, the absorption spectra can be analyzed and E_g can be deduced from a Tauc plot [49] according to the following equation [50, 51]:

$$\alpha h\nu = C(h\nu - E_g)^n \tag{3.7}$$

where α is the absorption coefficient, $h\nu$ is the energy of incident radiation, C is a constant relative to the material, E_g is the band gap energy, and n is either 1/2 for a direct band gap semiconductor or 2 for an indirect band gap semiconductor .

By plotting $(\alpha h \nu)^{1/n}$ versus the photon energy $h\nu$ in a Tauc plot, a curve with a section of straight line can be obtained. If the straight line is extended to the x-axis, the intercept ($(\alpha h \nu)^{1/n} = 0$) shows the value of the band gap energy.

When a specimen is exposed to UV-Vis radiation that matches the energy difference of a possible electron transition in a molecule, part of the radiant energy will be absorbed and the electrons in the molecule will be excited to higher energy orbital. An UV-Vis spectroscope records the absorption at different wavelengths and a spectrum of absorbance (A) versus wavelength (λ) can be plotted. UV-Vis spectra usually show a few broad absorbance peaks. Compared with IR spectroscopy, which is featured by sharp and strong peaks, UV-Vis spectroscopy provides limited qualitative information. The wavelength, at which the specimen absorbs the maximum amount of energy, is known as λ_{max}. The position of λ_{max} is not fixed but depends on many parameters such as the molecular environment, the solvent, the PH-value and the temperature. Conjugation of multiple bonds reduces the required energy for excitation and also increases both intensity and λ_{max}.

In this work, optical spectra in UV-Vis region of powder samples were collected in a wavelength interval of 250-900 nm with a Cary 100 spectrometer from VARIAN (Palo Alto, USA). The spectrometer was equipped with an integrating sphere from LABSPHERE (North Sutton, USA). A deuterium lamp was used as the UV-light source; a quartz halogen lamp was used as the visible light source. To eliminate background noise, barium sulfate was applied as the reference for powder samples.

3.3.3 Fluorescence Spectroscopy

The fluorescence spectroscopy is applied to study fluorescence and phosphorescence of specimens during their molecular relaxation from electronic excited states to ground state by generating emission or excitation spectra. Furthermore, it is also possible to investigate the time-dependent development of specimen fluorescence and to determine quantum yields.[44, 52]

With most fluorescence spectroscopes, both emission and excitation spectra can be recorded. An emission spectrum is the wavelength distribution of an emission measured at a single constant excitation wavelength. But recording an excitation spectrum is a converse procedure. An excitation spectrum is the dependence of emission intensity, measured at a fixed emission wavelength, on scanning the excitation wavelength. Figure 3.7 shows a schematic diagram of a fluorescence spectroscope, which consists normally of the following components: a light source, an excitation monochromator, a specimen chamber, an emission monochromator and a detector. At present a xenon arc lamp is often used as a source of exciting light, which provides a relatively continuous radiation from 250 to 700 nm. The monochromators are applied to select both the excitation and emission wavelengths. The dual grating monchromator, containing two gratings as shown in Figure 3.7, suppresses stray light (light with wavelengths different from the chosen one). In the specimen chamber, there are versatile and stable optical components surrounding the sample holder, which are essential for a fluorescence spectroscope, such as shutters, filters, beam splitters and polarizers. Almost all state-of-arts fluorescence spectroscopes utilize photomultiplier tubes (PMT) as detectors.
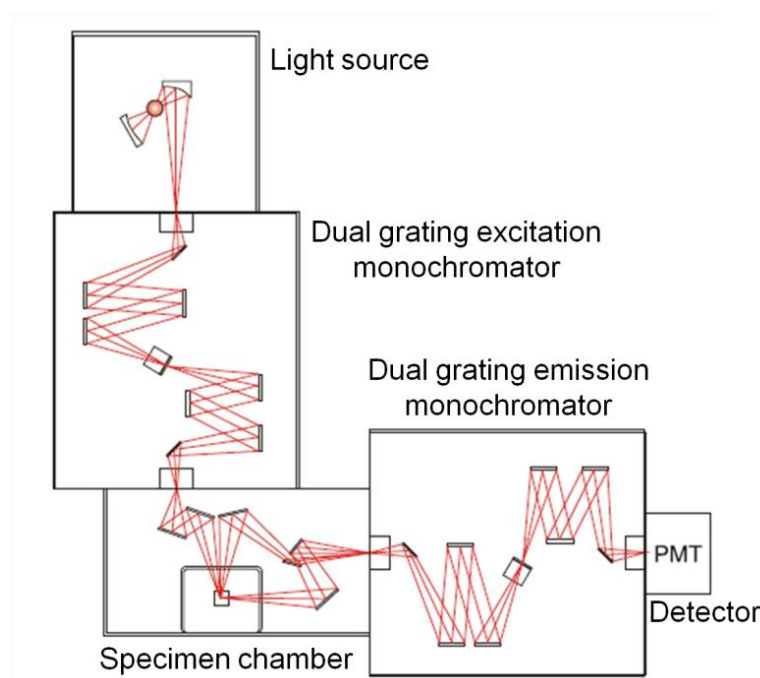
Figure 3.7: Schematic diagram of a Jobin Yvon Spex Fluorolog 3.

The photoluminescence is a simultaneous light emission of a specimen during the electronic transition from an excited state to the ground state after absorbing higher energy radiation. The efficiency of this process can be quantified by the quantum yield, which is expressed in percentage and defined as the ratio between the number of emitted photons and the number of absorbed photons. For most fluorophores, the quantum yields and emission spectra are independent from excitation wavelength, so these fluorophores, served as quantum yield standard references, can be used at any given wavelength with useful absorption. The easiest way to measure the quantum yield of a specimen is by comparison with standard references of known quantum yield with the following equation:

$$Q = \frac{E_S A_R}{E_R A_S} Q_R \tag{3.8}$$

where Q is the quantum yield of the specimen, Q_R is the quantum yield of reference, E_S and E_R are the measured emission intensities of the specimen and the reference, A_S and A_R are the measured absorbance of the specimen and the reference, respectively. The fluorescence spectroscope can also measure the absolute quantum yield as compared with an empty quartz cuvette in an integrating sphere.

In this work, photoluminescence was recorded with a Jobin Yvon Spex Fluorolog 3 equipped with a 450 W xenon arc lamp and double grating excitation and emission monochromator (Figure 3.7). The specimens were measured in quartz cuvettes of quality 6Q from STARNA (Pfungstadt, Germany) as a solid powder, in suspension or in solution.

3.4 Further Methods

3.4.1 Dynamic Light Scattering (DLS)

Dynamic light scattering (DLS) is a technique that can be used to determine the size distribution of small particles in suspension or polymers in solution. It is also known as photon correlation spectroscopy or quasi-elastic light scattering.[53, 54]

Small particles in suspension are constantly moving with a certain velocity due to Brownian motion. Brownian motion is the movement of particles resulting from the random collision with the atoms or molecules of the gas or liquid that surrounds the particles. An important feature of Brownian motion for DLS is that small particles move quickly but large particles move slowly. If the small particles are illuminated by a light source such as a laser, the light is scattered in all directions (Rayleigh scattering). Due to the moving particles, the constructive and destructive phase of the scattered light will cause fluctuation of the intensity. DLS measures the time-dependent fluctuation of the scattering intensity, uses these data to calculate the diffusion coefficient and the size of the particles. The relationship between the particle size and its diffusion coefficient is defined in the Stokes-Einstein equation.

$$D = \frac{kT}{3\pi\eta d} \tag{3.9}$$

where D is the diffusion coefficient, T is the absolute temperature, η is the viscosity of liquid, k is the Boltzmann's constant, d is the particle size.

In order to obtain reliable data of the particle size, temperature has to be kept constant within ±0.1 K. The stokes-Einstein equation is only valid for non-interacting, smooth, rigid, spherical particles and is an approximation for other cases.

A typical size distribution graph generated by DLS is an intensity distribution, which can be converted to a volume distribution using Mie theory. The volume distribution can be further converted to a number distribution.

In this work, DLS was used to determine the average particle size and the size distribution in diluted suspensions. The suspensions were measured in polystyrene cuvettes from VWR (Germany) with a Nanosizer ZS from Malvern Instruments (Herrenberg, Germany). The detection is via non-invasive back-scattering at an angle of 173 $^\circ$ and 256 detector channels. The light source was a 4.0 mW He-Ne laser emitting at 633 nm. For analysis, the as-prepared nanoparticles were redispersed in demineralised water, ethanol or isopropanol by ultrasonic treatment for 15 minutes. All the size distribution graphs were a number distribution.

3.4.2 Thermal Analysis

Thermal analysis is a group of techniques in which the physical and chemical properties of a substance are measured as a function of temperature while the substance is subjected to a controlled temperature program.[55] Especially, endothermic and exothermic effects, such as phase transitions, thermal decompositions or solid state reactions can be studied. Typical thermal analytical techniques include thermogravimetric analysis (TGA), differential scanning calorimetry (DSC) and differential thermal analysis (DTA).

Thermogravimetric analysis (TGA) is widely used to determine a material's thermal stability and/or its fraction of volatile components by measuring the changes in mass that occur in response to temperature changes. During the measurement, the specimen is heated at a constant heating rate to a defined temperature while the weight of the specimen is recorded. Various processes, such as adsorption, desorption, vaporization, sublimation, decomposition, degradation, oxidation and reduction, can result in weight changes, which helps to identify and characterize the properties of the specimen.

Differential scanning calorimetry (DSC) and differential thermal analysis (DTA) can be used to obtain the thermal critical points like melting point, enthalpy specific heat or glass transition temperature of a material by measuring the difference in energy inputs into a specimen and a reference material as a function of temperature. The

reference should not exhibit any transformation in the measured temperature range. Both DSC and DTA provide similar information, but DSC measures the energy required to keep both the specimen and the reference at the same temperature, whereas DTA measures the temperature difference between the specimen and the reference when supplying the same amount of energy.

The practical application of thermal analysis involves usually the integration of two or more techniques simultaneously to the same specimen, for instance, TG and DSC/ DTA, to achieve more accurate specimen characterization. A typical measurement setup is shown in Figure 3.8.
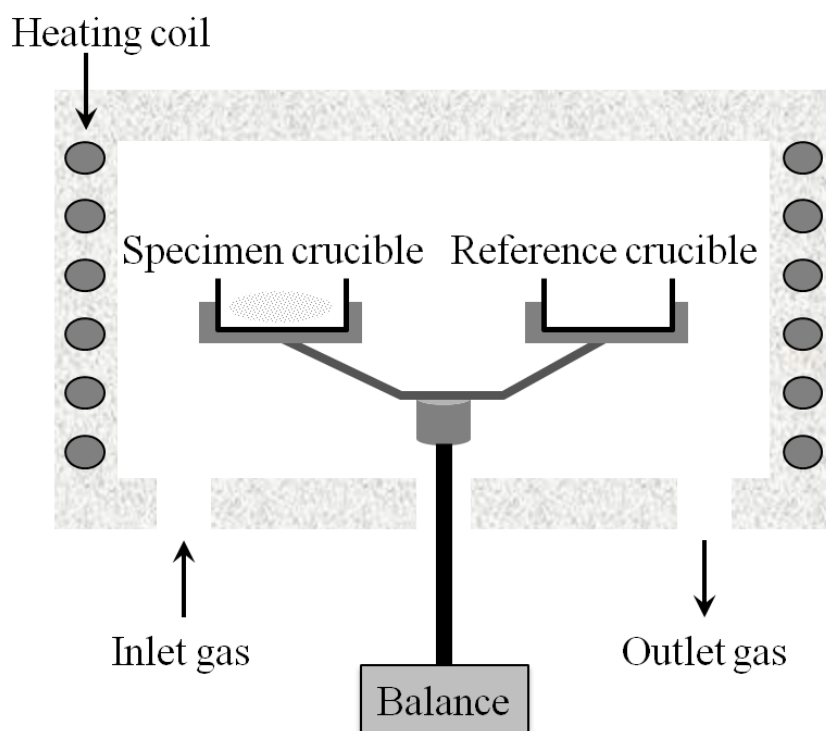
Figure 3.8: Schematic representation of a TG-DSC/DTA setup.

In this work, TGA and DSC were performed simultaneously with a STA 409C instrument from NETZSCH (Selb, Germany). The specimens were heated under N_2 flow (100 mL min^{-1}) or in air with a heating rate of 5 or 10 K min^{-1}. The crucibles made out of α-Al_2O_3 were applied as specimen holders and the reference sample.

3.4.3 Brunauer-Emmett-Teller (BET) Method

In order to measure the specific surface area of a substance quantitatively, a method was proposed by Brunauer, Emmett and Teller in 1938 and named BET method.[56, 57] The BET method is based on physical adsorption of gas molecules on a solid surface. The amount of gas adsorbed at a constant temperature, typically 77 K from the temperature of liquid N_2, can be measured as a function of the equilibrium pressure of gas. By applying an adsorption isotherm, the specific surface can be calculated.

When a gas comes into contact with a solid, the gas molecules (adsorptive) can be adsorbed to the surface of the solid (adsorbent) via physical or chemical interaction. The adsorption bound by weak van der Waals forces is known as physisorption, whereas the adsorption attracted by chemical bonding, generally covalent bonds, is chemisorption. Physisorption is practically reversible due to the very low activation energy. Because it is an exothermic process, the physisorption occurs more readily at lower temperatures and will decrease with increasing temperature. Under appropriate conditions, gas molecules can form multilayer adsorption. In chemisorption, a chemical bond, usually covalent, is formed between adsorptive and adsorbent, making chemisorption an irreversible process. Compared to physisorption, the activation energy for chemisorption is much higher, so the chemisorption process is in general much slower than the physisorption process. Although chemisorption is as well an exothermic process, it does not benefit from low temperature. Like most chemical changes, the extent of chemisorption increases with increasing temperature up to a certain limit and after that it starts decreasing. In most cases, only monolayer adsorption forms.

The assumptions of the BET method are: (a) gas is adsorbed physically on a homogeneous solid surface; (b) there is no lateral interaction between the adsorbed gas molecules; (c) when the surface is partially covered by adsorbed gas molecules, additional gas can be adsorbed either on the remaining free surface or on top of the already adsorbed layer. At saturation pressure, the number of layers becomes infinite and the uppermost layer is in equilibrium with the vapor phase. As the most common method used to determine the specific surface area, according to the theory derived by Braunauer, Emmett and Teller, the BET equation can be described as

$$\frac{p}{v(p_0 - p)} = \frac{1}{v_m c} + \frac{c-1}{v_m c}\frac{p}{p_0} \tag{3.10}$$

where p and p_0 are the equilibrium and saturation pressure of adsorptive, respectively, v is the volume of the adsorbed gas, v_m is the volume of monolayer and c is the BET constant.

By plotting p/v $(p_0 - p)$ against p/p_0 in the range of $0.05 < p/p_0 < 0.35$, a straight line is obtained with a slope (s) and an intercept (i) with y-axis.

$$i = \frac{1}{v_m c} , s = \frac{c-1}{v_m c} \tag{3.11}$$

where i is the intercept of the fitted straight line with y-axis, v_m is the volume of monolayer, c is the BET constant and s is the slope of the fitted straight line.

From Equation 3.11, the monolayer volume v_m can be calculated and the specific surface area S_{BET} is given by

$$S_{BET} = \frac{v_m N_A A_{cs}}{M_v w} \tag{3.12}$$

where S_{BET} is the specific surface area, v_m is the volume of monolayer, N_A is Avogadro's number, A_{cs} is the cross sectional area of the adsorptive, M_v is the molar volume of adsorptive and w is the specimen weight.

In this work, BET analyses of dried powder specimens were carried out with a BELSORP-mini II instrument from BEL JAPAN (Osaka, Japan) in order to determine the specific surface areas. The applied adsorptive was gaseous helium. The specimens were cooled with liquid N_2 to a temperature of 77 K during the measurement.

4 Results and Discussion

4.1 Chalcogenide Thin-film Solar Cells

4.1.1 Background

Generally, CISe/CIGSe layers are deposited by applying high-vacuum techniques. After thermal co-evaporation of the relevant elements (e.g., Cu, In, Ga and Se), sequential processes are often to be continued, where typically thermal-evaporated Se is deposited as thin top coating on Cu-/In-/Ga-containing precursor layers.[58] In a second step, these layers are chemically converted into the desired chalcopyrite structure of the CISe/CIGSe absorber via a thermal process at 550-600 °C, which is called "selenization". The Se capping layer supplies a sufficient Se source during the heating step. Usually, an additional treatment in harmful H_2S atmosphere is applied during the annealing step to improve the electronic quality of the absorber layers.[10]

CZTS/CZTSe recently attracted considerable attention since the raw materials are abundant and less expensive (In/Ga-free) than CIS/CISe or CIGS/CIGSe. It has low toxicity, as compared with CdTe semiconductors that are also intensely discussed for solar-cell applications.[11, 12, 15-17] The preparation of CZTS/CZTSe thin films has often been performed by gas-phase methods such as co-evaporation or sputtering of the elements.[17, 59] Using solution-processed CZTS/CZTSe thin-films and CZTS/ CZTSe nanoparticles have become versatile strategies that are interesting for large-scale printing of solar cells on glass or even on flexible substrates. The highest efficiencies of CZTS/CZTSe thin-film solar cells were yet reported with values up to 11 % from solution-based processing.[60] Currently, solution-processed CZTS/CZTSe thin-films mainly rely on metal-hydrazine complexes as precursor materials that are highly toxic, reactive and difficult to handle.[17, 59-63] In addition, they require high-temperature sulfurization/selenization treatments to form crystalline CZTS/ CZTSe.[17, 59] Hydrazine-processed CZTS/CZTSe thin-film solar cells have disadvantages in view of environmental issues, cost of production, and the thermal stability of the substrates. For CZTS/CZTSe nanoparticles, several studies have already shown that the concrete conditions of the liquid-phase syntheses dramatically influence the elemental composition (Cu:Zn:Sn ratio, excess/defective S/Se), the morphology (spheres, lens-shapes, rods), the crystallinity (almost amorphous to highly crystalline) and the structure (tetragonal or hexagonal) of the CZTS/CZTSe nanoparticles − and thereby the band gap, absorbance and solar-cell performance.[11, 15-17, 59, 64] The size and shape of CZTS/CZTSe nanoparticles can be precisely controlled in liquid-phase syntheses by using functionalized long-chained alkyl stabilizers, for example, oleylamine, oleic acid, dodecanethiol, polyvinylpyrrolidone (PVP).[11, 12, 59, 60, 64-72] Such stabilizers are highly beneficial to the particle nucleation, however, their removal during solar-cell

processing can be difficult, and the remaining stabilizers and carbon contents can significantly influence the solar-cell performance.

The vacuum co-evaporation techniques are the major deposition method resulting in the highest efficiencies of CIGS/CIGSe thin-film solar cells.[13, 73] However, the functional complexity, high initial investment and maintenance expenses, yield and throughput limitations of vacuum processes are still major obstacles in realizing substantial manufacturing cost reduction. Alternatively, non-vacuum processes, using simple and low cost devices, enable a fast processing speed. Besides, they have high material utilization efficiencies and low energy input, even though they sacrifice part of the solar cell efficiency.[74-77] In recent years, paste coating as one of the non-vacuum deposition methods has attracted increasing attention. One possibility for the paste formulation is to disperse nanoparticles such as metals/alloys (Cu, In, $CuIn/Cu_{11}In_9$),[78-80] metal oxides[81] or metal sufides/selenides ($CuInSe_2$, $Cu_2Se/CuSe$, In_2Se_3, Cu_2ZnSnS_4)[65, 82-85] with a desired stoichiometry in a liquid binder.

In this chapter, the syntheses of the binary (Cu_2Se and In_2Se_3) and the quaternary (Cu_2ZnSnS_4) chalcogenide nanoparticles via polyol-mediated syntheses and hot-injection techniques are introduced in order to prepare stoichimetric inks for paste coating. The Se@CuSe and Te@Bi_2Te_3 core@shell nanoparticles, synthesized as the selenium and tellurium sources for printable thin-film solar cells are presented next. In addition, the absorption layers prepared by these nanoparticles, and their solar-cell behaviors and efficiencies are investigated.

4.1.2   Copper Selenide and Indium Selenide Nanoparticles

CuSe nanoparticles without additional surfactant
The synthesis of CuSe nanoparticles was performed under argon inert-gas protection. In a typical synthesis, 72.6 mg (0.4 mmol) $Cu(CH_3COO)_2$ were added to 50 mL DEG in a three-neck flask. The powder precursor was dissolved under continuous stirring to form a homogeneous blue solution (solution I) at room temperature. 50.0 mg (0.4 mmol) Na_2Se were dissolved in 2 mL ethanol in a schlenk flask (solution II). After inserting the three-neck flask into the preheated oil bath at 180 ℃, solution I was heated to 150 ℃ in 5 minutes, solution II was then injected into the three-neck flask with a syringe. After 60 minutes of reaction, the three-neck flask was taken out of the oil bath and cooled to room temperature naturally. The final black suspension was diluted with ethanol, and the product was collected via centrifugation and washed by repeated redispersion/centrifugation in/from ethanol.

All analytic characterizations were carried out under air. The average particle size and the size distribution of the as-prepared CuSe nanoparticles in ethanol were determined by DLS (Figure 4.1). To this concern, particles with a relatively broad size distribution and a mean diameter of 128(54) nm were obtained. The SEM images

confirm the DLS result with respect to the particle size and the broad size distribution (Figure 4.2) and show that the as-prepared CuSe nanoparticles have irregular platelet morphology. The thickness of the CuSe platelet is about 20 nm.
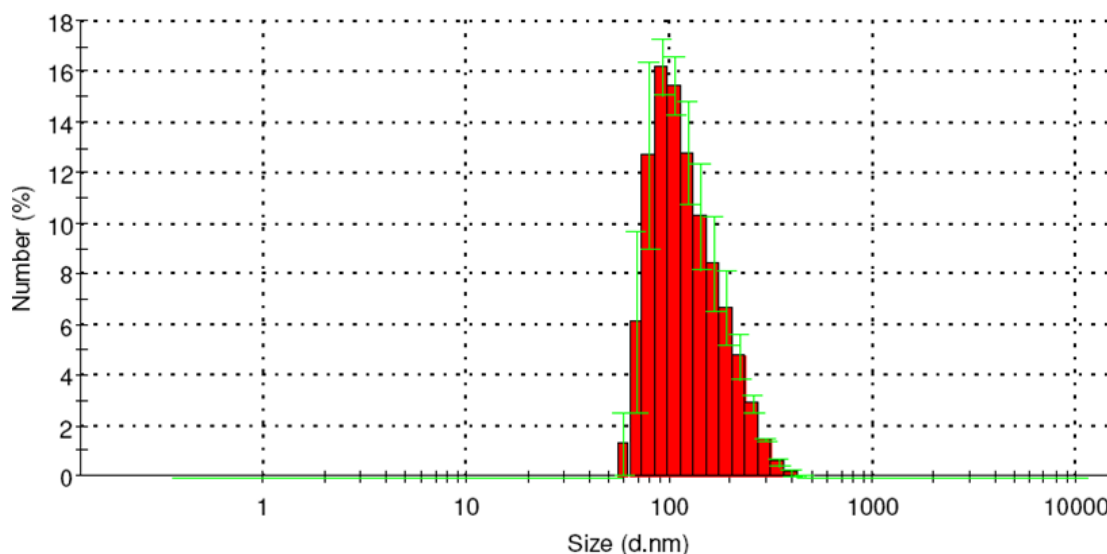
Figure 4.1: DLS analysis of the as-prepared CuSe nanoparticles in ethanol.
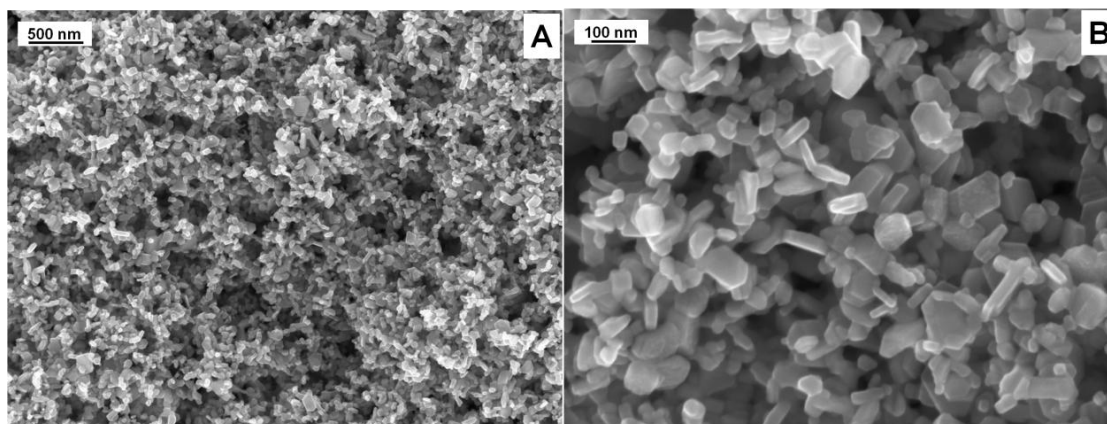
Figure 4.2: SEM images of the as-prepared CuSe nanoparticles (A: large scale overview; B: high resolution image).

The phase composition and the structure of the as-prepared CuSe nanoparticles were investigated by XRD. The XRD pattern of the as-prepared black powder, which fits well with the corresponding reference data (ICDD No. 27-184), proves the presence of crystalline CuSe (Figure 4.3).
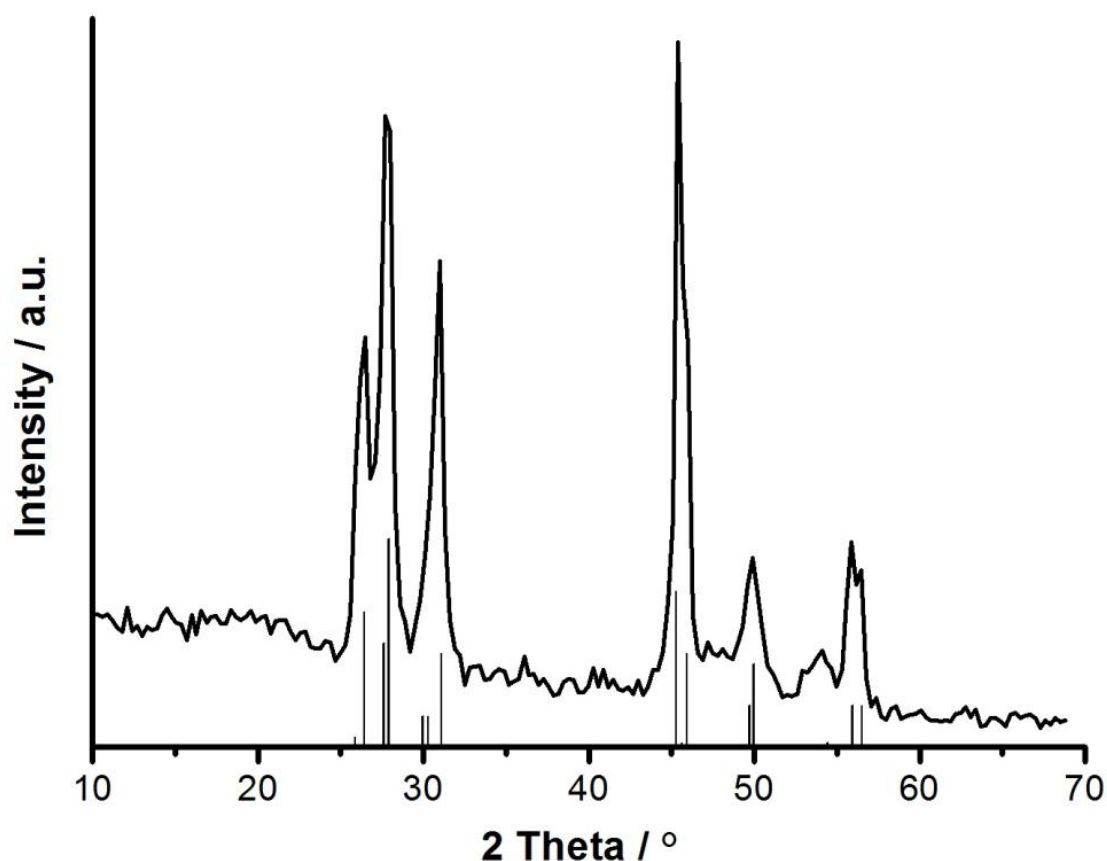
Figure 4.3: XRD pattern of the as-prepared CuSe nanoparticles (CuSe_ICDD No. 27-184 as a reference).

Such crystalline platelet CuSe nanoparticles with relatively large particle size and broad size distribution are not suitable for layer deposition and manufacturing of thin-film solar cells. Thus, 2,2'-thiodiethanethiol ($C_4H_{10}S_3$, Figure 4.4) was introduced to the synthesis as a surfactant to control the particle size and the morphology of CuSe nanoparticles.
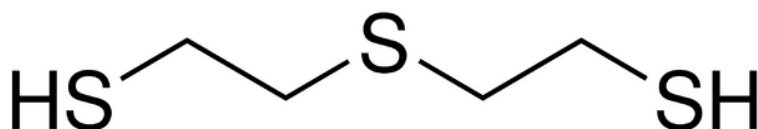
Figure 4.4: Skeletal formula of 2,2'-thiodiethanethiol.

Copper selenide nanoparticles with 2,2'-thiodiethanethiol as the surfactant
In a typical synthesis, 36.3 mg (0.2 mmol) $Cu(CH_3COO)_2$ were added to 50 mL DEG in a three-neck flask. The powder precursor was dissolved under continuous stirring to form a homogeneous blue solution (solution I) at room temperature. 25.0 mg (0.2 mmol) Na_2Se were dissolved in 3 mL $C_4H_{10}S_3$ and 1 mL ethanol in a schlenk flask (solution II). After solution I had been heated to 60 °C in an oil bath, solution II was injected with a syringe. After 1 minute of reaction, part of the resulting suspension was extracted from the system at 60 °C for further analysis (sample I). The residual part was put into another preheated oil bath of 180 °C for 15 minutes (sample

II). At last, the three-neck flask was removed from the oil bath and cooled to room temperature naturally. Two batches of the black suspensions from different temperatures were diluted with ethanol, and the copper selenide nanoparticles were collected via centrifugation and washed repeatedly with ethanol.
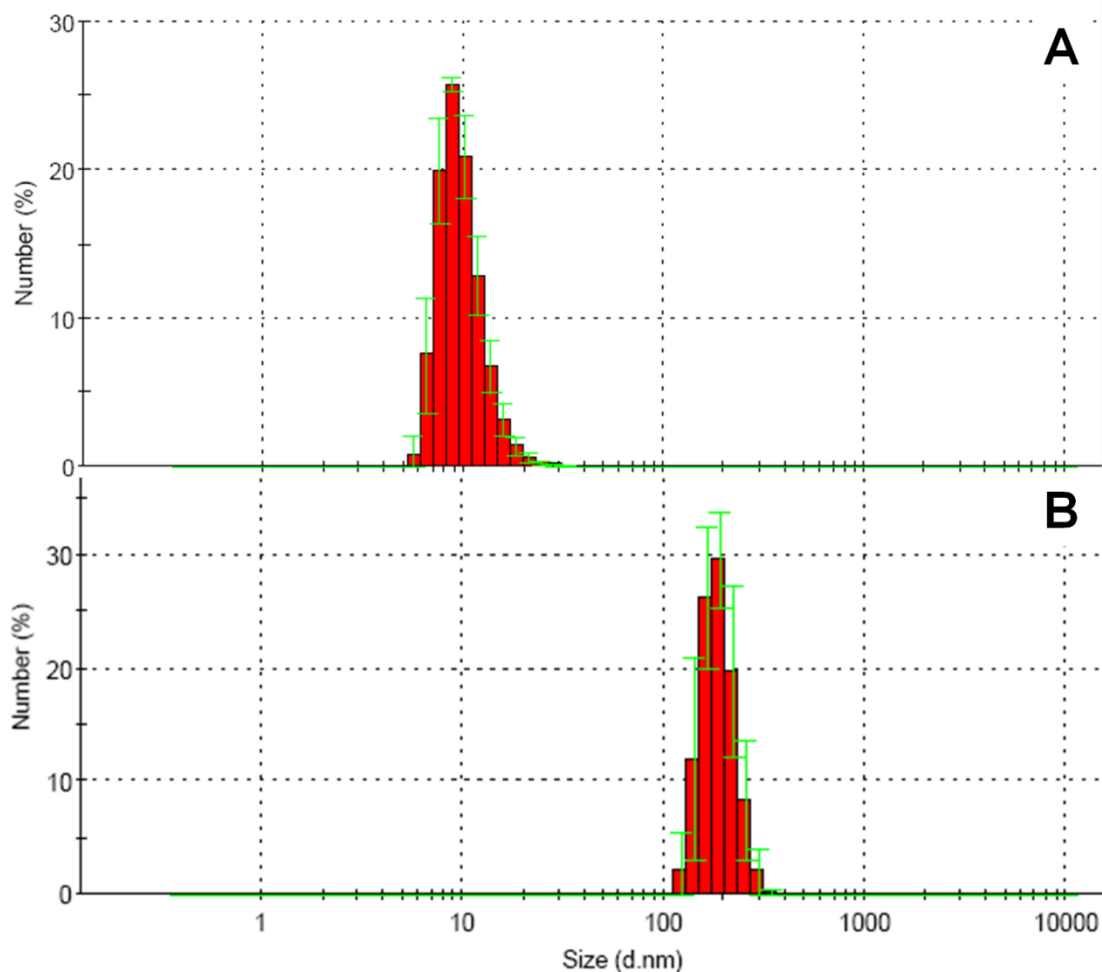
Figure 4.5: DLS analyses of the as-prepared copper selenide nanoparticles in DEG (A: sample I from 60 ℃ suspension; B: sample II from 180 ℃ suspension).

The as-prepared suspensions are colloidally stable for months, especially for sample I, its nanoparticles are more difficult to be separated from its as-prepared suspension by centrifugation as compared to sample II. The particle size and the size distribution of the sample I and II in DEG were quantified by DLS (Figure 4.5). Both suspensions were diluted with DEG prior to the DLS analysis in order to exclude the concentration artifacts. According to the DLS analyses, the mean diameters of the as-prepared copper selenide nanoparticles amount to 9(2) nm for sample I (from 60 ℃ suspension, Figure 4.5A) and 190(36) nm for sample II (from 180 ℃ suspension, Figure 4.5B). The extremely small particle size is the reason why the suspension of sample I is colloidally more stable than the suspension of sample II. The suspension of sample I exhibits a narrow size distribution. Subsequently, scanning electron microscopy of the as-prepared samples was applied to obtain a direct view of the copper selenide nanoparticles (Figure 4.6).

The SEM images of sample I reveal that the copper selenide nanoparticles prepared at 60 °C have a spherical shape and are very uniform in morphology. SEM images were also used for a statistical evaluation of the particle size and the size distribution. To this concern, a mean diameter of 38(6) nm was deduced based on 200 particles from Figure 4.6A. However, this value, which does not fit with the DLS analysis, is about four times larger than the hydrodynamic diameter. This is because after being centrifuged out of DEG suspension and redispersed in ethanol, the small nanoparticles were not as stable as in a DEG suspension and trended to form small agglomerates. From high resolution image (Figure 4.6B), we can clearly see that the agglomerates of 30-40 nm in diameter are formed by nanoparticles of about 10 nm in diameter.
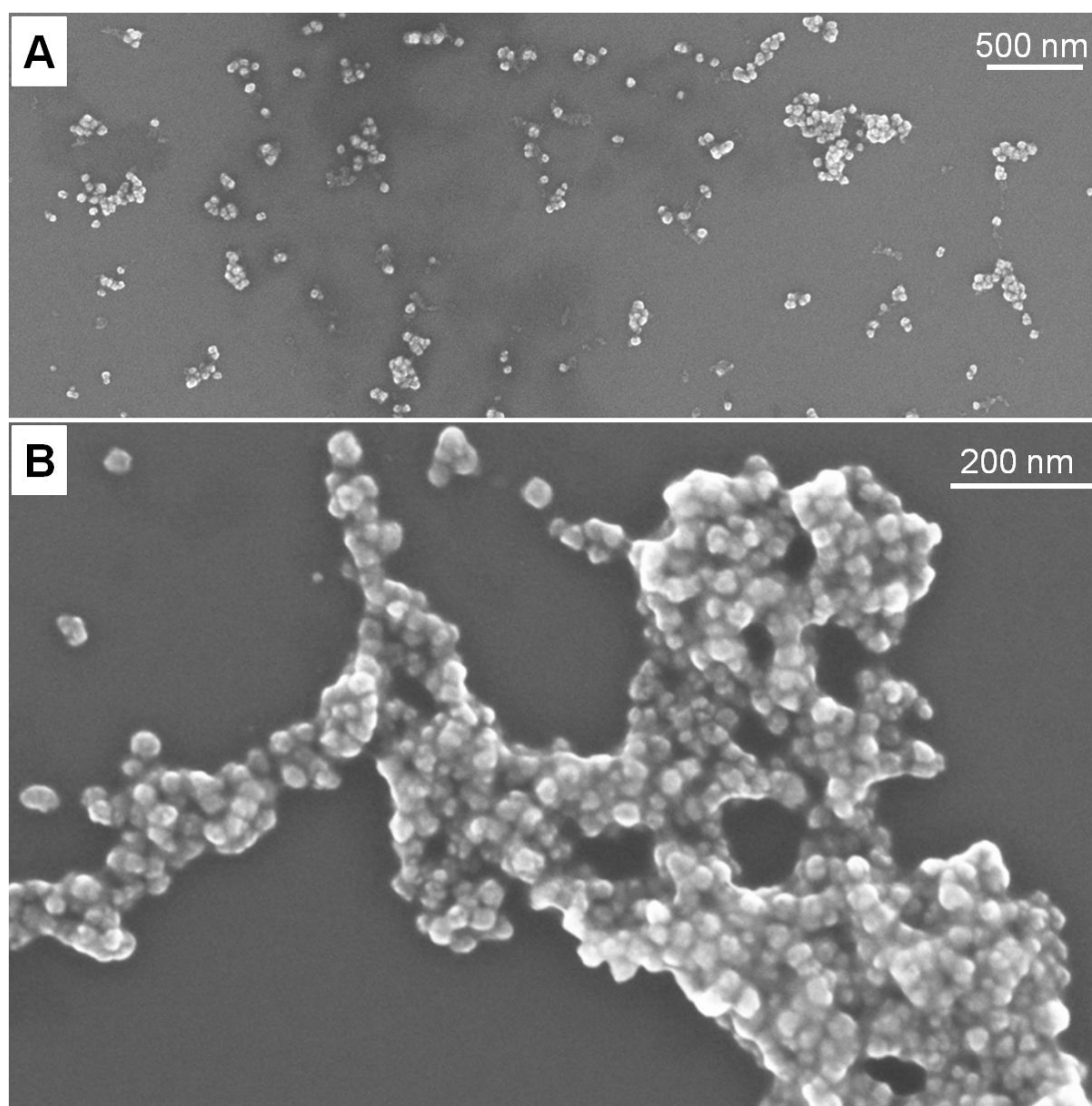
Figure 4.6: SEM images of the copper selenide agglomerates from sample I (A: large scale overview; B: high resolution image).

The SEM images of sample II prepared at 180 °C only show small and large aggregates without single agglomerates of 30-40 nm in diameter (Figure 4.7A). The individual nanoparticles of about 10 nm in diameter were not detectable because they

had merged together to form larger nanoparticles of 30-40 nm in diameter. Due to the high reaction temperature, the newly formed large nanoparticles also started to fuse together. The necks between particles are clearly visible in Figure 4.7B. This explains the reason why the DLS analysis of sample II shows a much larger particle size than sample I (Figure 4.5).
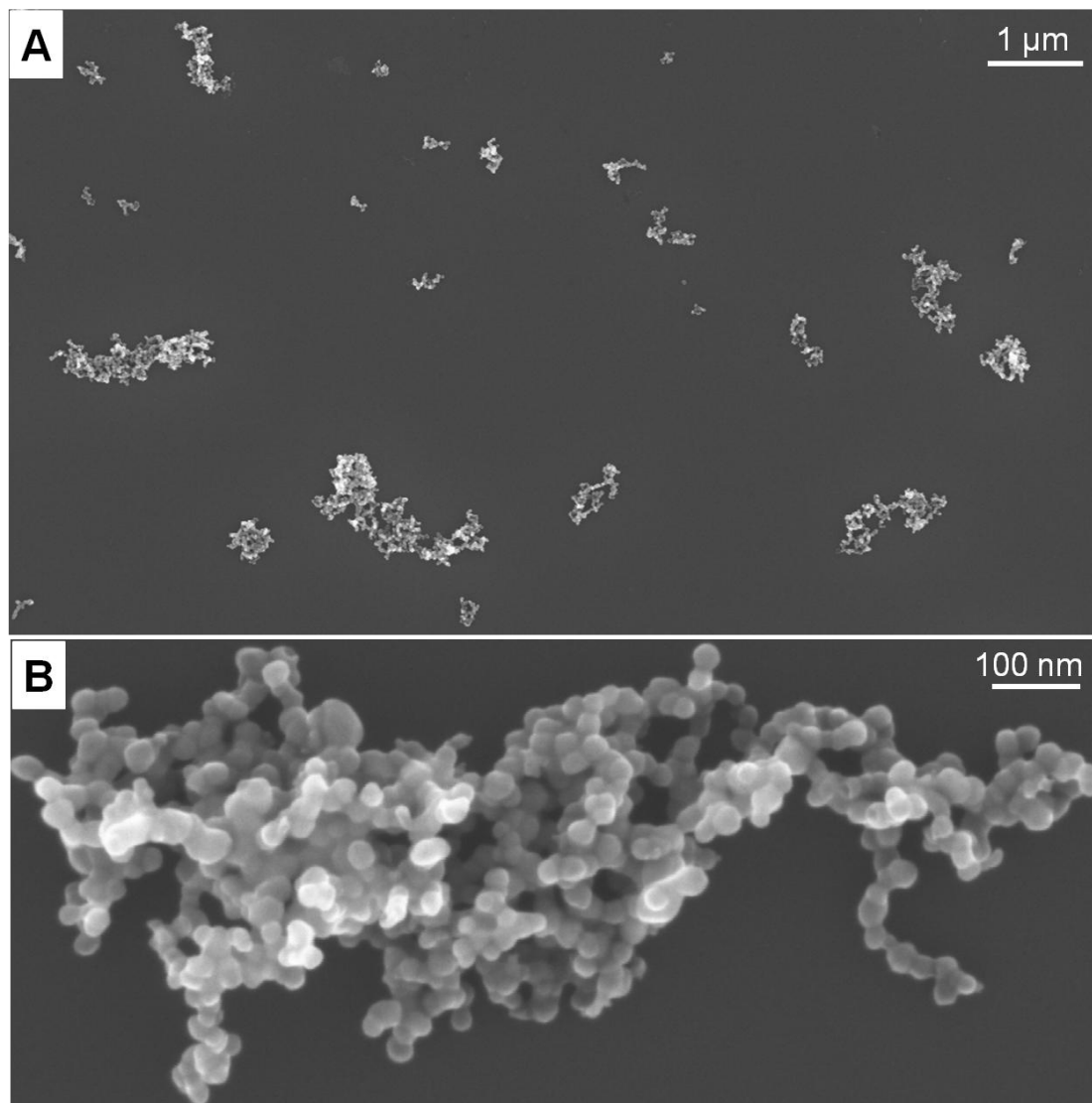
Figure 4.7: SEM images of the copper selenide aggregates from sample II (A: large scale overview; B: high resolution image).

The XRD pattern of sample I shows very broad peaks (Figure 4.8a), which may result from very small particle size of about 10 nm in diameter and a low degree of crystallinity due to the low reaction temperature (60 ℃). Because of the broad peaks, it is difficult to fit them with the reference patterns. After heating the suspension to 180 ℃, the XRD pattern of sample II presents many sharp peaks (Figure 4.8b) that are in agreement with several reference compounds. Besides Cu_2Se/Berzelianite (ICDD No. 1088-2043) and $CuSe$ (ICDD No. 20-1020) shown in Figure 4.8 as references, Cu_3Se_2/Umangite (ICDD No. 1071-45), γ-$CuSe$/Klockmannite (ICDD No. 1070-8585) and Cu_7Se_4 (ICDD No. 26-557) also exist in sample II.
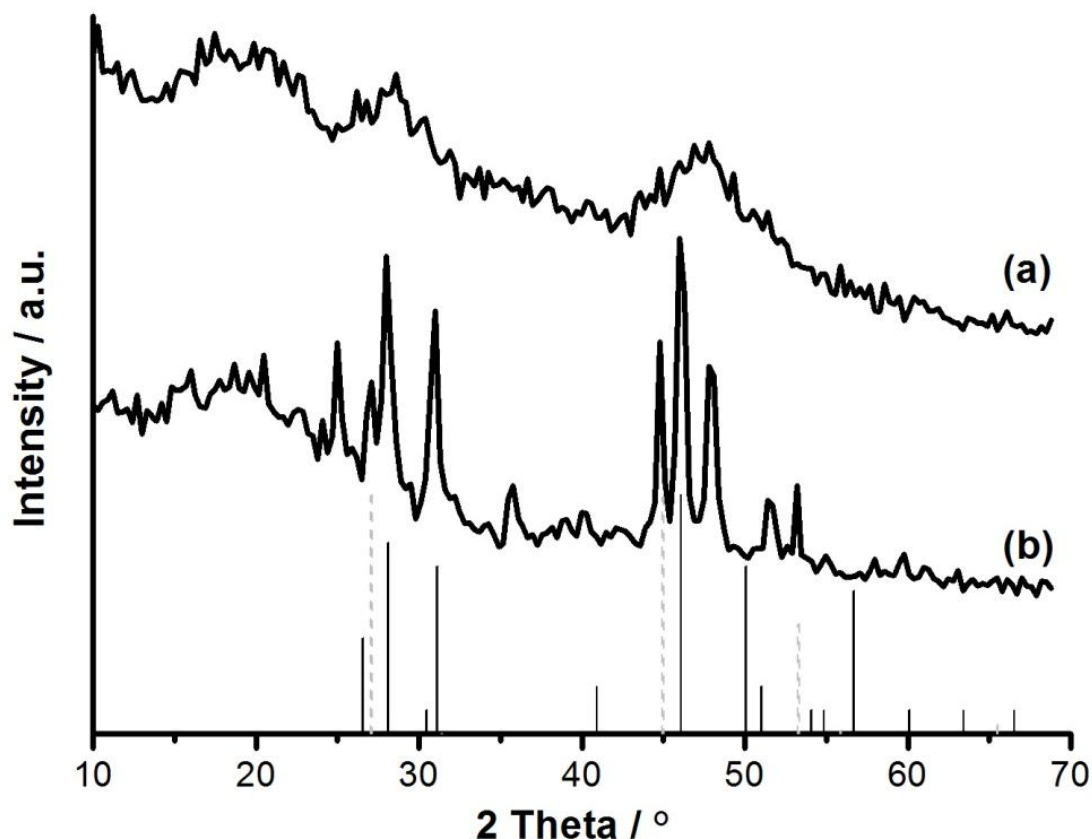
Figure 4.8: XRD patterns of the as-prepared copper selenide nanoparticles: (a) sample I prepared at 60 ℃; (b) sample II prepared at 180 ℃ (Cu_2Se/Berzelianite_ ICDD No. 1088-2043/grey dash lines and CuSe_ICDD No. 20-1020/black solid lines as references).

According to the XRD pattern of sample II, the product prepared at 180 ℃ is a mixture of Cu-rich phases (Cu_2Se, Cu_3Se_2 and Cu_7Se_4). Such mixture phases are difficult to quantify the amount of copper and to obtain a desired stoichiometry in precursor inks. From the XRD results, we can also conclude that the expected CuSe is not a stable phase in our reaction system; in contrast, Cu-rich phases of copper selenide are facile to obtain. Furthermore, it requires much effort to collect nanoparticles from the DEG suspension of sample I due to the small particle size and a large amount of surfactant in the suspension. High temperature reaction leads to large aggregates and a broad size distribution, which are not suitable for layer deposition and manufacturing of thin-film solar cells. Thus, pure Cu_2Se nanoparticles of 20 nm in diameter were synthesized by introducing more $Cu(CH_3COO)_2$ and less amount of surfactant with longer reaction time and a moderate reaction temperature.

Cu_2Se nanoparticles with 2,2'-thiodiethanethiol as the surfactant
In a typical synthesis, 72.6 mg (0.4 mmol) $Cu(CH_3COO)_2$ powder was dissolved in 50 mL DEG under continuous stirring in a three-neck flask (solution I). 25.0 mg (0.2 mmol) Na_2Se were added to 1 mL $C_4H_{10}S_3$ and 2 mL DEG in a schlenk flask (solution II). After solution I had been heated to 80 ℃ in an oil bath, solution II was

injected with a syringe. After the reaction at 80 ℃ for 5 minutes, the three-neck flask was taken out of the oil bath and cooled to room temperature naturally. The final black suspension was diluted with ethanol, and the Cu_2Se nanoparticles were collected via centrifugation and washed by repeated redispersion/centrifugation in/from ethanol.

The as-prepared black Cu_2Se suspension in DEG is less stable than the as-prepared copper selenide suspension of sample I. All Cu_2Se nanoparticles can be easily separated from the DEG suspension and a colorless clear supernatant was obtained after centrifugation. Due to a reduced amount of $C_4H_{10}S_3$ (from 3 to 1 mL) introduced to the synthesis, a higher reaction temperature (from 60 to 80 ℃) and a longer reaction time (from 1 to 5 minutes), an increase in particle size was expected. In order to determine the particle size and the size distribution of the as-prepared Cu_2Se nanoparticles in ethanol, DLS analysis was applied (Figure 4.9). The nanoparticles with a relatively broad size distribution and a mean diameter of 93(28) nm were obtained.
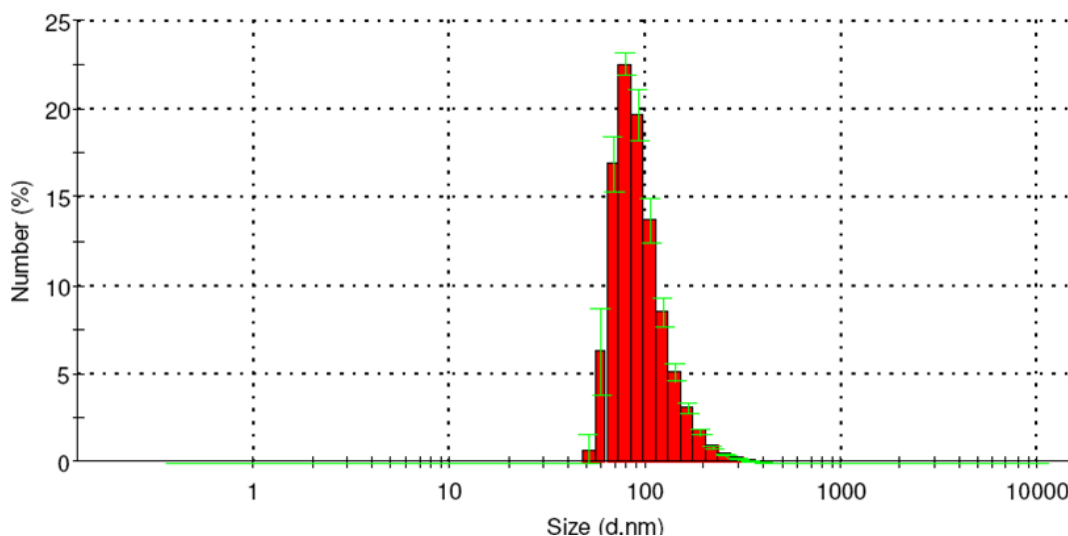
Figure 4.9: DLS analysis of the as-prepared Cu_2Se nanoparticles.

However, the SEM result does not confirm the particle size and the size distribution of the as-prepared Cu_2Se sample as obtained from DLS analysis. According to the SEM image (Figure 4.10), the as-prepared Cu_2Se nanoparticles exhibit a spherical shape and are very uniform in morphology. The SEM image was used for a statistical evaluation of the mean particle diameter. Based on 200 particles from Figure 4.10, a mean diameter of 17(2) nm was deduced. The SEM image also shows that there are no separated individuals but very large aggregates of Cu_2Se nanoparticles. Combining the DLS and the SEM analyses, we can conclude that after the washing process, the Cu_2Se nanoparticles are not colloidally stable and trend to form small aggregates of 4~6 individuals in ethanol. That may be the reason why the DLS analysis gives a much larger mean diameter of 93(28) nm. During the SEM sample preparation, small aggregates agglomerated to large aggregates as shown in Figure 4.10, when slowly evaporating the suspension.
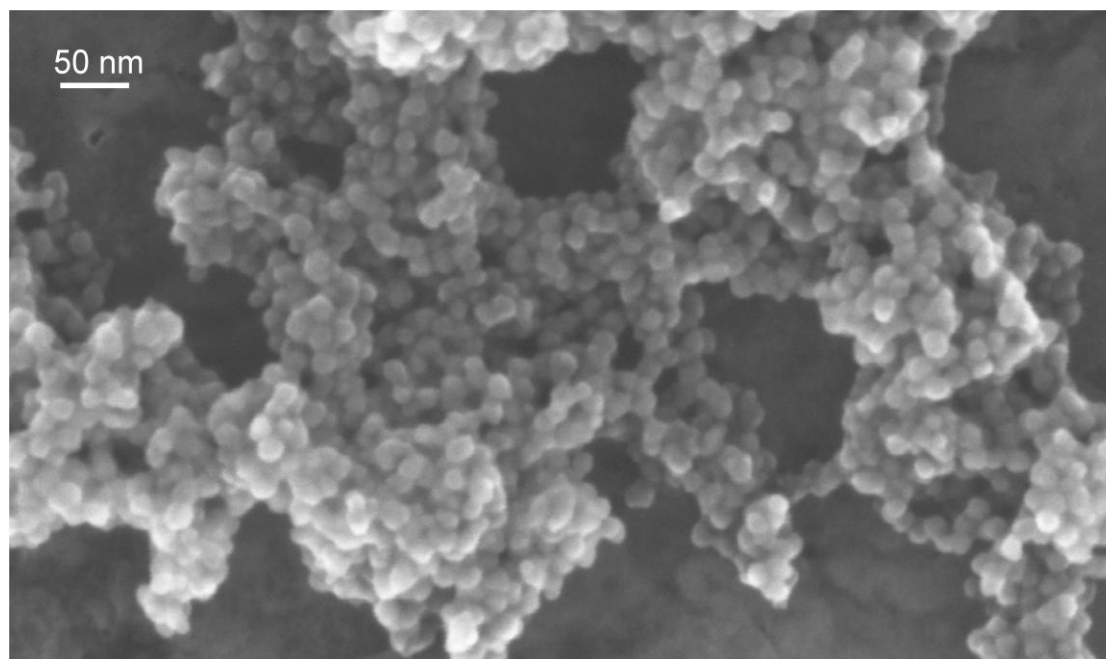
Figure 4.10: SEM image of the as-prepared Cu_2Se nanoparticles.

The phase composition and the structure of the as-prepared Cu_2Se nanoparticles were investigated by XRD. The XRD pattern of the as-prepared black powder reveals very broad peaks (Figure 4.11a), which may result from the small particle size of about 17 nm in diameter and a low degree of crystallinity due to the low reaction temperature (80 °C). After annealing the powder sample in argon atmosphere at 400 °C for 2 hours, Cu_2Se/Berzelianite is visible as the predominant phase. In addition, the main Bragg peak of CuSe/Klockmannite is also observed with low intensity at a 2θ value of 28.1 °(Figure 4.11b).

The surface conditioning of the as-prepared Cu_2Se nanoparticles was validated by FT-IR spectroscopy (Figure 4.12). As expected, the presence of large amounts of $C_4H_{10}S_3$ is indicated by its characteristic vibrational bands with strong absorption, including v(C–H) (3000-2750 cm^{-1}) and v(C–S) (1500-1050 cm^{-1}). These vibrations are in good agreement with the spectrum of pure $C_4H_{10}S_3$ as reference. A certain shift of the band position can be ascribed to the surface-bonding of the $C_4H_{10}S_3$ molecules on the surface of Cu_2Se nanoparticles. Based on previous investigation, additional bands can be attributed to OH-containing solvents such as DEG, water and ethanol adhered on the particle surface (v(O–H): 3650-3300 cm^{-1}), H_2O (δ(HOH): 1700-1550 cm^{-1}) and gaseous CO_2 (v(C=O): 2400-2250 cm^{-1}) in the sample cell.
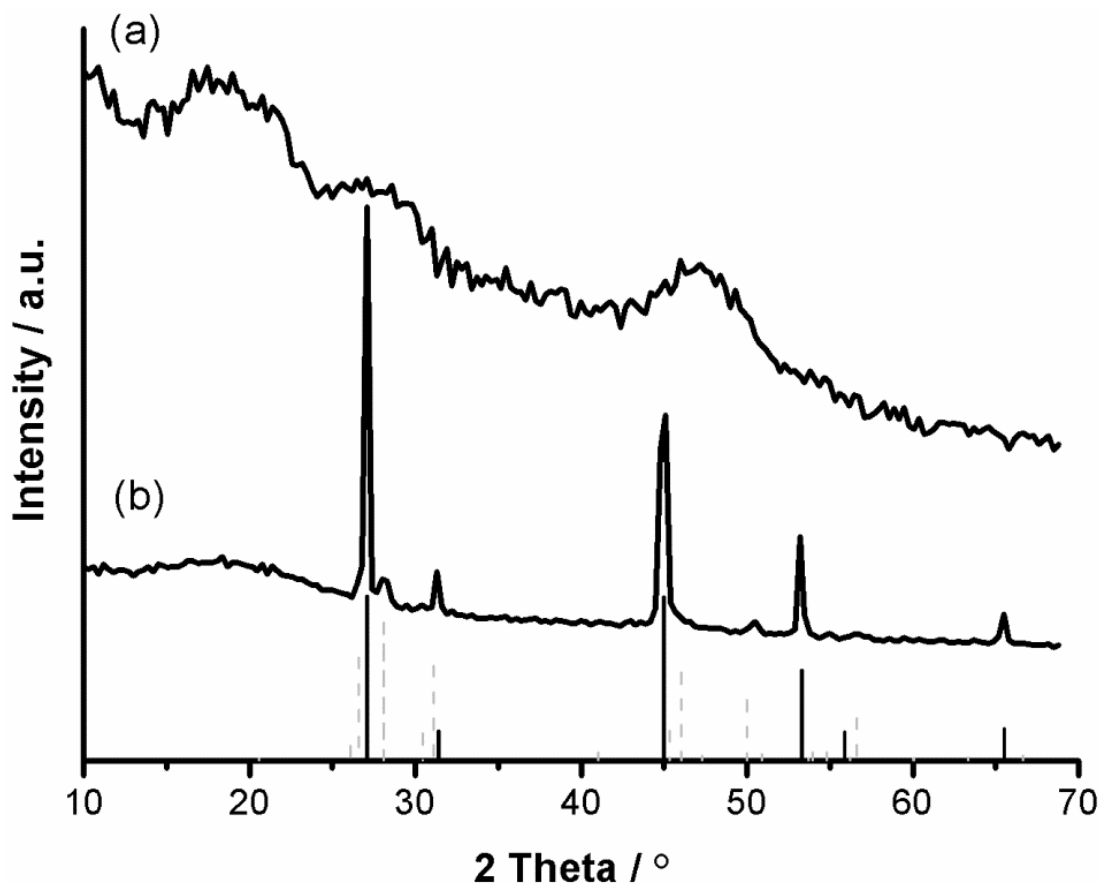
Figure 4.11: XRD patterns of the as-prepared Cu_2Se nanoparticles (a), and after annealing at 400 ℃ for 2 hours in argon atmosphere (b) (Cu_2Se/Berzelianite_ICDD No. 1088-2043/black solid lines and CuSe/Klockmannite_ICDD No. 34-171/grey dash lines as references).

Furthermore, to confirm the presence of 2,2'-thiodiethanethiol and to determine the overall atomic composition of Cu_2Se nanoparticles, the as-prepared black powder was pressed to a pellet to guarantee for a dense, semi-infinite layer with a smooth surface and used to apply EDX analysis (Table 4.1). Because only $C_4H_{10}S_3$ contains sulfur element, if sulfur was detected in the as-prepared Cu_2Se nanoparticles, it would be concluded the presence of $C_4H_{10}S_3$. Different areas of the pellet containing a huge number of nanoparticles were analyzed, resulting in an average Cu : Se ratio of 1.97 : 1 with high statistical relevance. Considering the limitation of EDX for quantitative analysis, the obtained Cu : Se ratio is quite similar to the ratio introduced in the synthesis. In addition, a large amount of sulfur (46 at %) is detected (Cu: 36 at % and Se: 18 at %). This confirms the results from FT-IR spectroscopy of the as-prepared Cu_2Se nanoparticles and proves the presence of $C_4H_{10}S_3$ on the sample surface.
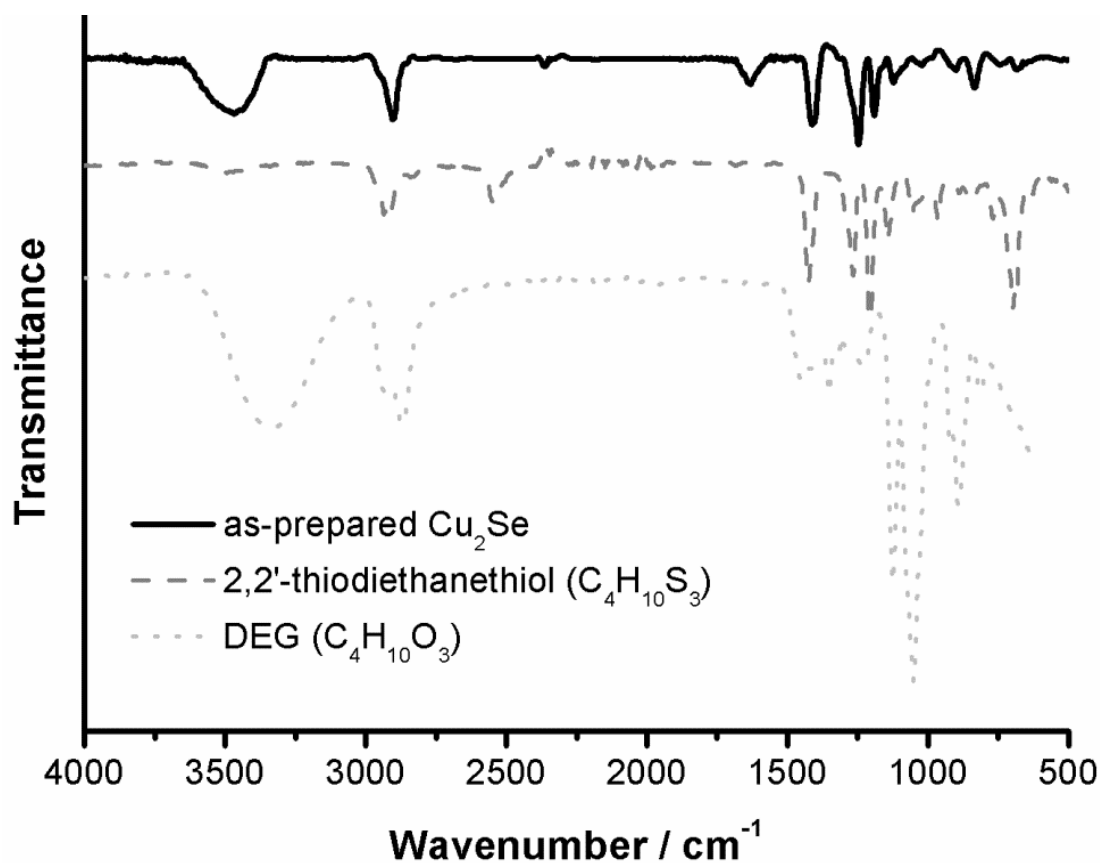
Figure 4.12: FT-IR spectrum of the as-prepared Cu_2Se nanoparticles (pure DEG and 2,2'-thiodiethanethiol as references).

Table 4.1: The overall compositions of the as-prepared Cu_2Se nanoparticles before and after TG according to EDX analysis.

As-prepared Cu_2Se	Cu (at %)	Se (at %)	S (at %)	Cu:Se	Cu:(Se+S)
Before TG	36	18	46	2.0	0.6
After TG	64	25	11	2.6	1.8
Theoretical value	66.7	33.3	—	2	—

(at %: atomic percent)

The thermal stability of the as-prepared Cu_2Se powder sample with $C_4H_{10}S_3$ surface capping was investigated by thermogravimetry in a temperature range from 30 ℃ to 900 ℃ with a heating rate of 10 K min^{-1} in nitrogen atmosphere (Figure 4.13). The slight weight loss (about 3 %) up to temperatures of 130 ℃ can be ascribed to an evaporation of H_2O and ethanol that are adsorbed on the particles' surface. Heating to 350 ℃ is accompanied by a significant weight loss of about 30 %. This finding can be ascribed to the desorption of $C_4H_{10}S_3$ from the particles' surface in nitrogen atmosphere, but it is worth mentioning that not all $C_4H_{10}S_3$ surface capping is removed. Further annealing to 900 ℃, the weight loss (about 6 %) is probably due to the slow evaporation of Se or the slow reaction between $C_4H_{10}S_3$ and copper at high temperatures to form copper sulfide and release the residual part as gases.
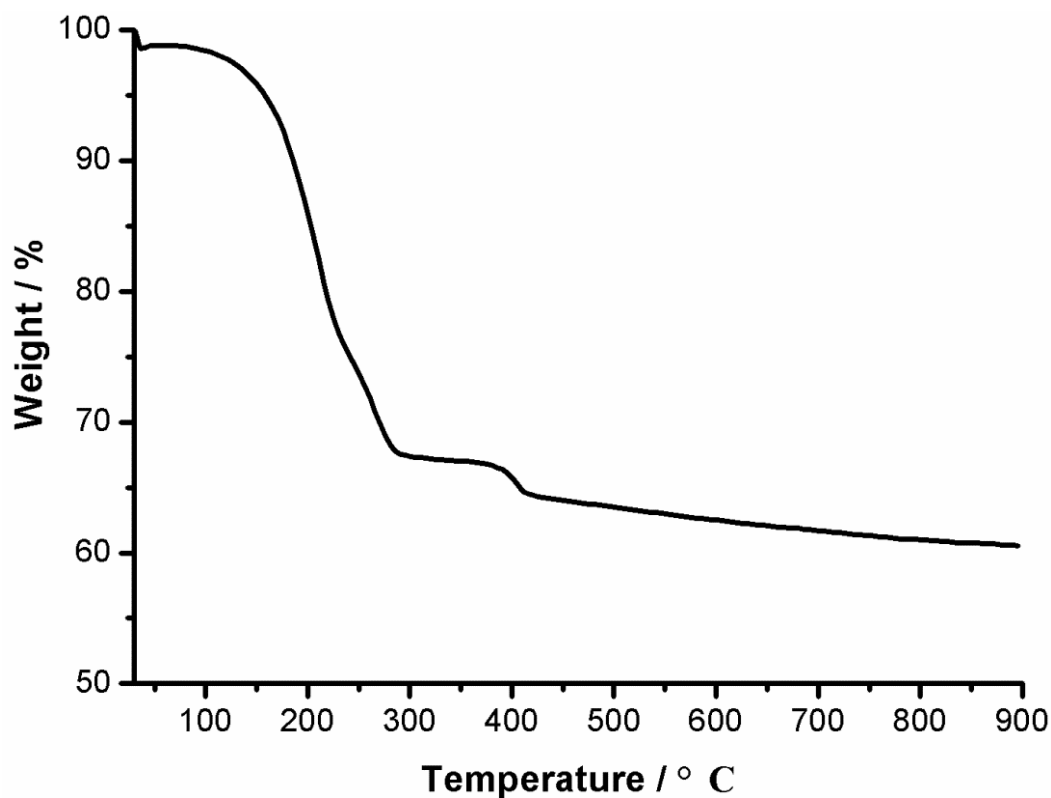
Figure 4.13: Thermogravimetry of the as-prepared Cu_2Se nanoparticles under nitrogen atmosphere.
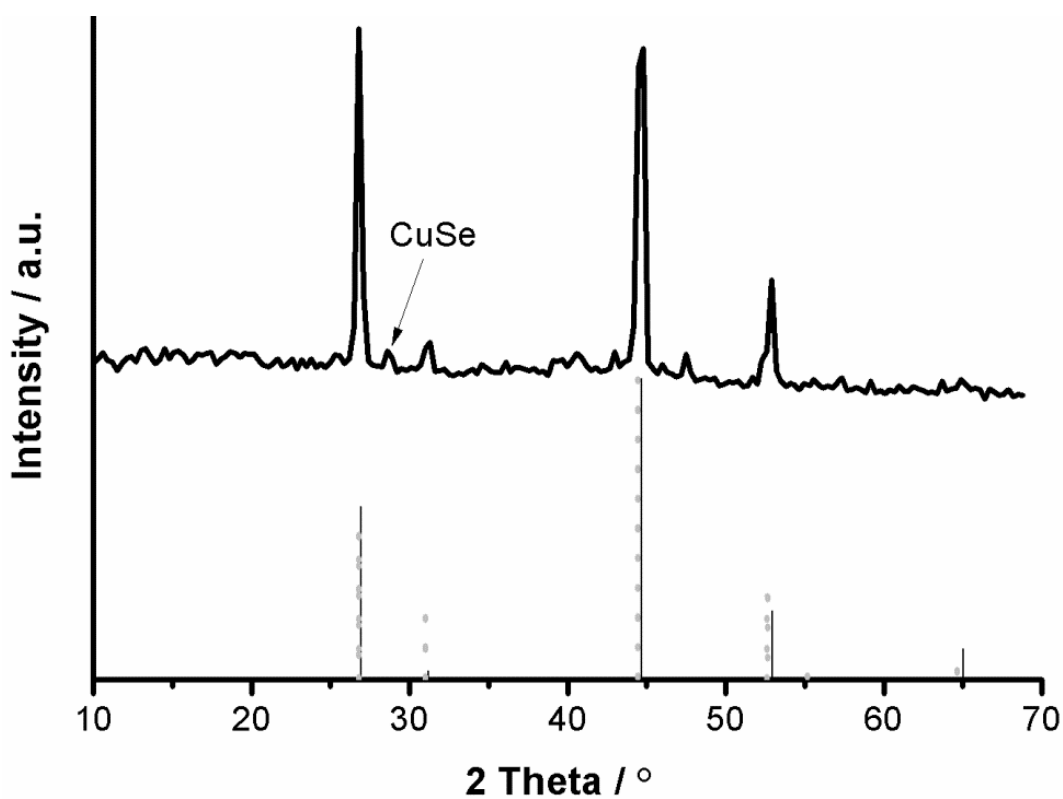
Figure 4.14: XRD pattern of the sample after TG measurement (900 °C in nitrogen atmosphere) ($Cu_{1.8}Se$/Berzelianite_ICDD No. 1071-6180/black solid lines and Cu_2S/ Digenite_ICDD No. 1070-9135/grey dot lines as references).

In order to prove the presence of sulfur and to determine the overall atomic composition of the sample after TG (900 ℃ in nitrogen atmosphere), the black powder was pressed to a pellet and different areas of the pellet were again analyzed by EDX analysis (Table 4.1). The EDX analysis shows an average composition of 64 at % Cu, 25 at % Se, 11 at % S and a Cu : (Se + S) ratio of about 1.8. The Cu : Se ratio after TG change from 2.0 to 2.6, which may result from the slow evaporation of Se at high temperatures. The XRD pattern of the sample after TG reveals sharp peaks of $Cu_{1.8}Se$/Berzelianite (Figure 4.14). Because the Cu_2S/Digenite has similar peak positions as $Cu_{1.8}Se$/Berzelianite shown in Figure 4.14 as references, and taking into account the EDX analysis in Table 4.1, we can conclude the present of Cu_2S/Digenite phase in the sample, which confirms the reaction between $C_4H_{10}S_3$ and copper at high temperatures. In addition, the main Bragg peak of CuSe/Klockmannite is also observed with low intensity at a 2θ value of 28.3 °.
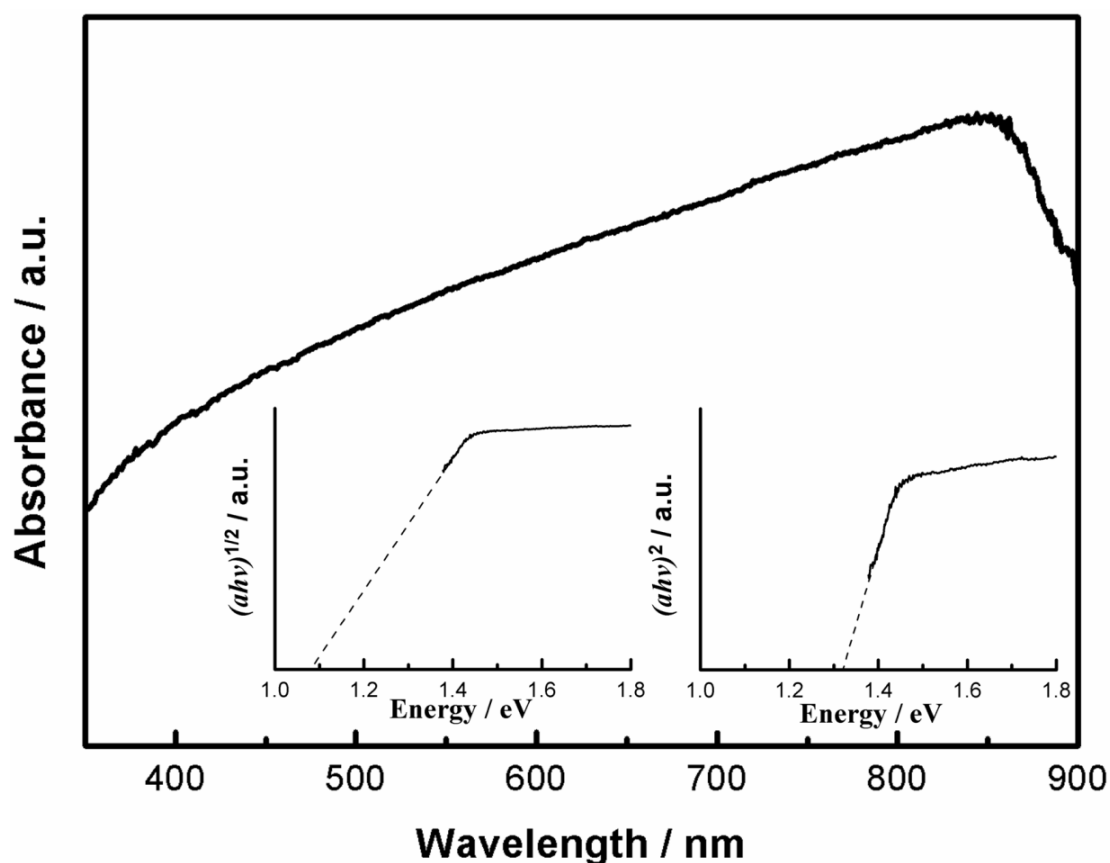
Figure 4.15: UV-Vis spectrum of the as-prepared Cu_2Se nanoparticles with insets showing Tauc plots with an indirect band gap of 1.1 eV (left) and a direct band gap of 1.3 eV (right).

Finally, the optical characterization and the determination of the band gap of the as-prepared Cu_2Se nanoparticles were performed by UV-Vis spectroscopy (Figure 4.15). The as-prepared Cu_2Se nanoparticles display an absorption maximum at 848 nm. A strong absorption with a steep increase of the absorption edge is observed between 850 and 900 nm. By plotting $(\alpha h v)^{1/2}$ and $(\alpha h v)^2$ versus the photon energy

($h\,v$), optical indirect band gap and direct band gap can be obtained, respectively, as shown in the insets of Figure 4.15. The as-prepared Cu_2Se nanoparticles have an indirect band gap of 1.1 eV and a direct band gap of 1.3 eV. Both values are consistent with the literature data, in which the nonstoichiometric $Cu_{2-x}Se$ (0≤x≤0.25) possesses an indirect band gap of 1.1-1.7 eV and a direct band gap of 1.3-2.3 eV.[86-90]

Flower-shaped indium selenide paticles

The synthesis was performed under argon inert-gas protection. In a typical synthesis, 88.5 mg (0.4 mmol) $InCl_3$ were added to 50 mL DEG in a three-neck flask. The white powder precursor was dissolved under continuous stirring to form a homogeneous colorless solution (solution I) at room temperature. 75.0 mg (0.6 mmol) Na_2Se were dissolved in 2 mL DEG and 0.5 mL $C_4H_{10}S_3$ in a schlenk flask (solution II). After solution I had been heated to 80 ℃ in an oil bath, solution II was injected with a syringe. The temperature was then increased to 170 ℃ and kept for 30 minutes. At last, the three-neck flask was removed from the oil bath and cooled to room temperature naturally. The final dark-red suspension was diluted with ethanol, and the product was collected via centrifugation and washed by repeated redispersion/ centrifugation in/from ethanol.

All analytic characterizations were carried out under air. The average particle size and the size distribution of the as-prepared indium selenide particles synthesized at 170 ℃ were determined by DLS in ethanol (Figure 4.16). To this concern, particles with a broad size distribution and a mean diameter of 411(97) nm were obtained. The SEM images, which confirm the DLS analysis with regard to the particle size and the broad size distribution, show that the as-prepared dark-red particles have a flower-like morphology with diameters around 300 to 500 nm (Figure 4.17D). When dripping a drop of the concentrated indium selenide suspension on a silicon wafer, after slowly evaporating the ethanol, the individual particles trend to form a dense layer structure as shown in Figure 4.17A and B.
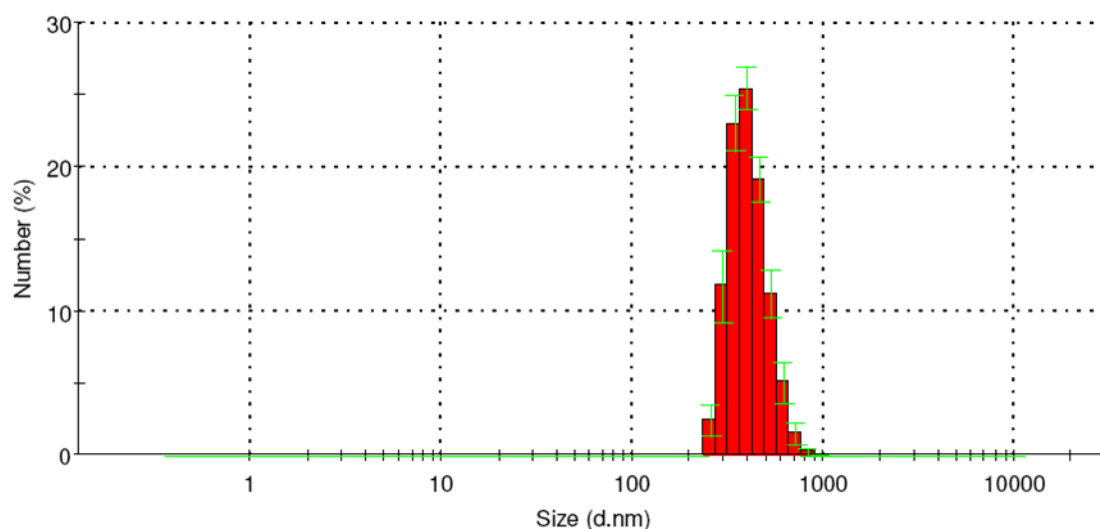
Figure 4.16: DLS analysis of the as-prepared indium selenide particles synthesized at 170 ℃.
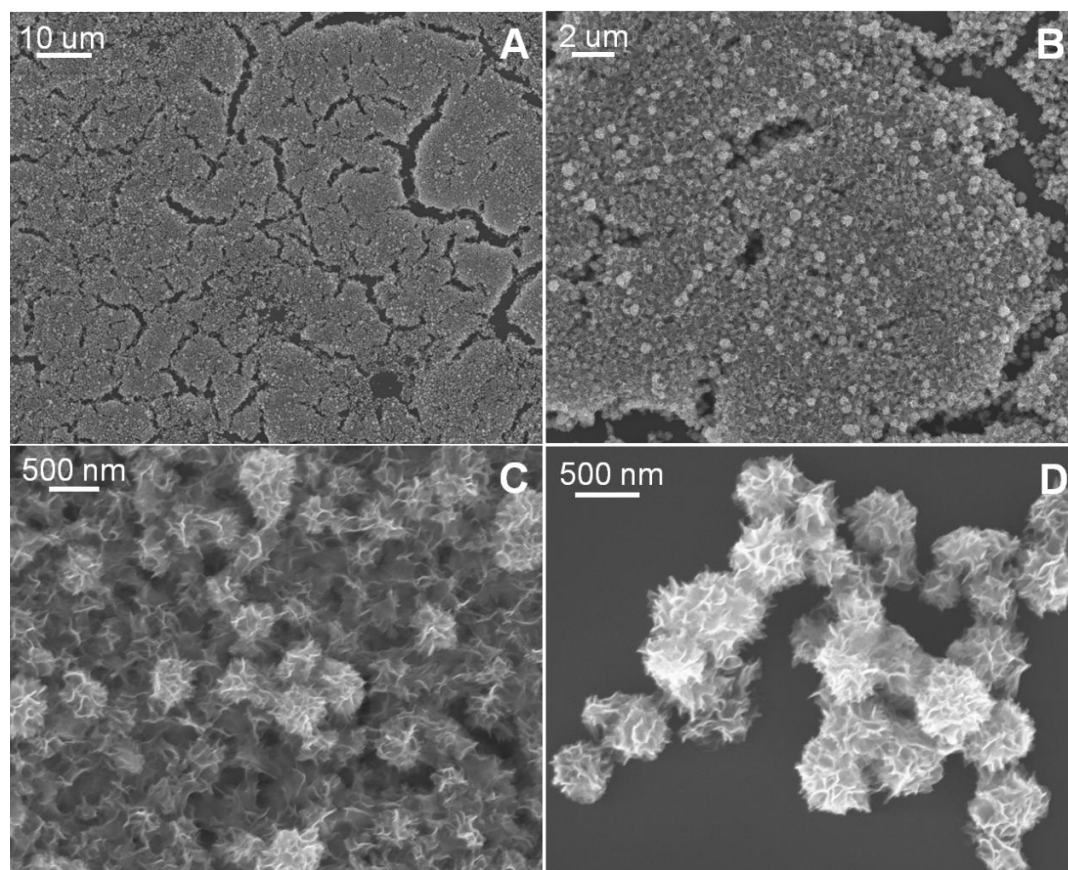
Figure 4.17: SEM images of the as-prepared indium selenide particles synthesized at 170 ℃ (A, B: large scale overview; C, D: high resolution images).
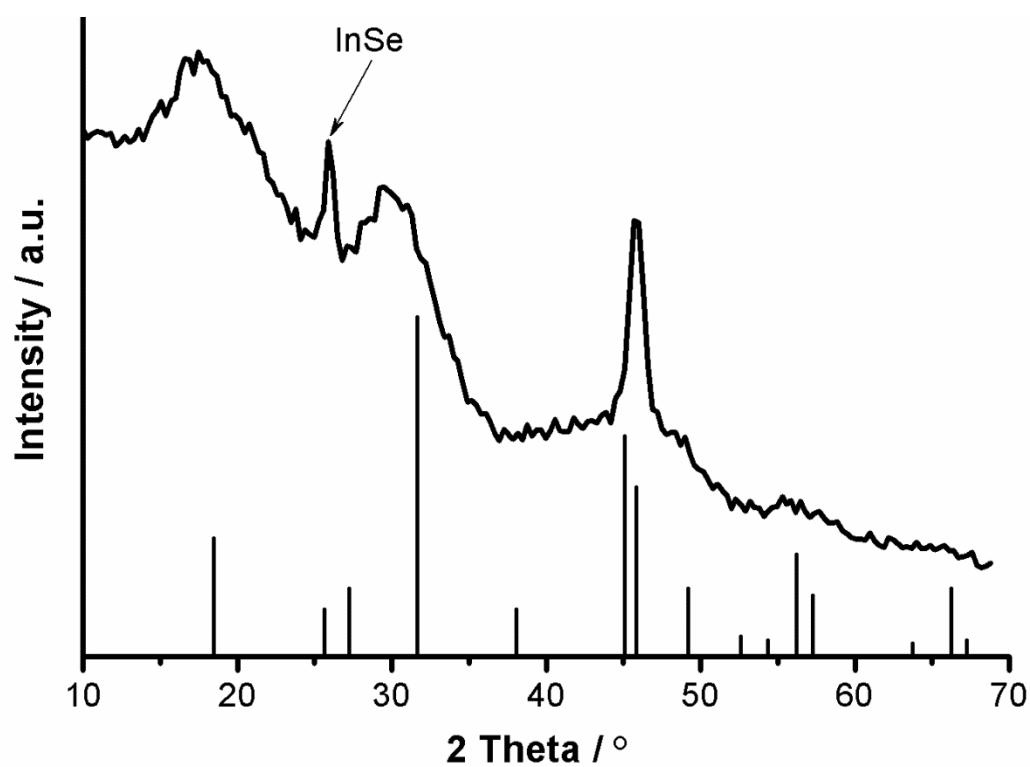
Figure 4.18: XRD pattern of the as-prepared indium selenide particles synthesized at 170 ℃ (δ-In_2Se_3_ICDD No. 34-1313 as a reference).

The XRD pattern of the dark-red powder synthesized at 170 °C reveals a combination of broad and sharp peaks (Figure 4.18), which may result from the low degree of crystallinity and the mixture phases of indium selenide. Thus, it's difficult to fit the Bragg peaks with references. In Figure 4.18, δ-In_2Se_3 (ICDD No. 34-1313) shown as the reference presents the best peak-fit to the XRD patterns. In addition, the main Bragg peak of InSe (ICDD No. 1070-2541) is observed at a 2θ value of 25.9 °.

After annealing the powder sample in argon atmosphere at 400 °C for 2 hours, the XRD pattern of the sample shows many sharp peaks (Figure 4.19), which are in agreement with several In_2Se_3 reference compounds such as γ-In_2Se_3 (ICDD No. 1089-658), β-In_2Se_3 (ICDD No. 40-1408) and β-In_2Se_3 (ICDD No. 45-1041). The main Bragg peak of InSe (ICDD No. 1070-2541) is still observed at a 2θ value of 25.9 °, the other Bragg peaks of InSe overlap with the Bragg peaks of In_2Se_3. From the XRD results, we can conclude that the annealed powder sample is a mixture containing γ-In_2Se_3, β-In_2Se_3 and InSe crystals.
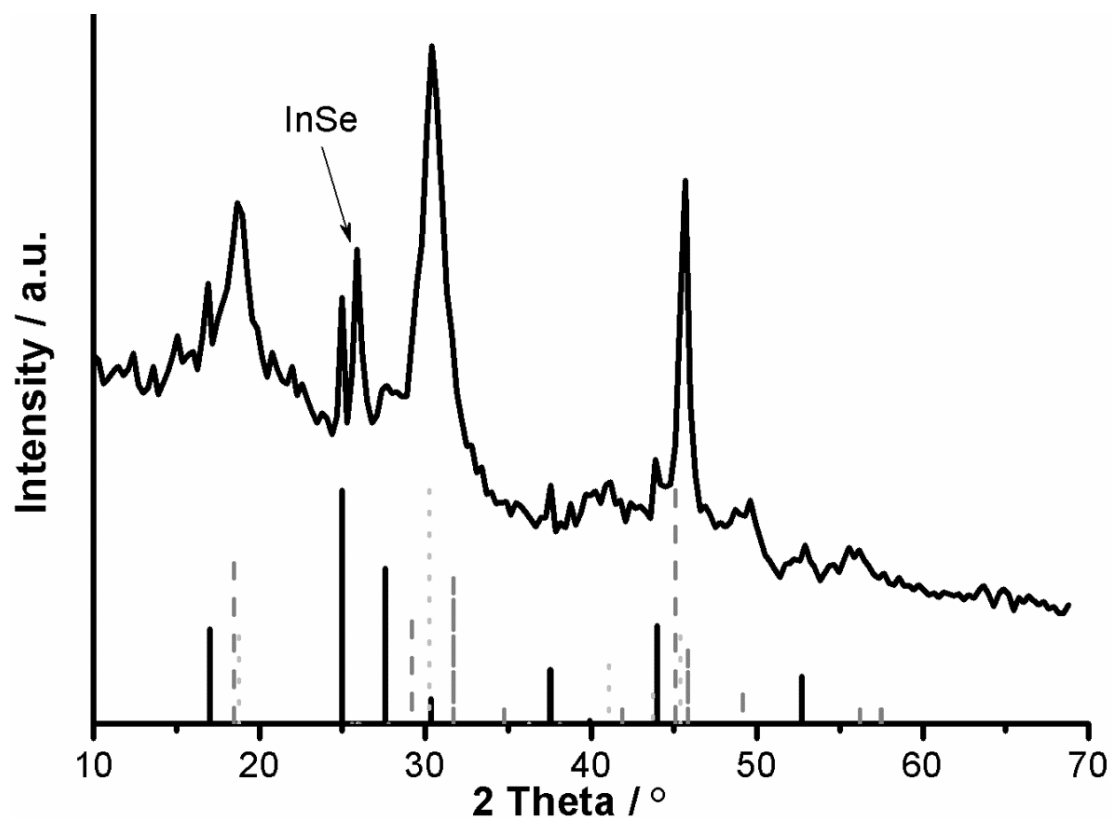
Figure 4.19: XRD pattern of the sample after annealing in argon atmosphere at 400 °C for 2 hours (γ-In_2Se_3_ICDD No. 1089-658/black solid lines, β-In_2Se_3_ICDD No. 40-1408/grey dash lines and β-In_2Se_3_ICDD No. 45-1041/grey dot lines as references).

Such flower-like indium selenide particles with a large particle size and a broad size distribution are not suitable for layer deposition and manufacturing of thin-film solar cells. High reaction temperature (170 °C) leads to different phases of indium selenide. In addition, with the mixture phases of In_2Se_3 and InSe, it is difficult to quantify the

amount of indium and to obtain a desired stoichiometry in precursor inks. Thus, small In_2Se_3 nanoparticles with pure phase were synthesized by introducing more $C_4H_{10}S_3$, reducing the reaction time and decreasing the reaction temperature.

In_2Se_3 nanopaticles

In a typical synthesis, 88.5 mg (0.4 mmol) $InCl_3$ white powder was dissolved in 50 mL DEG under continuous stirring in a three-neck flask (solution I). 75.0 mg (0.6 mmol) Na_2Se were added to 1 mL $C_4H_{10}S_3$ and 2 mL DEG in a schlenk flask (solution II). After solution I had been heated to 80 °C in an oil bath, solution II was injected with a syringe. The temperature was then increased to 120 °C and kept for 10 minutes. Thereafter the complete system was led to cool to room temperature. The final orange suspension was diluted with ethanol, and the In_2Se_3 nanoparticles were collected via centrifugation and washed repeatedly with ethanol. The color of the sample turns to red after drying the orange suspension at room temperature in air.

The average particle size and the size distribution of the as-prepared In_2Se_3 nanoparticles synthesized at 120 °C were verified via DLS in ethanol, which shows a relatively narrow size distribution and a mean diameter of 41(10) nm (Figure 4.20). However, the SEM images are not in agreement with the DLS analysis and exhibit aggregates and individuals of In_2Se_3 nanoparticle, which have an average particle size of about 20 nm in diameter (Figure 4.21). DLS analysis actually reveals the particle size and the size distribution of small aggregates consisting of several individual In_2Se_3 nanoparticles. Thus, we can conclude that the as-prepared In_2Se_3 nanoparticles synthesized at 120 °C are not highly colloidally stable in suspension, which is good for collecting nanoparticles from the suspension. During the SEM sample preparation, as ethanol was slowly evaporated, small aggregates agglomerated to large aggregates.
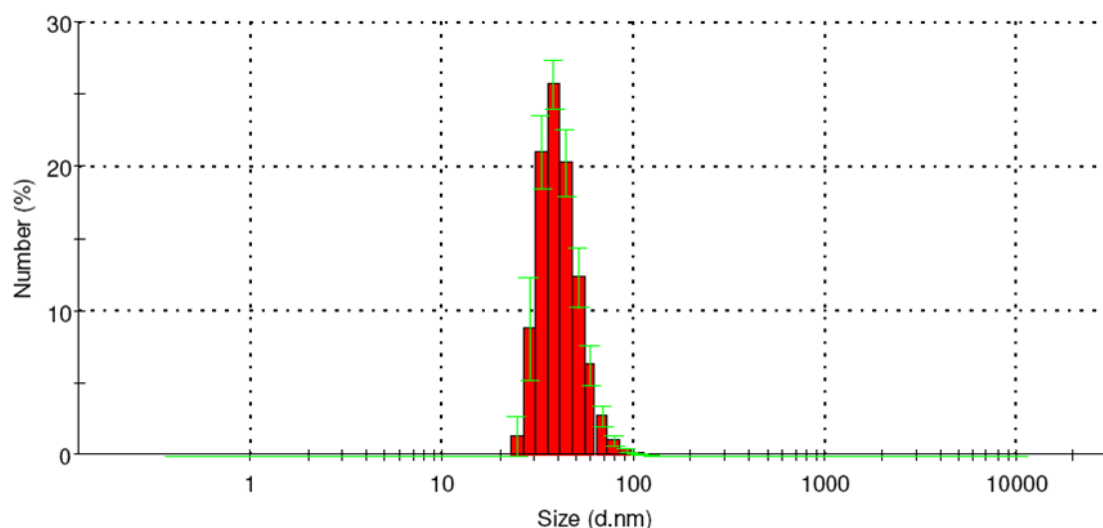
Figure 4.20: DLS analysis of the as-prepared In_2Se_3 nanoparticles synthesized at 120 °C.
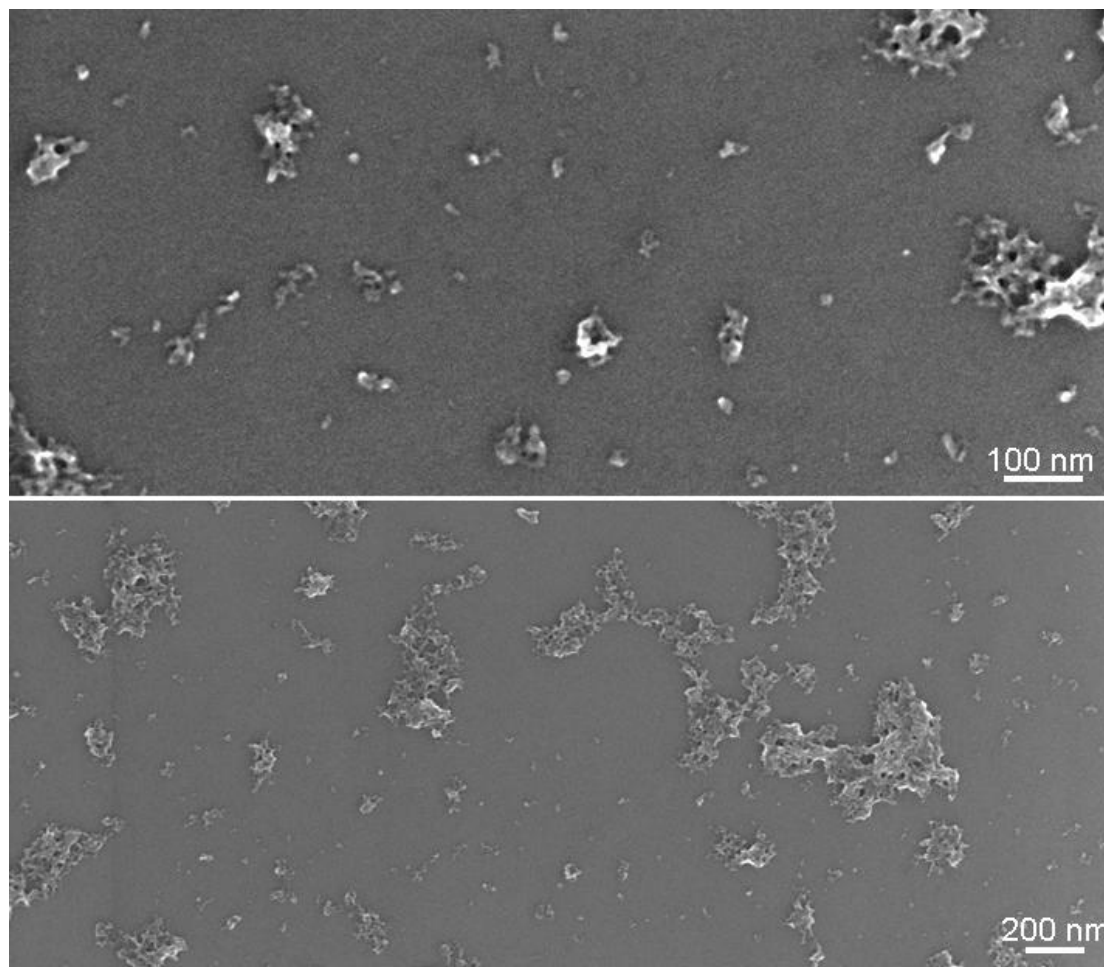
Figure 4.21: SEM images of the as-prepared In_2Se_3 nanoparticles synthesized at 120 °C.

The XRD pattern without any Bragg peaks proves the non-crystalline nature of the as-prepared sample synthesized at 120 °C (Figure 4.22a). After annealing the red powder sample in argon atmosphere at 400 °C for 3 hours, the color of the annealed sample turned to black. Thereafter, the XRD pattern fits well with the reference compound of γ-In_2Se_3 (ICDD No. 1071-250), which proves the presence of crystalline γ-In_2Se_3 (Figure 4.22b).

The surface conditioning of the as-prepared In_2Se_3 nanoparticles was investigated by FT-IR spectroscopy (Figure 4.23). It proves the presence of both DEG and $C_4H_{10}S_3$ in the as-prepared sample even after carefully washing with ethanol. The presence of DEG is indicated by its characteristic vibrational bands of ν(O–H) (3700-3150 cm^{-1}), ν(C–H) (3000-2750 cm^{-1}) and ν(C–O) (1350-900 cm^{-1}). These vibrations match well with the spectrum of pure DEG as reference in Figure 4.23. A certain shift of the band position can be ascribed to the surface-bonding of DEG and $C_4H_{10}S_3$ molecules on the surface of In_2Se_3 nanoparticles. Based on previous investigation, additional bands can be attributed to H_2O (δ(HOH): 1700-1550 cm^{-1}) in the sample. Unlike the FT-IR spectrum of the as-prepared Cu_2Se nanoparticles shown in Figure 4.12, the FT-IR

spectrum of the as-prepared In_2Se_3 nanoparticles shows the vibrational bands of DEG with strong absorption and $C_4H_{10}S_3$ with weak absorption, which means more DEG left in the sample than $C_4H_{10}S_3$. This can also be confirmed by the EDX analysis described later.
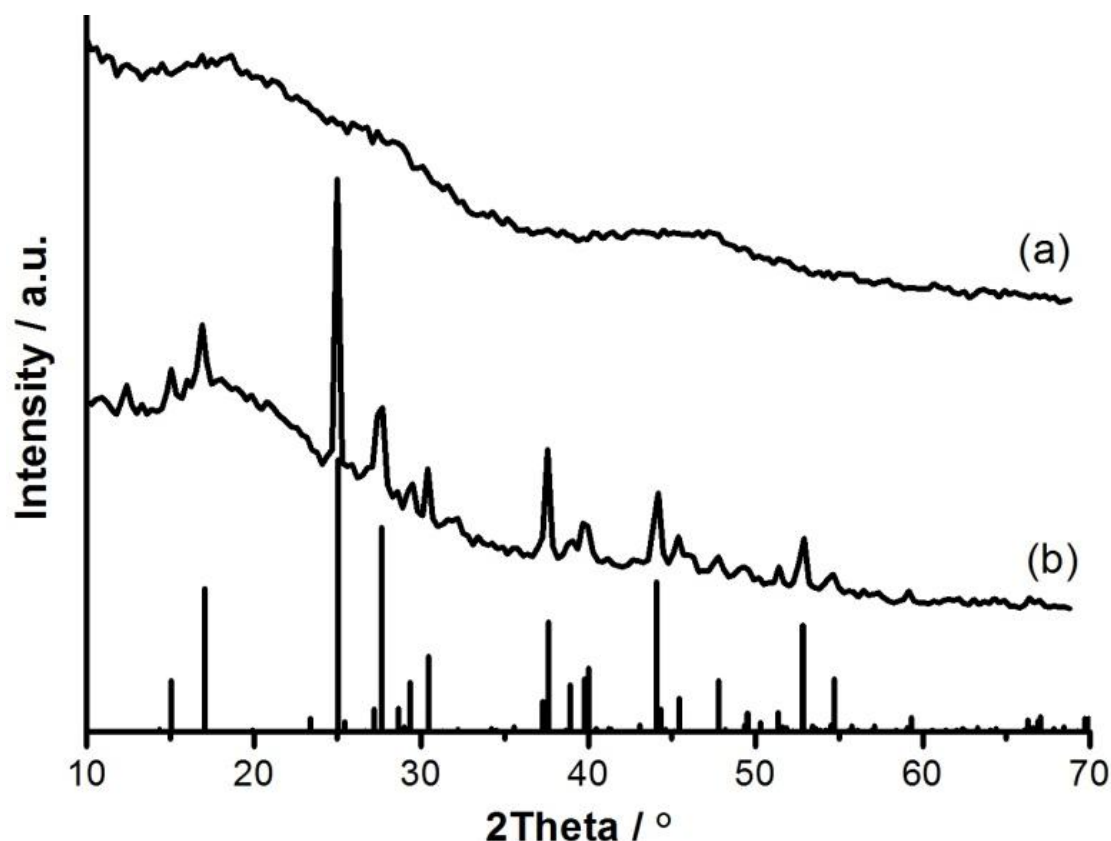
Figure 4.22: XRD patterns of the as-prepared In_2Se_3 nanoparticles (a), and after annealing (400 °C, 3 h, in argon) (b) (γ-In_2Se_3_ICDD No. 1071-250 as a reference).

Table 4.2: The overall compositions of the as-prepared In_2Se_3 nanoparticles before and after TG according to EDX analysis.

As-prepared In_2Se_3	O (at %)	S (at %)	In (at %)	Se (at %)	Se:In
Before TG	25	4	28	43	1.6
After TG	8	2	36	54	1.5
Theoretical value	—	—	40	60	1.5

(at %: atomic percent)

In order to determine the overall atomic composition of In_2Se_3 nanoparticles and to confirm the presence of DEG and 2,2'-thiodiethanethiol in the powder sample, the as-prepared red powder was pressed to a pellet to guarantee for a dense, semi-infinite layer with a smooth surface, and was measured by EDX analysis (Table 4.2). Because only $C_4H_{10}S_3$ contains sulfur element, if sulfur was detected in the as-prepared In_2Se_3 nanoparticles, it would be concluded the presence of $C_4H_{10}S_3$. For the same reason, the presence of DEG could be also qualitatively verified. Different areas of the pellet were analyzed, resulting in an average Se : In ratio of 1.6 : 1. Considering the

limitation of EDX for quantitative analysis, the obtained Se : In ratio is quite similar to the ratio introduced in the synthesis (Se : In ratio of 1.5 : 1). In addition, a large amount of oxygen (25 at %) as well as 28 at % of In, 43 at % of Se and 4 at % of S are found in the sample. But not all the oxygen is from DEG, since there are still water and ethanol molecules adhered on the particle surface. The EDX analysis confirms the results from FT-IR spectroscopy of the as-prepared In_2Se_3 nanoparticles and proves the presence of a large amount of DEG and a small amount of $C_4H_{10}S_3$ on the sample surface.
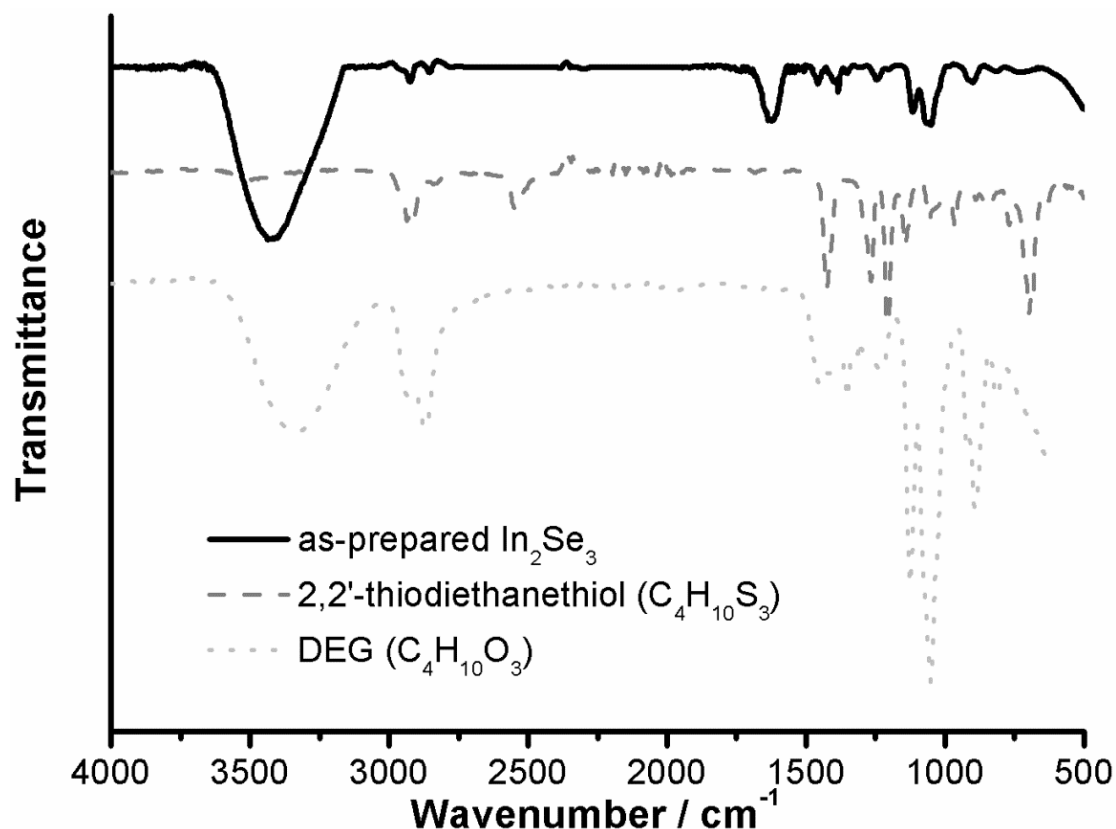
Figure 4.23: FT-IR spectrum of the as-prepared In_2Se_3 nanoparticles (pure DEG and 2,2'-thiodiethanethiol as references).

The thermal stability of the as-prepared In_2Se_3 powder sample with DEG and $C_4H_{10}S_3$ surface capping was investigated by thermogravimetry in a temperature range from 30 °C to 900 °C with a heating rate of 10 K min^{-1} in nitrogen atmosphere (Figure 4.24). The weight loss (about 8 %) up to temperatures of 100 °C can be ascribed to an evaporation of water and ethanol that are adsorbed on the particle's surface. Heating to 380 °C is accompanied by another weight loss of about 10 %. This finding can be ascribed to the desorption of DEG and $C_4H_{10}S_3$ from the particle's surface in nitrogen atmosphere, but it is worth mentioning that not all DEG and $C_4H_{10}S_3$ surface capping is removed in this step. Further annealing to 900 °C generates a weight loss of about 5 %, which is probably due to the slow evaporation of Se or the slow reaction between indium and DEG/$C_4H_{10}S_3$ at high temperatures to form indium oxide and indium sulfide, releasing the residual part as gases.
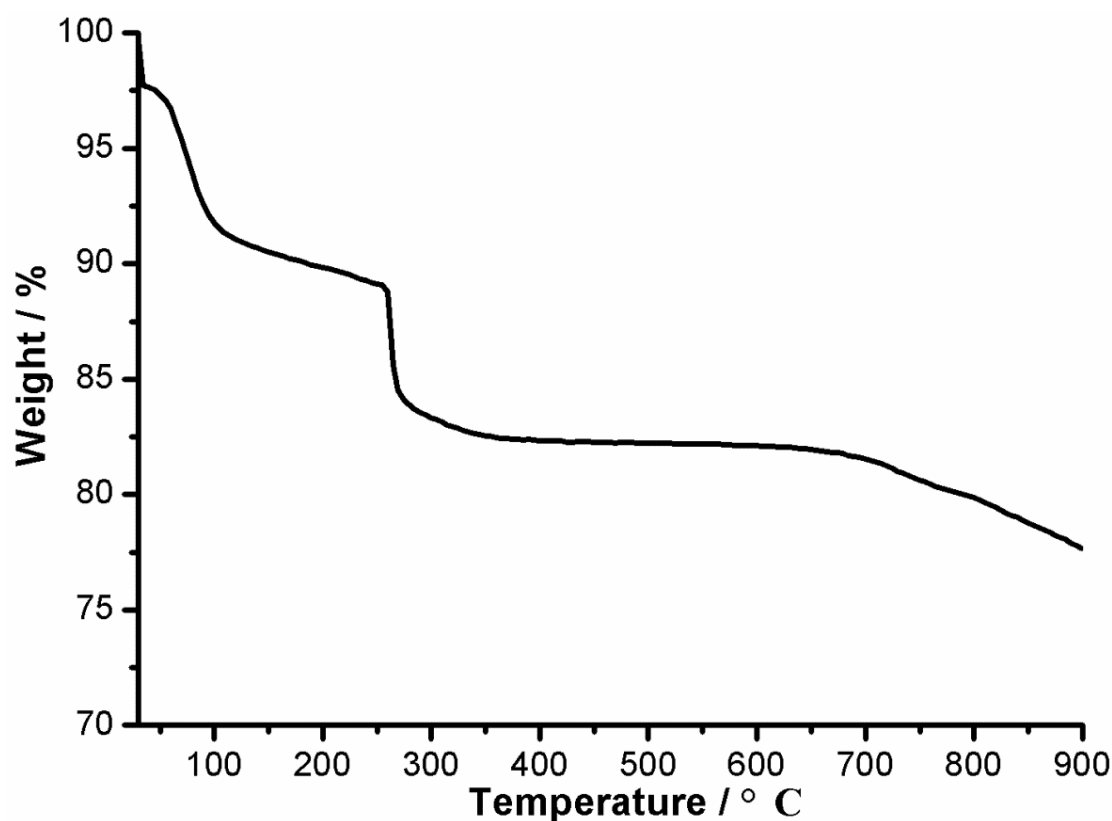
Figure 4.24: Thermogravimetry of the as-prepared In_2Se_3 nanoparticles under nitrogen atmosphere.

Furthermore, to prove the presence of oxygen and sulfur and to determine the overall atomic composition of the sample after TG (900 ℃ under nitrogen atmosphere), the black powder was pressed to a pellet and different areas of the pellet were analyzed by EDX again (Table 4.2). As compared to the EDX analysis before TG, the result shows the declines in the content of O (from 25 to 8 at %) and S (from 4 to 2 at %) and the increase in the contents of In (from 28 to 36 at %) and Se (from 43 to 54 at %), which confirms the TG analysis. The Se : In ratio after TG change from 1.6 to 1.5, which may result from the slow evaporation of Se at high temperatures.

Finally, the optical properties and the band gap of the as-prepared In_2Se_3 nanoparticles were performed by UV-Vis spectroscopy (Figure 4.25). The resulting UV-Vis spectrum shows the strong absorption in the range of 400 to 550 nm with an absorption maximum at 491 nm. A steep decrease of the absorption is observed between 500 and 650 nm. By plotting $(\alpha h v)^2$ versus the photon energy ($h v$), the optical direct band gap can be obtained as shown in the inset of Figure 4.25. The as-prepared In_2Se_3 nanoparticles have a direct band gap of 2.04 eV, which is in the same range as that of indium selenide in literature (1.4-2.5 eV).[91-93]
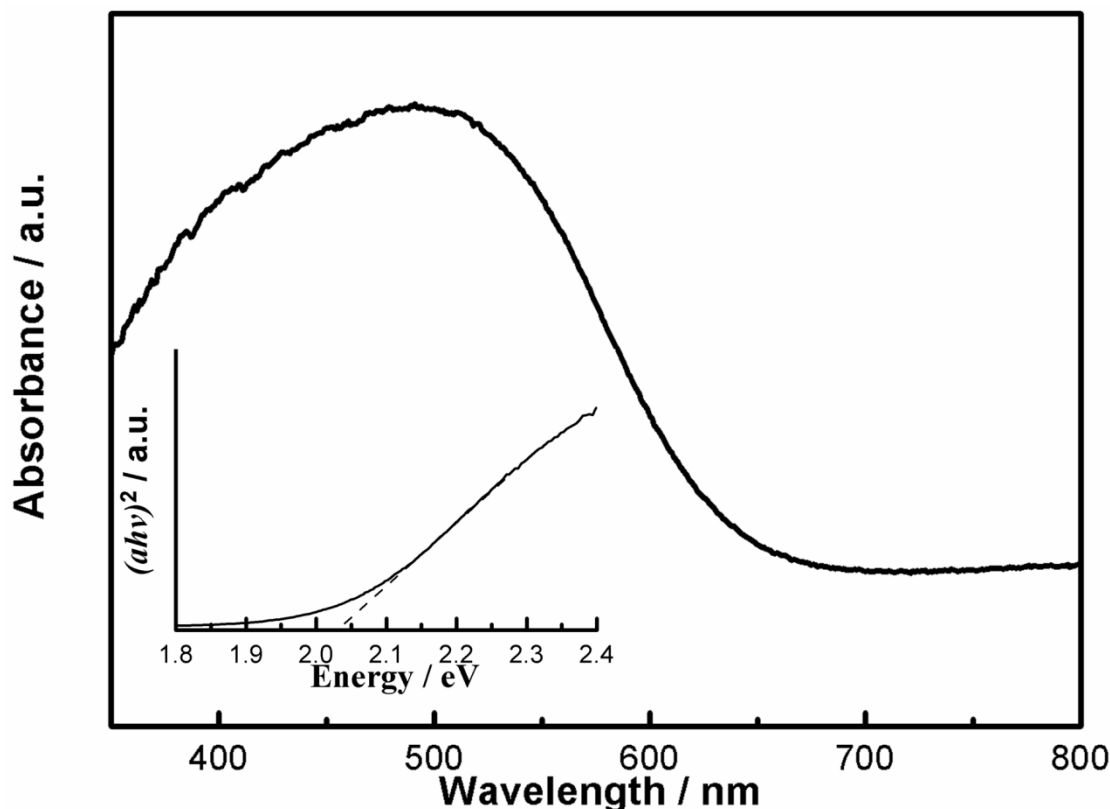
Figure 4.25: UV-Vis spectrum of the as-prepared In$_2$Se$_3$ nanoparticles with inset showing a Tauc plot with a direct band gap of 2.04 eV.

Preparation of absorption layers and manufacturing of thin-film solar cells

The syntheses and preparing inks of the as-prepared Cu$_2$Se and In$_2$Se$_3$ nanoparticles were accomplished in our research group. The preparation of absorption layers and manufacturing of CISe thin-film solar cells, using the mixture inks were done by Dr. Erik Ahlswede, Dr. David Blazquez, Dr. Aina Quintilla and Marco Cemernjak from ZSW in Stuttgart (Germany).

Suitable suspensions of Cu$_2$Se or In$_2$Se$_3$ nanoparticles were obtained by redispersing the as-prepared powders in ethanol with a solid load of less than 50 mg mL^{-1}. The binary nanoparticles act as stress-relief and crack-deflection centers to support the layer structure, ethanol as the precursor solvent is facile to remove from the system and form a compact thin-film layer. The mixture inks were prepared right before layer deposition by mixing Cu$_2$Se and In$_2$Se$_3$ inks in the ultrasonic bath in order to prevent large agglomeration. Layer deposition was done via doctor-blade coating, using an Erichsen film applicator and an adjustable blade by Zehntner (Sissach, Switzerland), on Molybdenum covered sodalime-glass substrates of 1 mm thickness. The resulting thin-films were dried at 300 °C in air to evaporate remaining solvents and stabilizers being adhered on the particle surface as well as to initiate a certain sintering of the nanoparticles. The coating procedure was repeated several times to build up a certain film thickness. Figure 4.26 shows the doctor-bladed thin-film of the mixture ink with a thickness of 893 nm. The crystalline structure of the mixture powder after annealing

at 500 ℃ for 2 hours in the argon atmosphere was investigated by XRD (Figure 4.27). The XRD pattern fits very well with the reference data of $CuInSe_2$ (ICDD No. 40-1487), which proves the presence of crystalline $CuInSe_2$.
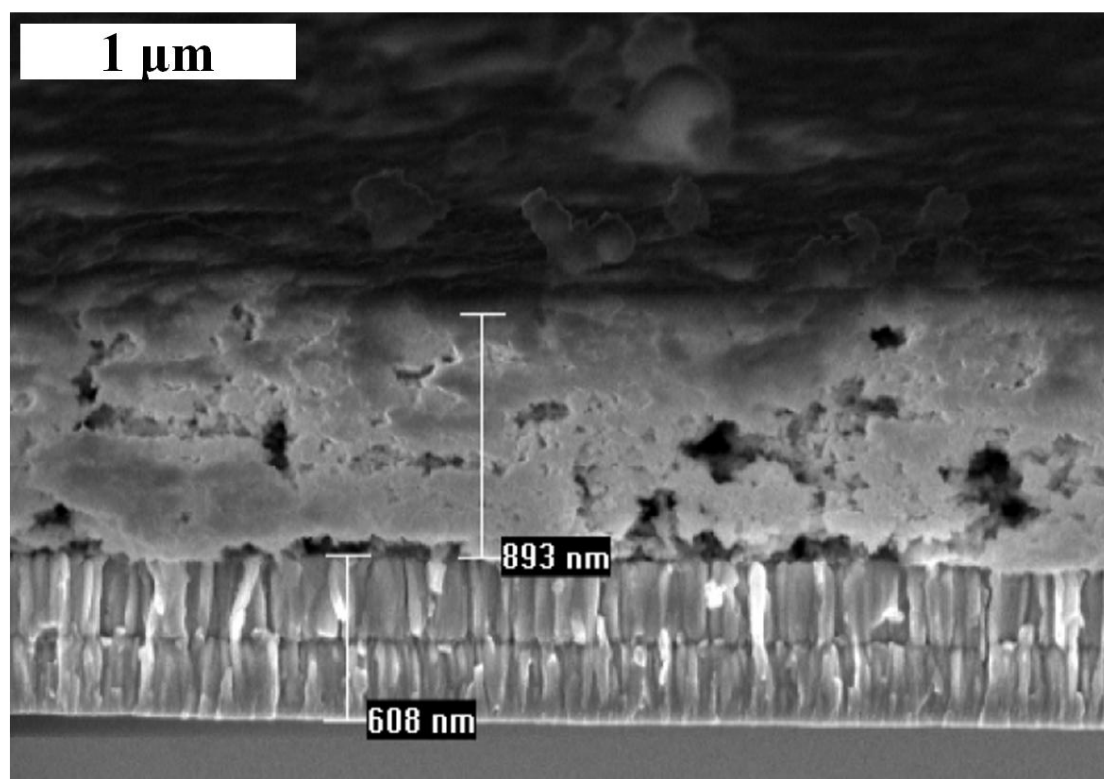
Figure 4.26: Doctor-bladed thin-film of the mixture ink comprising the as-prepared Cu_2Se and In_2Se_3 nanoparticles.

In this work, the conventional selenization process[75] and a novel laser annealing process were both performed to convert the precursor thin-film layers to chalcopyrite-type CISe absorber layers. For the conventional selenization process, the precursor layers were annealed in selenium-containing nitrogen atmosphere by heating them in a graphite box in the presence of Se pellets inside a tube furnace. The temperature was kept at 500 ℃ for 50 minutes. The detailed information about the laser annealing is still confidential and will not be discussed here. Afterwards, the annealed precursor layers for both cases were allowed to cool down naturally.

The CISe absorber layers were further treated by selective KCN etching to remove undesired binary CuSe phases, which would typically lead to shunted cell behaviour due to its good conductivity. The resulting CISe absorber layers were coated with about 50 nm of CdS buffer layer via chemical bath deposition (CBD), followed by sputtering a ZnO window layer (i-ZnO) and a transparent ZnO:Al front-contact layer to obtain functional solar cells.[94] By mechanical scribing, the final CISe thin-film absorber layer was divided into eight cells of approximately 0.25 cm^2 each in size.
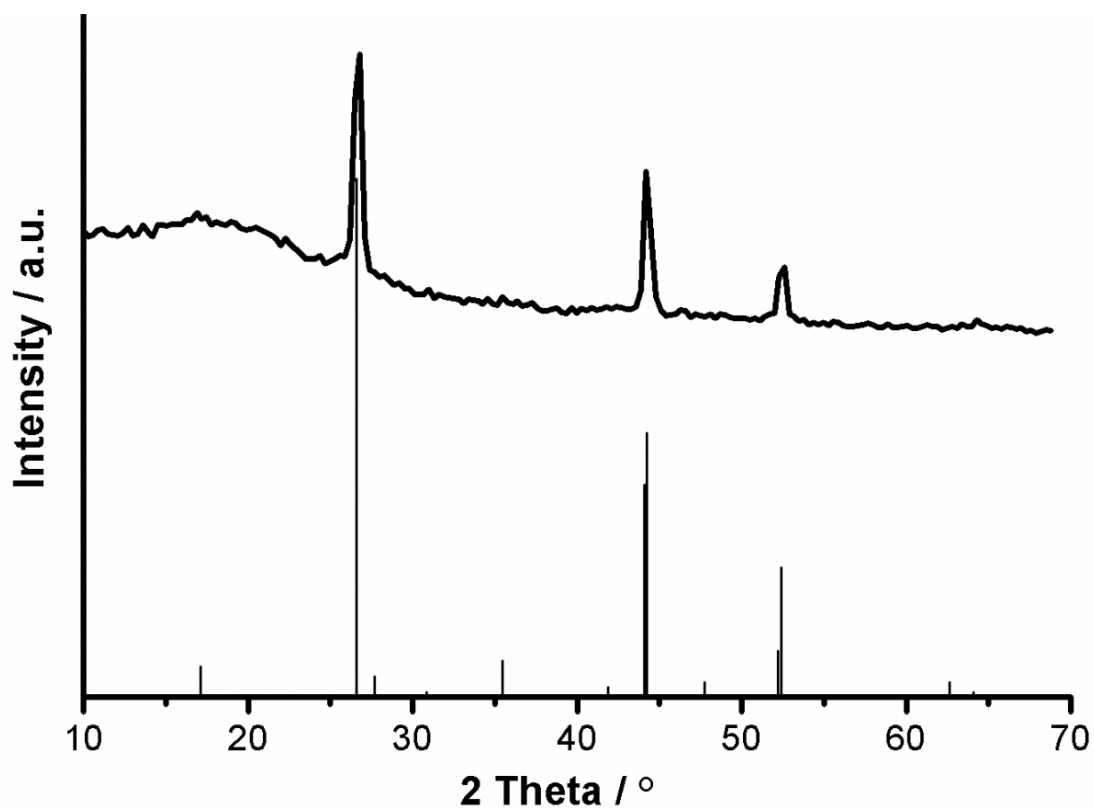
Figure 4.27: XRD pattern of the mixture powder after annealing at 500 ℃ for 2 hours in the argon atmosphere (CuInSe$_2$_ICDD No. 40-1487 as a reference).
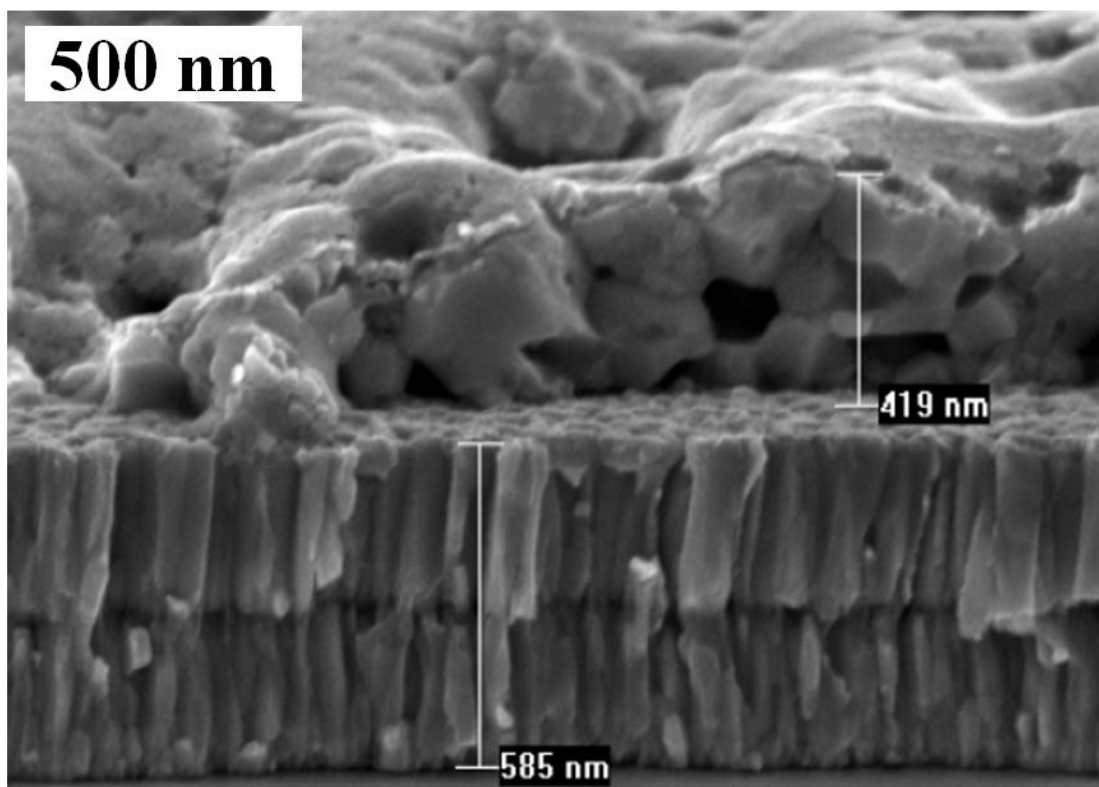
Figure 4.28: CISe absorber layer after laser annealing.

For the precursor layers of the mixture inks after laser annealing, densification and crystal growth are clearly visible (Figure 4.28). Crystal morphology and layer structure are significantly different from the precursor layer, indicating the reaction between Cu_2Se and In_2Se_3 nanoparticles. Thus, laser annealing can become an alternative choice to convert the precursor films to chalcopyrite-type absorber layers. The detailed information about laser annealing and the further characterization of the CISe absorber layer and the solar cell behavior are beyond the scope of this dissertation, and will be published in detail by our cooperative partner in ZSW (Stuttgart, Germany).

The CISe thin-film solar cells made out of Cu_2Se and In_2Se_3 inks with the selenization process or after laser annealing have already achieved the conversion efficiencies of 1-2 %, which is so far not as promising as compared to the state-of-the-art CIS/Se thin-film solar cells. Much more efforts and optimization of the experimental conditions in terms of chemical composition, Cu_2Se : In_2Se_3 ratio, particle diameter, layer thickness and morphology, duration and temperature of the selenization process, etc. are necessary to improve the morphology of CISe absorber layers and to increase the overall solar-cell performances.

4.1.3 $Cu_2ZnSn(S/Se)_4$ Kesterite Nanoparticles

Synthesis of CZTS nanoparticles

Cu_2ZnSnS_4 (copper zinc tin sulfide/CZTS) nanoparticles were synthesized with a polyol-mediated method combined with hot injection of the sulfide precursor. DEG was applied as the solvent, which allows controlling the particle size and suppressing the particle agglomeration.[22, 26] Due to its high boiling point (248 ℃),[18] crystalline phases can often be obtained directly from liquid-phase synthesis at a relatively high reaction temperature close to the boiling point.

In a typical synthesis that was performed under argon inert-gas protection, 113.0 mg (0.84 mmol) $CuCl_2$, 75.0 mg (0.55 mmol) $ZnCl_2$, and 95.0 mg (0.5 mmol) $SnCl_2$ were added to 60 mL DEG filled in a three-neck flask. The powder precursors were dissolved under continuous stirring to form a homogeneous brownish-yellow solution (solution I). After solution I had been heated to 80 ℃ in an oil bath, 147.5 mg (1.89 mmol) Na_2S dissolved in 4 mL DEG were injected. The formation of CZTS was indicated by the instantaneous color change from a brownish-yellow solution to a black suspension. To support the crystallization, the temperature of the CZTS suspension was increased to 190 ℃ for 30 minutes. Thereafter, the whole system was allowed to cool to room temperature naturally. The final black suspension was diluted with isopropanol, and the as-prepared CZTS nanoparticles were collected via centrifugation, washed repeatedly and redispersed in isopropanol for further analyses. According to the applied recipe, the overall composition of the as-prepared CZTS nanoparticles is expected to be copper-poor as well as zinc- and tin-rich. This has been frequently reported as an optimization concerning the solar-cell performance,

since an excess of copper can lead to detrimental structural defects of Cu atoms on the Zn sites and the formation of stable binary and/or ternary copper chalcogenides after the sulfurization or selenization process.[15, 95, 96] Therefore, the amounts of Cu, Zn and Sn were adjusted to ratios of Cu : (Zn + Sn) = 0.8 and Zn : Sn = 1.1.

Characterization of CZTS nanoparticles

All analytic characterizations were carried out under air. The average particle size and the size distribution of the as-prepared CZTS nanoparticles were verified via DLS measurement based on diluted CZTS suspension in isopropanol (Figure 4.29). According to the DLS analysis, particles with a relatively narrow size distribution and a mean diameter of 74(20) nm are obtained. Subsequently, scanning electron microscopy and scanning transmission electron microscopy of the as-prepared samples were applied to obtain a direct view of CZTS nanoparticles.
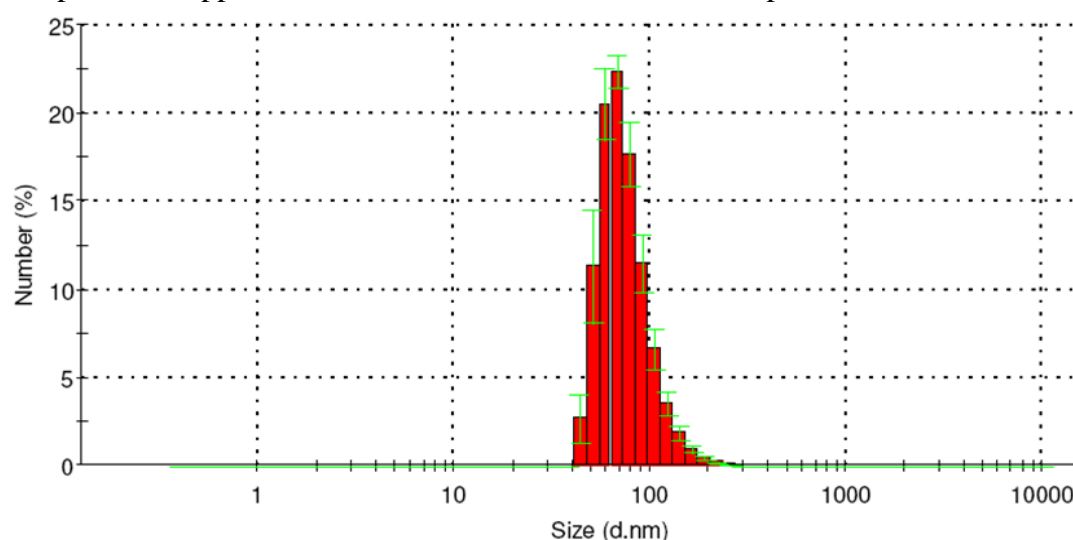
Figure 4.29: DLS analysis of the as-prepared CZTS nanoparticles in isopropanol.

SEM and STEM images of the as-prepared CZTS sample show individual as well as agglomerated nanoparticles with particle diameters ranging from 10 to 20 nm (Figure 4.30). Based on a statistical evaluation of at least 100 particles on STEM images, the mean particle diameter was determined to be 13(2) nm. However, this value is not in agreement with the DLS analysis. An explanation therefore is that after being centrifuged out of DEG suspension and redispersed in isopropanol, the individual nanoparticles were not colloidally stable and trended to form small agglomerates in suspension. Other solvents were also used, but similar DLS results were obtained. From the SEM image (Figure 4.30a), we can clearly see that the agglomerates are formed by nanoparticles of about 13 nm in diameter. Nitrogen sorption analysis and determination of the specific surface area according to the Brunauer-Emmett-Teller (BET) formalism resulted in a value of 153 $m^2\,g^{-1}$ that is in accordance with the above mentioned particle size.
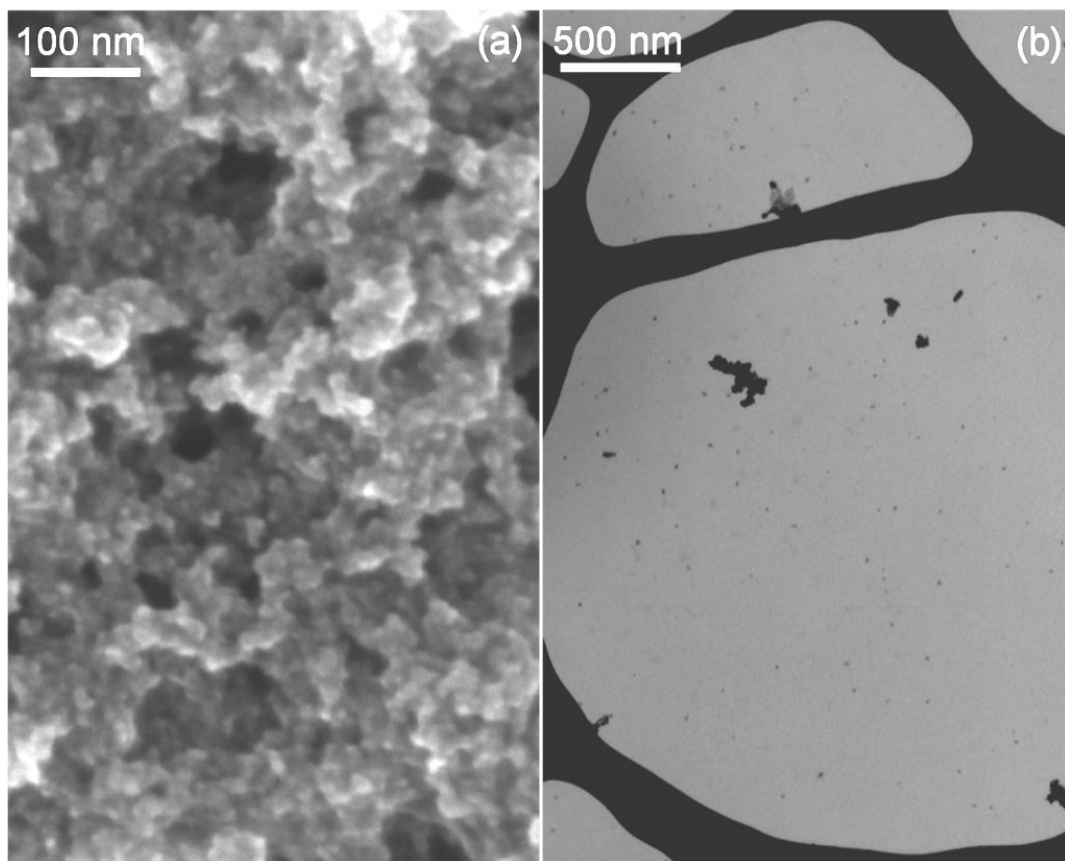
Figure 4.30: SEM (a) and STEM (b) images of the as-prepared CZTS nanoparticles.
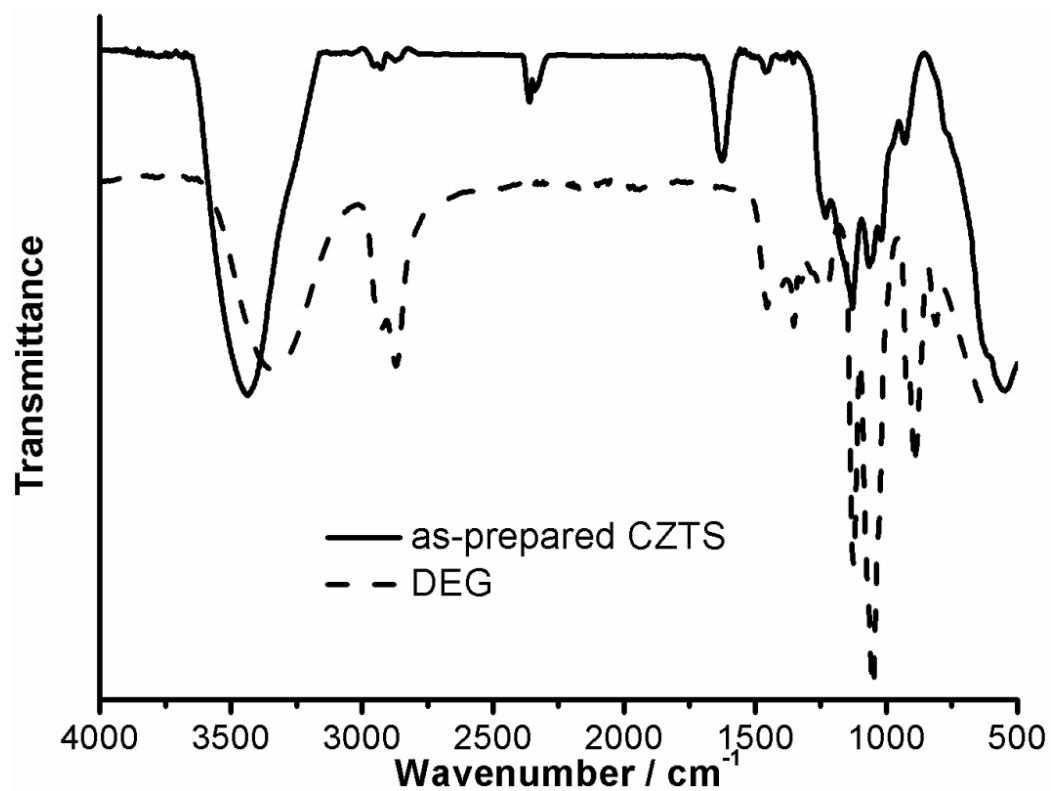
Figure 4.31: FT-IR spectrum of the as-prepared CZTS nanoparticles (pure DEG as a reference).[97]

The surface conditioning of the as-prepared nanoparticles was validated by FT-IR spectroscopy (Figure 4.31). As expected, the presence of small amounts of DEG is indicated by its characteristic vibrational bands, including v(O–H) (3750-3250 cm^{-1}), v(C–H) (3000-2750 cm^{-1}) and v(C–O) (1350-900 cm^{-1}).[22] These vibrations are in good agreement with the spectrum of pure DEG as a reference (Figure 4.31). A certain shift of the band positions can be ascribed to the surface-bonding of DEG molecules on CZTS particles' surface. Based on previous investigations, additional bands can be attributed to H$_2$O (δ(HOH): 1700-1550 cm^{-1}) and gaseous CO$_2$ (v(C=O): 2400-2250 cm^{-1}) in the sample cell. Small amounts of DEG as a surface capping in previous investigations did not restrict the manufacturing and performance of thin-film solar cells, since DEG is completely removed during the selenization process.[80]
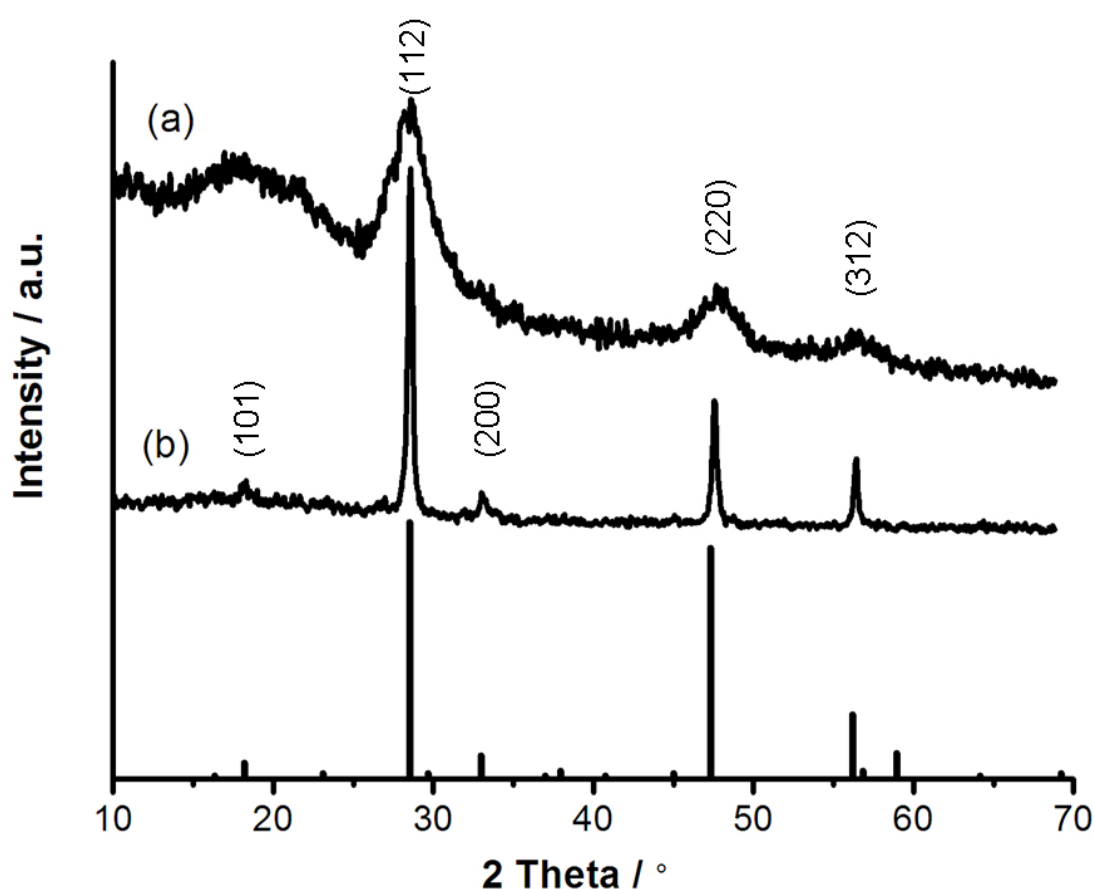
Figure 4.32: Indexed XRD patterns of the as-prepared CZTS nanoparticles (a), and after annealing (500 °C, 2 hours, in argon) (b) (tetragonal CZTS/Kesterite_ICDD No. 26-575 as a reference).[97]

The phase composition and the structure of the as-prepared CZTS nanoparticles were investigated by XRD. Accordingly, the XRD pattern of the as-prepared sample shows broad Bragg peaks, which can originate from the small particle size (Figure 4.32a). The phase composition and the presence of tetragonal CZTS are nevertheless obvious. After annealed the as-prepared powder sample at 500 °C for 2 hours under argon

protection, the Bragg peaks become much sharper and are in well accordance with the reference of tetragonal CZTS/ Kesterite (ICDD No. 26-575). This is to be welcomed since the tetragonal modification was frequently reported for its higher power-conversion efficiency as compared to the hexagonal modification. In addition, low temperature synthesis has been most often limited to the formation of the hexagonal phase till now.[11, 12, 15-17, 59, 64] Additional Bragg peaks that indicate eventual impurity phases (e.g., binary metal sulfides or metal oxides) are not observed (Figure 4.32).

In order to determine the cation composition of the tetragonal CZTS nanoparticles, the as-prepared black powder sample was pressed to a pellet to guarantee for a dense, semi-infinite layer with a smooth surface for EDX analysis (Table 4.3). Based on six different regions of the pellet, the average composition can be concluded to $Cu_{1.35}Zn_{1.11}SnS_{3.96}$ with high statistical relevance. The Cu : (Zn + Sn) and the Zn : Sn ratios are 0.64 and 1.11, respectively. As aimed with the synthesis, the as-prepared CZTS sample is indeed copper-poor, Zn-, Sn- and S-rich. This changed stoichiometry as compared to the molar ratios of the starting materials (Cu : (Zn + Sn) = 0.8 and the Zn : Sn = 1.1) can be rationalized, on the one hand, on the chelating properties of DEG as a solvent. Due to this complexation, the divalent cations partly remain in solution. On the other hand, Sn^{2+} or Cu^{2+} may oxidize S^{2-} under formation of elemental sulfur. Taking both effects together explains the metal deficiency as well as the excessive sulfur. The excessive sulfur is beneficial to the solar-cell performance, because a shortfall of sulfur/selenium may lead to defective absorber layers during layer sintering.[15-17, 59, 61]

Table 4.3: Detailed composition of the as-prepared CZTS nanoparticles according to EDX analysis with six different regions of the pellet.[97]

Cu (at %)	Zn (at %)	Sn (at %)	S (at %)	S_{excess} (at %)	Sn/Cu	Zn/Cu	Zn/Sn	Cu/(Zn+Sn)
18.2	15.1	13.7	53.0	6.0	0.75	0.83	1.11	0.63
18.2	14.8	13.5	53.5	7.0	0.74	0.81	1.09	0.64
18.1	15.0	13.4	53.5	7.0	0.74	0.83	1.12	0.64
18.1	15.1	13.4	53.4	6.8	0.74	0.83	1.12	0.64
17.9	15.0	13.5	53.6	7.2	0.75	0.84	1.11	0.63
18.2	15.1	13.9	52.8	5.6	0.76	0.83	1.09	0.63
av. 18.1	*av. 15.0*	*av. 13.5*	*av. 53.4*	*av. 6.8*	*av. 0.75*	*av. 0.83*	*av. 1.11*	*av. 0.64*

(*av.*: the average value)

The thermal stability of the as-prepared CZTS powder sample was investigated by thermogravimetry (Figure 4.33). The slight weight loss (~2 %) up to a temperature of 160 ℃ can be ascribed to an evaporation of H_2O, isopropanol and DEG that are adsorbed on the particle surface. Further annealing to 340 ℃ is accompanied by a significant weight loss of about 13 %. This finding is ascribed to a loss of sulfur that does not actually incorporate into the CZTS lattice.[60-62, 64, 65] During solar cell manufacturing, the evaporation of sulfur is compensated, on the one hand, due to the

presence of a sulfur/selenium atmosphere, and on the other hand, due to the excess of sulfur as indicated by the chemical formula $Cu_{1.35}Zn_{1.11}SnS_{3.96}$, which was determined based on the EDX analysis shown in Table 4.3 (6.8 at % excess sulfur relates to 4.0 wt %). The gradual weight loss of 1% observed in the final stage at temperatures above 340 ℃ results from a Sn loss through the sublimation of SnS.[95, 96] XRD pattern of the annealed sample indicates that the tetragonal CZTS phase still exists up to a temperature of 500 ℃ if the heating is performed in argon atmosphere (Figure 4.32b).
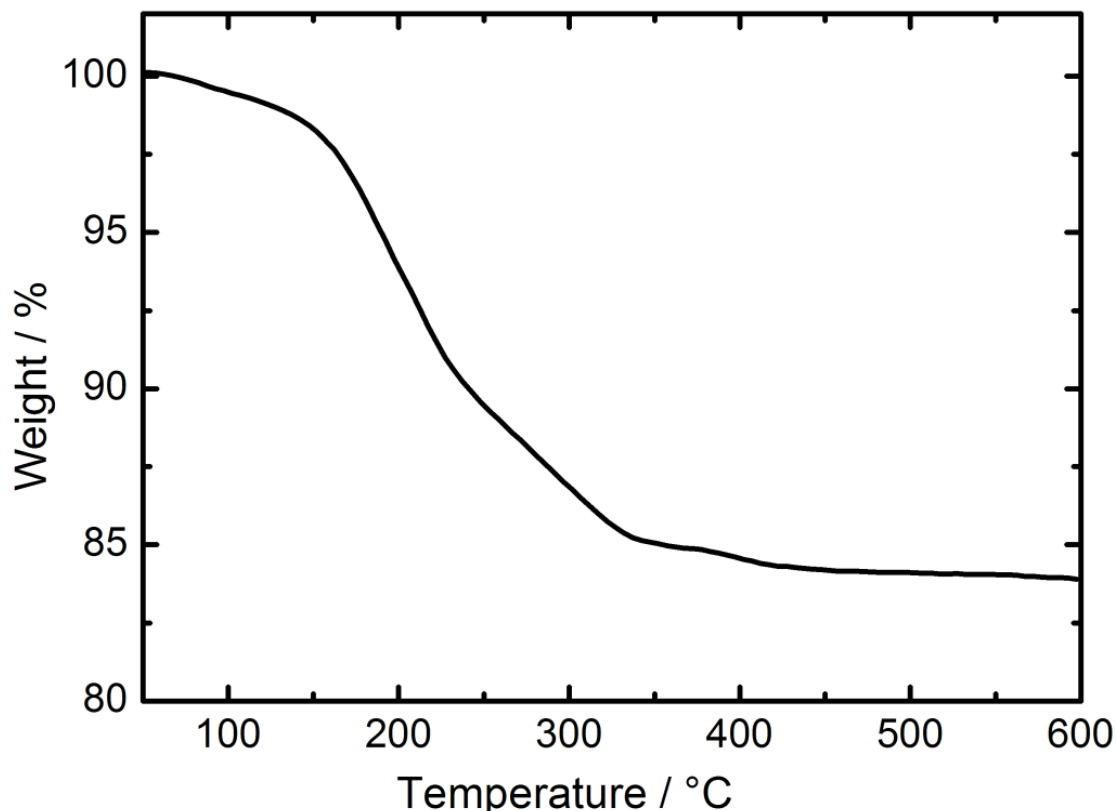
Figure 4.33: Thermogravimetry of the as-prepared CZTS nanoparticles under nitrogen atmosphere.[97]

Finally, optical properties and the band gap of the as-prepared CZTS nanoparticles were determined by UV-Vis spectroscopy (Figure 4.34). To this concern, a strong absorption with a steep increase of the absorption edge is observed between 850 and 900 nm. By plotting $(\alpha\, h\, v)^2$ versus photon energy in a Tauc plot as shown in the inset of Figure 4.34, the optical band gap of the as-prepared CZTS nanoparticles can be deduced to 1.37(3) eV, which is slightly lower as compared to literature data (1.45-1.51 eV).[11, 12, 15-17, 59]

Manufacturing and testing of thin-film solar cells based on CZTS nanoparticles
This part of work was mainly done by Dr. Erik Ahlswede and Thomas Schnabel from ZSW in Stuttgart (Germany). Similar processes for absorption layer preparation and solar-cell manufacture were used as described in the chapter of 4.1.2. The highly

concentrated CZTS suspension in isopropanol was deposited on Mo-coated soda-lime glass via doctor-blade coating, followed by a subsequent drying step at 300 ℃ in air. This coating and drying procedure was repeated two times to build up a certain film thickness. The CZTS absorption layer was then annealed at 500 ℃ for 50 minutes in nitrogen-diluted selenium vapor (selenization process).[75] After cooling naturally to room temperature, the resulting crystalline absorber layer was coated with CdS in a thickness of about 50 nm via CBD, followed by sputtering a ZnO window layer and a transparent ZnO:Al front contact to obtain functional solar cells.
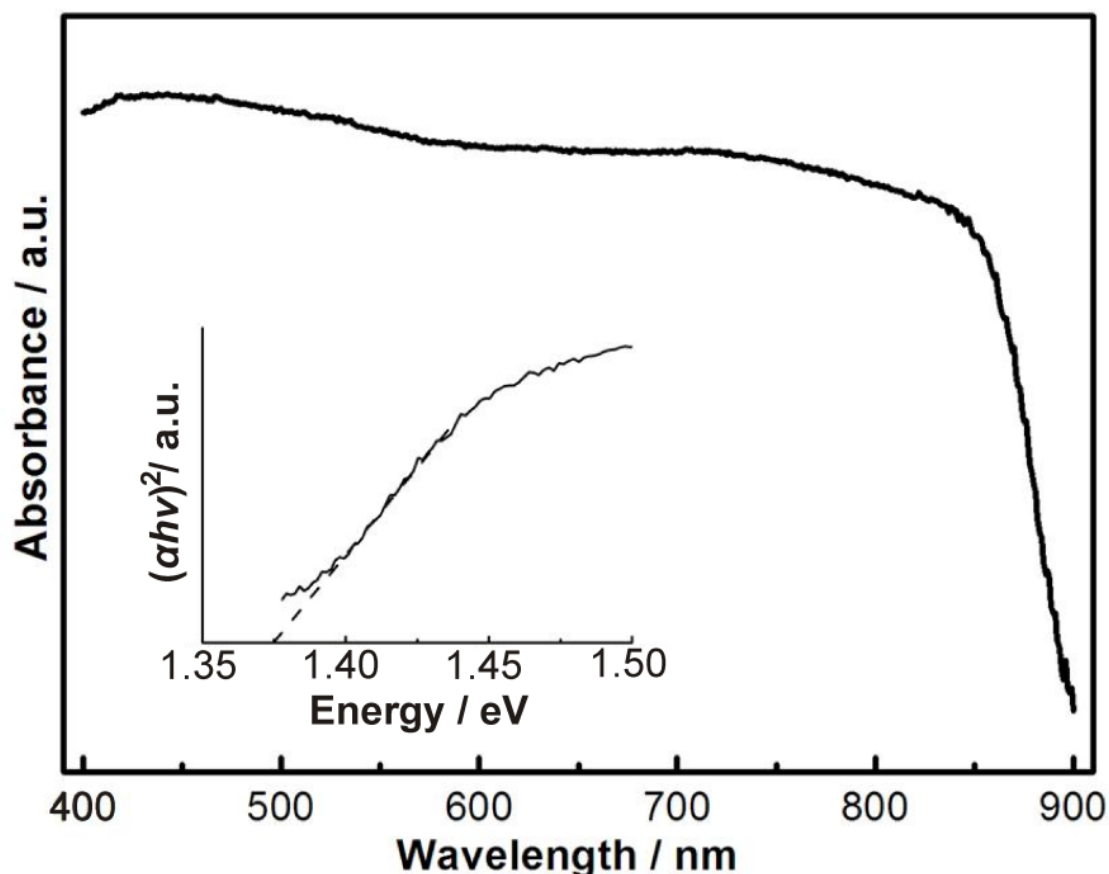
Figure 4.34: UV-Vis spectrum of the as-prepared CZTS nanoparticles with inset showing a Tauc plot for determining the optical band gap (1.37(3) eV).[97]

After the selenization process, the conversion of CZTS to CZTSSe is beneficial to the absorber-layer quality and solar-cell performance.[65] On the one hand, the volume increase of about 15% while exchanging sulfur in CZTS (unit cell volume of CZTS: 320 Å^3)[98] against selenium in CZTSe (unit cell volume of CZTSe: 367 Å^3)[99] supports the formation of a dense layer that exhibits less interparticulate grain boundaries and defects. On the other hand, CZTSSe shows a tendency of having a lower defect density than pure sulfur samples[100] and has demonstrated the highest efficiencies according to literature reports.[65, 101] Furthermore, the band gap of CZTSSe, which was determined by EQE analysis, is decreased to 1.14 eV. As CZTSSe has a smaller band gap than CZTS, the improved cell performance may also

be related to a beneficial intrinsically implemented band-gap grading within the active layer.
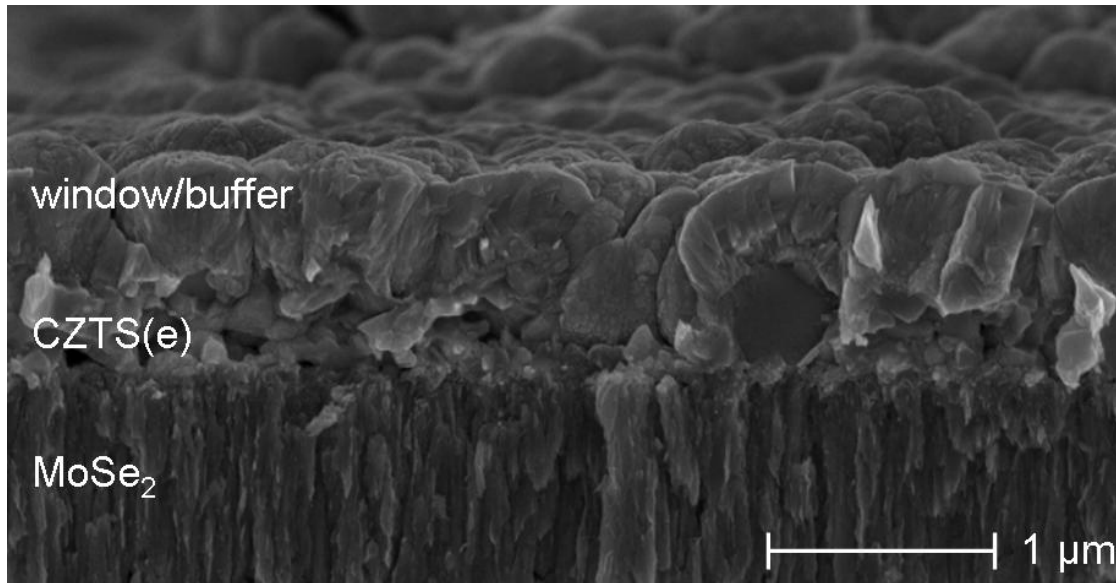
Figure 4.35: SEM image showing a cross section of the CZTSSe thin-film solar cell.[97]
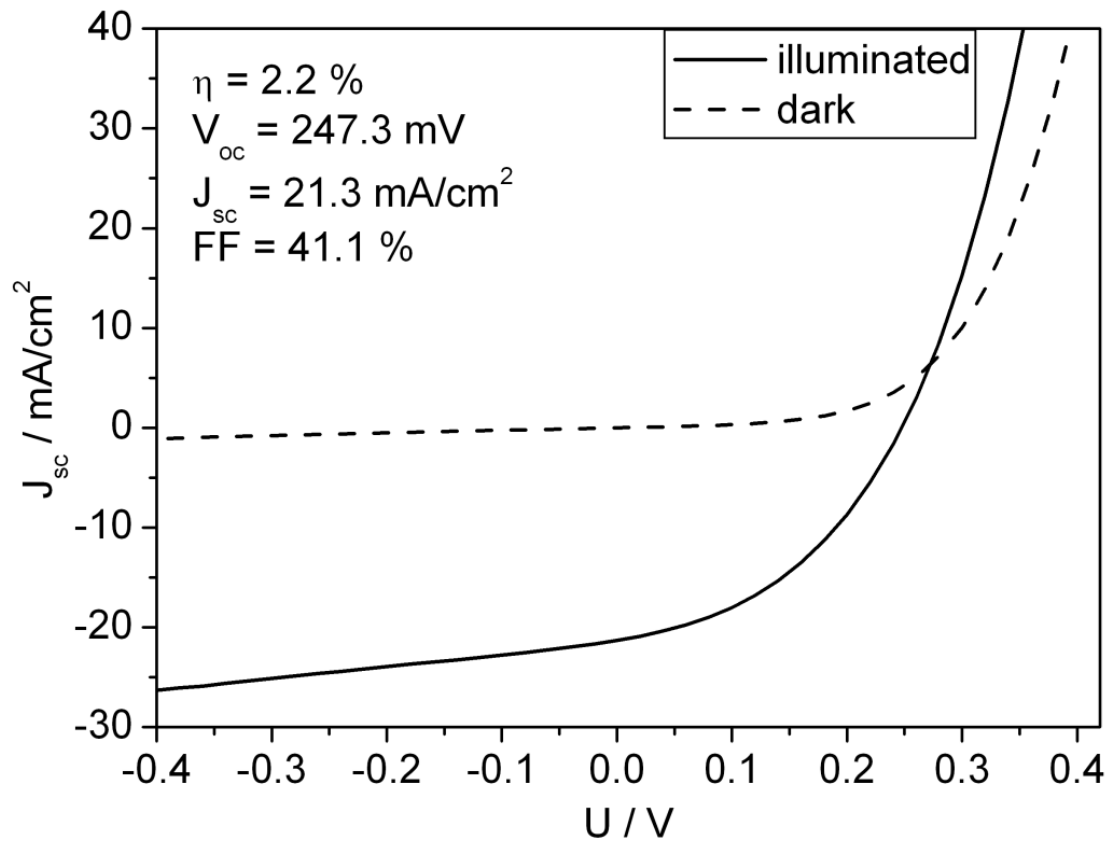
Figure 4.36: Illuminated and dark current-voltage characteristics of the CZTSSe thin-film solar cell.[97]

For solar-cell performance tests, the as-manufactured CZTSSe solar cell was divided into eight small cells of approximately 0.25 cm^2 each in size for further characterization. The cross section of the final CZTSSe thin-film solar cell was investigated by SEM. In Figure 4.35, the CZTSSe absorber layer is clearly visible with a thickness of about 500 nm, as well as kesterite crystals of few hundred nanometers in size. Below the absorber layer, a MoSe$_2$ layer with a thickness of about 1 µm is detected. The CdS buffer layer and the sputtered ZnO/ZnO:Al top electrode are observed on top of the absorber layer. The current-voltage characteristics of the CZTSSe thin-film solar cell, measured by a Keithley 238 source measuring unit under standard conditions (simulated AM 1.5 global solar irradiation with a WACOM sun simulator at 1000 W m^{-2}), are presented in Figure 4.36. The device shows an open-circuit voltage of 247.3 mV, a short-circuit current density of 21.3 mA cm^{-2} and a fill factor of 41.1 %, thus leading to a power-conversion efficiency of 2.2 %.

For the lab-scale CZTSSe thin-film solar cells, additional characterization, such as Raman spectroscopy, X-ray fluorescence analysis and EQE measurement, and their detailed results and analyses are provided in the submitted manuscript.[97]

In summary, the function of a lab-scale CZTSSe-based thin-film solar cell is proven as a conceptual study. The polyol-mediated synthesis already leads to crystalline CZTS nanoparticles and can be easily up-scaled, in principle.[102, 103] Nevertheless, much more efforts and optimization of the experimental conditions (particle size and overall composition of CZTS, thickness of CZTS/CZTSe thin-films, duration and temperature of the selenization process, etc.) are necessary to improve the morphology of the CZTSSe absorber layer and to increase the overall solar-cell performance.

4.1.4   Se@CuSe Core@Shell Nanoparticles

Motivation
In order to reach high efficiencies of CISe/CIGSe, the precursor layers are always annealed in a selenium vapour atmosphere as selenization process to compensate for a possible loss of selenium during the heating step or to reach denser polycrystalline absorption layers. So far, only conventional sources of selenium, either as an evaporated capping layer that requires a vacuum system or as additional selenium vapour/H$_2$Se in the gas phase were investigated. The preparation and use of inks containing Se nanoparticles as a selenium source are still a missing link. The availability of colloidally stable Se inks would allow avoiding vacuum-techniques and gas-phase deposition completely. Ideally, just a simple heat treatment of the as-deposited metal and the selenium precursor thin films could generate dense and crystalline CISe/CIGSe absorption layers.

However, it is very difficult to synthesize Se nanoparticles and to prepare Se inks. Different approaches were attempted to synthesize Se particles, however, the room-temperature phase transition of selenium (31 °C for bulk-Se)[104] is known as a general restriction, which hinders the preparation of Se inks. At room temperature, the red amorphous selenium (*a*-Se) obtained via low-temperature liquid-phase synthesis shows a phase transition to the grey trigonal selenium (*t*-Se), which is a thermodynamically stable crystalline phase. This phase transition leads to rapid agglomeration and merging of the as-prepared *a*-Se particles, followed by instantaneous formation of large crystalline needles.[105-112] Such Se particles are not suitable for layer deposition and manufacturing of thin-film solar cells.

In this chapter, we focus on the synthesis of stable spherical Se nanoparticles that are capped by CuSe to form Se@CuSe core@shell nanostructures. Based on this newly introduced CuSe capping, the phase-transition temperature of elemental selenium is shifted to >100 °C. As a result, colloidally stable inks of Se@CuSe core@shell nanoparticles can be obtained. In the first conceptual study, CISe thin-film solar cells can be manufactured, using Se@CuSe inks and $Cu_{11}In_9$ nanoparticles via a non-vacuum process.

Synthesis of Se nanoparticles
Colloidal particles of elemental selenium have been reported to be prepared by different synthesis routes. Most often selenious acid (H_2SeO_3) is reduced by hydrazine (N_2H_4).[110, 113] Alternatively, reduction of H_2SeO_3 by ascorbic acid,[109] dismutation of SeO_2,[108] and melting of bulk-Se in high-boiling solvents[107] were applied. Here, we used a hydrazine-driven reduction of H_2SeO_3 as suggested by *Smith*[113] and *Xia*.[110] Via the variation of the $N_2H_4 : H_2SeO_3$ ratio and the duration of the reaction as well as via the addition of polyvinylpyrrolidone (PVP), the size of the as-prepared *a*-Se nanoparticles can be controlled. The synthesis results in uniform spherical *a*-Se nanoparticles, which show the well-known phase transition with merging of particles (Figure 4.37A) and formation of large *t*-Se crystalline needles (Figure 4.37B). For nano- and micro-sized particles, due to huge specific surfaces, the *a*-Se to *t*-Se transition is observed even at below room temperature as compared to bulk-Se.[105-112] In fact, even when Se inks are kept at about 0 °C, the phase transition occurs after a certain period of time (typically 1-3 days). The phase transition can easily be followed by naked eyes due to the colour change of suspensions/powders from orange to grey (Figure 4.38 and Figure 4.43). In summary, the phase transition severely restricts practical handling of Se particles in view of storing for a certain period, gentle heating (e.g., due to centrifugation or particle redispersion in ultrasonic bath) as well as regarding layer deposition or printing of thin-films. Thus, these *a*-Se nanoparticles and their suspensions are not suitable for manufacturing CISe thin-film solar cells.
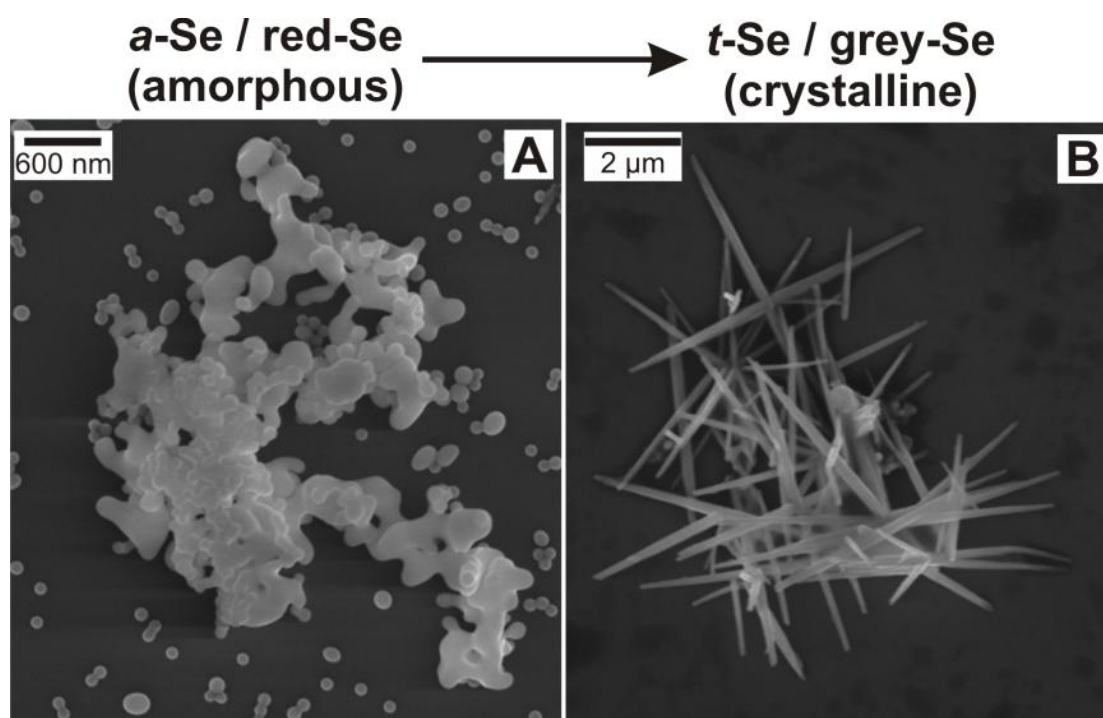
Figure 4.37: SEM images showing the merging (A) and crystallization (B) while red *a*-Se is passing through a phase transition to crystalline grey *t*-Se.[112]
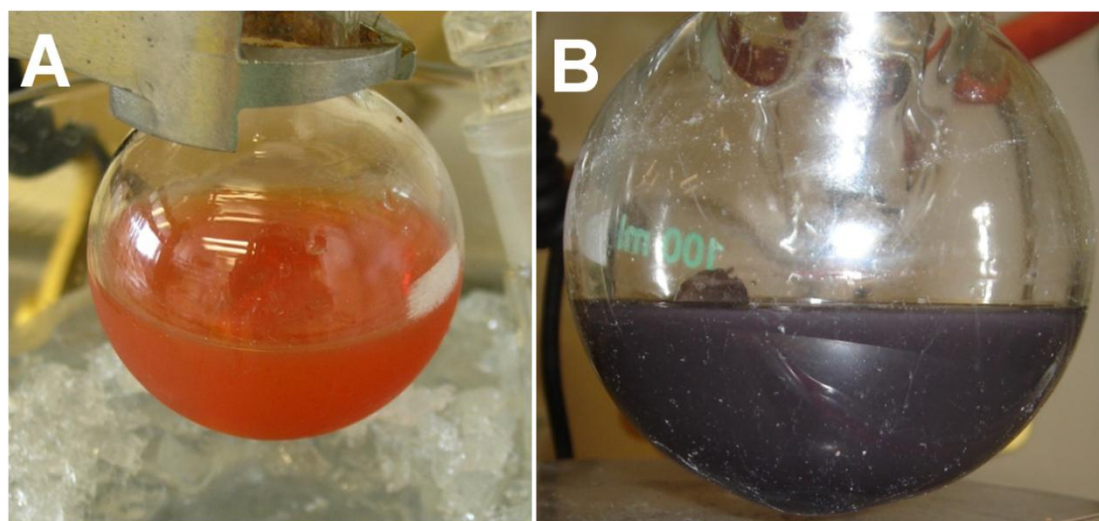
Figure 4.38: Photographs of the Se nanoparticle suspension in DEG: A) directly after the synthesis; B) overnight at room temperature.

Synthesis of Se@CuSe core@shell nanoparticles

To obtain inks of Se nanoparticles with sufficient colloidal and phase stability that are suitable for layer deposition and manufacturing of CISe thin-film solar cells, the as-prepared *a*-Se nanoparticles were capped with CuSe, which formed Se@CuSe core@shell nanostructure. In a typical synthesis that was performed under argon inert-gas protection, 0.5 to 2.5 mL $N_2H_4 \cdot H_2O$ (10 to 50 mmol, Table 4.4) and 200 mg PVP were added to 50 mL DEG in a three-neck flask. These precursors were mixed to form a homogeneous solution (solution I) under continuous stirring. Solution I was

then cooled to 0 ℃ in an ice bath. Thereafter, 103.2 mg (0.8 mmol) H_2SeO_3 dissolved in 3 mL DEG (solution II) were injected into the pre-cooled solution I. The reaction was allowed to proceed for different periods of time (t, Table 4.4). The gradual colour shift from a colourless solution to an orange suspension allows following the process of the reaction even by naked eyes. Afterwards, all residual $N_2H_4 \cdot H_2O$ in the reaction system was removed by vacuum distillation for 30 minutes at 0 ℃, followed by 150 minutes at room temperature. Thereafter, 7.3 mg (0.04 mmol) copper acetate ($Cu(Ac)_2$) dissolved in 3 mL DEG (solution III) were added dropwise. The addition of $Cu(Ac)_2$ again resulted in colour changes, from orange via orange-red to brick-red. Detailed information about the experimental parameters for the syntheses is listed in Table 4.4. Finally, the suspensions were diluted with demineralised water and the Se@CuSe core-shell nanoparticles were collected via centrifugation, washed repeatedly and redispersed in demineralised water for further analyses and treatments.

Table 4.4: Detailed experimental conditions to adjust mean diameters of Se@CuSe core@shell nanoparticles.

Sample	$N_2H_4 \cdot H_2O$	H_2SeO_3	$\dfrac{c\,(N_2H_4 \cdot H_2O)}{c\,(H_2SeO_3)}$	Reaction time t^*	$Cu(Ac)_2$	Mean diameter
	/ mmol	/ mmol	r^*	/ min	/ mmol	/ nm**
A	10	0.8	13	90	0.04	410(90)
B	20	0.8	25	90	0.04	310(63)
C	20	0.8	25	75	0.04	179(48)
D	20	0.8	25	30	0.04	162(48)
E	40	0.8	50	30	0.04	100(27)
F	50	0.8	63	30	0.04	85(20)
G	40	0.8	50	30	0.16	105(29)

(r^*: molar ratio of $N_2H_4 \cdot H_2O$ and H_2SeO_3)

(t^*: reaction time of $N_2H_4 \cdot H_2O$ and H_2SeO_3)

(**: mean diameter according to DLS)

The strategy of synthesising Se@CuSe core@shell nanoparticles is schematically depicted in Figure 4.39. The coordinating and reducing properties of DEG as well as performing the reaction at a reduced temperature (0 ℃) allow controlling the particle nucleation and growth. The residual $N_2H_4 \cdot H_2O$ has to be removed via vacuum distillation prior to the addition of $Cu(Ac)_2$, since Cu^{2+} would have been reduced to elemental Cu otherwise. In order to prove the condensed colourless liquid to be N_2H_4, several drops of blue $Cu(Ac)_2$ solution were added, resulting in a brown suspension (Figure 4.40). The colour change from the blue solution to a brown suspension is due to the reduction reaction of $Cu(Ac)_2$ and N_2H_4, which verifies the presence of N_2H_4. Finally, the Se@CuSe core@shell nanoparticles were obtained as a brick-red powder that can be easily redispersed (e.g. in ethanol) for manufacturing CISe solar cells. Powder samples as well as inks of Se@CuSe core@shell nanoparticles show sufficient stability in view of practical handling without any phase transition to t-Se.
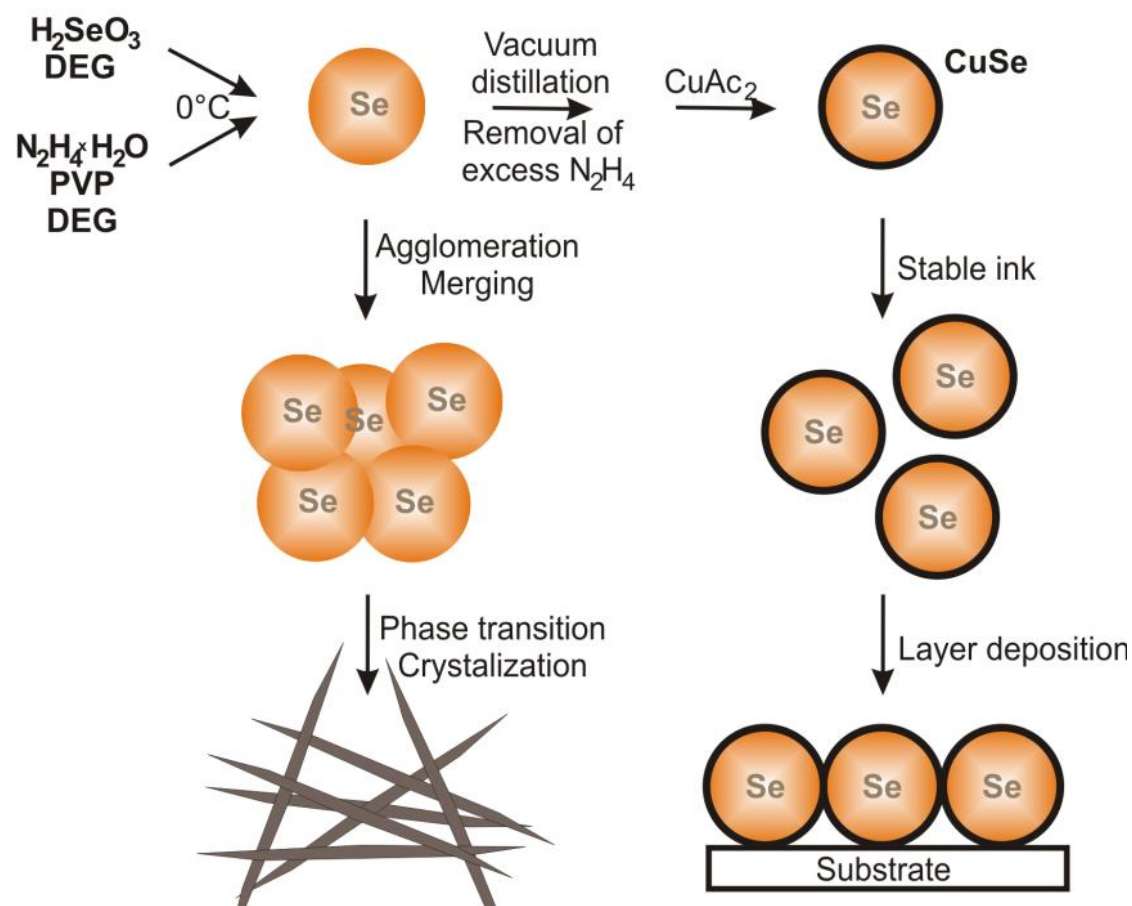
Figure 4.39: Schematic representation of the synthesis, agglomeration and crystallization of red *a*-Se as well as the formation of Se@CuSe core@shell nanoparticles for stable inks and subsequent layer deposition.[112]
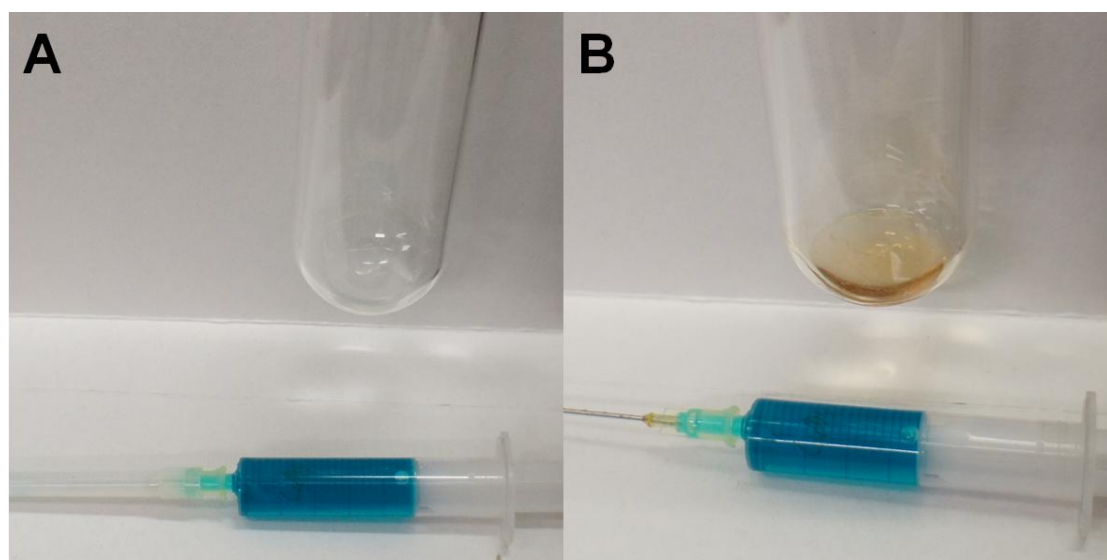
Figure 4.40: Photographs of condensed colorless N_2H_4 via vacuum distillation (A) and after the reaction with blue $Cu(Ac)_2$ solution (B).

Characterization of Se@CuSe core@shell nanoparticles

All analytic characterizations were carried out under air. The average size and the size distribution of the as-prepared Se@CuSe core@shell nanoparticles were determined by DLS based on diluted Se@CuSe aqueous suspensions (Figure 4.41). To this concern, nanoparticles with relatively narrow size distribution and clearly different mean diameters of 410(90) nm (sample A), 310(63) nm (sample B), 179(48) nm (sample C), 162(48) nm (sample D), 100(27) nm (sample E) and 85(20) nm (sample F) were obtained. The diameter control is predominantly guaranteed by variation of the molar ratio of N_2H_4 and H_2SeO_3 (r), and the reaction time (t) (Table 4.4). At constant r (*cf.* samples B, C and D), the diameter of the Se@CuSe core@shell nanoparticles can be reduced from 310 nm to 162 nm by decreasing t from 90 minutes to 30 minutes. With t remaining constant (*cf.* samples D, E and F), the average particle size can be decreased from 162 nm to 85 nm by increasing r from 25 to 63.
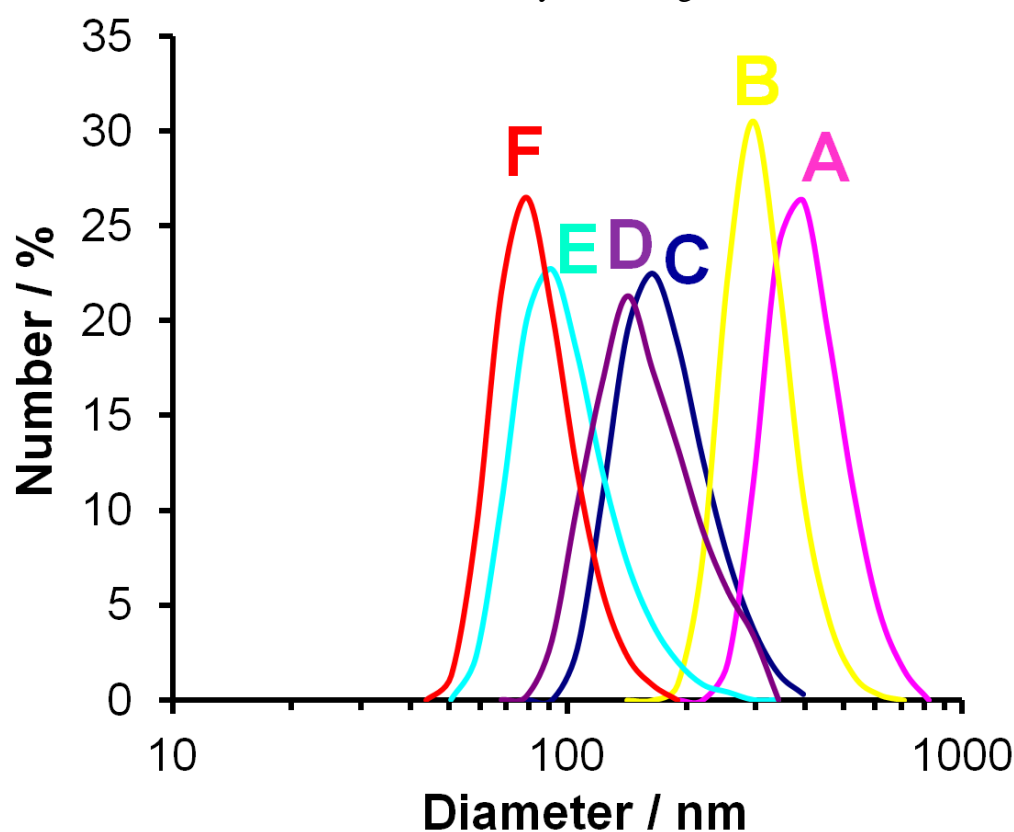
Figure 4.41: DLS analyses of the as-prepared Se@CuSe core@shell nanoparticles in demineralised water (samples A, B, C, D, E and F according to Table 4.4).

The SEM images confirm the particle size and the size distribution of the as-prepared Se@CuSe core@shell samples (Figure 4.42 and Figure 4.47). A significant decrease in particle size from sample A to sample F is observed in Figure 4.42, where all the SEM images have the same scale bars. Due to the relatively uniform size distribution, partial formation of dense-packed particle layers is clearly visible. Notably, the spherical nanoparticles of sample E and F started merging at very high magnification and losing contrast on a time scale over 10 seconds due to a large amount of high-energy electron bombardment. Samples A to G were prepared to study the

relevant experimental conditions as well as to perform material characterization; sample E was used to manufacture CISe thin-film solar cells.
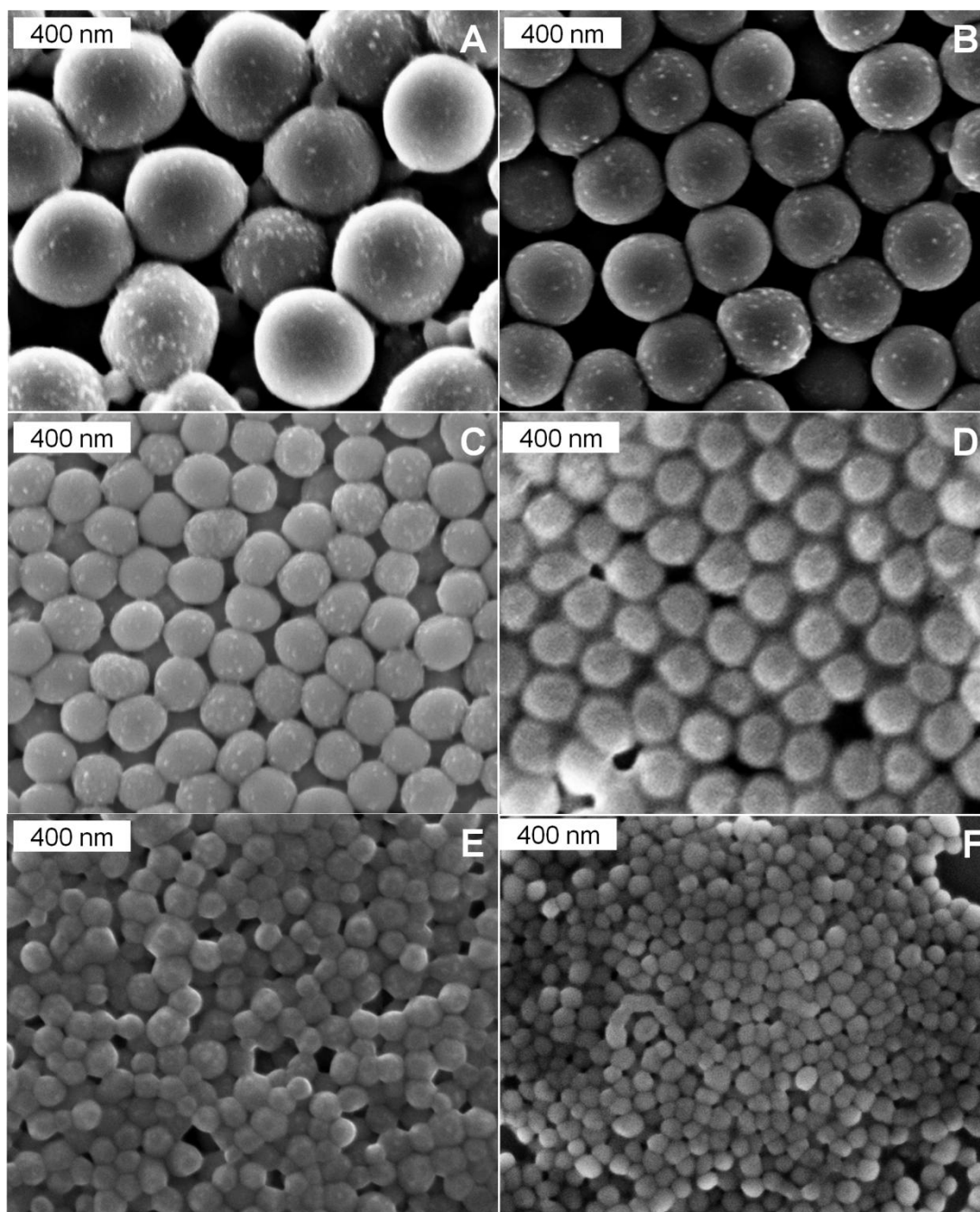
Figure 4.42: SEM images of different Se@CuSe core@shell nanoparticles (samples A, B, C, D, E and F according to Table 4.4).

After slowly evaporating the demineralised water at room temperature, the brick-red powder was collected and investigated by XRD (Figure 4.43). XRD patterns of the as-prepared samples (A to F, *cf.* Table 4.4), first of all, do not show any Bragg peaks in the entire 2θ range from 10 to 70 °, which indicated the non-crystalline nature of *a*-Se (Figure 4.43A). Moreover, no Bragg peaks of any Cu_xSe_y phase are visible

likewise. After annealing the as-prepared brick-red powder samples at 175 °C, the crystalline *t*-Se was obtained (Figure 4.43B). The phase transition was also followed by the colour change from brick-red to grey. In addition, the main Bragg peak of CuSe/Klockmannite becomes visible with low intensity at a 2θ value of 28 °.
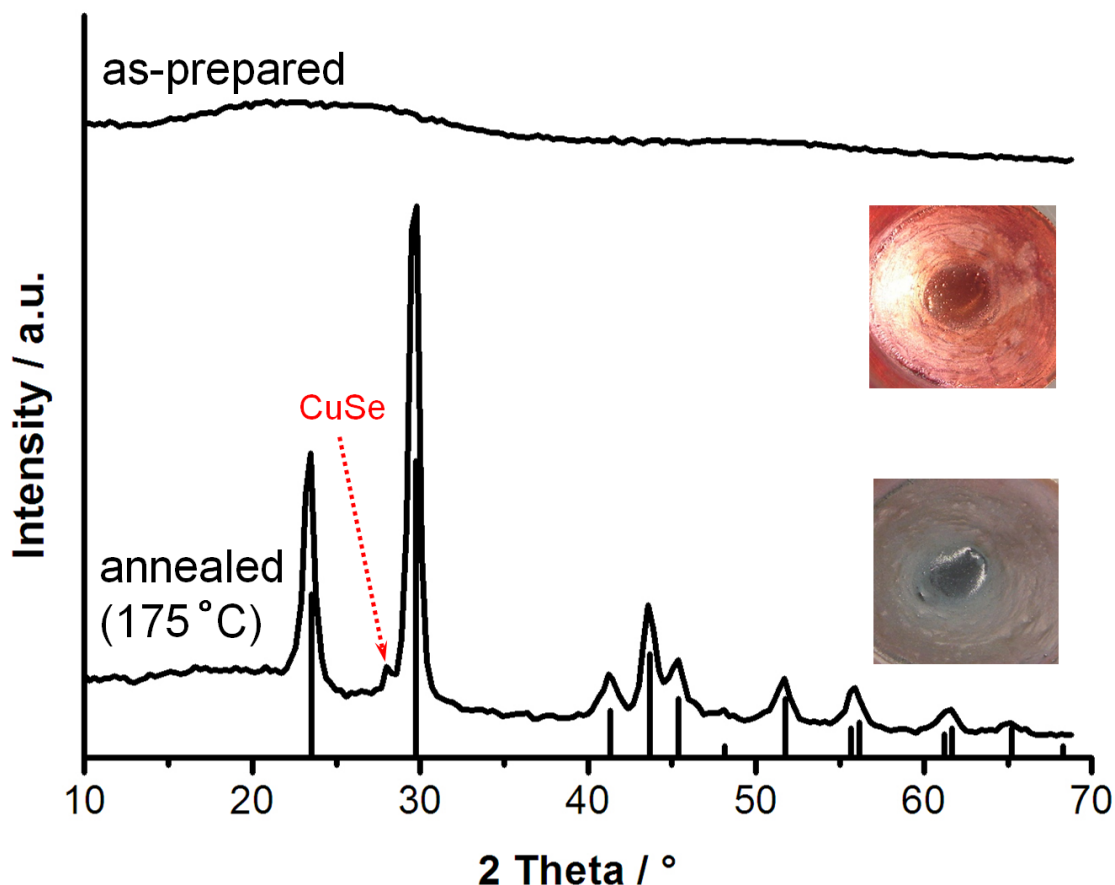
Figure 4.43: XRD patterns and photographs of the as-prepared and annealed at 175 °C Se@CuSe core@shell nanoparticles (sample A to F, *cf.* Table 4.4; *t*-Se_ICDD No. 6-362 as a reference).

The thermal stability and the phase transition of the as-prepared Se@CuSe core@shell nanoparticles were analyzed by DSC-TG (Figure 4.44A). The DSC result shows the phase transition from *a*-Se to *t*-Se with its onset at 107 °C. Thus, the phase-transition temperature of Se@CuSe core@shell nanomaterial is significantly increased, even when compared with bulk-Se (31 °C).[104] TG analysis, furthermore, indicates that no weight loss (e.g. due to the evaporation of Se) occurs in a temperature range up to the melting point with its onset at 217 °C (melting point of bulk-Se: 221 °C) (Figure 4.44A). Even more surprisingly, the spherical shape of the Se@CuSe core@shell nanoparticles is still retained after annealing the powder samples at 175 °C, although the samples clearly show crystalline feature of *t*-Se thereafter (Figure 4.44B). Altogether, the significantly increased phase-transition temperature and the spherical shape retained after annealing impressively confirm the colloidal stability of the Se@CuSe core@shell nanoparticles and the effectiveness of the core@shell concept.
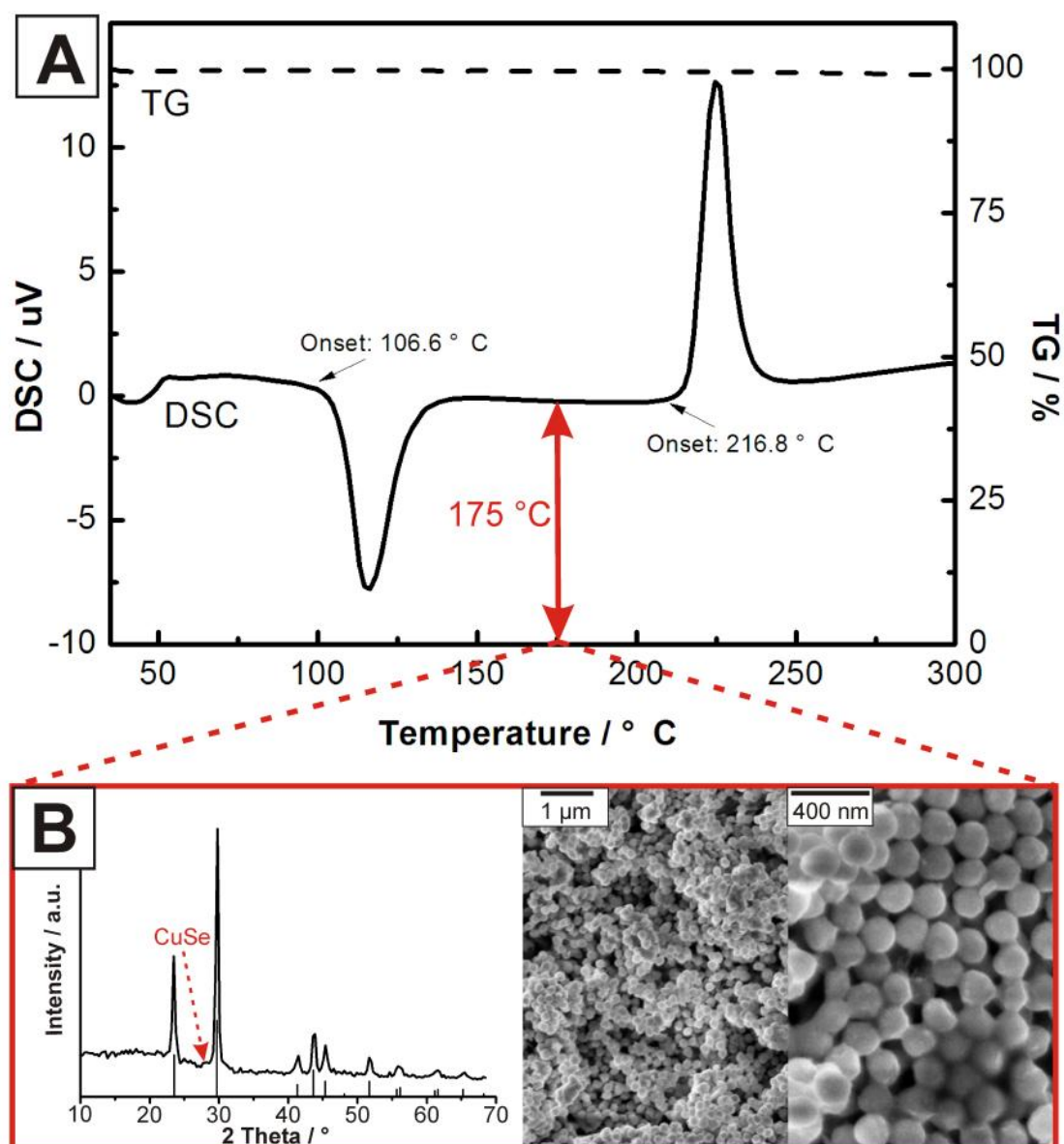
Figure 4.44: DSC and TG analyses of the as-prepared Se@CuSe core@shell nanoparticles (sample E, *cf.* Table 4.4) showing the onset of the phase transition at 107 °C and the onset of the melting point at 217 °C (A); (B) crystallinity and spherical shape of sample E after annealing at 175 °C with XRD and SEM (*t*-Se_ ICDD No. 6-362 as a reference; arrow indicating CuSe from the shell).[112]

The increased phase-transition temperature and the improved colloidal stability of the Se@CuSe core@shell nanoparticles can be ascribed to CuSe serving as a protecting layer. On the one hand, CuSe obviously stabilizes the red *a*-Se modification. Traces of Cu^{2+} that might diffuse into the inner Se core could further support this effect. On the other hand, the CuSe shell separates the nanoparticles from each other, so that a direct contact of the Se cores is excluded.

FT-IR spectrum of the as-prepared Se@CuSe core@shell nanoparticles indicates the

presence of PVP as a surface capping (Figure 4.45). The vibrational bands observed at 3050-2800 cm^{-1} (ν(C–H)), 1850-1550 cm^{-1} (ν(C=O)) and the fingerprint region (1500-600 cm^{-1}) are in good agreement with PVP reference spectrum. The additional strong bands can be attributed to OH-containing solvents (water, ethanol) adhered on particle surface at 3700-3250 cm^{-1} (ν(O–H)) and CO_2 from air (2400-2350 cm^{-1} and 2350-2275 cm^{-1}).
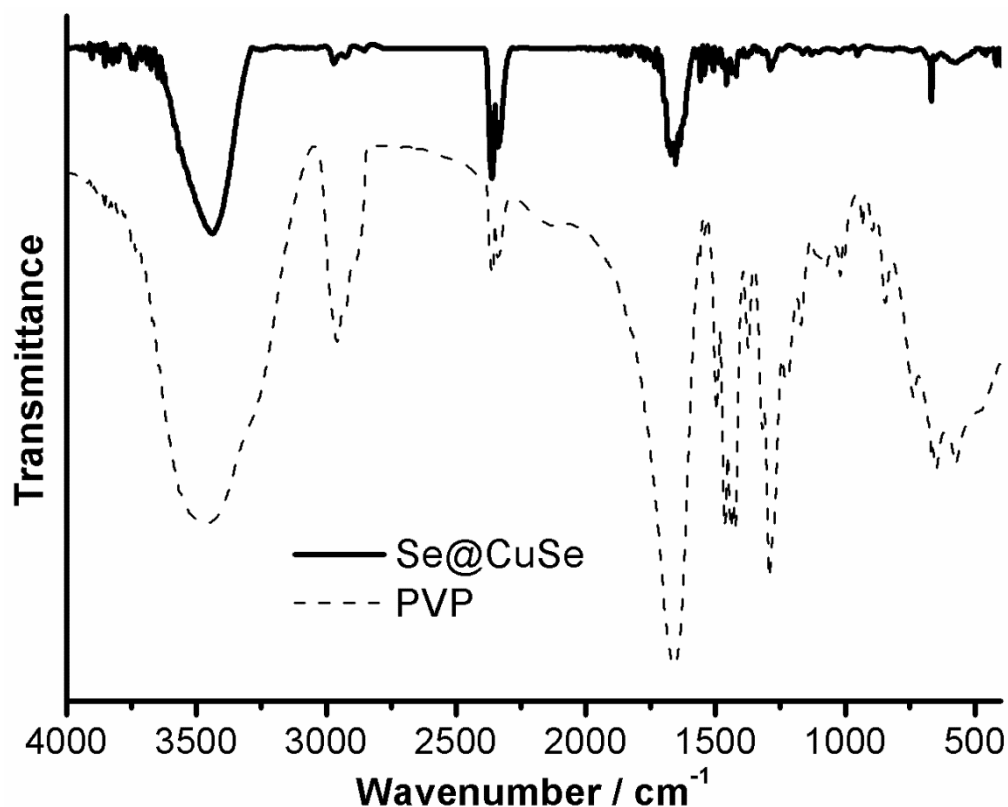
Figure 4.45: FT-IR spectrum of PVP-capped Se@CuSe core@shell nanoparticles (sample E, *cf.* Table 4.4; pure PVP as a reference).
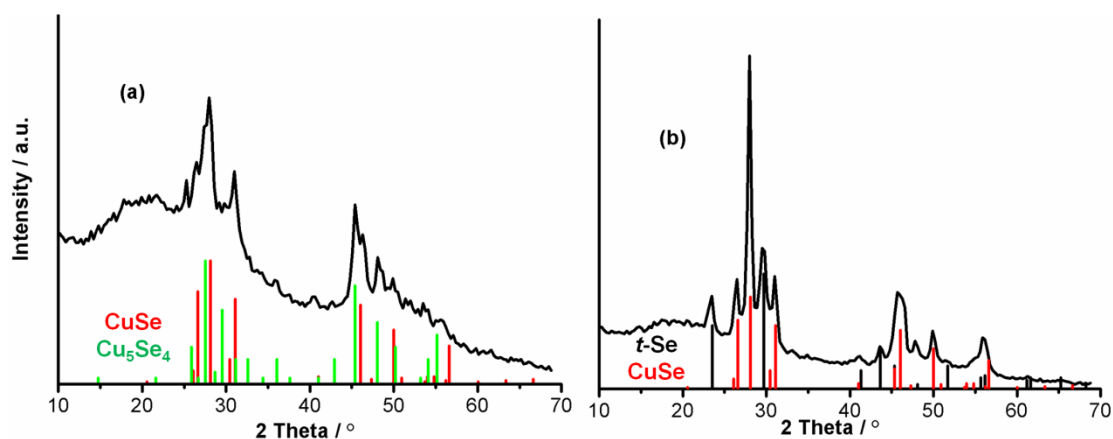
Figure 4.46: XRD patterns of the as-prepared (a) and annealed (b) Se@CuSe core@shell nanoparticles (Cu-rich sample G, *cf.* Table 4.4) with the references: *t*-Se_ICDD No. 6-362/black lines; CuSe/ Klockmannite_ICDD No. 34-171/red lines; Cu_5Se_4/Athabascaite_ICDD No. 21-1016/green lines.

In order to prove the presence of a CuSe shell encapsulating the Se core, a copper-rich sample F with a molar ratio Se : Cu = 5 : 1 (Table 4.4) was synthesized in addition to samples A to F exhibiting a lower Cu concentration (samples A to F with Se : Cu = 20 : 1, Table 4.4). According to DLS (Figure 4.41) and SEM (Figure 4.42), this Cu-rich sample G is very comparable to sample E in terms of the particle size and the size distribution (Table 4.4). XRD pattern of the as-prepared Cu-rich sample G, which was different from the amorphous structure of the as-prepared sample A to F (Figure 4.43A), indeed evidences the presence of crystalline Cu_xSe_y phases (Figure 4.46a). CuSe/Klockmannite and Cu_5Se_4/Athabascaite are visible as the predominant phases. When annealing the Cu-rich sample G at 175 ℃, crystalline t-Se is obtained as expected, in addition to CuSe/Klockmannite (Figure 4.46b). The use of a large amount of $Cu(Ac)_2$ in the reaction leads to an obvious formation of a CuSe shell. Sample A to F also have a core@shell structure, but due to the small amount of $Cu(Ac)_2$ introduced, the CuSe shell is very thin and hard to detect by XRD. After annealing at 175 ℃, sample A to F show the main Bragg peak of CuSe/Klockmannite at a 2θ value of 28.0 °(Figure 4.43B and Figure 4.44B).

Finally, the Se@CuSe core@shell nanostructure was investigated based on HAADF-STEM combined with high-resolution EDX line-scan analysis, which were conducted with an aberration-corrected FEI Titan[3] 80-300 microscope at 300 kV. The drift-corrected EDX line-scans were taken with a probe diameter of 0.5 nm and a distance of about 1.0 nm between two measuring points. With respect to a quantification of the EDX spectra from the core@shell nanoparticles, one has to keep in mind that only compositions are obtained that are averaged along the electron-beam direction. In concrete, the whole volume along the electron trajectory contributes to the detected X-ray signal. To evaluate the composition of different shells of a core@shell nanoparticle, a procedure was developed that is described in detail in Ref. [114]. This part of work, including HAADF-STEM, high-resolution EDX line-scan analysis and the evaluation of the concentration profile, was done by Dr. Radian Popescu from the Laboratory of Electron Microscopy, Karlsruhe Institute of Technology (KIT) in Karlsruhe (Germany).

Figure 4.47C shows a HAADF-STEM image of a single Se@CuSe core@shell particle with about 330 nm in diameter from sample B (Table 4.4). The red dashed line indicates the position of a high-resolution EDX line-scan analysis. Quantification analysis of the EDX spectra yields the selenium and copper composition profiles shown in Figure 4.47D, which demonstrates the core@shell structure. Here, a significant increase of the copper concentration is observed at the surface region of the Se@CuSe core@shell nanoparticles. The inner section of the particle, in contrast, shows a high Se concentration. Copper is always detectable for the inner particle core since the electron beam has to pass through the CuSe shell (Figure 4.47D). Using the evaluation procedure described in Ref. [114], the composition and the thickness of the shell and the core can be reconstructed as shown schematically in Figure 4.47E.

Notably, the relatively large error for the composition given in Figure 4.47E results from the evaluation procedure and is not caused by the statistics of the EDX spectra. The evaluation yields an outer shell with a thickness of about 20 nm and an average chemical composition of $Cu_{36(10)}Se_{64(10)}$. The particle core has a diameter of about 340 nm and an average composition of $Cu_{15(12)}Se_{85(12)}$.

In summary, the as-prepared Se@CuSe core@shell nanoparticles of sample B exhibit an inner core of almost pure elemental selenium with a diameter of about 340 nm and a shell with a thickness of about 20 nm significantly enriched by copper. Together with the XRD result (Figure 4.43A and Figure 4.46), these findings can conclude the presence and the structure of the Se@CuSe core@shell nanoparticle comprising a CuSe shell and an almost pure Se core.
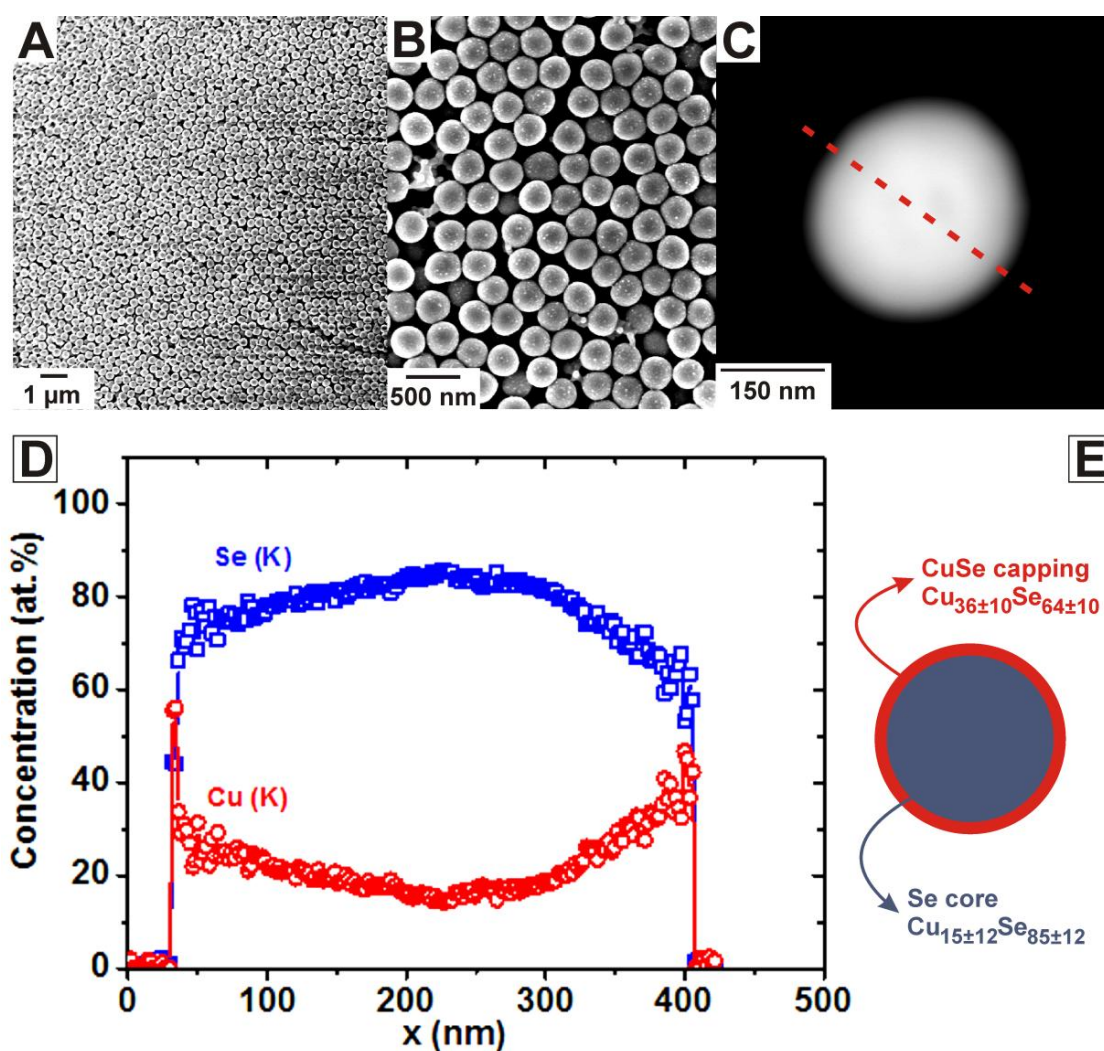
Figure 4.47: SEM overview images (A, B), HAADF-STEM image (C), concentration profile obtained from high-resolution EDX line-scan analysis (D, along red dashed line as indicated in C) and scheme with core and shell compositions (E) of the Se@CuSe core@shell particle (sample B, *cf.* Table 4.4).[112]

Manufacturing and testing of CISe thin-film solar cells based on Se@CuSe core@shell nanoparticles

The potential of the here prepared Se@CuSe core@shell nanoparticles for manufacturing CISe thin-film solar cells was investigated as a conceptual study in combination with $Cu_{11}In_9$ nanoparticles, which have been already successfully developed and tested in CISe solar cells.[80] Because sample E (Table 4.4) exhibits a small size, it was used for solar-cell manufacturing in the following throughout. This part of work was mainly done by Dr. Erik Ahlswede, Dr. Aina Quintilla and Marco Cemernjak from ZSW in Stuttgart (Germany). Inks of Se@CuSe core@shell nanoparticles were obtained by redispersing the as-prepared powders in ethanol with a solid load of typically 200 mg mL^{-1}. The precursor inks were prepared right before layer deposition in order to prevent particle agglomeration over time. For layer deposition, two different strategies were applied: Scenario 1 – Se@CuSe core@shell nanoparticles were co-dispersed with $Cu_{11}In_9$ nanoparticles in ethanol and deposited thereafter to form a mixed Se@CuSe/$Cu_{11}In_9$ precursor layer. Scenario 2 – a $Cu_{11}In_9$ layer was deposited first, followed by a stacked layer of the Se@CuSe core@shell nanoparticles on top of the $Cu_{11}In_9$ particle film.
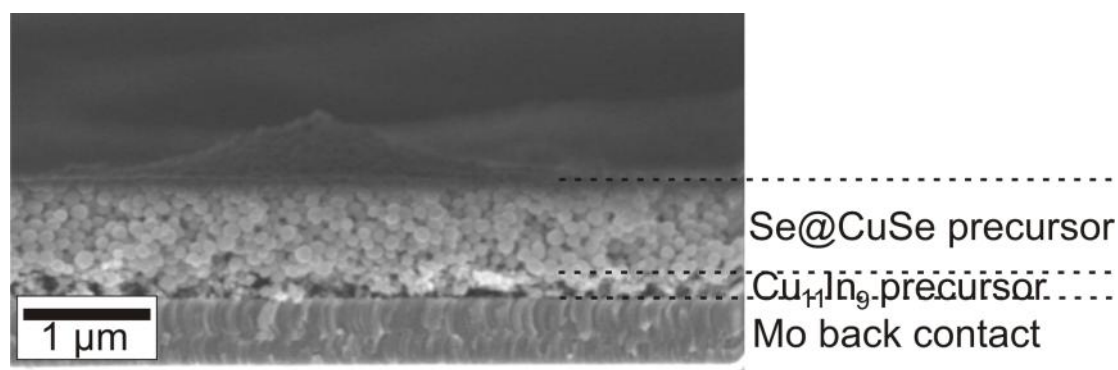
Figure 4.48: Doctor-bladed thin-film of Se@CuSe core@shell nanoparticles on top of pre-deposited $Cu_{11}In_9$ nanoparticle thin-film (scenario 2).

The preparation of dense, homogenous precursor layers is not yet as convenient as for the $Cu_{11}In_9$ system, but well feasible as can be seen in Figure 4.48. The Se@CuSe precursor together with $Cu_{11}In_9$ could make an additional Se atmosphere during the chemical conversion step; however, too much Se can lead to an excessive $MoSe_2$ formation at solar cells' back contact. Thus, precise optimization of the relevant conditions will be necessary as a next step. By now, both of the scenarios were tested and evaluated. Figure 4.48 exemplarily shows a thick layer of Se@CuSe nanoparticles on top of a thin $Cu_{11}In_9$ precursor layer. Notably, the diameter (~20 nm) and the layer thickness (~250 nm) of $Cu_{11}In_9$ nanoparticles are much smaller as compared to the Se@CuSe precursor (diameter: ~100 nm, layer thickness: ~600 nm). In addition to the above mentioned scenarios 1 and 2, different selenization environments were tested: either heated in pure nitrogen or in selenium rich atmosphere for different times.

After selenization of the precursor layers at 550 °C,[80, 94] densification and crystal

growth are clearly visible for both scenarios (Figure 4.49). Crystal morphology and layer structure are significantly different from the precursor layer, indicating the reaction between Se@CuSe and $Cu_{11}In_9$. Considering that these first lab-cells were manufactured under non-optimized conditions (e.g. in terms of chemical composition, Cu : In : Se ratio, layer thickness and morphology, duration/temperature of annealing), the resulting CISe solar cells show promising performance for both scenarios of adding the Se@CuSe precursor. Thus, efficiencies of 1.8 % for the Se@CuSe-$Cu_{11}In_9$ mixed film (scenario 1) and 3.0 % for the Se@CuSe capping layer (scenario 2) were obtained. Current-voltage characteristics of the best lab-cells are shown in Figure 4.50, which were measured using a Keithley 238 source-measuring unit under simulated AM 1.5 global solar irradiation with an ORIEL sun simulator at 100 mW cm^{-2}. So far, the best results were still obtained via the classical reference procedure (550 °C, 1 hour) with an additional Se atmosphere during the tube furnace process.[80, 94]
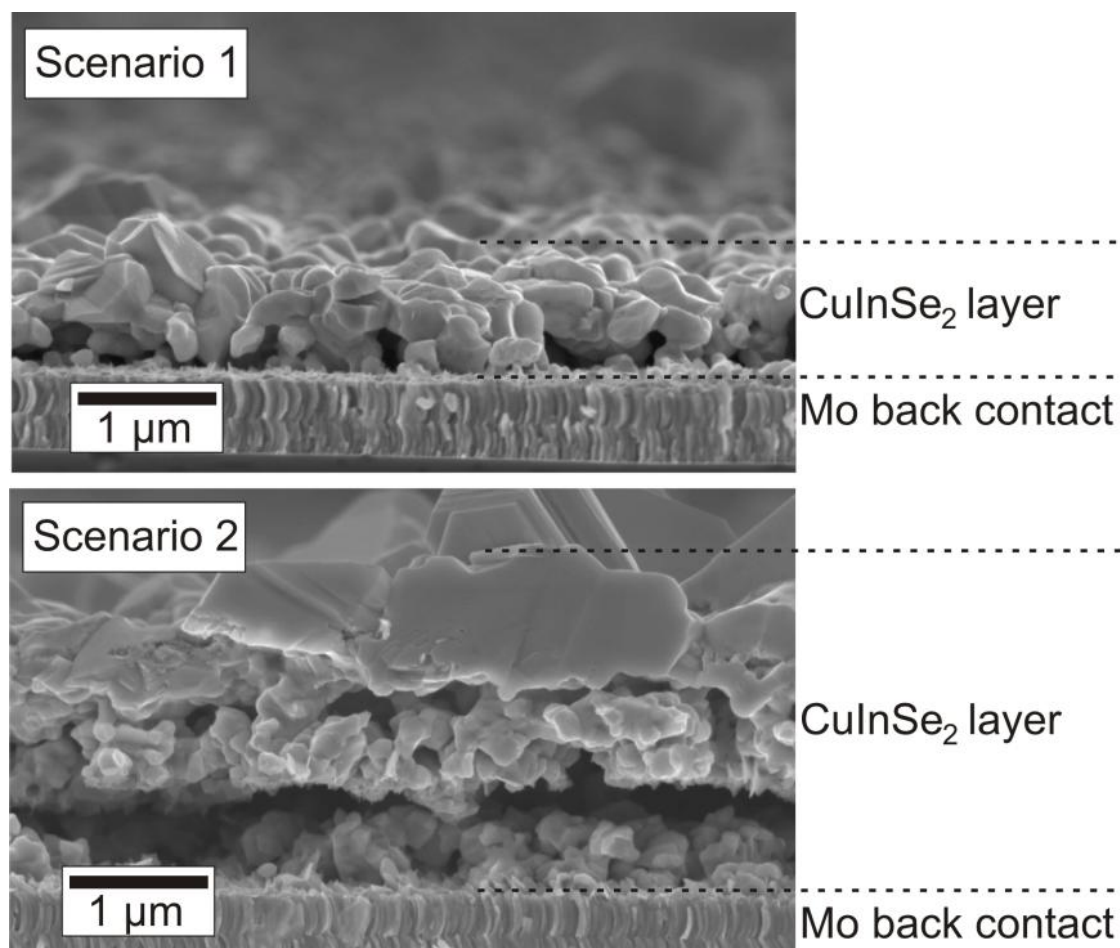
Figure 4.49: CISe absorber layers after selenization (550 °C, 1 hour) – Scenario 1: Se@CuSe core@shell nanoparticles and $Cu_{11}In_9$ nanoparticles mixed in suspension prior to thin-film deposition; Scenario 2: Se@CuSe core@shell nanoparticles as a capping on top of a pre-deposited $Cu_{11}In_9$ nanoparticle layer.[112]
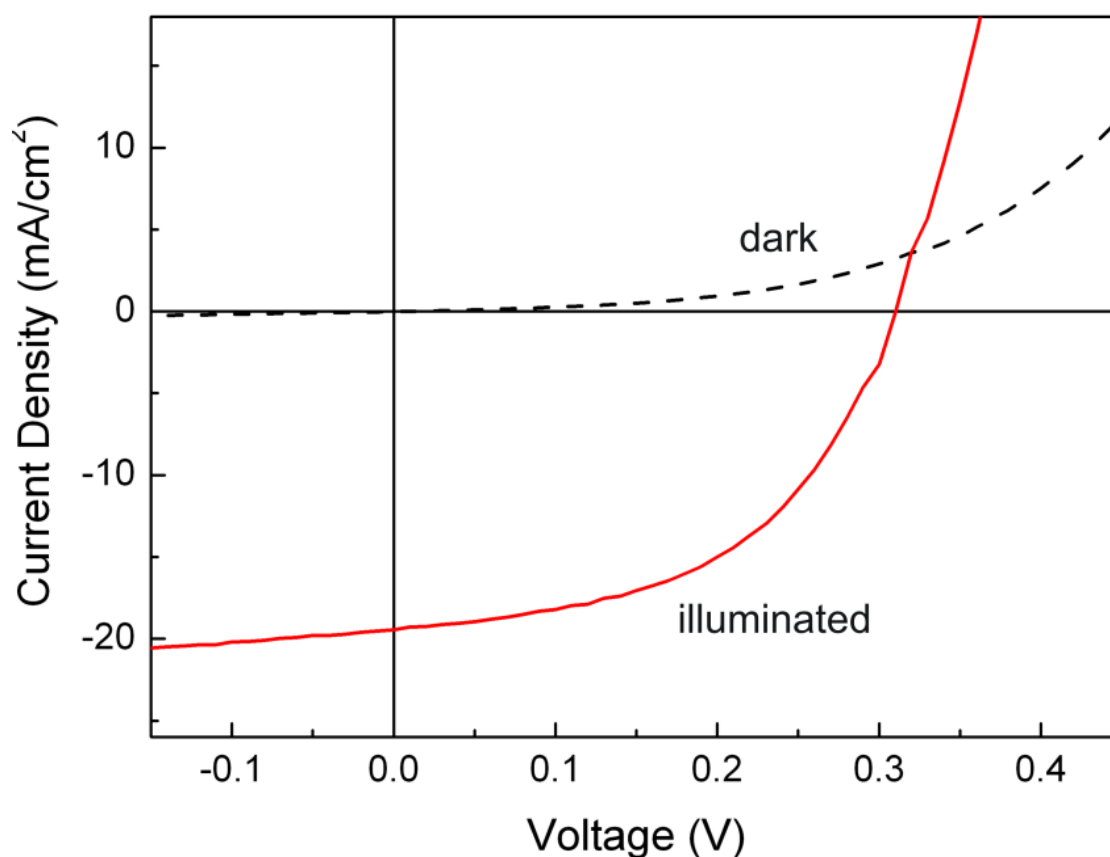
Figure 4.50: Current-voltage characteristics of the best CISe solar cell manufactured with Se@CuSe core@shell nanoparticles and $Cu_{11}In_9$ nanoparticles as precursors.[112]

4.1.5 Te@Bi$_2$Te$_3$ Core@Shell Nanorods

Tellurium has recently become highly relevant for thermoelectrics, thin-film solar cells or topological insulators.[115-119] Here, the most promising materials include compounds such as CdTe, Bi_2Te_3, HgTe, β-Ag_2Te, or $(Bi_{1-x}Sb_x)_2Te_3$.[115-119] For all applications, nanostructured materials and elemental tellurium as precursors are typically required. Current knowledge on how to prepare tellurium nanoparticles and nanostructures via liquid-phase methods, however, is limited.

In this chapter, the syntheses of tellurium nanorods with different sizes that are capped by Bi_2Te_3 to form Te@Bi$_2$Te$_3$ core@shell nanostructures will be discussed. Based on this newly introduced Bi_2Te_3 capping, the shape of the tellurium nanorods is stabilized; rapid agglomeration and merging of the particles are prevented. As a result, colloidally stable inks of Te@Bi$_2$Te$_3$ core@shell nanorods can be obtained.

Synthesis of Te nanowires/nanorods
Crystalline Te nanowires with high aspect ratios (>20) have been prepared by different solution-based approaches. Most often tellurium dioxide (TeO_2),[120] telluric acid dihydrate ($H_2TeO_4 \cdot 2H_2O$),[121] or sodium tellurite (Na_2TeO_3)[122, 123] served as Te precursors and had been reduced by hydrazine (N_2H_4). Alternatively, PVP,[124]

starch[125] and glucose[126] were also used as reducing agents. A microwave-assisted approach in ionic liquids[127] and a surfactant-assisted growth process[128, 129] were developed to synthesize crystalline Te nanowires with hexagonal structure. Based on these strategies, nanowires with diameters of 10 to 100 nm and lengths of several hundreds of nanometers to tens of micrometers were obtained, meaning that the as reported Te nanowires exhibit high aspect ratios (>20). Surprisingly, spherical Te nanoparticles or nanorods with low aspect ratios (<5) and limited length (<100 nm) were seldom described.[130] This can be ascribed to a rapid agglomeration and merging of small Te nanoparticles or nanorods. However, Te nanoparticles or nanorods with a low aspect ratio are needed with regard to colloidally stable inks for layer deposition and printing.[131]
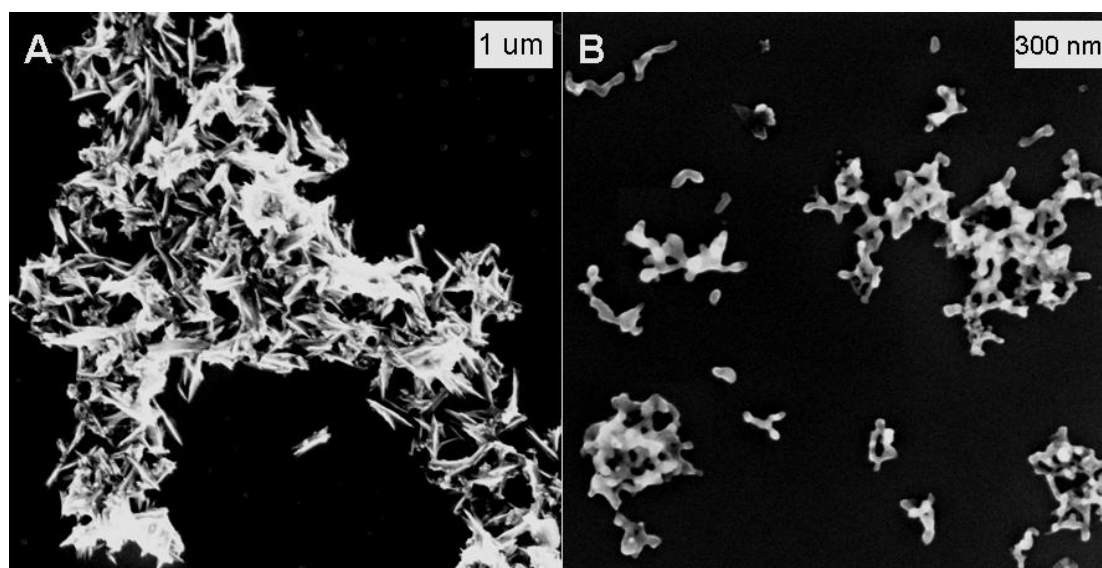
Figure 4.51: SEM images showing a rapid merging and the formation of large agglomerates of the as-prepared Te nanowires without PVP (A, sample 3, *cf.* Table 4.5) and nanorods with PVP (B, sample 1 and 2, *cf.* Table 4.5).

To obtain stable Te nanorods with a low aspect ratio (<5) and lengths of less than 100 nm, we applied a hydrazine-driven reduction of $H_2TeO_4 \cdot 2H_2O$ in DEG at 0 °C with PVP as a stabilizer. The synthesis without PVP results in large agglomerated Te nanowires (Figure 4.51A). By introducing PVP to the reaction, Te nanorods were obtained. Via the variation of the $N_2H_4 \cdot H_2O : H_2TeO_4 \cdot 2H_2O$ molar ratio as well as the addition of PVP as a stabilizer, the size of the as-prepared Te nanorods can be controlled. For nano- and micro-sized particles that exhibit high specific surface areas, the question how to avoid agglomeration and merging is a well-known challenge. This, especially, holds for metals and main-group elements with relatively low melting points (<500 °C). And the latter is even more reduced for nanomaterials as compared to the corresponding bulk phase.[132] Agglomeration, merging as well as the limited phase and shape stability hamper a practical handling of such nanoparticles in view of storing for certain periods, gentle heating due to nanoparticles redispersion in ultrasonic bath as well as in terms of nanoparticle deposition and the formation of thin

films. In the case of nanostructured tellurium (the melting point of bulk-Te: 449.5 °C), such agglomeration and merging have been frequently observed.[132, 133] Similarly, our as-prepared Te nanorods also showed a rapid merging and the formation of large agglomerates (Figure 4.51B). These unstable changes can restrict the applications of Te nanoparticles or nanorods for various applications.

Synthesis of Te@Bi$_2$Te$_3$ core@shell nanorods
In order to increase the colloidal and shape stability, the as-prepared Te nanorods were capped with Bi$_2$Te$_3$ by adding C$_{18}$H$_{15}$Bi, resulting in stable Te nanorods with uniform size and shape. The synthesis was performed under argon inert-gas protection. In a typical recipe, 0.3 or 1 mL N$_2$H$_4$·H$_2$O (6 or 20 mmol, Table 4.5) and 200 mg PVP were added to 30 mL DEG in a three-neck flask. These precursors were stirred continuously to form a homogeneous solution (solution I) at 0 °C within an ice bath. Thereafter, 45.9 mg H$_2$TeO$_4$·2H$_2$O (0.2 mmol) dissolved in 2 mL DEG (solution II) were injected into the pre-cooled solution I. The reaction was allowed to proceed for 40 minutes. Afterwards, all residual N$_2$H$_4$·H$_2$O was removed by vacuum distillation for 30 minutes at 0 °C, followed by 90 minutes at room temperature. The gradual color shift from a colorless solution to a brownish black suspension allows following the process of the reaction even by naked eyes. Finally, 35.2 mg C$_{18}$H$_{15}$Bi (0.08 mmol) dissolved in 4 mL DEG (solution III) were added dropwise. Detailed information regarding the experimental parameters of the syntheses is listed in Table 4.5. The as-prepared suspensions were diluted with demineralized water and the Te@Bi$_2$Te$_3$ core@shell nanorods were collected via centrifugation, washed repeatedly with demineralized water, and then redispersed in demineralized water for further analyses and treatments.

Table 4.5: Detailed experimental conditions to synthesize Te@Bi$_2$Te$_3$ core@shell nanorods.

Sample	N$_2$H$_4$·H$_2$O / mmol	H$_2$TeO$_4$·2H$_2$O / mmol	PVP / mg	C$_{18}$H$_{15}$Bi / mmol	Mean diameter / nm*	Mean length / nm*
1	6	0.2	200	0	merged/agglom.	merged/agglom.
2	20	0.2	200	0	merged/agglom.	merged/agglom.
3	20	0.2	0	0.08	merged/agglom.	merged/agglom.
4	6	0.2	200	0.08	19(2)	55(12)
5	20	0.2	200	0.08	14(1)	28(4)

(*: mean sizes calculated by counting 250 nanorods from the SEM images; standard deviations (σ) calculated by assumption of log-normal distribution)

The strategy of synthesizing Te@Bi$_2$Te$_3$ core@shell nanorods is schematically depicted in Figure 4.52. Subsequent to the hydrazine-reducing synthesis of Te nanorods using DEG as the solvent, the suspension was maintained at 0 °C. This low

temperature allows reducing the reaction rate, which supports the particle growth and size uniformity. Prior to the addition of $C_{18}H_{15}Bi$, the residual $N_2H_4 \cdot H_2O$ had to be removed via vacuum distillation, since Bi^{3+} would have been reduced to elemental Bi otherwise. Finally, the $Te@Bi_2Te_3$ core@shell nanorods were obtained as a black powder that can be easily redispersed in water or ethanol. Considering the potential applications of thin-film solar cells, thermoelectrics and topological insulators, such Bi_2Te_3 capping on Te nanorods is not necessarily an impurity. For instance, this holds for several widely addressed materials, including Bi_2Te_3, $(Bi_{1-x}Sb_x)_2Te_3$, $PbBi_2Te_4$, or $Pb(Bi_{1-x}Sb_x)_2Te_4$[116, 118] as well as complex nanostructures such as multi-segmented Bi_2Te_3-Te stacks or $Bi_2Te_3@Te$ core@shell structures.[134-136]
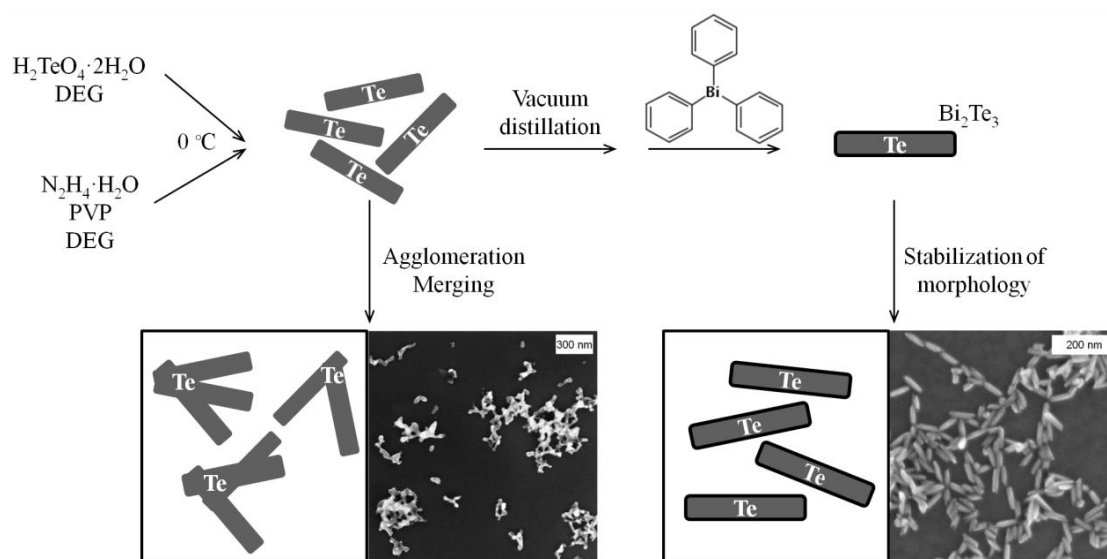
Figure 4.52: Schematic representation and SEM images of the synthesis and merging/ agglomeration of pure Te nanorods as well as the alternative formation of $Te@Bi_2Te_3$ core@shell nanorods.[137]

Characterization of $Te@Bi_2Te_3$ core@shell nanorods

All analytic characterizations were carried out under air. SEM images show the size and morphology of the as-prepared $Te@Bi_2Te_3$ core@shell nanorods (Figure 4.53A and B). The mean diameter and length as well as the size distribution histogram were determined based on the statistical evaluation of 250 nanorods from the SEM images. The standard deviations (σ) were calculated based on the assumption of log-normal distributions of the nanorods in each sample. For sample 4 (*cf.* Table 4.5), nanorods with a mean length of 55(12) nm and a mean diameter of 19(2) nm were obtained (Figure 4.53A and C). The length distribution is much broader as compared to that of the sample 5, which shows a narrow length distribution with a mean length of 28(4) nm and a mean diameter of 14(1) nm (Figure 4.53B and D). According to Table 4.5, size control is predominantly guaranteed via the variation of the $N_2H_4 \cdot H_2O$: $H_2TeO_4 \cdot 2H_2O$ molar ratio. The more $N_2H_4 \cdot H_2O$ was added, the smaller were the nanorods and the narrower the resulting size distribution.
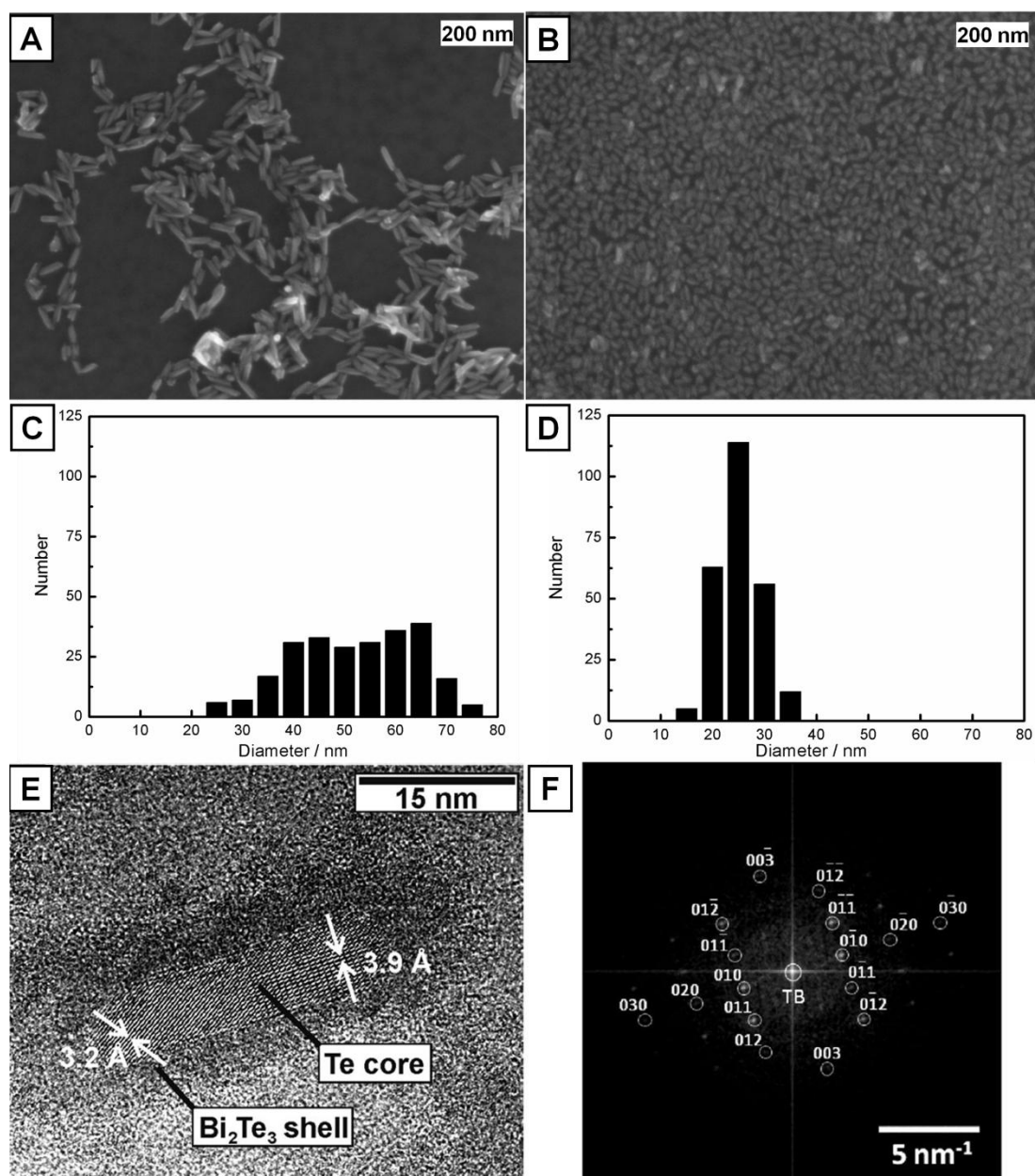
Figure 4.53: Electron microscopic images of the as-prepared Te@Bi$_2$Te$_3$ core@shell nanorods: A) and B) SEM overview images recorded on sample 4 and sample 5, respectively; C) and D) length distribution histograms of sample 4 and sample 5, respectively; E) HRTEM image of a single Te@Bi$_2$Te$_3$ nanorod with lattice distances (sample 4); F) experimental diffractogram of the nanorod core region shown in E and calculated diffraction pattern of hexagonal bulk-Te ([100] zone axis, reflections marked by white circles, TB: transmitted beam) (Te samples according to Table 4.5).

The structure of the as-prepared Te@Bi$_2$Te$_3$ core@shell nanorods was studied in detail by TEM analysis. HRTEM image shows a single Te@Bi$_2$Te$_3$ core@shell nanorod (sample 4, *cf.* Table 4.5) with a length of 54 nm and a diameter of 19 nm (Figure 4.53E). The core of the nanorod with a length of 29 nm and a diameter of 7 nm, presents a hexagonal Te crystal as indicated by the good agreement between its diffractogram and the calculated diffraction pattern of hexagonal bulk-Te in the [100]-

zone axis ($a = 445.8$ pm, $c = 592.7$ pm)[138] (Figure 4.53F). For legibility reasons, not all reflections are marked and indexed in the diffractogram. In addition, the crystalline Te core is verified by the observed lattice fringes of 3.9 and 3.2 Å (bulk-Te: $d_{100} = 3.88$ Å, $d_{101} = 3.23$ Å)[138] as shown in Figure 4.53E. The different contrast observed on the HRTEM image, furthermore, confirms the presence of an external shell around the crystalline Te core, which indicates a core@shell structure of the nanorods. The absence of any lattice fringes within this outer region is ascribed to an amorphous feature of the nanorod shell, which is supported by the XRD pattern of the as-prepared Te@Bi_2Te_3 core@shell nanorods (Figure 4.54A).

The phase composition of Te@Bi_2Te_3 core@shell nanorods was further investigated by SAED and XRD. As suggested by HRTEM, all observed Bragg peaks on SAED pattern refer to crystalline hexagonal tellurium (Figure 4.54A inset). Bragg peaks of the Bi_2Te_3 shell are not visible. Similarly, the XRD pattern of the as-prepared Te@Bi_2Te_3 core@shell nanorods shows a single phase of well-crystallized elemental tellurium with a hexagonal structure (Figure 4.54A). The lattice parameters of $a = 447.1(5)$ pm and $c = 589.2(7)$ pm calculated from XRD peak positions fit very well with the corresponding reference data ($a = 445.8$ pm, $c = 592.7$ pm)[138]. Notably, no other Bragg peaks are observed, confirming that the Bi_2Te_3 shell is indeed amorphous. After annealing the as-prepared sample at 500 °C for 30 minutes in argon, the Bragg peaks of hexagonal tellurium become sharper due to the thermally increased crystallinity. In addition, rhombohedral Bi_2Te_3 is visible as a crystalline phase (Figure 4.54B). The calculated lattice parameters of $a = 445.5(2)$ and $c = 592.9(2)$ pm for elemental tellurium as well as $a = 438.0(4)$ and $c = 3046(3)$ pm for Bi_2Te_3 are in good agreement with the reference data (bulk-Te: $a = 445.8$ pm, $c = 592.7$ pm;[138] bulk-Bi_2Te_3: $a = 438.5$ pm, $c = 3048$ pm[139]).

The overall atomic composition of Te@Bi_2Te_3 core@shell nanorods was analyzed by EDX after pressing the as-prepared powder samples to pellets to guarantee for a dense, semi-infinite layer with a smooth surface. Because the pellets contain a huge number of Te@Bi2Te3 core@shell nanorods, the obtained 35.6 at % of bismuth and 64.4 at % of tellurium reflect the overall atomic composition with high statistical relevance and fit quit well with high-resolution EDX line-scan of a single nanorod (Figure 4.56C).

FT-IR spectrum of the as-prepared Te@Bi_2Te_3 core@shell nanorods indicates the presence of PVP as a surface capping (Figure 4.55). The weak vibrational bands observed at 2950-2800 cm^{-1} (v(C–H)), 1750-1550 cm^{-1} (v(C=O)) and in the fingerprint region (1500-600 cm^{-1}) fit well with the PVP reference spectrum. The additional strong bands can be attributed to OH-containing solvents (water, ethanol) adhered on particle surface at 3700-3250 cm^{-1} (v(O–H)) and CO_2 from ambient air (2400-2350 cm^{-1} and 2350-2275 cm^{-1}). While comparing to the $C_{18}H_{15}Bi$ reference spectrum, the weak intensity vibration at 3050 cm^{-1} (=C–H stretching) can be attributed to $C_{18}H_{15}Bi$. Thus, we can conclude that only negligible amounts of $C_{18}H_{15}Bi$ as the starting precursor remain on the particle surface.
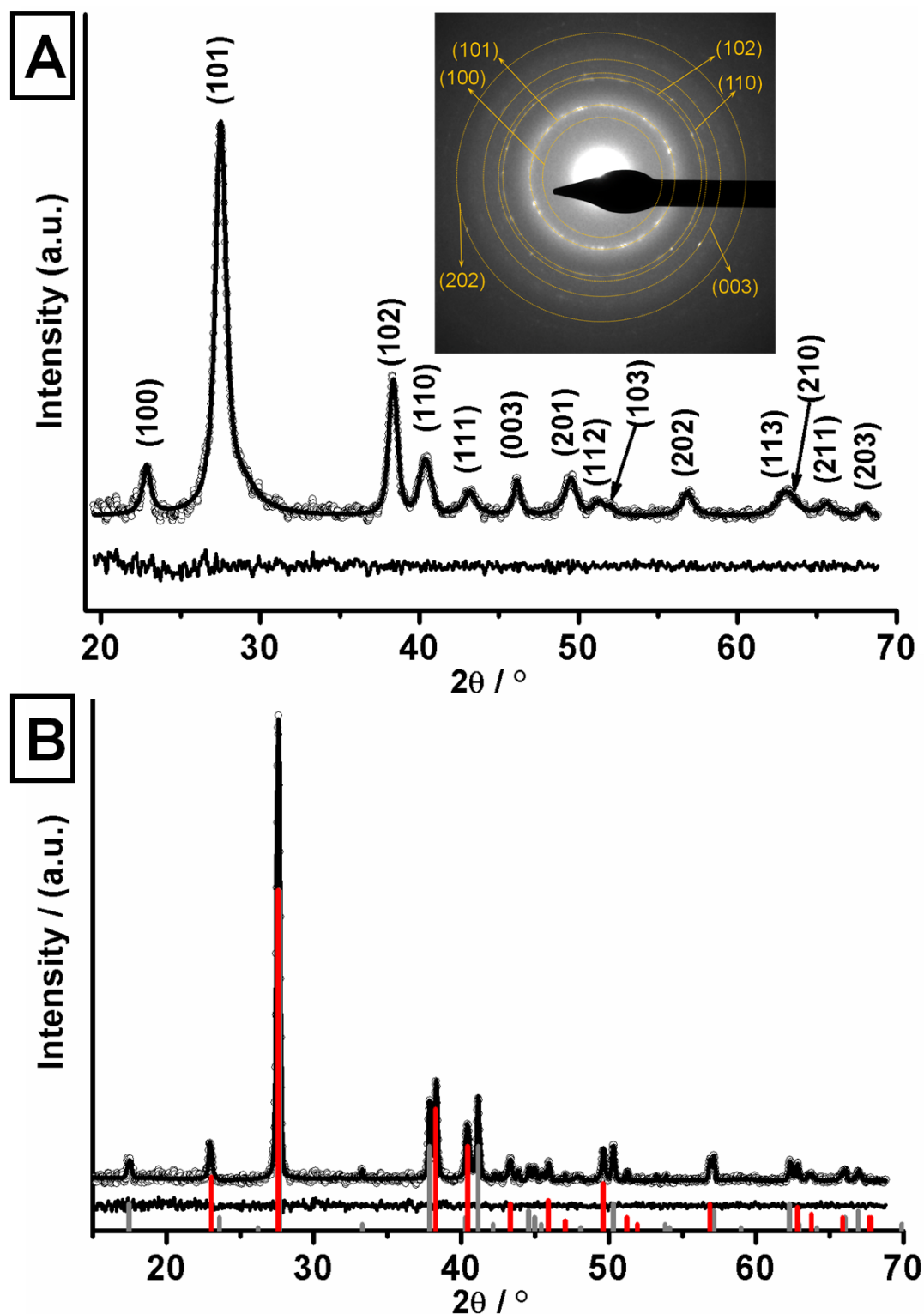
Figure 4.54: A) Indexed XRD pattern with the whole-pattern-diffraction fits (solid line) and difference plot for the as-prepared Te@Bi$_2$Te$_3$ core@shell nanorods with inset showing an indexed SAED pattern; B) XRD pattern with the whole-pattern-diffraction fits (solid line) and difference plot for annealed Te@Bi$_2$Te$_3$ core@shell nanorods (500 °C, 30 minutes, argon atmosphere) with reference diffractograms: hexagonal Te_ICDD No. 36-1452/red lines; Bi$_2$Te$_3$_ICDD No. 15-863/gray lines.[137]
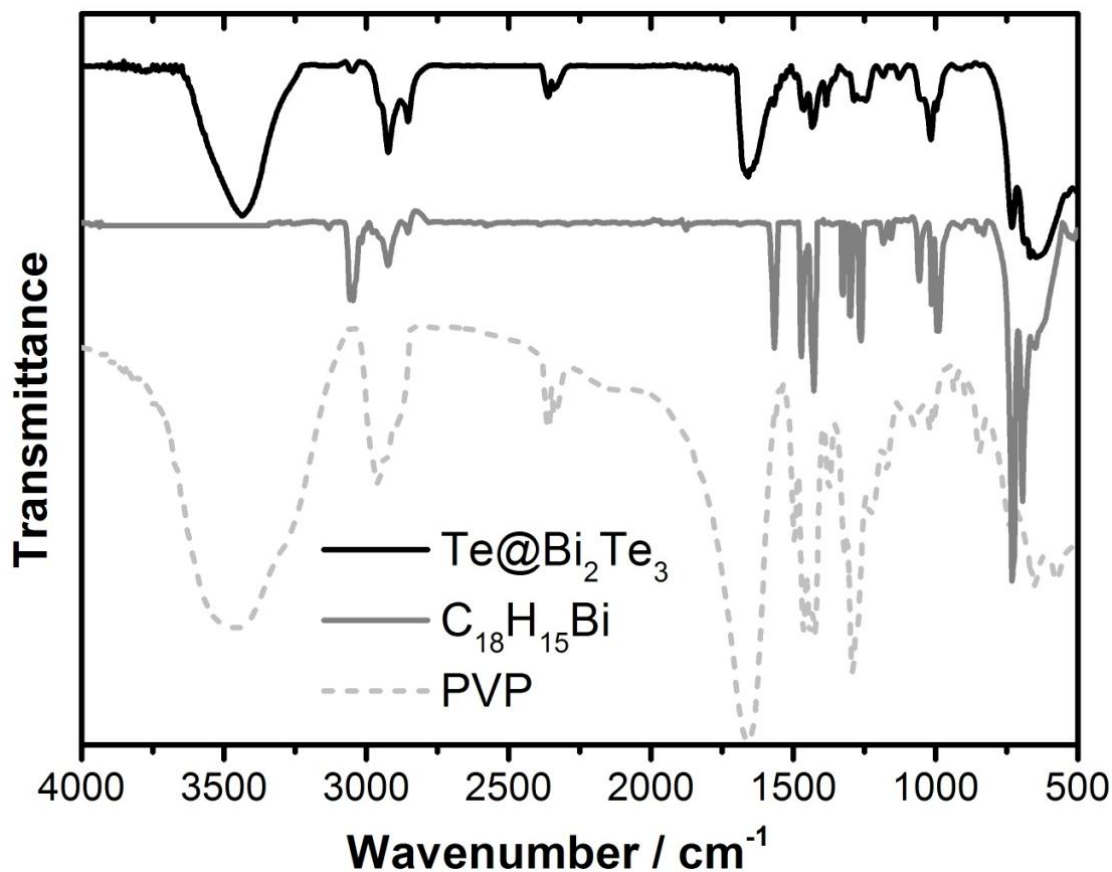
Figure 4.55: FT-IR spectrum of PVP-capped Te@Bi$_2$Te$_3$ core@shell nanorods (pure PVP and C$_{18}$H$_{15}$Bi as references).[137]

The Te@Bi$_2$Te$_3$ core@shell nanostructure was investigated based on HAADF-STEM images and high-resolution EDX line-scan analysis (Figure 4.56). The detailed information about the devices and operating parameters has been described in chapter 4.1.4. This part of work, including HAADF-STEM, high-resolution EDX line-scan analysis and the evaluation of the concentration profile, was done by Dr. Radian Popescu from the Laboratory of Electron Microscopy, Karlsruhe Institute of Technology (KIT) in Karlsruhe (Germany).

A HAADF-STEM image presents a Te@Bi$_2$Te$_3$ core@shell nanorod with a length of about 60 nm and a diameter of about 25 nm (Figure 4.56A). EDX line-scans measured across the nanorod diameter show the Te and Bi concentration profiles, which demonstrate the core@shell structure (Figure 4.56B). A significant increase of the Bi concentration is observed at the surface region of the Te@Bi$_2$Te$_3$ nanorod. The inner section shows a high Te concentration. Bismuth is even detectable for the inner core since the electron beam has to pass through the Bi$_2$Te$_3$ shell. Using the evaluation procedure described in Ref. [114], the composition and the thickness of the shell and the core can be reconstructed as shown schematically in Figure 4.56C. The evaluation yields an outer shell with a thickness of about 6 nm and an average chemical composition of Bi$_{37(7)}$Te$_{63(7)}$, which is in good agreement with the expected composition of Bi$_2$Te$_3$ (Figure 4.56C). The nanorod core has a diameter of about

13 nm and consists of pure tellurium, as suggested also by the HRTEM image (Figure 4.53E) and the XRD result (Figure 4.54A).
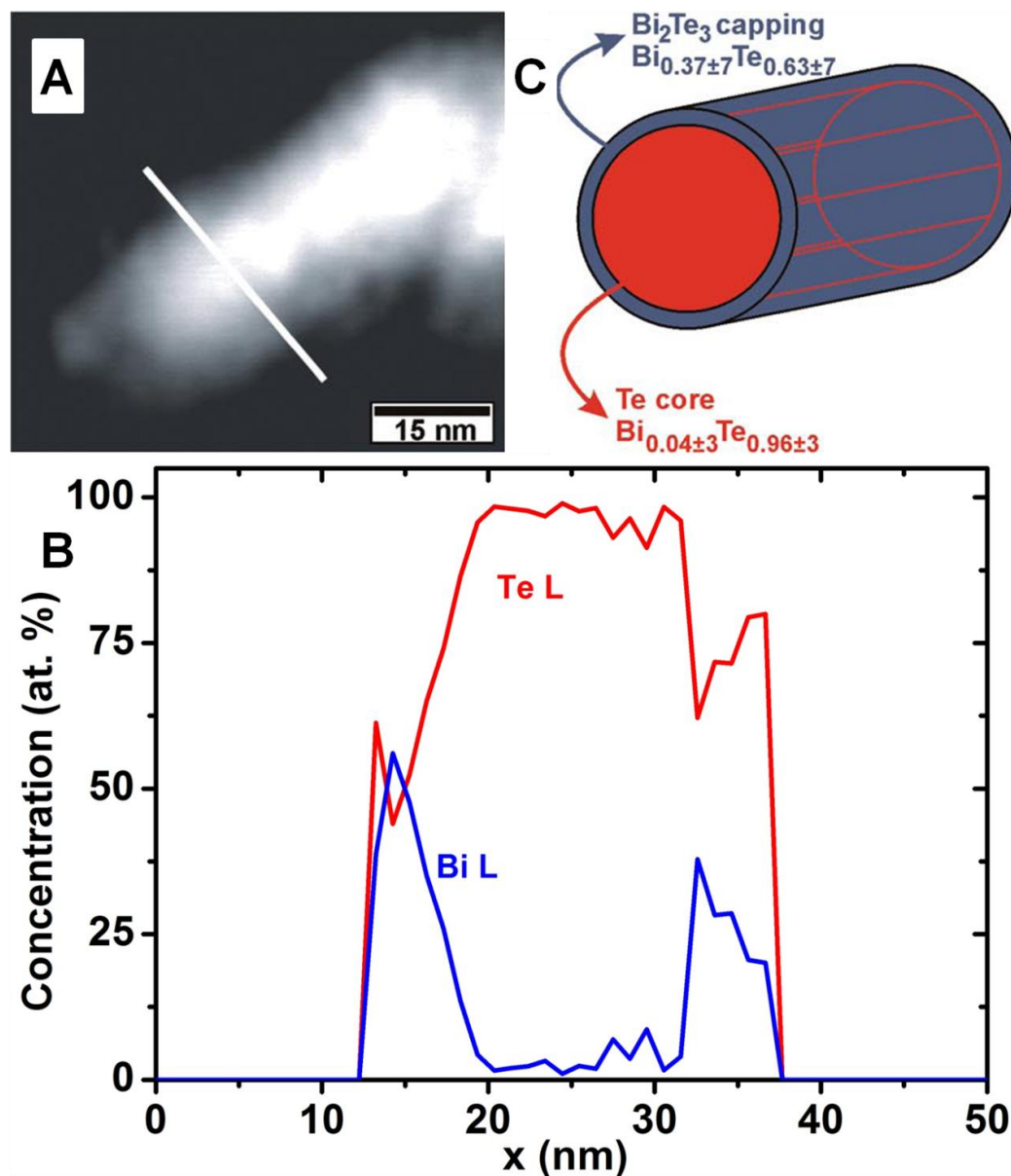
Figure 4.56: HAADF-STEM image (A), high-resolution EDX line-scan (B, along white line as indicated in A) and schematic illustration with core and shell compositions (C) of a Te@Bi_2Te_3 core@shell nanorod (sample 4, *cf.* Table 4.5).[137]

Altogether, the presence and the structure of the Te@Bi_2Te_3 core@shell nanorod consisting a Bi_2Te_3 shell that is about 6 nm in thickness, and a Te core that is about 13 nm in diameter, are reliably validated.

4.2 Pure and Doped Porous ZnO Platelets

Motivation

Nanostructured zinc oxide has high relevance to application such as UV-protection and sunblocking,[140] catalysis (photocatalysis),[132] dye-sensitized solar cells[141] and transparent oxide conductors.[142] A variety of gas- and liquid-phase methods have been applied to synthesize nanostructured ZnO, which are summarized in several recent reviews.[143-146] In fact, via selecting a suitable method, ZnO can be accurately controlled in size all over the complete nanoscale range from 1 to 100 nm. Due to the hexagonal symmetry of the ZnO lattice,[147] rod-like particles and assemblies are quite often obtained.[148, 149] Non-isotropic morphologies such as platelets are less often observed although they could be highly interesting for thin-films that exhibit an oriented reflection of light or a directed electrical conductivity. The platelet-like ZnO has already been produced by physicochemical techniques, such as electrochemical deposition,[150] radio-frequency sputtering,[151] ultrasonic spray pyrolysis[152] as well as by applying long-chained amines or carboxylates for a structure-directed growth in solution.[153-155]

The polyol-mediated method is widely applied to synthesize high-quality ZnO nanoparticles.[156, 157] Typically, zinc acetate dihydrate is hydrolyzed by heating in a polyol. Nowadays, the polyol-mediated method represents a standard synthesis of various compounds that are accessible as monodisperse, non-agglomerated and crystalline nanoparticles.[22, 158] Although the polyol-mediated method is quite beneficial to the formation of ZnO nanoparticles, it is well-known that the synthesis fails if glycerol as the polyol is involved in the reaction. In this case, large crystals of zinc glycerolate (Zn(gly)) are obtained as the only product.[159] So far, only spherical Zn(gly) particles have been produced via microemulsion approaches.[160-162]

In this chapter, pure Zn(gly) and Al/In-doped Zn(gly) platelets are prepared by the polyol-mediated method. Via a suitable thermal treatment, these as-prepared Zn(gly) platelets decompose to pure ZnO or doped ZnO, maintaining the platelet-like morphology. Depending on the concrete conditions of thermal treatments and dopants, the morphology, porosity and surface of the ZnO platelets can be adjusted. Such porous ZnO platelets are here observed for the first time.[163]

Syntheses of pure Zn(gly) and Al/In-doped Zn(gly) platelets

In a typical synthesis of pure Zn(gly) platelets, 2.0 g (9.1 mmol) zinc acetate dihydrate (Zn(Ac)$_2 \cdot$2H$_2$O), 50 mL glycerol and 1 mL demineralized water were added into a 100 mL three-neck flask. The starting precursors were heated to 160 °C for 1 hour under continuous stirring. After cooling naturally to room temperature, the resulting white suspension was diluted with ethanol, and the Zn(gly) platelets were collected via centrifugation, washed repeatedly with ethanol. Finally, the product was dried at 80 °C for 60 minutes and white powder was obtained for further analyses and

treatments. For Al- and In-doped Zn(gly) platelets, in addition to the starting precursors mentioned above, 120.7 mg (0.5 mmol) $AlCl_3$ $6H_2O$ or 146.6 mg (0.7 mmol) $InCl_3$ were also added to the reaction system. After the same experimental procedures, white powder samples were produced.

Pure Zn(gly) platelets were synthesized via the polyol-mediated method utilizing a solution of $Zn(Ac)_2$ $2H_2O$ in glycerol. The doped Zn(gly) platelets required the addition of the corresponding doping reagent. At a temperature of about 120 ℃, the solution became turbid, indicating the precipitation of solid Zn(gly). After the system was cooled naturally to room temperature, the resulting milky suspension was diluted with ethanol and centrifuged. The white remnant was redispersed repeatedly in and centrifuged from ethanol in order to remove all residual glycerol and remaining salts. Finally, all the white powder samples were dried (60 minutes, 80 ℃) and thereafter investigated based on SEM, XRD, FT-IR and TGA with regard to the particle size, morphology, the chemical composition and crystallinity.

Characterization of the as-prepared Zn(gly) platelets
SEM image of the as-prepared pure Zn(gly) evidences the presence of platelet-like particles with diameters of 5-15 μm and a thickness of about 100-500 nm (Figure 4.57). The as-prepared pure Zn(gly) has an irregular-shaped morphology. For the as-prepared Al-doped Zn(gly), it presents the shuttle-shaped platelets with diameters of 5-15 μm and a thickness of about 100-500 nm (Figure 4.58A). The as-prepared In-doped Zn(gly) is irregular-shaped bulk material without platelet-like morphology (Figure 4.58B).
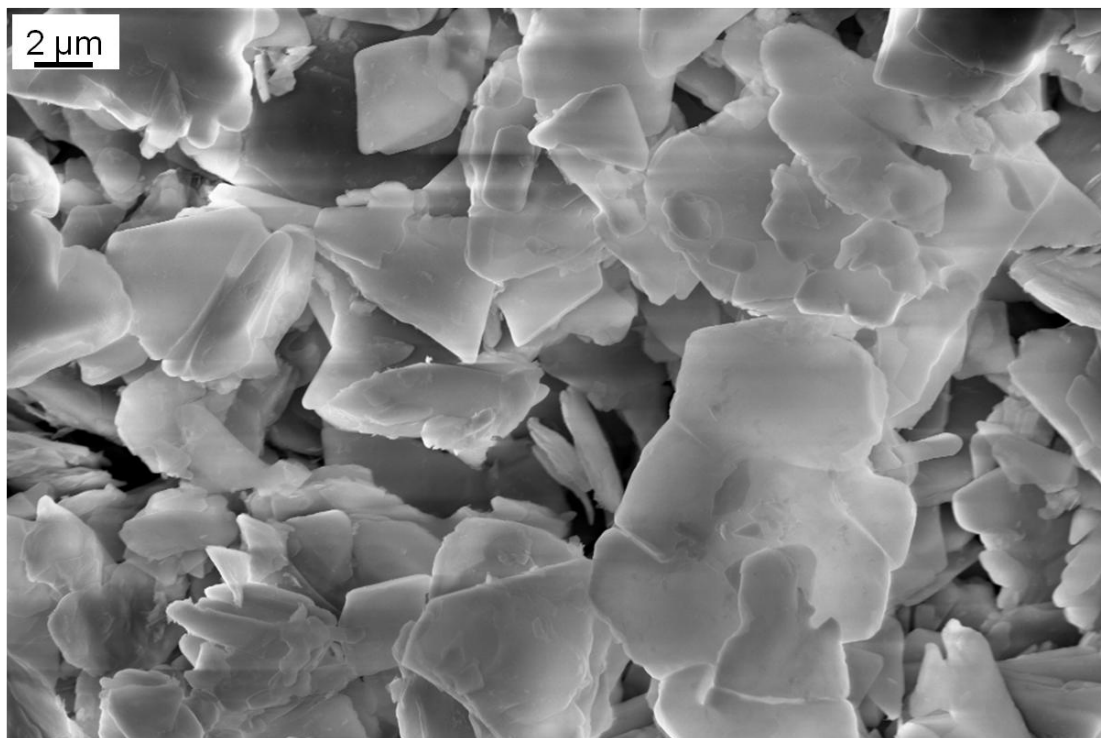
Figure 4.57: SEM images of the as-prepared pure Zn(gly) platelets.
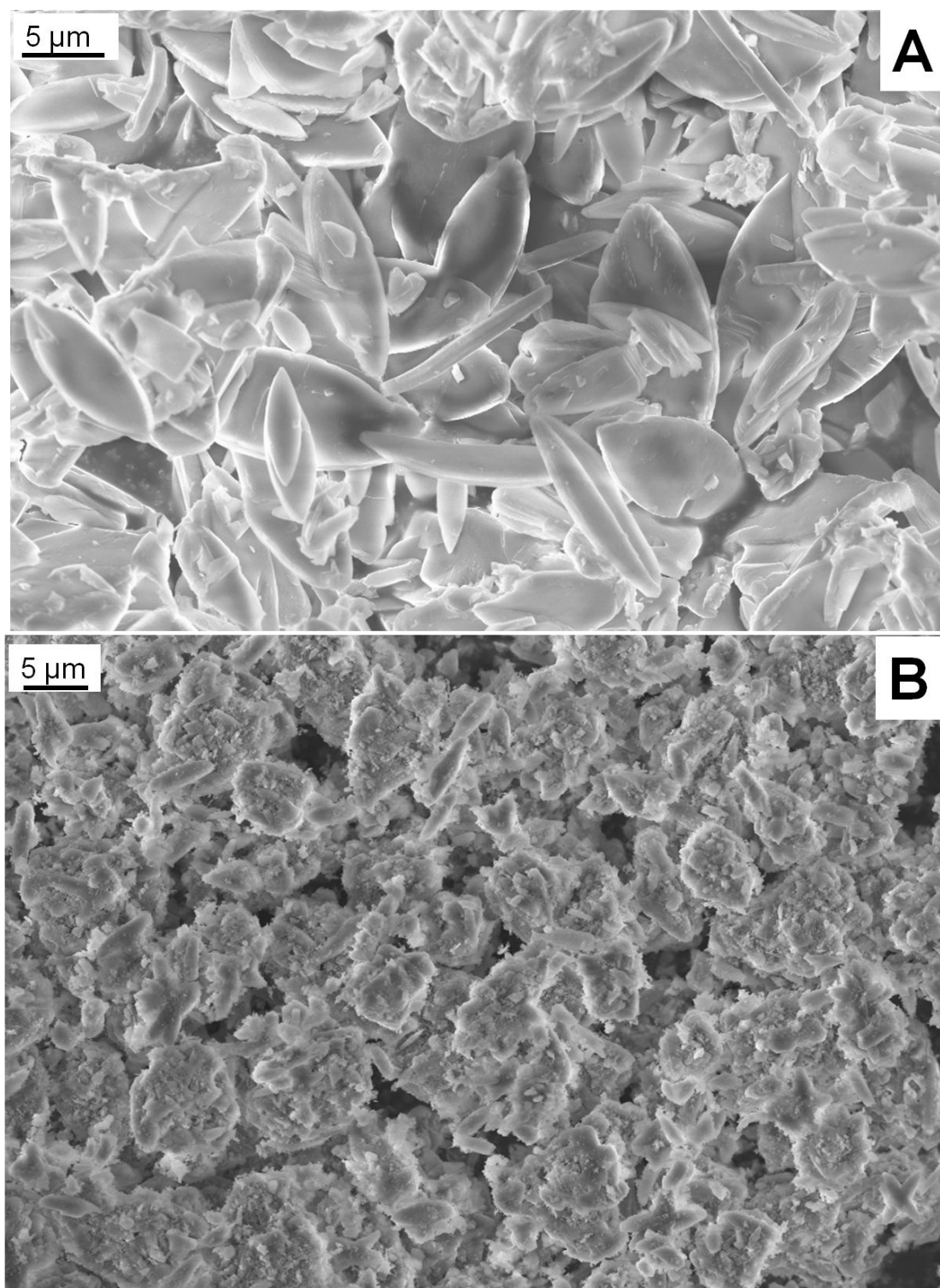
Figure 4.58: SEM images of the as-prepared Zn(gly) platelets: (A) Al-doped Zn(gly) and (B) In-doped Zn(gly).

XRD patterns confirm that the chemical composition of the as-prepared Zn(gly) platelets is zinc glycerolate (Figure 4.59 and Figure 4.60). All Bragg peaks observed in pure Zn(gly) and Al-doped Zn(gly) are in good agreement with the literature

data.[162] For In-doped Zn(gly), many weak-intensity peaks are not visible, however, the main Bragg peaks still fit quite well with the reference (Figure 4.60B). The XRD pattern of pure Zn(gly) in Figure 4.59 shows a totally different relative intensity of the main Bragg peaks as compared to Al- and In-doped Zn(gly). The difference in the intensities of the Bragg reflexes results from the different preferential crystal growth of nanostructure along one/two crystallographic axes.
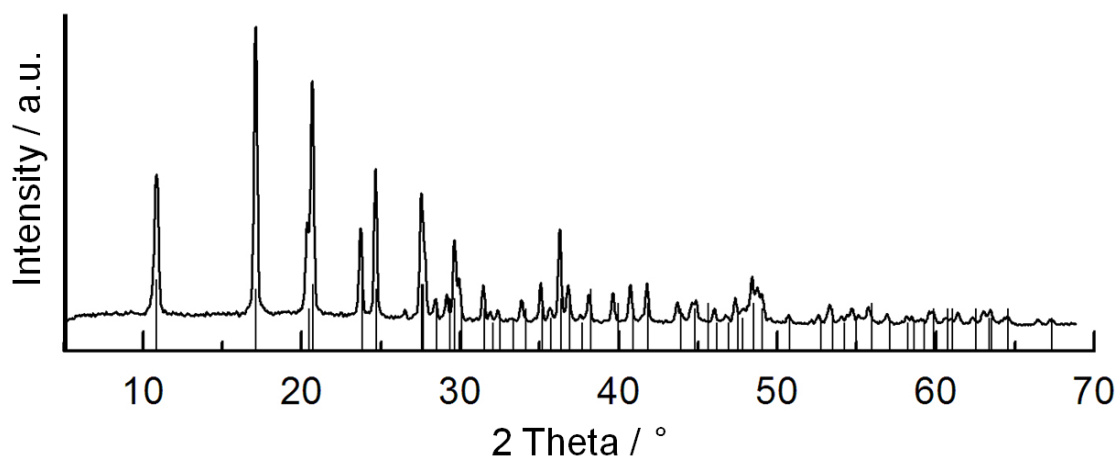
Figure 4.59: XRD pattern of the as-prepared pure Zn(gly) (zinc glycerolate_ICDD No. 23-1975 as a reference).
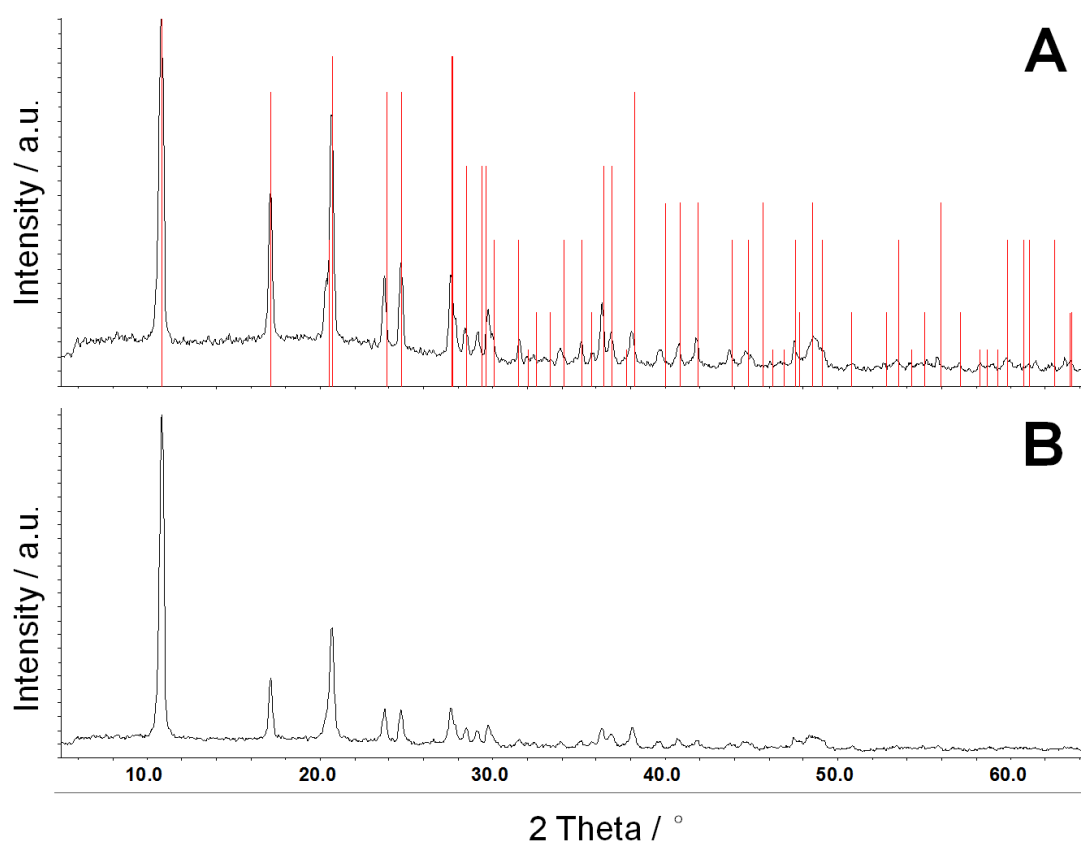
Figure 4.60: XRD patterns of the as-prepared doped Zn(gly): (A) Al-doped Zn(gly) and (B) In-doped Zn(gly) (zinc glycerolate_ICDD No. 23-1975 as a reference).

FT-IR spectrum of the as-prepared Zn(gly) platelets is also in complete agreement with the literature data of bulk-Zn(gly).[164] Note that the splitting of vibrational bands as observed for Zn(gly) originates from the reduced site symmetry of the solid lattice as compared to the non-bound molecule in the liquid phase. When comparing to pure glycerol as a reference (Figure 4.61), the strong bands at 2700-2400, 2050-1900 and 1500-1350 cm^{-1} look somewhat unusual. However, these strong bands are observed in all available reference spectra with similar intensity and shape, which are ascribed to O–H···O bending modes that are not specified in detail here.[159, 162]
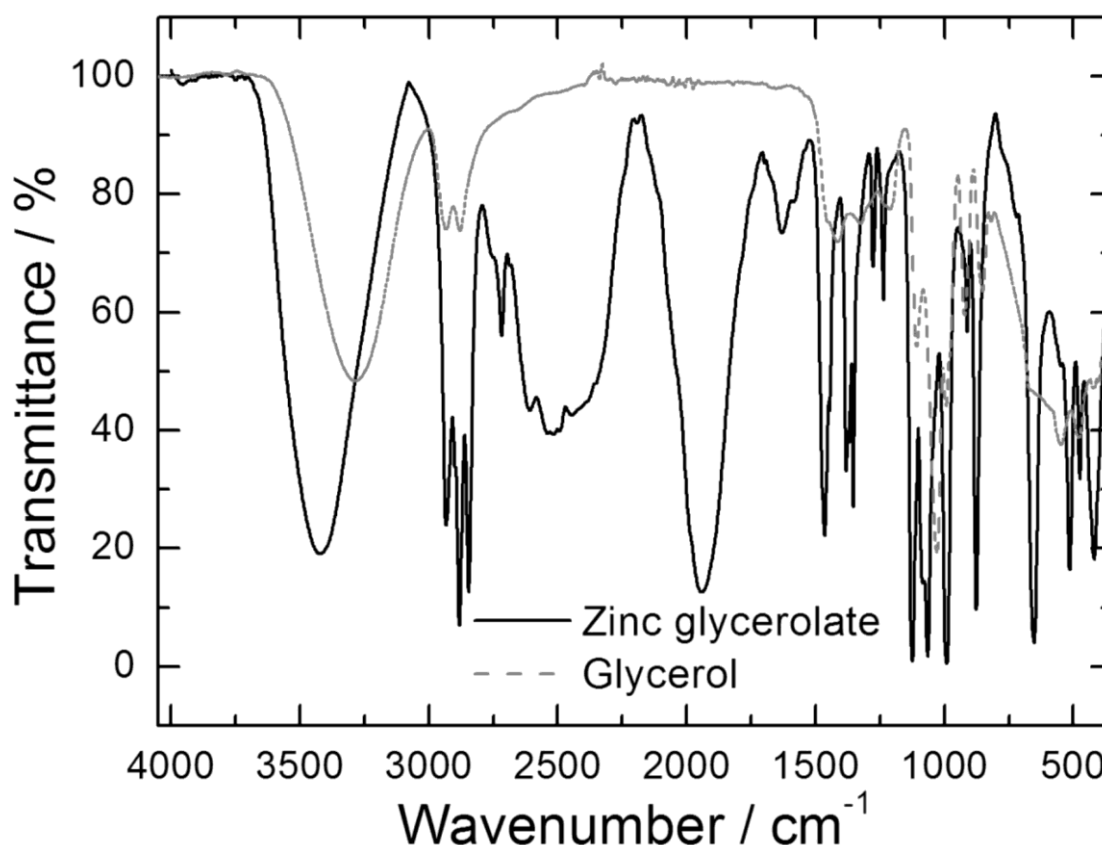
Figure 4.61: FT-IR spectrum of the as-prepared Zn(gly) platelets (pure glycerol as a reference).[163]

Thermogravimetric analysis elucidates the thermal decomposition of the as-prepared pure Zn(gly) platelets (Figure 4.62). To this concern, the decomposition occurs with a single massive weight loss of about 47 % between 310 ℃ and 470 ℃. This value fits precisely with the expectation (48 %) when assuming a thermal decomposition of Zn(gly) in air and the formation of ZnO. Based on the TG analysis, a temperature of 470 ℃ is required for the complete decomposition of Zn(gly). A large amount of as-prepared pure Zn(gly) was used for a controlled decomposition at 500-600 ℃ inside of a tube furnace. The resulting white powder as the thermal remnant was again investigated by XRD (Figure 4.63). Accordingly, pure crystalline ZnO is obtained by thermal decomposition of Zn(gly).
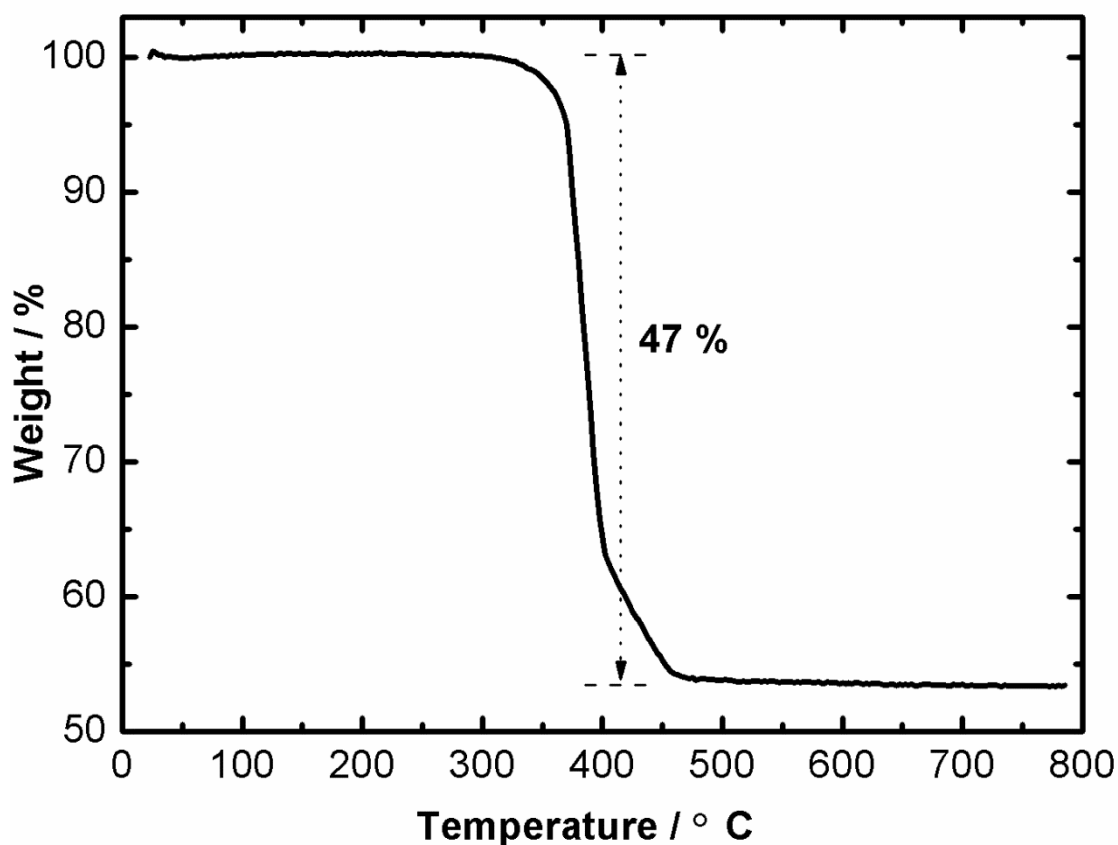
Figure 4.62: Thermogravimetry of the as-prepared pure Zn(gly) platelets in air with a heating rate of 20 K min^{-1}.[163]
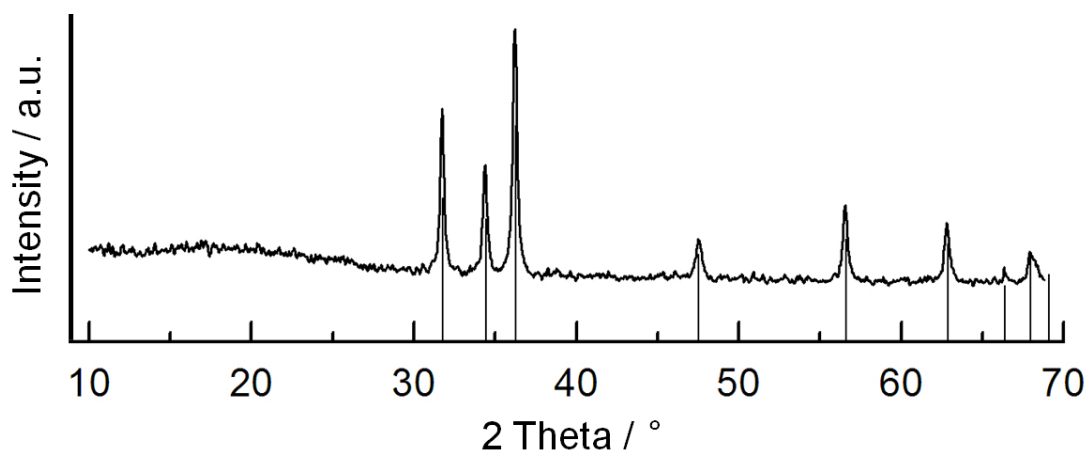
Figure 4.63: XRD pattern of the thermal remnant after the TG measurement on pure Zn(gly) platelets (ZnO_ICDD 34-1451 as a reference).

Thermal decomposition of the as-prepared Zn(gly) platelets
50 mg of the as-prepared pure Zn(gly) powder were heated with different thermal procedures as listed in Table 4.6. The as-prepared Al/In-doped Zn(gly) powder was heated via moderate thermal decomposition. Heating was performed in a tube furnace (HTM Reetz LOBA 1200) via programmed temperature control under air. All powder

samples were deposited in alumina crucibles.

Table 4.6: Experimental conditions for the thermal decomposition of the as-prepared Zn(gly) platelets and the specific surface area (BET) of the resulting ZnO.

Sample	Heating rate / $°C \, h^{-1}$	T_{max} / $°C$	Duration at T_{max} / min	Specific surface area (BET) / $m^2 \, g^{-1}$
Zn(gly)	/	/	/	2.2
ZnO (fast)	∞ *	600	30	5.2
ZnO (moderate)	60	500	30	17.6
ZnO (slow)	10 (20→300 $°C$) 5 (300→500 $°C$)	500	30	5.9

(*: Sample was directly introduced into the hot tube furnace at 600 $°C$)

Characterization of porous ZnO platelets
So far, the availability of platelet-like ZnO is limited,[150-155] and such a material with non-isotropic morphology could be highly interesting. Considering its catalytical, optical and electronical properties, the question arises whether thermal decomposition of platelet-like Zn(gly) to ZnO leads to the retaining of the platelet-like morphology. To this concern, the as-prepared pure Zn(gly) sample was decomposed with fast, moderate and slow heating rates inside of a tube furnace. The detailed conditions of heating, including heating rate, maximum temperature and duration of heating are listed in Table 4.6.

According to SEM images (Figure 4.63-4.65), the morphology of the resulting ZnO particles depends significantly on the heating conditions (Table 4.6). In the case of fast heating, the morphology of the initial Zn(gly) platelets remains obviously intact. The resulting ZnO with a similar platelet-like morphology has 10-15 μm in diameter and 100-300 nm in thickness. Thus, the platelets exhibit a large aspect ratio of ~100. In contrast to Zn(gly) platelets, the platelet-like ZnO shows a granulated morphology consisting of aggregated particles of 200-300 nm in diameter (Figure 4.64). The massive glycerolate-driven weight-loss, moreover, causes the formation of large amounts of pores inside of the granulated platelets. These pores have diameters of up to 100 nm. While performing nitrogen sorption measurement, BET analysis results in a specific surface area of 5.2 $m^2 \, g^{-1}$. In fact, this value is only doubled as compared to as-prepared pure Zn(gly), which has the value of 2.2 $m^2 \, g^{-1}$ (Table 4.6).

In the case of moderate heating, the platelet-like morphology remains also intact (Figure 4.65). Again the ZnO platelets exhibit a granulated structure with lots of pores. When comparing with the findings for fast heating, the granulated structure is, however, established by much smaller particles, which have diameters of only about 10-30 nm. This ten times smaller granulated structure is accompanied by a significant increase of the specific surface area. Thus, the value of 17.6 $m^2 \, g^{-1}$ (BET) is obtained (Table 4.6).

By further reducing the heating rate, a further increased specific surface area could have been expected. Slow heating, on the contrary, leads to very low specific surface area (5.9 m^{2}g^{-1}, Table 4.6). Scanning electron microscopic images, furthermore, indicate that the platelet-like morphology is not maintained in this case (Figure 4.66). In contrast, irregularly agglomerated, more or less spherical nanoparticles with diameters of 100-200 nm are observed.
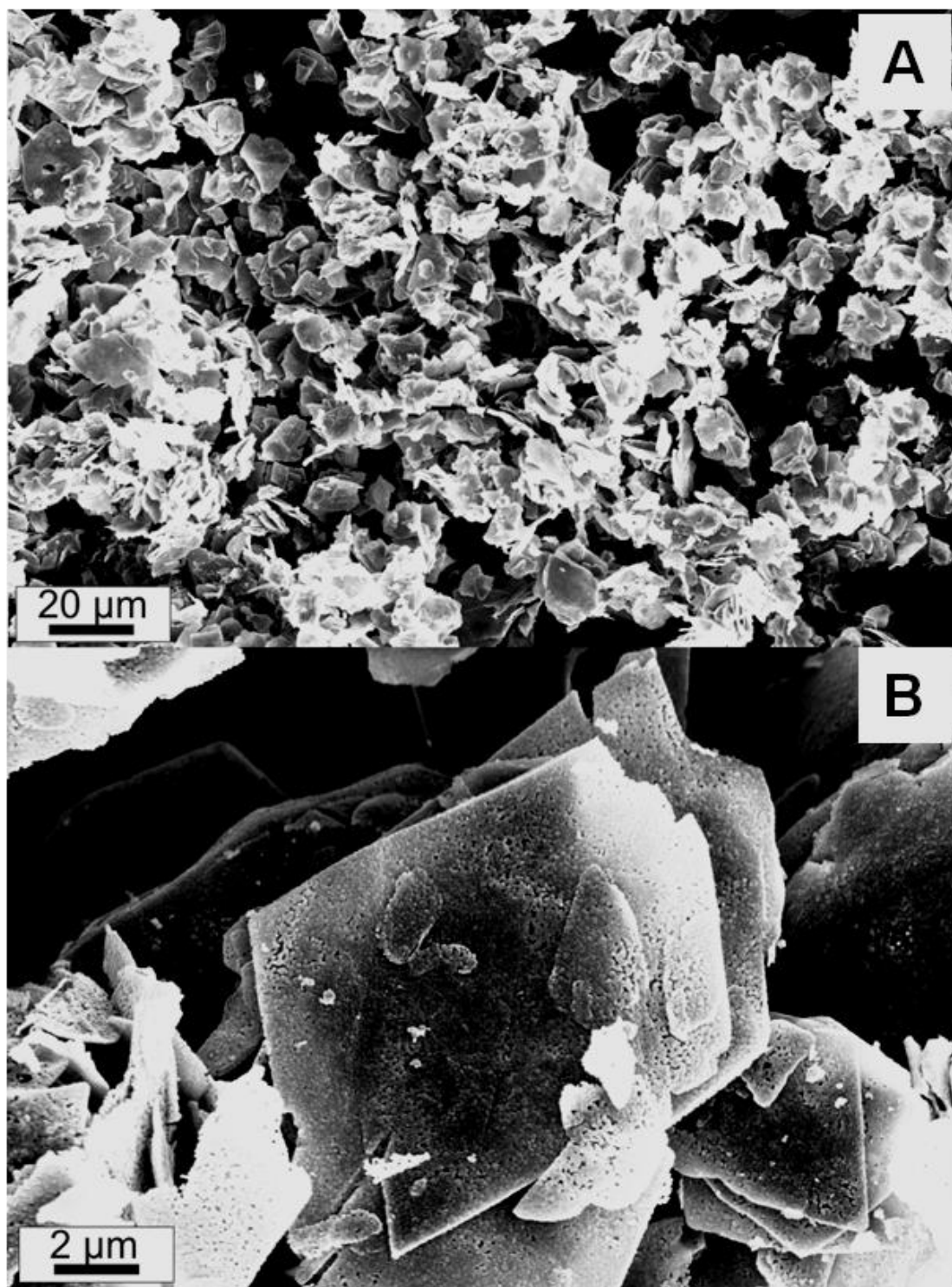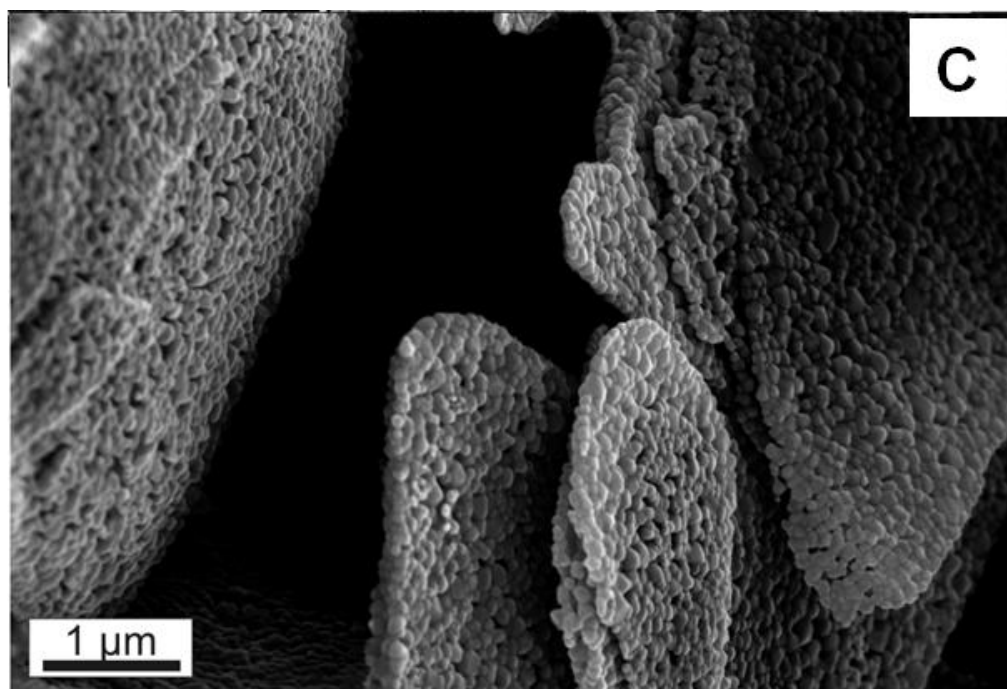
Figure 4.64: SEM images of porous ZnO platelets obtained via fast thermal decomposition of Zn(gly) at different levels of magnification (A: large scale overview; B: top-view of porous ZnO platelets with high resolution; C: side-view of porous ZnO platelets with high resolution).[163]
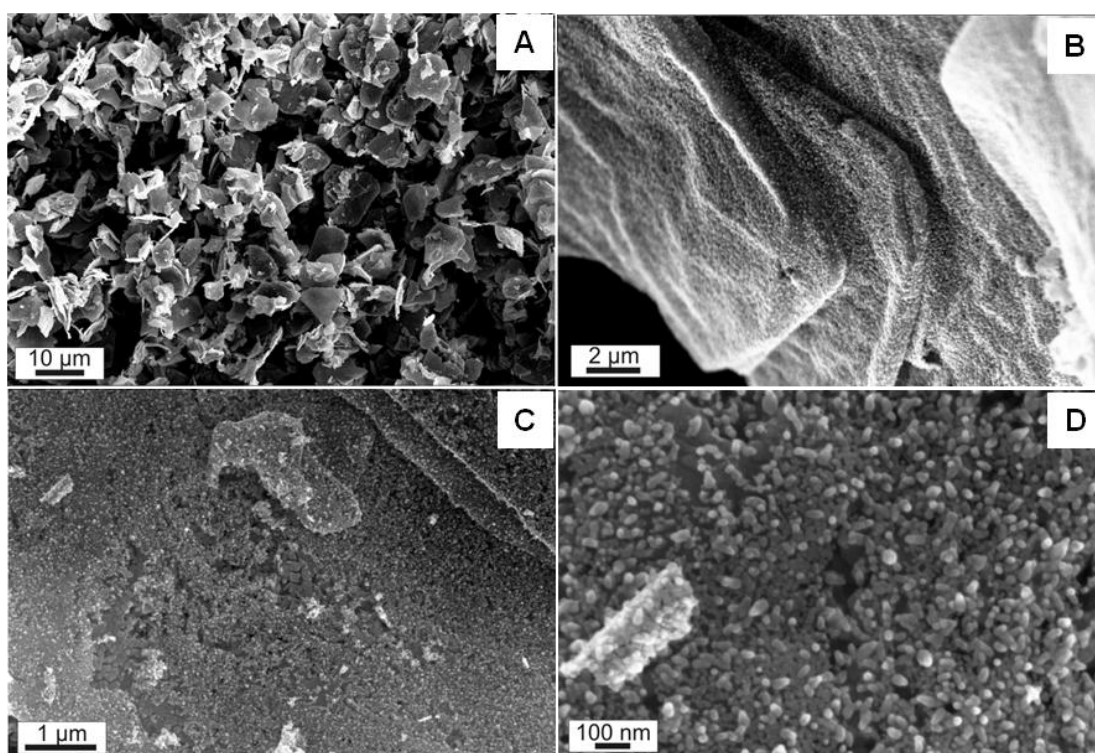
Figure 4.65: SEM images of porous ZnO platelets obtained via moderate thermal decomposition of Zn(gly) at different levels of magnification (A: large scale overview; B: side-view of porous ZnO platelets with high resolution; C, D: top-view of porous ZnO platelets with high resolution).[163]
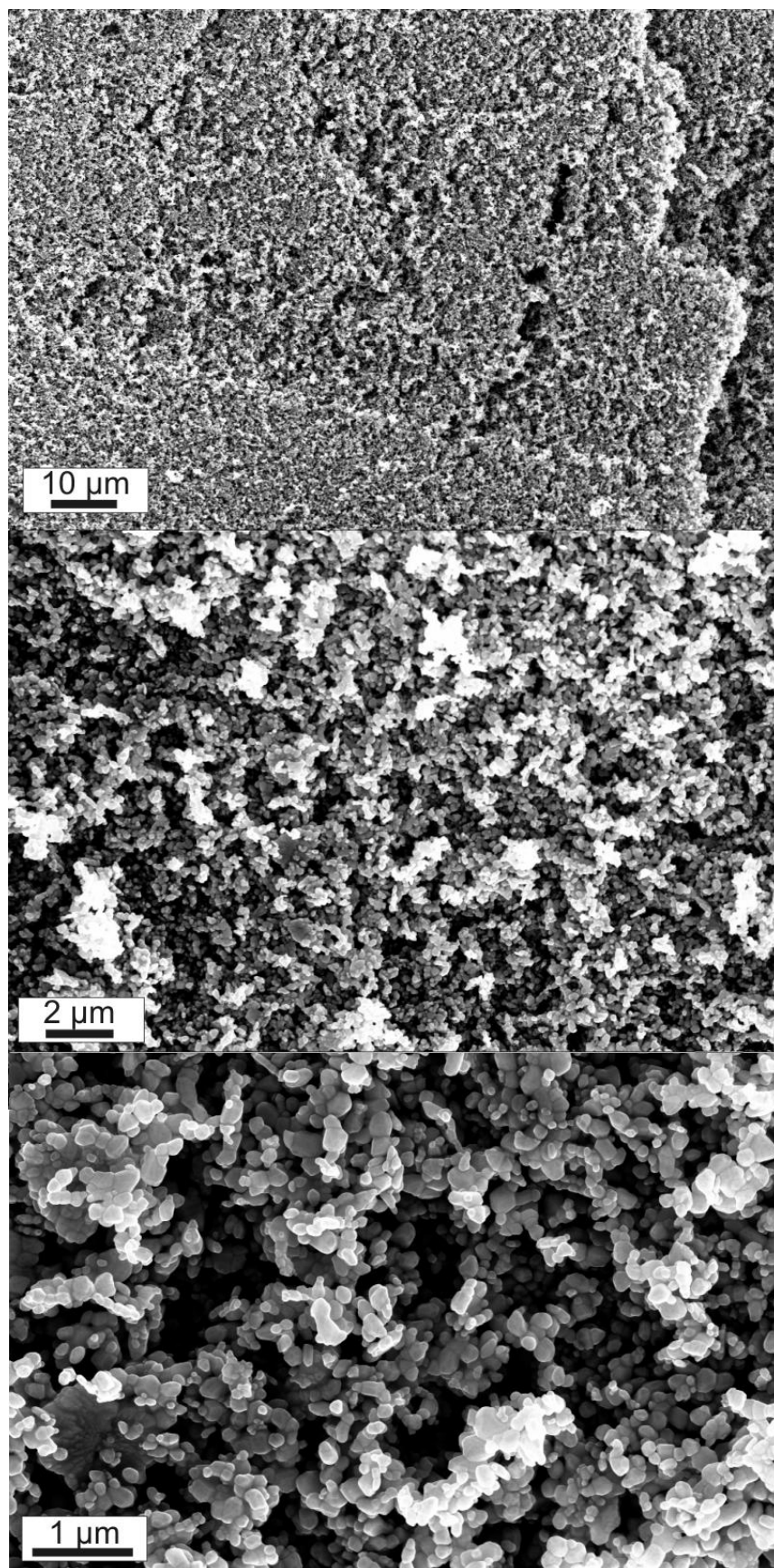
Figure 4.66: SEM images of spherical ZnO particles obtained via slow thermal decomposition of Zn(gly) at different levels of magnification.[163]

Characterization of doped ZnO platelets

Since ZnO platelets obtained via moderate thermal decomposition of pure Zn(gly) present the best result of the specific surface area, Both Al- and In-doped Zn(gly) samples were heated to 500 ℃ with a heating rate of $60 \, \mathrm{K \, h^{-1}}$. Depending on different dopants, the thermal remnants exhibit different colours as shown in Figure 4.67. XRD patterns of the both remnants confirm the crystal structure of pure ZnO (Figure 4.63).
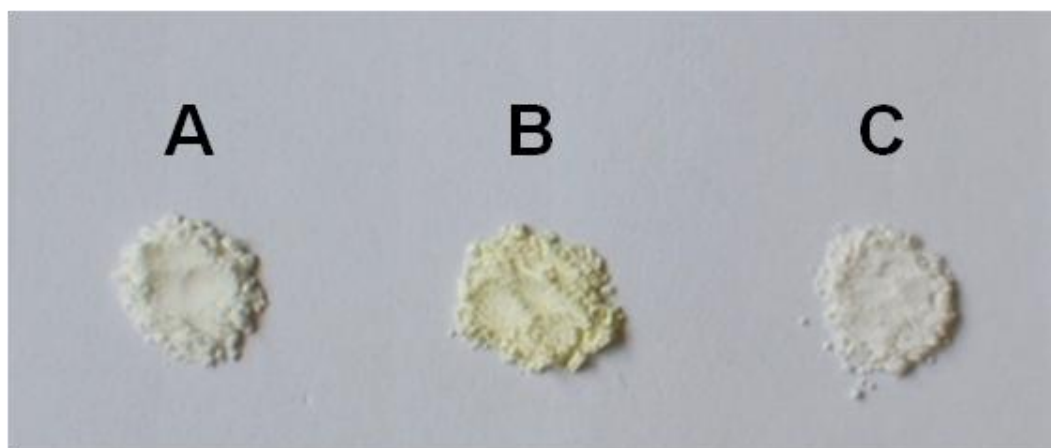
Figure 4.67: Photographs of doped ZnO obtained via moderate thermal decomposition of doped Zn(gly) (A: Al-doped ZnO; B: In-doped ZnO; C: pure ZnO).
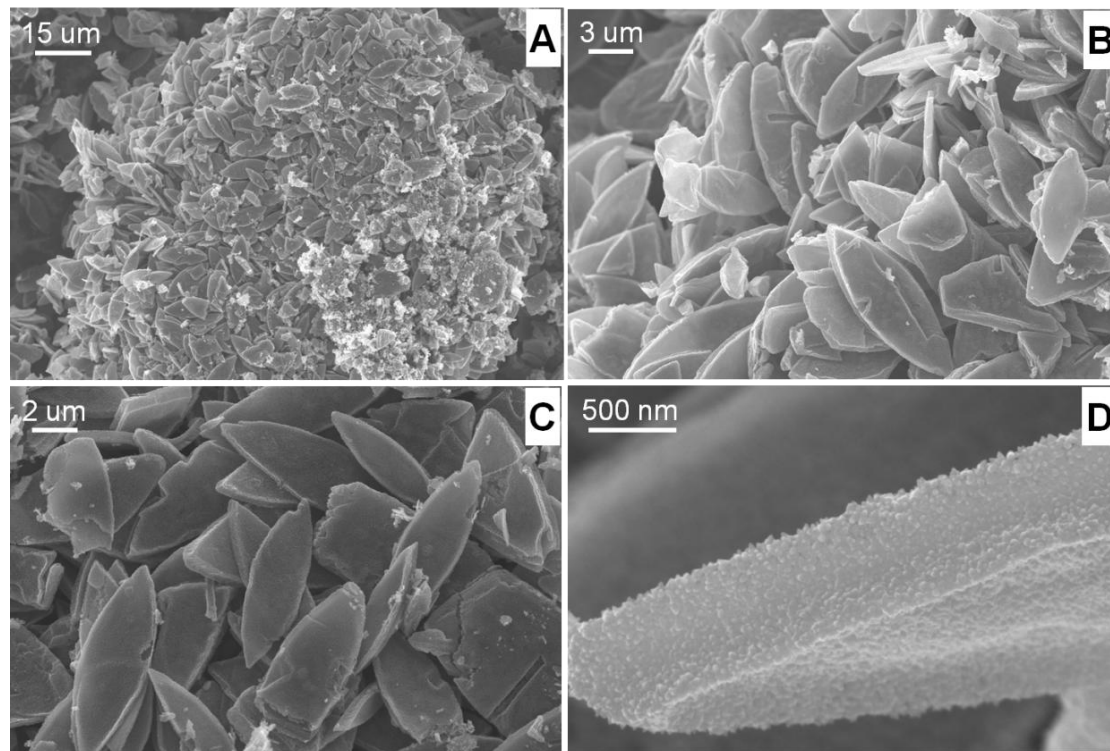
Figure 4.68: SEM images of Al-doped ZnO platelets at different levels of magnification (A: large scale overview; B, C: top-view of shuttle-shaped platelets with high resolution; D: side-view of a shuttle-shaped platelet with high resolution).

According to SEM images, the morphology of the resulting ZnO particles obtained via moderate thermal decomposition of doped Zn(gly) depends on the dopant. In the case of Al-doped ZnO, the morphology of the initial Zn(gly) obviously remains intact. The resulting Al-doped ZnO shows shuttle-shaped platelet-like morphology, which is 5-15 μm in diameter and 300-500 nm in thickness (Figure 4.68). Thus, the platelets exhibit a large aspect ratio of ~30. In contrast to the Al-doped Zn(gly) (Figure 4.57B), the Al-doped ZnO platelets present a granulated morphology consisting of dense aggregated nanoparticles of 10-30 nm in diameter, but no pores on the surface are observed (Figure 4.68D).
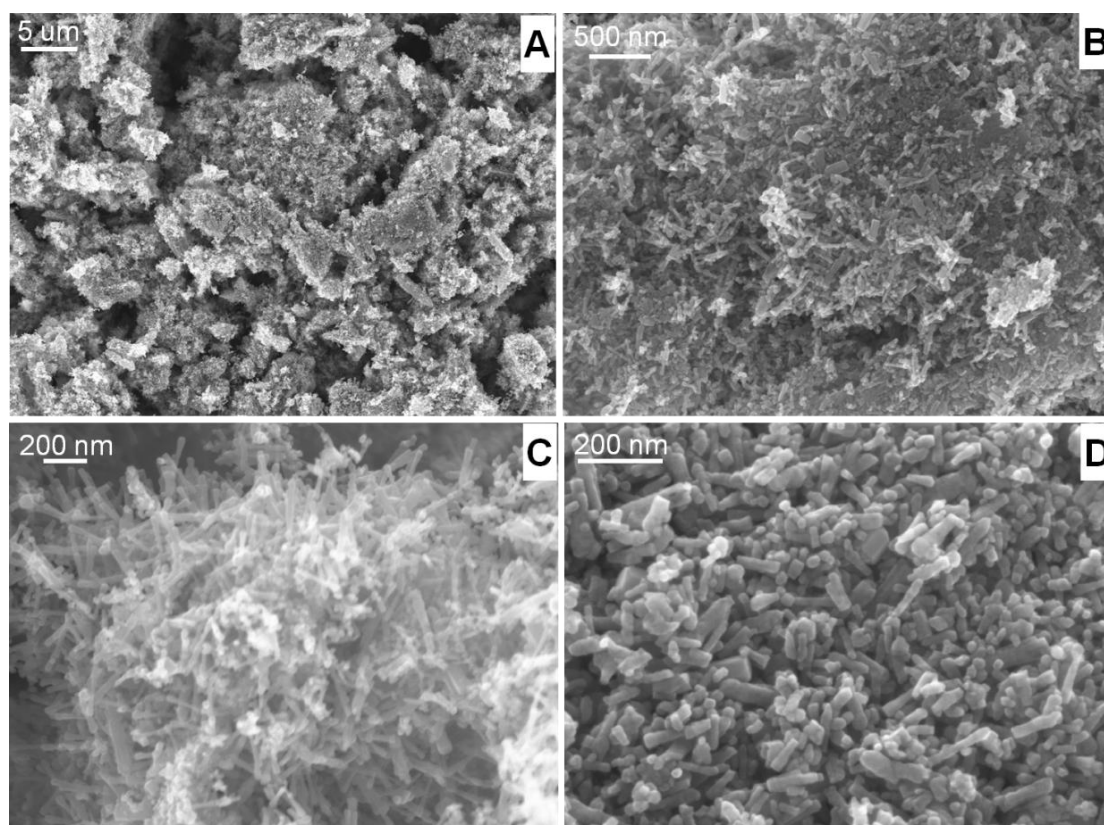
Figure 4.69: SEM images of In-doped ZnO nanowires at different levels of magnification (A: large scale overview; B: top-view of In-doped ZnO agglomerates; C: side-view of In-doped ZnO nanowires with high resolution; D: top-view of the center part of the agglomerate with high resolution).

In the case of In-doped ZnO, SEM images indicate that platelet-like morphology is not preserved here, but show large bulk agglomerates (Figure 4.69A), which are formed by rod-like particles with different sizes (Figure 4.69B). In-doped ZnO rods of more than 300 nm in length and about 20 nm in diameter are found at the borders of the bulk agglomerates (Figure 4.69C). In the center parts, there are mostly close assembled nanorods of less than 100 nm in length and less than 20 nm in diameter (Figure 4.69D).

In order to confirm the presence and amount of dopant, both Al- and In-doped ZnO powders were analyzed by EDX after pressing the samples to pellets to guarantee for a dense, semi-infinite layer with a smooth surface. Aluminium and indium can be clearly found and the EDX results show an Al : Zn molar ratio of 4 % for Al-doped ZnO and an In : Zn molar ratio of 8 % for In-doped ZnO. Considering the limitation of EDX for quantitative analysis, the presence of dopants is evidenced with about the similar amount as introduced to the synthesis.

In summary, the thermal decomposition of Zn(gly) platelets, as expected, leads to the formation of ZnO platelets. If the decomposition speed is fast, the platelet-like morphology of the starting material remains intact for the product as well. The dramatic volume reduction due to the loss of the spacious glycerolate-ligand is accompanied by pore formation and platelets showing a granulated sub-structure. Because the decomposition of Zn(gly) is more controlled at slower heating rates, smaller grains and a higher specific surface area are obtained for the granulated ZnO platelets in the latter case. Thus, moderate heating leads to a higher porosity than fast heating. On the other hand, merging of ZnO particles occurring at temperatures as low as 400 °C has to be considered.[165] The smaller the ZnO particles are, the faster is the merging. In the case of slow heating, the ZnO particles first become very small, but the prolonged time at relatively high temperatures (> 400 °C) leads to the merging of nanostructured ZnO. As a result, the loss of the platelet-like morphology and the formation of spherical and dense ZnO particles with diameters of 100-200 nm are observed. Via advanced heating processes, it would be possible to further increase the specific surface area. Depending on different dopants and via moderate thermal decomposition, the shuttle-shaped Al-doped ZnO platelets and In-doped ZnO nanowires are obtained.

4.3 Photoluminescence of Polyols

According to the previous investigations in this work, the polyol-mediated synthesis had been proven to be a promising method for synthesizing many kinds of nanoparticles.[22-26, 80, 112, 137] Polyols as chelating agents and weak surfactants were always detected on the particle surface by FT-IR spectroscopy.[19, 80, 112, 137] In our research group, some nanomaterials prepared by polyol-mediated synthesis show unexpected luminescence within the blue spectral region. In this chapter, the unexpected luminescence was proven to be directly related to heated polyols and the interesting phenomena of polyol photoluminescence were, for the first time, discovered and investigated.
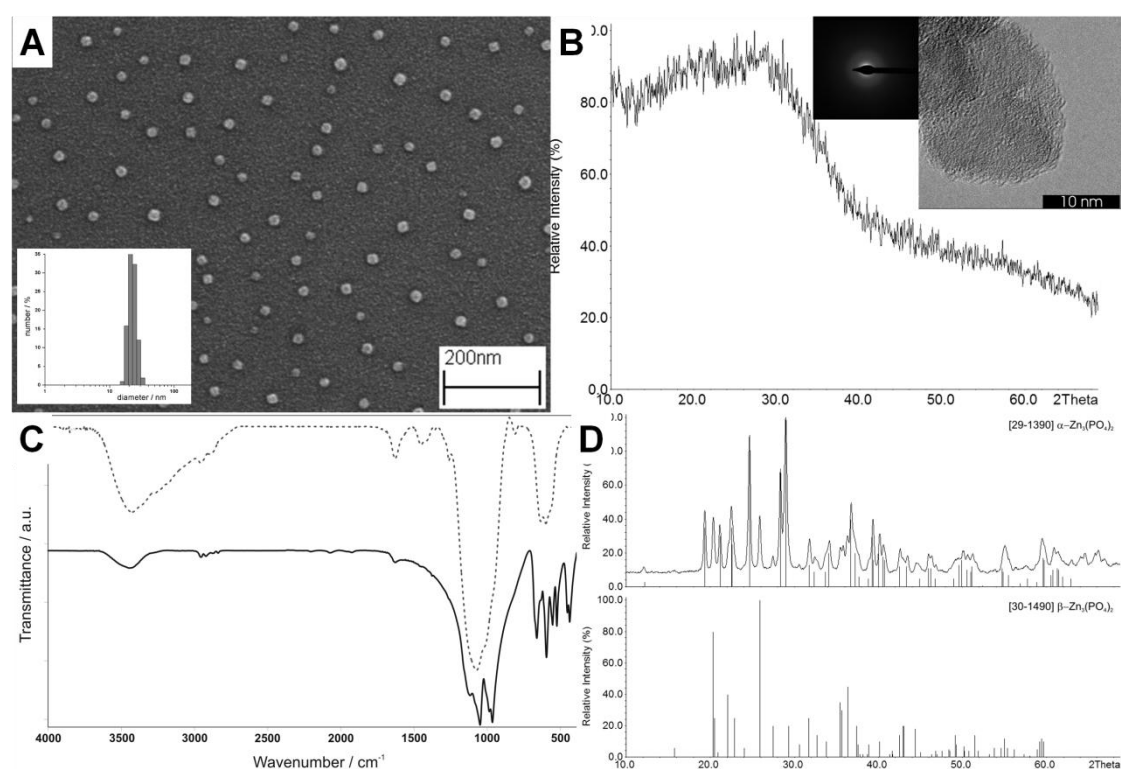
Figure 4.70: (A): DLS analysis and SEM image, (B): XRD pattern, electron diffraction and HRTEM image of the as-prepared $Zn_3(PO_4)_2$ nanoparticles, (C): FT-IR spectra of the as-prepared sample/dotted line and the annealed sample (600 °C, 3 hours, in argon)/solid line, (D): XRD pattern of the annealed $Zn_3(PO_4)_2$ nanoparticles at 600 °C for 3 hours under argon protection.[166]

The research started from the polyol-mediated synthesis of $Zn_3(PO_4)_2$ nanoparticles, which was performed by Dr. Marcus Roming.[166] $Zn_3(PO_4)_2$ nanoparticles were synthesized at a maximum reaction temperature of 230 °C in DEG, and the resulting suspension is with a slightly opalescent appearance and colloidally stable for weeks (Figure 4.71). The particle size and the size distribution of the as-prepared $Zn_3(PO_4)_2$ nanoparticles were investigated by DLS and SEM (Figure 4.70A). Non-agglomerated spherical nanoparticles with about 20 nm in diameter and a narrow size distribution

were obtained. The XRD pattern, electron diffraction and HRTEM image prove the non-crystalline nature of the as-prepared $Zn_3(PO_4)_2$ nanoparticles (Figure 4.70B). EDX analysis evidences the presence of Zn, P and O, as well as a Zn : P ratio of 3 : 2, corresponding to the chemical formula of $Zn_3(PO_4)_2$. FT-IR spectrum shows not only the vibrational bands of $(PO_4)^{3-}$ ($\nu(PO_4)^{3-}$: 1066 cm^{-1} and $\delta(PO_4)^{3-}$: 596 cm^{-1}), but also the vibrational bands of OH and CH ($\nu(OH)$: 3500-3000 cm^{-1}, $\nu(CH)$: 3000-2800 cm^{-1}, and $\nu(CO)$: superpositioned by $\nu(PO_4)^{3-}$) (Figure 4.70C), which prove the presence of residual DEG on the sample surface. After annealing the as-prepared $Zn_3(PO_4)_2$ nanoparticles at 600 ℃ for 3 hours in argon atmosphere, crystalline α-$Zn_3(PO_4)_2$ as the majority phase and β-$Zn_3(PO_4)_2$ as the minority phase were obtained as shown in Figure 4.70D. Taking all these different analyses and results into account, the as-prepared material can be denoted to amorphous $Zn_3(PO_4)_2$.

Surprisingly, the as-prepared amorphous $Zn_3(PO_4)_2$ nanoparticles exhibit an intense blue emission under UV excitation at a wavelength of 366 nm (Figure 4.71). This blue emission is observed for both the powder sample and the DEG suspension, although the as-prepared $Zn_3(PO_4)_2$ is neither crystalline nor doped. Luminescence is quantified by recording the excitation and emission spectra. When exciting the DEG suspension of $Zn_3(PO_4)_2$ with a wavelength of 370 nm, a broad band of emission with a maximum at 445 nm occurs (Figure 4.71). The emission spectrum is extended with weak intensity up to about 690 nm, which corresponds to the whitish-blue appearance under 370 nm excitation. By comparing with $BaMgAl_{10}O_{17}$:Eu as a reference, the quantum yield was measured, resulting in a value of 10 %.
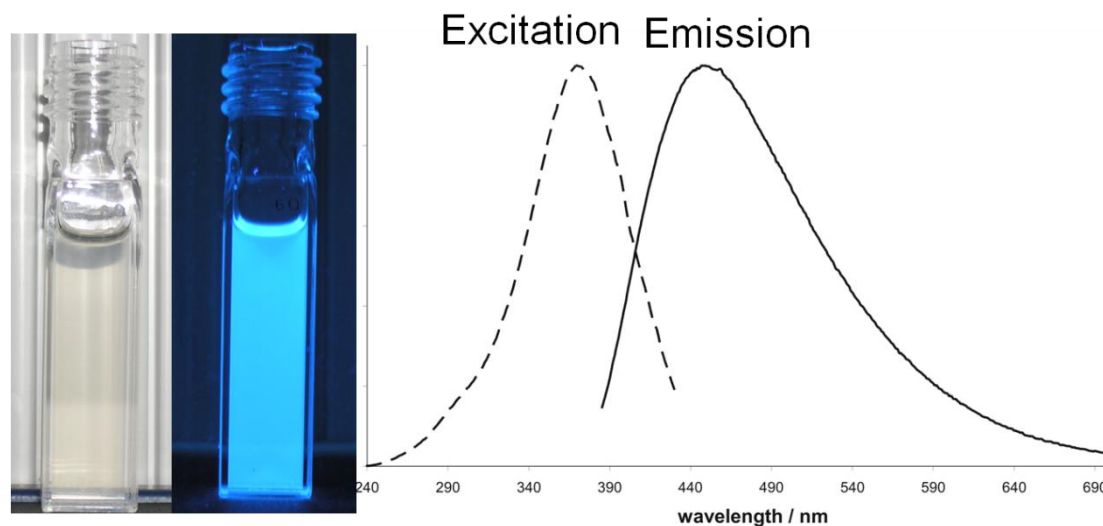
Figure 4.71: Photos in daylight and under UV ($\lambda_{excitation}$ = 366 nm), excitation (dotted) and emission (solid) spectra of the as-prepared $Zn_3(PO_4)_2$ nanoparticles suspended in DEG (unpublished results from Dr. Marcus Roming).

Doped metal phosphates, in general, are widely applied as luminescent materials, exhibiting excellent properties regarding the material's stability and the quantum yield. To this concern, crystalline materials such as $LnPO_4$:A (Ln = La, Ce, Eu or Lu; A = Eu, Ce, and/or Tb) represent standard phosphors in fluorescent lamps, light-emitting

diodes or X-ray detectors.[22, 167-174] Especially, $CePO_4$:Tb/$LaPO_4$ core/shell particles and $LaPO_4$:Ce,Tb materials are known for their outstanding high quantum yield.[35, 175] $Zn_3(PO_4)_2$ that altogether crystallizes with three different structural modifications is also used as a common host lattice for fluorescent materials. Depending on the lattice symmetry and the coordination of the zinc sites, green or red emission is observed while introducing luminescent centers of Mn^{2+} into the lattice.[176, 177] The weak yellow emission of Mn^{2+} has also been observed in case of zinc metaphosphate glasses singly and doubly doped with Ce^{3+} and Mn^{2+} ions.[178] Recently, β-$Zn_3(PO_4)_2$:Mn,M (with M = Al, Ga or Zn) has also been discussed as novel red long lasting phosphorescent materials.[179, 180]

With concern to the luminescence of inorganic materials, highly crystalline lattices and the presence of luminescent centers (conventionally by doping with rare earth metals) are essential prerequisites.[181, 182] Luminescence of non-doped $Zn_3(PO_4)_2$ as well as the emission of blue light has not been reported before. Moreover, relatively intense emission of a non-crystalline nanomaterial is also observed for the first time. Similar to the $Zn_3(PO_4)_2$ from our research group, several other materials in literature, such as ZnO,[183, 184] Al_2O_3,[185] ZnSe,[186] PbS,[187] $Bi_4Ti_3O_{12}$,[188] and carbon dots,[189-193] also show unexpected luminescence. Although these reported luminescent materials are different and from different research groups, they all have broad emissions in the blue spectral region under UV excitation. After checking the synthetic precursors or preparation processes in the above-mentioned publications, we have found that polyols are always involved, either as solvents and stabilizers, or as passivation agents. Thus, an idea comes to us that the unexpected luminescence might originate from polyols.

Comparing polyols: DEG and glycerol
In order to prove that the unexpected luminescence of materials is directly related to polyols, following experiments using DEG and glycerol were designed. The reason why DEG and glycerol were studied first is because these two polyols are the most common reagents and can be easily obtained in the laboratory. In a typical recipe, 0.5 mmol metal salts ($ZnCl_2 \cdot 2H_2O$, $MgCl_2 \cdot 6H_2O$ or without metal salts) and 10 mL DEG or glycerol were filled in a three-neck flask with magnetic stirring. The final samples were obtained by rapidly heating the system to about 220 °C in 7 minutes with a heating mantle and maintaining the reaction temperature higher than 220 °C in the following 1 hour. At last, the heating mantle was turned off and the whole system was cooled naturally to room temperature. The reaction was performed under argon inert-gas protection. Detailed information regarding names, used metal salts and polyols of the final samples is listed in Table 4.7.

The photoluminescence and the photoluminescent excitation spectra of the as-prepared samples were directly measured by fluorescence spectroscopy. After the reaction of different metal salts in DEG/glycerol at 220 °C, very light yellow (with metal salts) and colorless (without metal salts) suspensions were obtained (Figure

4.72A). Surprisingly, all the samples exhibit intense blue emissions under UV light with a wavelength of 366 nm as shown in Figure 4.72B to G. These blue emissions are similar to the emission of the as-prepared $Zn_3(PO_4)_2$ suspension (Figure 4.71) and luminescent carbon dots.[189, 190, 192, 193] Upon excitation at 366 nm, the maximum photoluminescence peaks of the samples with different intensities were observed at 400 to 450 nm in the blue spectral region (Figure 4.73 and Table 4.7), where the unexpected emissions occur.[183-193] Among all six samples, Mg^{2+}/Gly has the highest intensity that can also be confirmed by comparing the direct photographs (Figure 4.72), and shows a maximum emission peak at 429 nm with a Stokes shift of 63 nm.

Table 4.7: Detailed information of final DEG/glycerol samples with maximum excitation, emission wavelengths and Stokes shift.

Sample name	Metal salt	Polyol	$\lambda_{max.exc}$ / nm	$\lambda_{max.emi}$ / nm	Stokes shift* / nm
Zn^{2+}/DEG	$ZnCl_2$ $2H_2O$	DEG	364	443	77
Zn^{2+}/Gly	$ZnCl_2$ $2H_2O$	Glycerol	336	434	68
Mg^{2+}/DEG	$MgCl_2$ $6H_2O$	DEG	351	420	54
Mg^{2+}/Gly	$MgCl_2$ $6H_2O$	Glycerol	331	429	63
T/DEG	—	DEG	351	444	78
T/Gly	—	Glycerol	338	438	72

($\lambda_{max.exc}$: maximum excitation wavelength according to Figure 4.76)
($\lambda_{max.emi}$: maximum emission wavelength according to Figure 4.73)
(*: Stokes shift according to Figure 4.73 with 366 nm excitation)
(T/DEG and T/Gly: heated DEG and glycerol without metal salts)
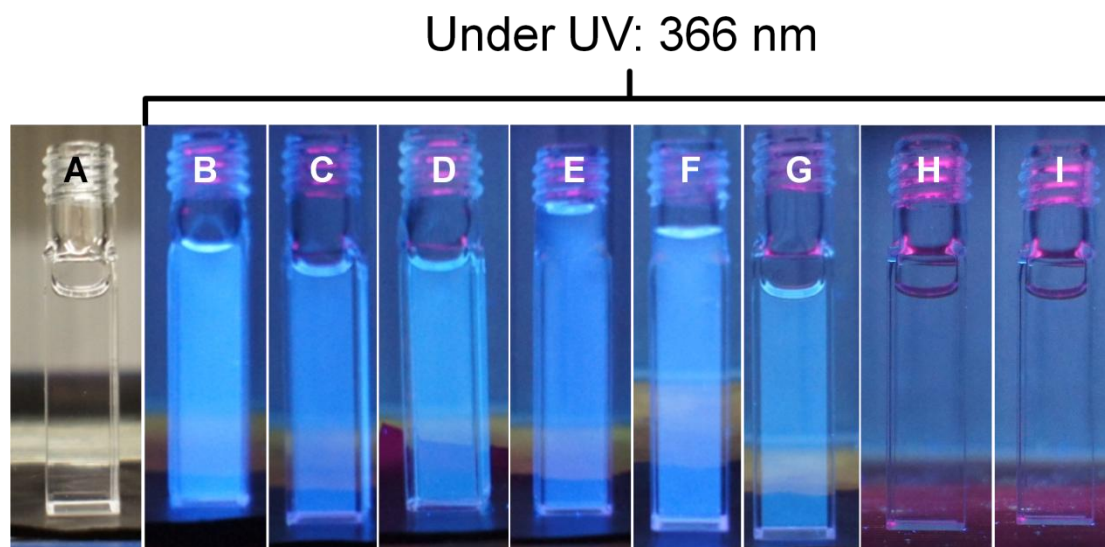
Figure 4.72: Direct photographs of DEG/glycerol samples taken under ambient light (A), and under UV light with a wavelength of 366 nm (B to G, referring to Mg^{2+}/Gly, Mg^{2+}/DEG, T/DEG, T/Gly, Zn^{2+}/Gly and Zn^{2+}/DEG, respectively; Pure DEG (H) and glycerol (I) without heating as references).
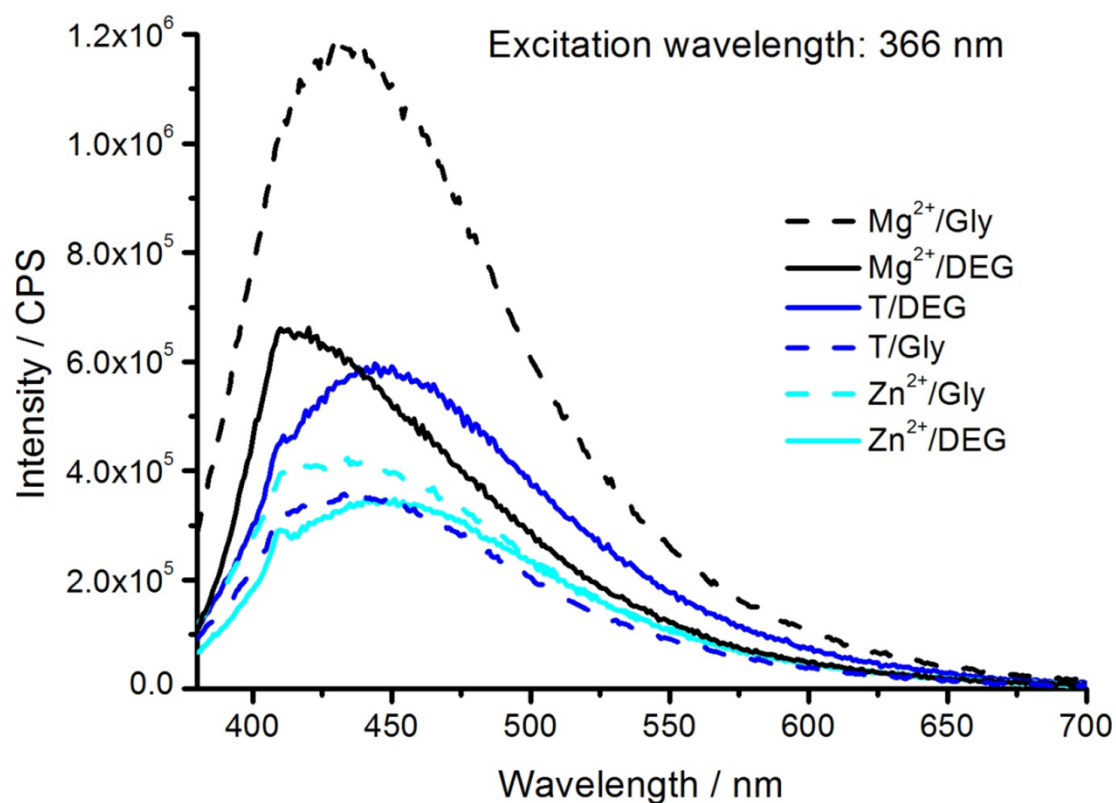
Figure 4.73: Photoluminescent emission spectra of DEG/glycerol samples excited at 366 nm.
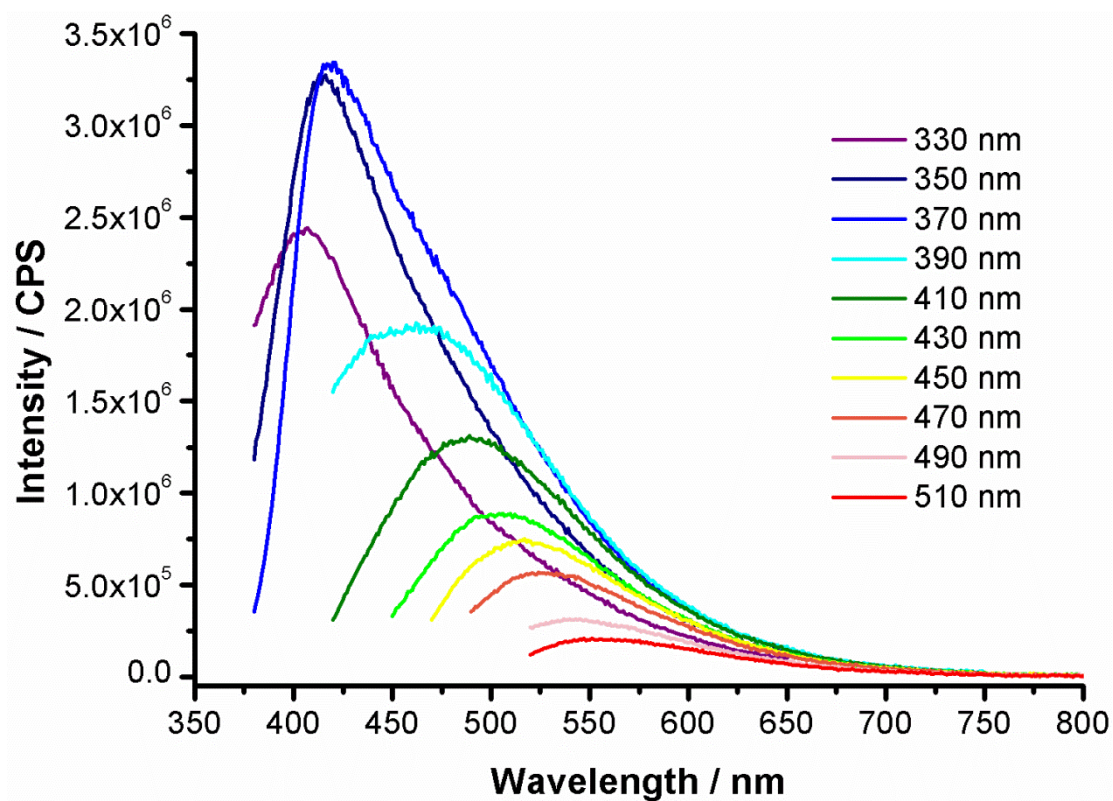
Figure 4.74: Photoluminescent emission spectra of Mg^{2+}/DEG with progressively increased excitation wavelengths from 330 nm to 510 nm in 20 nm increments.

As shown in Figure 4.74, the photoluminescent emission spectra of Mg^{2+}/DEG are broad and dependent on the excitation wavelengths. The emission peak shifts from 406 nm with a medium intensity, then 421 nm with the highest intensity to 547 nm with the lowest intensity as the excitation wavelength increases from 330 nm, then 370 nm to 510 nm. The maximum emission wavelengths according to the excitation wavelengths are shown in Table 4.8. The excitation wavelength can be red-shift beyond 510 nm and blue-shift beyond 330 nm, but the intensities of the emission spectra will decrease further, which is not presented here. It should be pointed out that neither the pure polyols without heat treatment nor the metal salts themselves are emissive in the UV-Vis range (Figure 4.72H and I). Therefore, the observed blue emission under UV light and other colorful luminescent emissions at different excitation wavelengths must be due to the heat-treated polyols.

It is worth mentioning that all samples with the heated polyols show luminescent emissions with a dependence on the excitation wavelengths. As shown in Figure 4.75, the photoluminescent emission spectra of glycerol samples are also broad and dependent on the excitation wavelengths. The emission peaks shift from 400 nm to 430 nm with decreasing intensities, when the excitation wavelength increases from 338 nm to 366 nm.
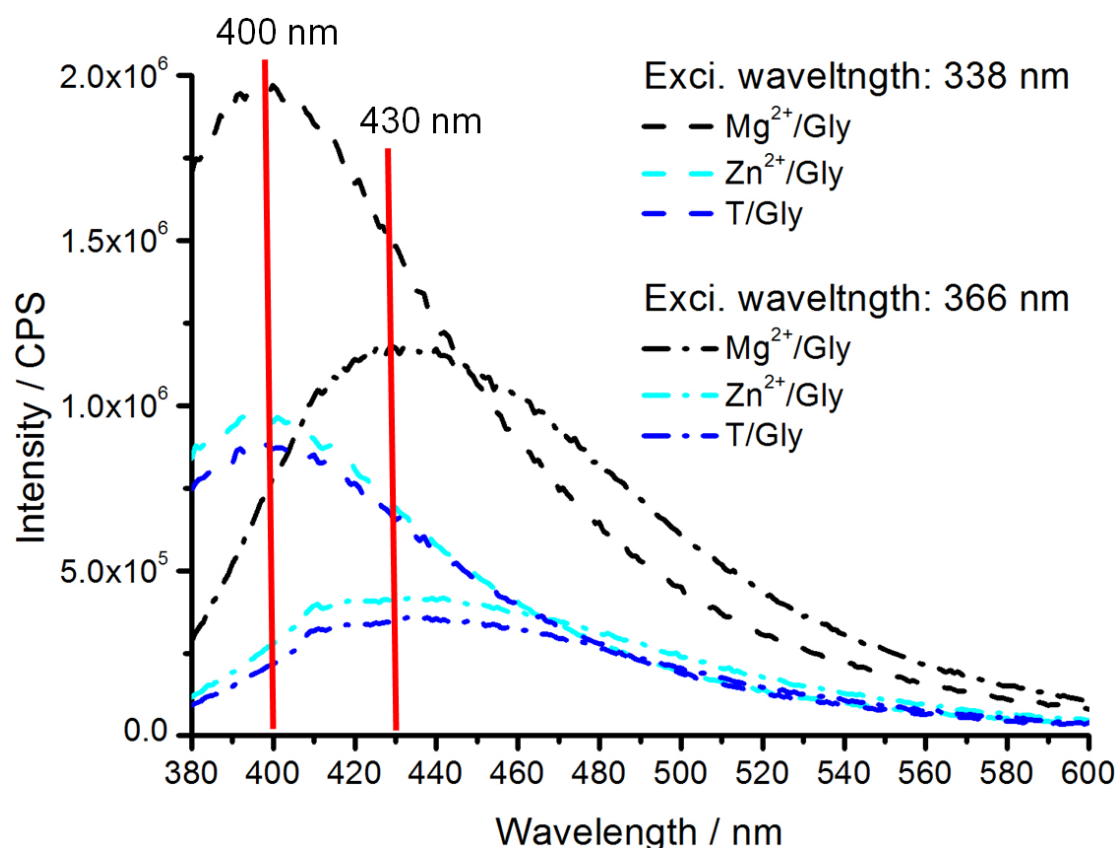
Figure 4.75: Photoluminescent emission spectra of glycerol samples at different excitation wavelengths (338 nm/dash lines and 366 nm/dash-dot lines) with red lines indicating different maximum emission peaks.

Table 4.8: Maximum emission wavelengths of Mg^{2+}/DEG at excitation wavelengths progressively increasing from 330 nm to 510 nm in 20 nm increments according to Figure 4.74.

λ_{exc} / nm	330	350	370	390	410	430	450	470	490	510
$\lambda_{max.emi}$ / nm	406	413	421	462	489	510	517	524	543	547

The influence of the reaction precursors (metal salts and polyols) on the luminescence properties of samples was also investigated. Mg^{2+} samples exhibit higher intensities than the other samples for both the emission and excitation spectra (Figure 4.73 and Figure 4.76). Figure 4.76 shows the photoluminescent excitation spectra of samples prepared in DEG and glycerol. The results indicate the polyols can affect the excitation properties. All three glycerol samples shift to a shorter wavelength (~15 nm) as compared to the DEG samples.
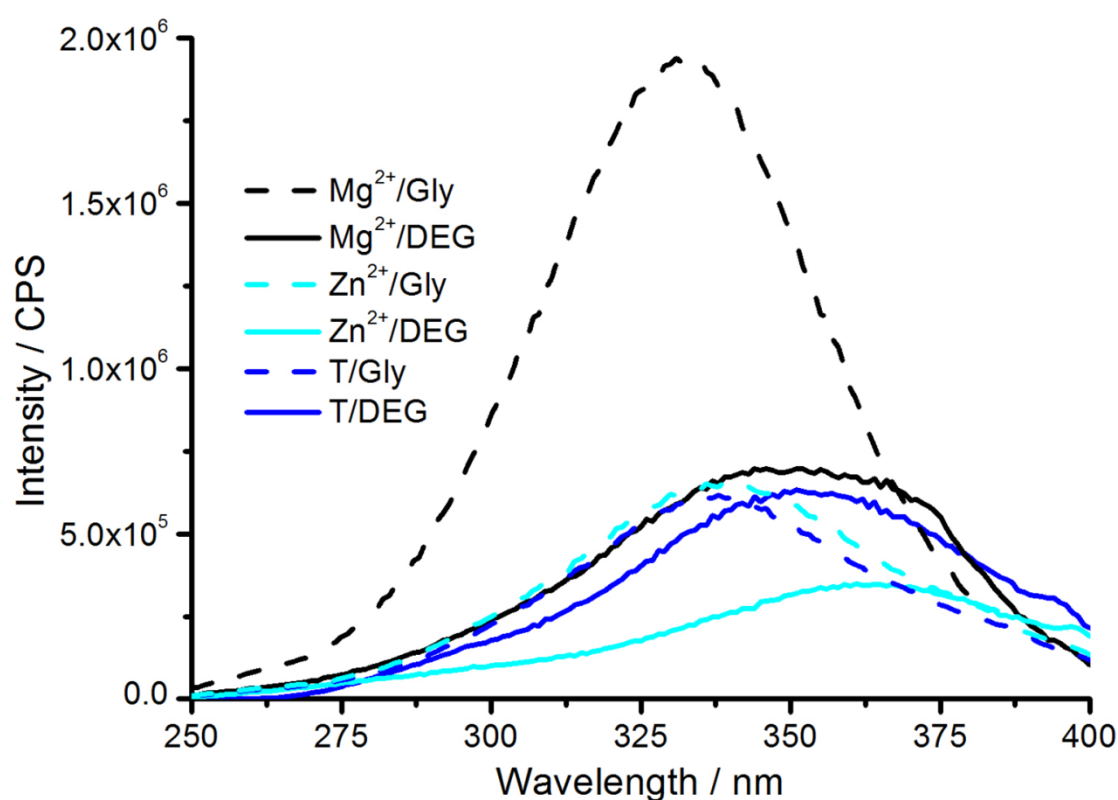
Figure 4.76: Photoluminescent excitation spectra of DEG/glycerol samples acquired with maximum detection wavelengths according to Figure 4.73.

Comparing polyols: PEG400

Polyethylene glycol (PEG) is a well known stabilizer for the synthesis of nanomaterials[194] and passivation agents.[189-193] In this thesis, PEG400 was chosen because of the liquid nature at room temperature. Similar to the preparation of DEG/glycerol samples, 0.5 mmol of different metal salts were heated with 10 mL PEG400 to approximately 220 °C in a three-neck flask under argon protection. Detailed information regarding names and used metal salts of the PEG samples is listed in Table 4.9.

Table 4.9: Detailed information of PEG samples with maximum emission wavelengths and Stokes shift.

Sample name	Metal salt	Heated polyol	$\lambda_{max.emi}$ / nm	Stokes shift*/ nm
Na^+/PEG	NaCl	PEG400	440	74
K^+/PEG	KCl	PEG400	436	70
Zn^{2+}/PEG	$ZnCl_2\ 2H_2O$	PEG400	450	84
Mg^{2+}/PEG	$MgCl_2\ 6H_2O$	PEG400	445	79
T/PEG	—	PEG400	437	71
PEG400	—	—	—	—

($\lambda_{max.emi}$: maximum emission wavelength according to Figure 4.78)

(*: Stokes shift according to Figure 4.78 with 366 nm excitation)
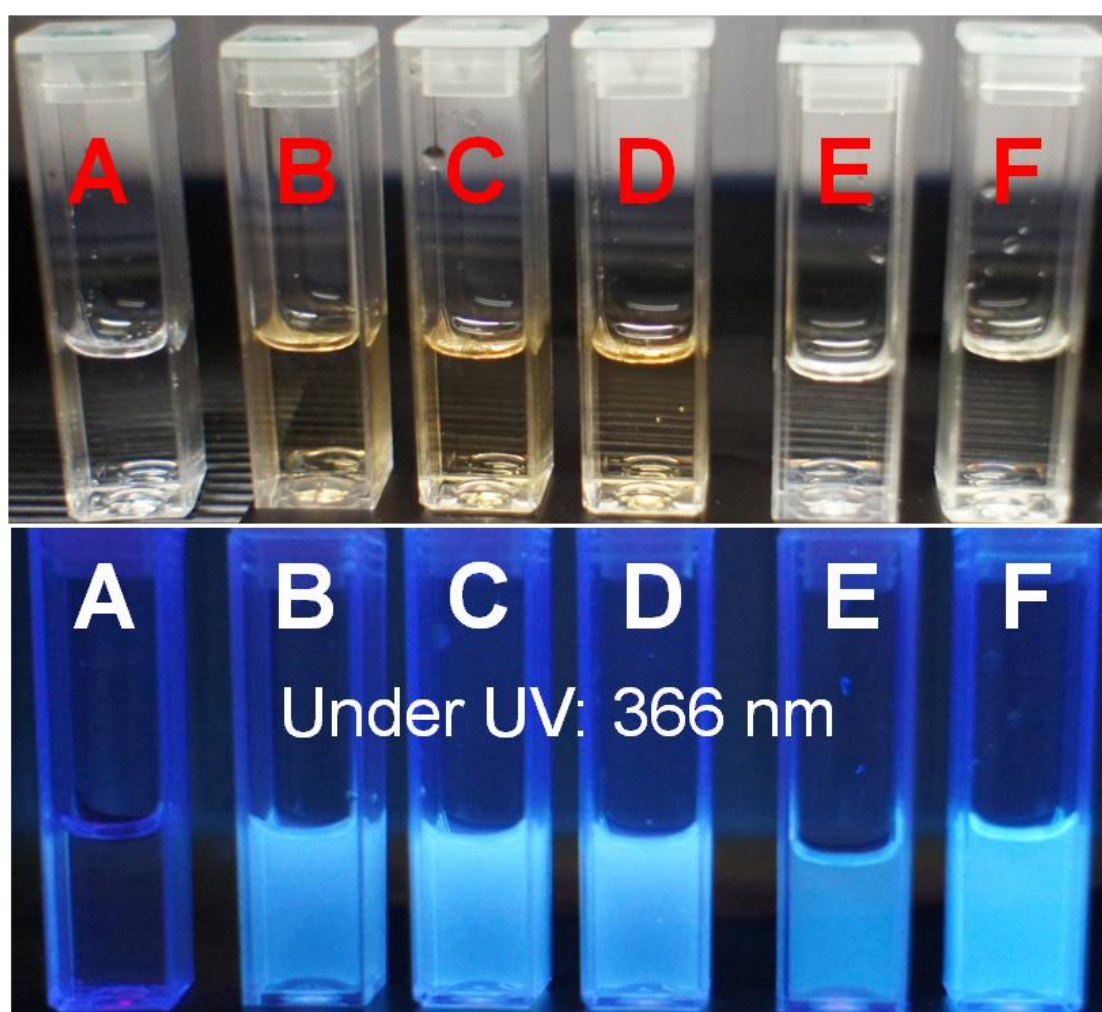
Figure 4.77: Direct photographs of PEG samples taken under ambient light (top) and under UV light (bottom) with a wavelength of 366 nm (A to F refer to pure PEG400 without heating, T/PEG, K^+/PEG, Na^+/PEG, Zn^{2+}/PEG and Mg^{2+}/PEG, respectively).

After keeping the reaction temperature higher than 220 °C for 1 hour, the colorless PEG400 (Figure 4.77A) turns to light brown for T/PEG, K^+/PEG and Na^+/PEG (Figure 4.77B, C, D) and very light yellow for Zn^{2+}/PEG and Mg^{2+}/PEG (Figure

4.77E, F). All heated samples under UV light show intense blue emissions, which are brighter than those of DEG/glycerol samples (Figure 4.72). From Figure 4.77 (bottom), we can clearly observe no emission for pure PEG400, lowest intensity for Zn^{2+}/PEG and highest intensity for Mg^{2+}/PEG. These findings can be also confirmed by the luminescent emission spectra of PEG samples as shown in Figure 4.78. Upon excitation at 366 nm, the maximum photoluminescence peaks of PEG samples with different intensities were observed at 435 to 450 nm in the blue spectral region (Figure 4.78 and Table 4.9). Among all the heated samples, Mg^{2+}/PEG has the highest intensity and Zn^{2+}/PEG has the lowest intensity. In order to compare the emission intensities of DEG/glycerol and PEG samples, the measurements were done with the same parameters in a short period of time. By comparing Figure 4.73 and Figure 4.78, the emission intensities of PEG samples are approximately an order of magnitude higher than those of DEG/glycerol samples. Accordingly, PEG samples look much brighter than DEG/glycerol samples under UV excitation (Figure 4.72 and Figure 4.77). By comparing with an empty quartz cuvette in an integrating sphere and 370 nm as the excitation wavelength, the absolute quantum yield of Mg^{2+}/PEG was measured and calculated to be around 25 %.
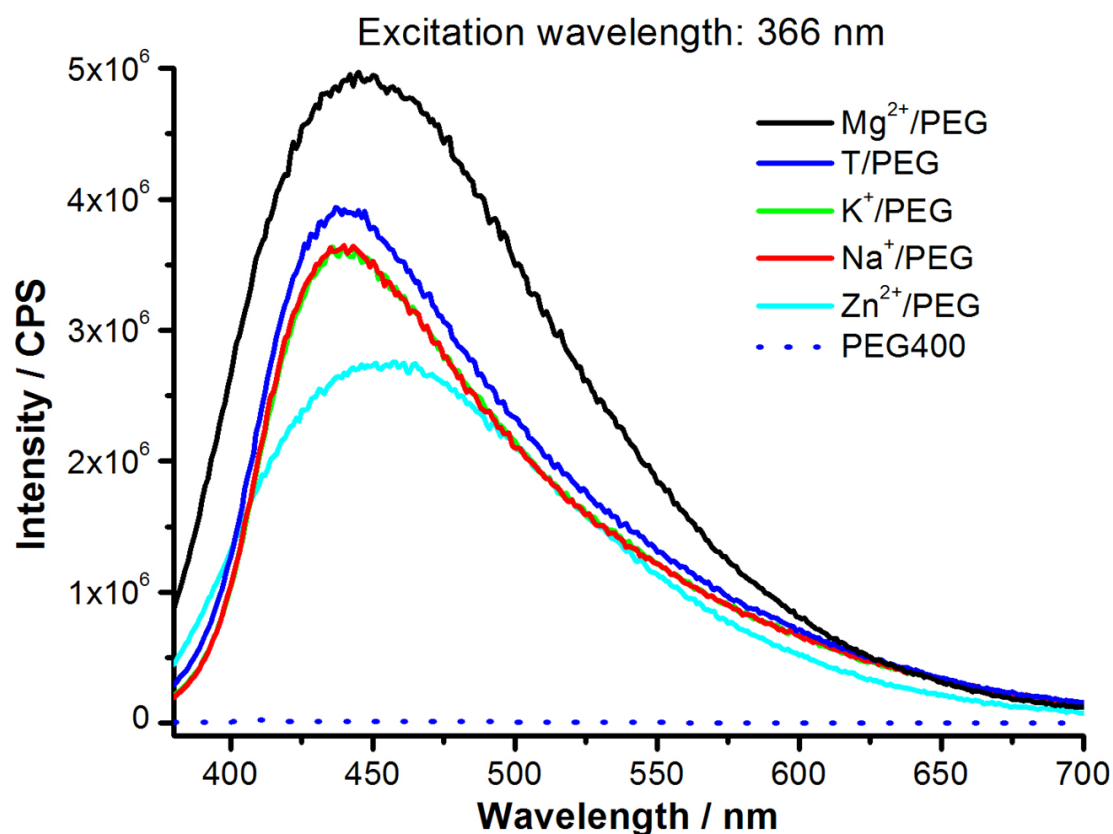
Figure 4.78: Photoluminescent emission spectra of PEG samples excited at 366 nm (pure PEG400 without heating as a reference).

As mentioned before, all heated polyol samples show luminescent emissions with a dependence on the excitation wavelengths. To this concern, the photoluminescent emission spectra of T/PEG were recorded with progressively increasing the excitation wavelength from 330 nm to 490 nm in 20 nm increments (Figure 4.79). The broad

emission peak shifts from 431 nm with a medium intensity, then 444 nm with the highest intensity to 568 nm with the lowest intensity as the excitation wavelength increases from 330 nm, then 370 nm to 490 nm. The maximum emission wavelengths according to the increasing excitation are shown in Table 4.10. As compared with Mg^{2+}/DEG (Figure 4.74 and Table 4.8), the whole emission spectra shift to longer wavelengths.
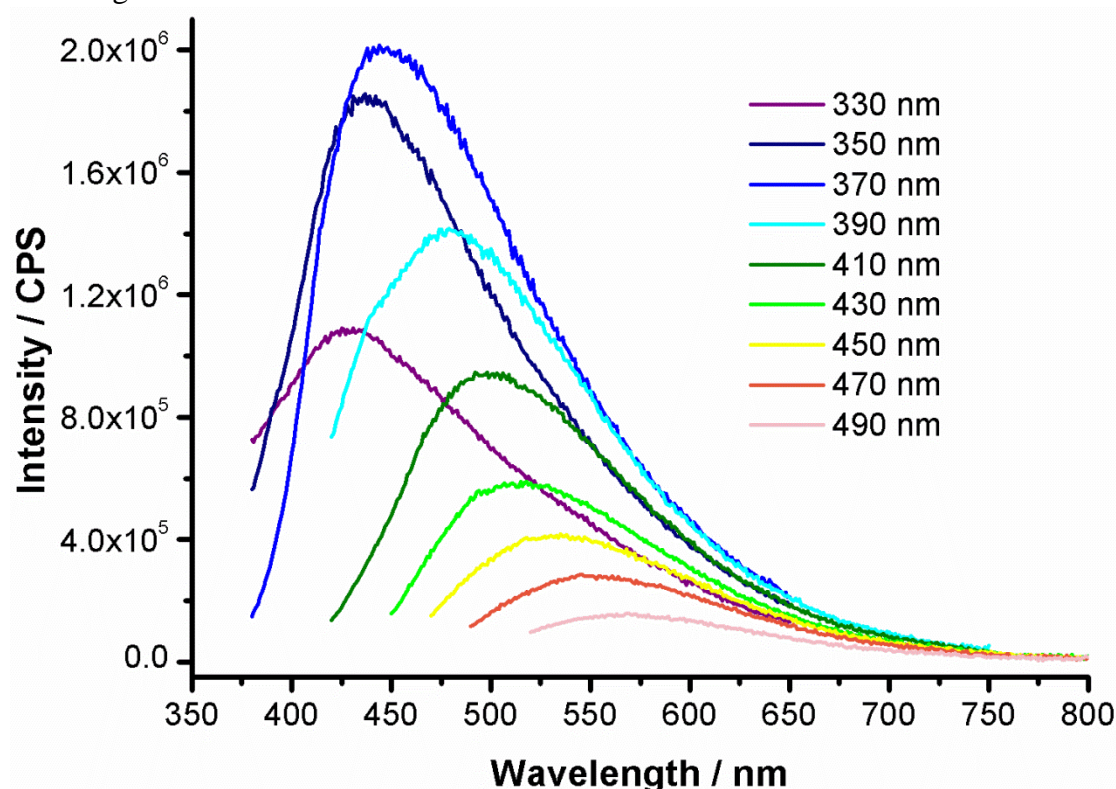
Figure 4.79: Photoluminescent emission spectra of T/PEG with progressively increased excitation wavelengths from 330 nm to 490 nm in 20 nm increments.

Table 4.10: Maximum emission wavelengths of T/PEG at excitation wavelengths progressively increasing from 330 nm to 490 nm in 20 nm increments according to Figure 4.79.

λ_{exc} / nm	330	350	370	390	410	430	450	470	490
$\lambda_{max.emi}$ / nm	431	437	444	479	506	515	535	545	568

So far, only non rare-earth metal salts with heated polyols were tested, showing the unexpected luminescence. The next question arises that how rare-earth metal salts behave when being heated with polyols. The rare-earth metal terbium (Tb) and its metal salt are well known for the green emission as doping agents. In this work, 0.5 mmol $TbCl_3$ $6H_2O$ and 10 mL PEG400 were heated together to 220 °C. The light yellow Tb^{3+}/PEG exhibits green emission at 256 nm and much brighter green emission at 366 nm (Figure 4.80D, E, F). In order to prove the luminescence is related to the heated PEG, 0.5 mmol $TbCl_3$ $6H_2O$ were dissolved in 10 mL distilled water. The resulting colorless solution shows no luminescence at 254 nm and green luminescence (very low intensity) at 366 nm (Figure 4.80A, B, C).
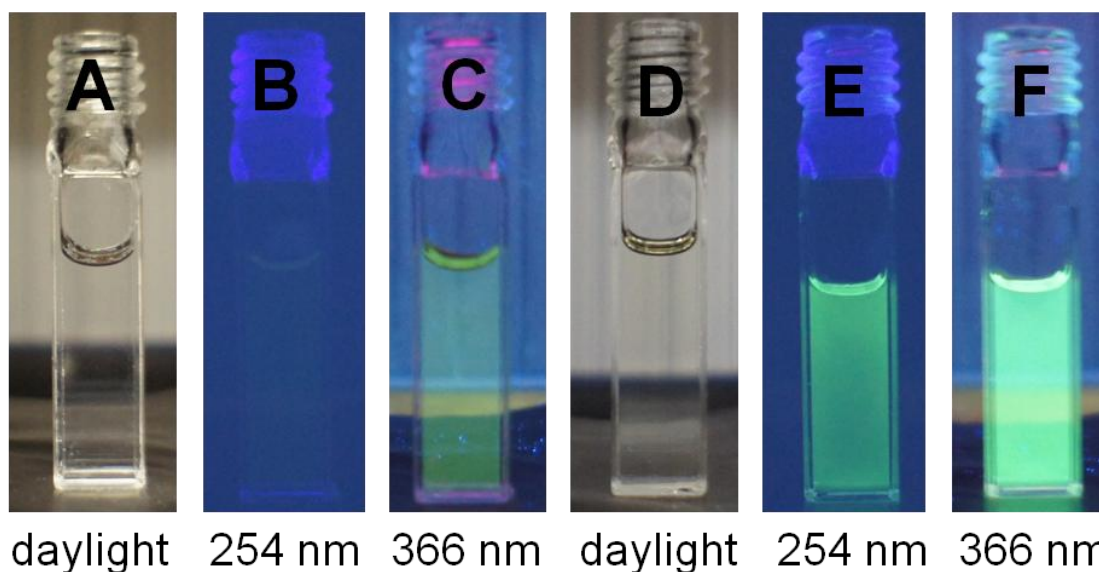
Figure 4.80: Direct photographs of TbCl$_3$ in water (A to C) and Tb^{3+}/PEG (D to F) taken under ambient light and UV light with wavelengths of 254 nm and 366 nm.
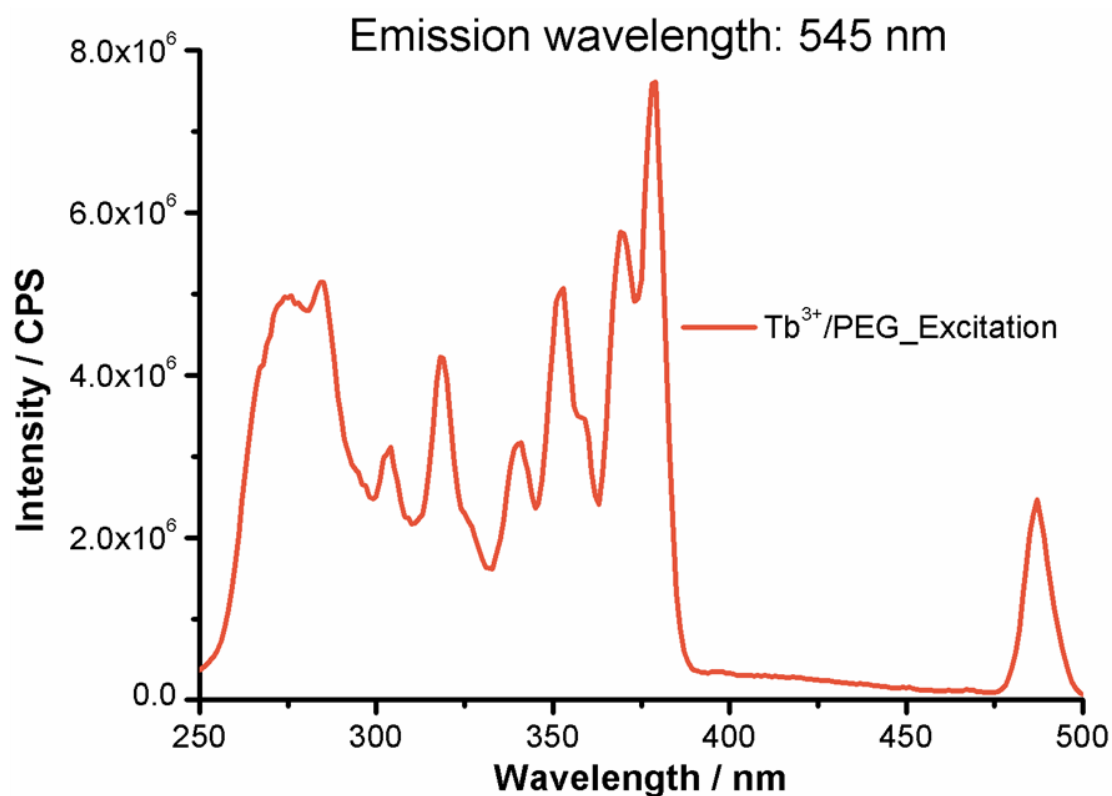
Figure 4.81: Photoluminescent excitation spectrum of Tb^{3+}/PEG acquired with 545 nm detection wavelength.

The photoluminescent excitation and emission spectra of Tb^{3+}/PEG were directly measured by fluorescence spectroscopy. Figure 4.81 presents the photoluminescent excitation spectrum of Tb^{3+}/PEG acquired with the detection wavelength of 545 nm, which is a typical Tb excitation spectrum. Comparing the emission spectra at different

excitation wavelengths (Figure 4.82), the emission spectrum excited at 366 nm shows not only a typical Tb emission as the emission spectrum excited at 274 nm, but also a broad peak in the blue spectral region, which results from the heated polyols. The combination of the typical Tb emission and the blue emission of heated polyols leads to a bright green luminescence under a 366 nm UV lamp (Figure 4.80F). The absolute quantum yield of Tb^{3+}/PEG was measured and calculated to be around 46 %, comparing with an empty quartz cuvette in an integrating sphere and 370 nm as the excitation wavelength.
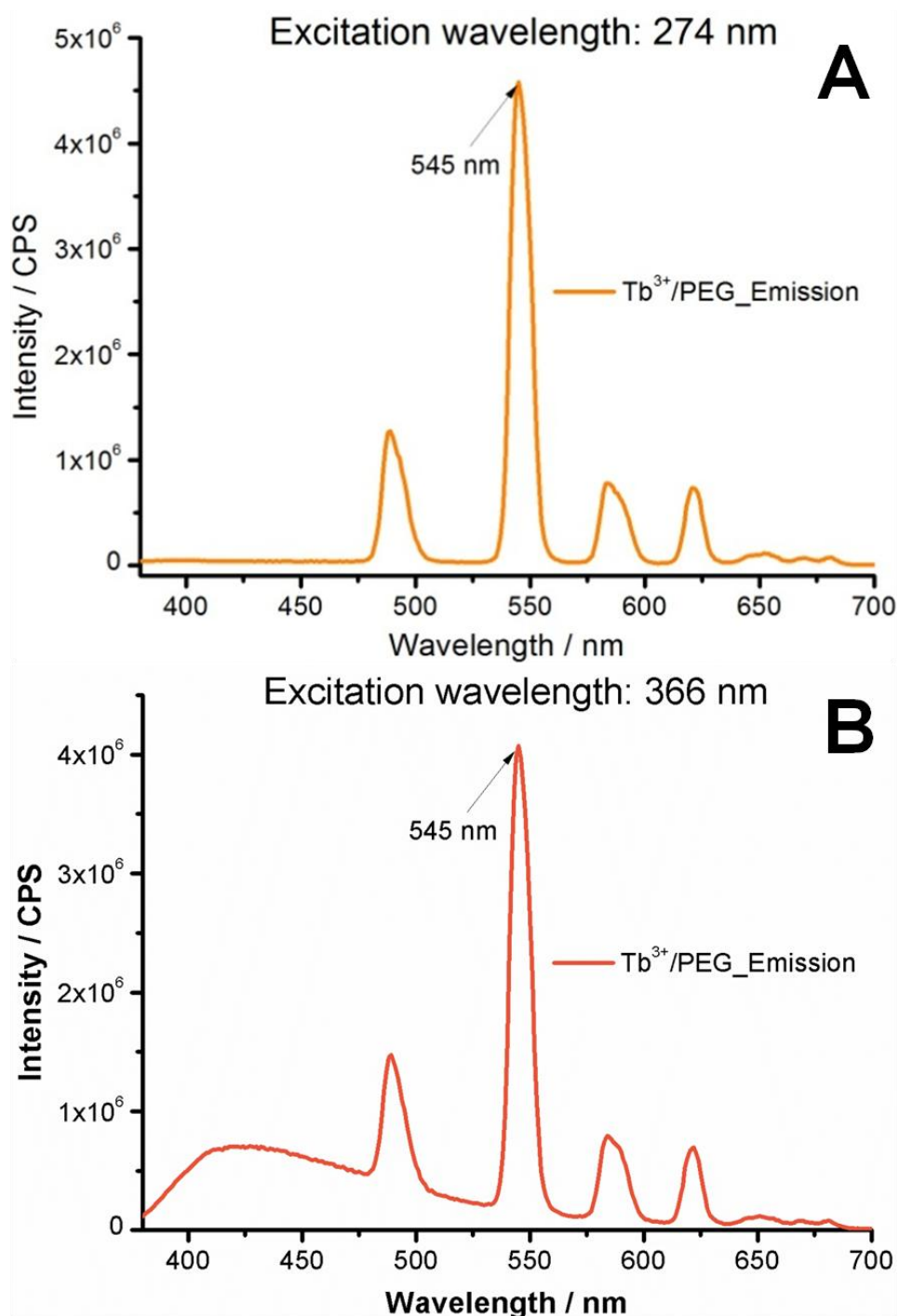
Figure 4.82: Photoluminescence emission spectra of Tb^{3+}/PEG excited at wavelengths of 274 nm (A) and 366 nm (B).

Even after diluting 2 mL Mg^{2+}/PEG and Tb^{3+}/PEG in 50 mL ethanol respectively, the resulting colorless suspensions (Figure 4.83A) show blue luminescence under a 366 nm UV lamp for Mg^{2+}/PEG (Figure 4.83C) and green luminescence under both 254 nm and 366 nm UV lamps for Tb^{3+}/PEG (Figure 4.83B, C).
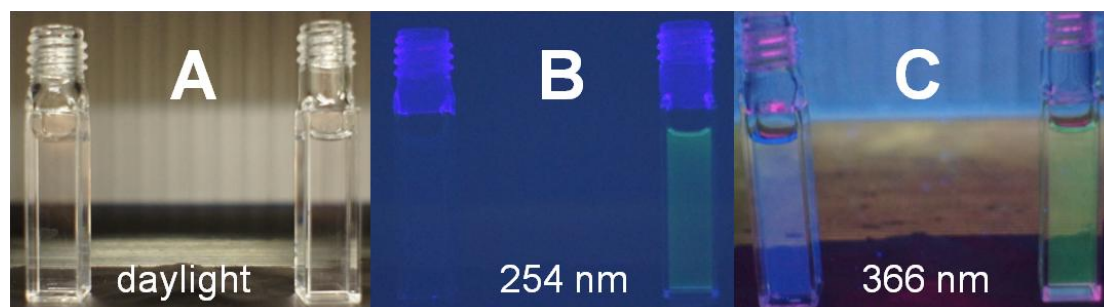
Figure 4.83: Direct photographs of diluted Mg^{2+}/PEG (left) and Tb^{3+}/PEG (right) in ethanol taken under daylight and UV light with wavelengths of 254 nm and 366 nm.

Comparing polyols: PEG400 with Fluorescein

Fluorescein (Fc) is a dark red fluorophore and wildly used as a fluorescent tracer for many applications. Its aqueous solution generally emits green light under UV excitation.[195] In order to test how fluorescein behaves with heated polyols, the following experiments were designed. First, 65 mmol (21.6 mg) fluorescein were dissolved in 50 mL PEG400 (Solution A). Then, 1 mL of Solution A was used as reactant to prepare PEG+Fc, T/PEG+Fc and Mg^{2+}/PEG+Fc (similar experimental procedures as described before). Detailed information about experiments and names of samples is listed in Table 4.11.
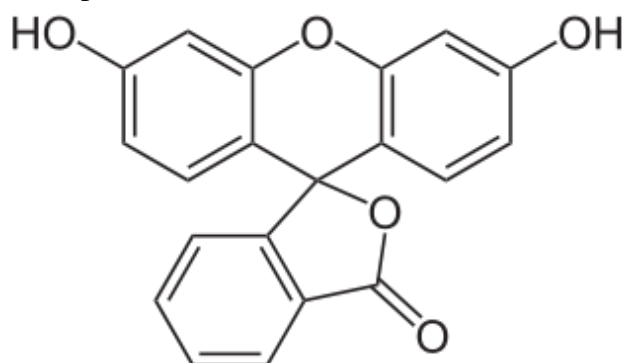
Figure 4.84: Skeletal formula of fluorescein.

Table 4.11: Detailed experimental information of fluorescein samples.

Sample name	Metal salt	Polyol	Temperature
PEG+Fc	—	9 mL PEG400+1 mL SA	RT
T/PEG+Fc	—	9 mL PEG400+1 mL SA	220 ℃
Mg^{2+}/PEG+Fc	0.5 mmol $MgCl_2$ $6H_2O$	9 mL PEG400+1 mL SA	220 ℃

(SA: 65 mmol fluorescein powders dissolved in 50 mL PEG400)
(RT: room temperature)

The photoluminescent emission spectra of PEG+Fc, T/PEG+Fc and Mg^{2+}/PEG+Fc

shown in Figure 4.85, were recorded by fluorescence spectroscopy with a 366 nm excitation. For PEG+Fc that is the dissolution of fluorescein in PEG400, its spectrum only shows one broad peak with lowest intensity in green spectral region, which can be attributed to the luminescence of fluorescein (Figure 4.84C). For T/PEG+Fc and Mg^{2+}/PEG+Fc, the main emission from fluorescein shifts to longer wavelength with much higher intensity as compared to PEG+Fc. Due to the heated polyols, the broad emission in the blue spectral region occurs. Direct photographs of three samples under daylight and UV are compared in Figure 4.86. The light yellow PEG+Fc only emits green light from fluorescein. The luminescence of orange T/PEG+Fc and yellow Mg^{2+}/PEG+Fc is in good agreement with their emission spectra. The combination of green emission and the blue emission leads to very bright yellow luminescence under a 366 nm UV lamp (Figure 4.86C).
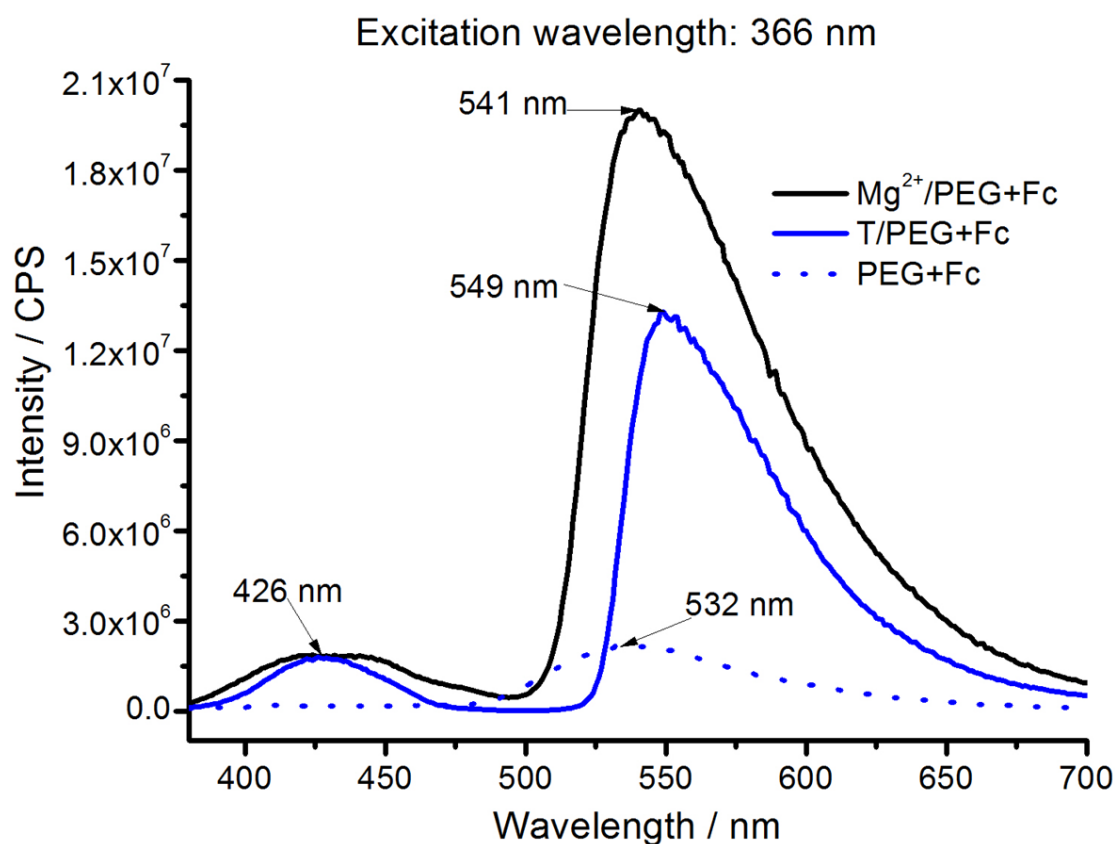
Figure 4.85: Photoluminescent emission spectra of fluorescein samples excited at 366 nm.

The intrinsic mechanism of polyol luminescence is still under investigation. After heating the polyols, suspensions were always obtained. In order to identify the naoparticles in the heated polyols, water-diluted Mg^{2+}/PEG was characterized by TEM. As shown in Figure 4.87A, the crystalline nanoparticles are well dispersed and narrowly distributed with diameters in the range of 3-5 nm. HRTEM confirms a lattice spacing of 2.04 Å (Figure 4.87B). The experimental diffractogram of the nanoparticle fits quite well with calculated diffraction pattern of bulk-carbon (Figure 4.87C), which indicates that the nanoparticles are carbon dots.
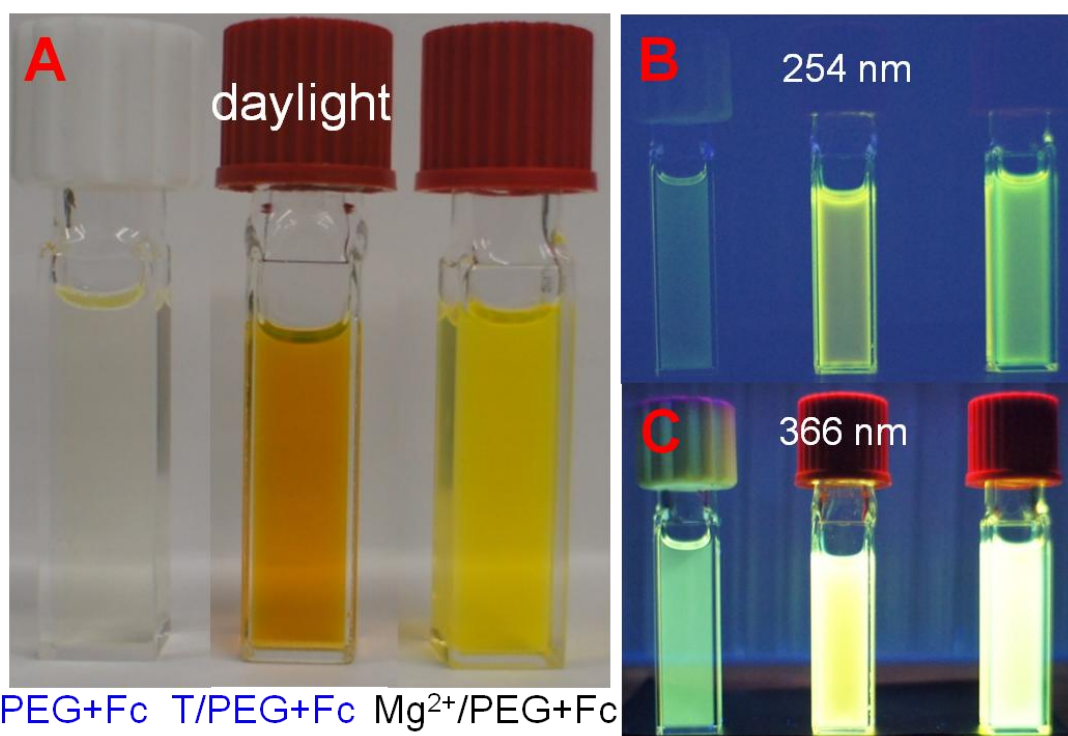
Figure 4.86: Direct photographs of fluorescein samples taken under daylight (A) and UV light with wavelengths of 254 nm (B) and 366 nm (C).
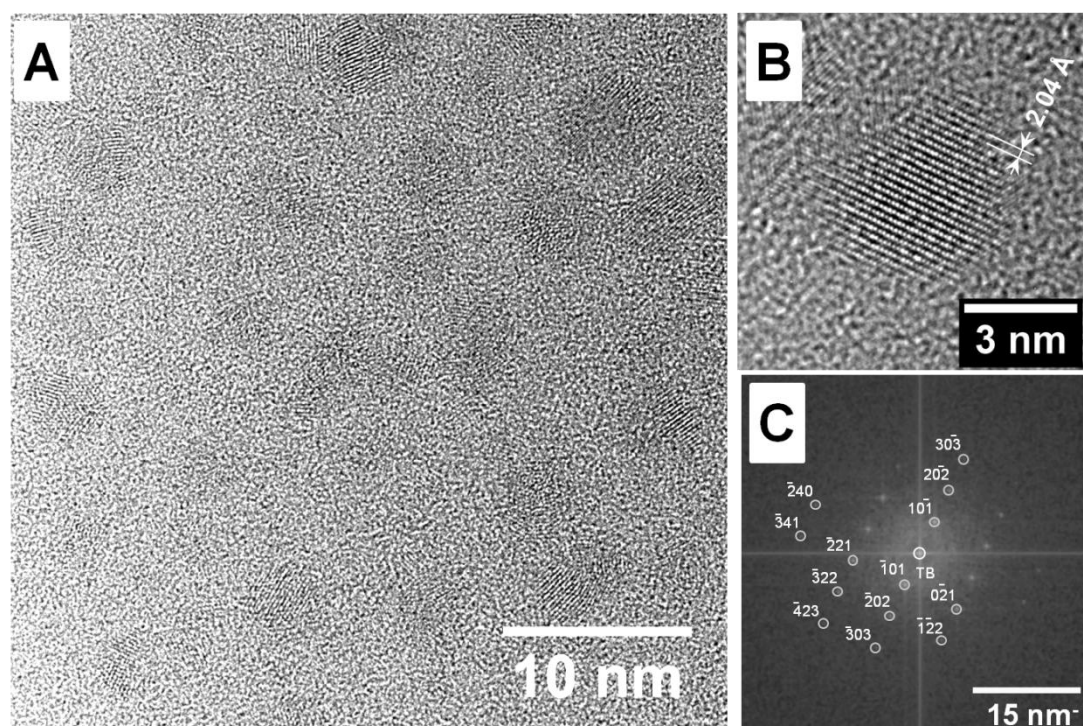
Figure 4.87: TEM images of water-diluted Mg^{2+}/PEG sample: A) TEM image of nanoparticles in Mg^{2+}/PEG; B) HRTEM image of a nanoparticle with lattice distance; C) experimental diffractogram of the nanoparticle shown in B and calculated diffraction pattern of bulk-carbon ([-101] zone axis, reflections marked by white circles, TB: transmitted beam).

In summary, the heated polyols with or without metal salts all exhibit an intense blue emission under UV excitation at a wavelength of 366 nm and show different luminescent emissions with a dependence on the excitation wavelengths. Different kinds of polyols (DEG, glycerol and PEG400) and different metal salts (NaCl, KCl, $ZnCl_2$ and $MgCl_2$) were investigated, which only influence the intensity of the blue emission. Among all the samples, Mg^{2+}/PEG under 366 nm excitation presents a blue emission with the highest intensity and shows the absolute quantum yield of about 25 %. After heating PEG400 with rare-earth metal salt ($TbCl_3$) or fluorophor (fluorescein), the luminescent properties of the resulting sample are enhanced. The emission spectrum excited at 366 nm shows not only the typical emission of Tb or fluorescein, but also a broad peak in the blue spectral region that comes from the heated polyol. The combination of the emissions leads to a much brighter luminescence under a 366 nm UV lamp. The absolute quantum yield of Tb^{3+}/PEG is about 46 %.

5 Summary and Outlook

The aim of this work was polyol-mediated syntheses of chalcogenide nanoparticles for printable thin-film solar cells. In order to apply non-vacuum coating or printing techniques, stable inks of chalcogenide nanoparticles are required. In this thesis, chalcogenide nanoparticles, such as Cu_2Se, In_2Se_3, CZTS, Se@CuSe and Te@Bi_2Te_3, have been successfully synthesized via a polyol-mediated method. All the nanoparticles can be dispersed in demineralised water, ethanol or isopropanol and form stable inks for non-vacuum layer deposition. Promising CISe thin-film solar cells, using our own precursor layers, have been successfully manufactured as well.

Initially, binary chalcogenide compounds, namely copper selenide and indium selenide, were synthesized via a polyol-mediated method combined with hot injection technique in the solvent of DEG. The use of $C_4H_{10}S_3$, maximum temperature and duration of the reaction have a strong effect on the size and shape of the nanoparticles. The as-prepared spherical Cu_2Se nanoparticles exhibit an average diameter of 17 nm and an indirect band gap of 1.1 eV / a direct band gap of 1.3 eV. The as-prepared In_2Se_3 nanoparticles have an average particle size of 20 nm in diameter and a direct band gap of 2.0 eV. Both of the as-prepared samples are amorphous and can be crystallized after annealing at 400 ℃. Stable inks of Cu_2Se, In_2Se_3 or their mixture were deposited on molybdenum-covered soda-lime-glass substrates via doctor-blade coating. The CISe thin-film solar cells with conversion efficiencies of 1-2 % had been achieved by selenization or laser annealing of the precursor layers. Much more efforts and optimization of the experimental conditions in terms of chemical composition, $Cu_2Se : In_2Se_3$ ratio, particle diameter, layer thickness and morphology, duration and temperature of the selenization process, etc. are necessary to improve the morphology of CISe absorber layers and to increase the overall solar-cell performances.

Cu_2ZnSnS_4 kesterite nanoparticles (CZTS) with a particle diameter of 10-20 nm were prepared by a polyol-mediated synthesis. DEG was applied as solvent, which allows controlling the particle size and suppressing the particle agglomeration. Due to its high boiling point, crystalline phases can often be obtained directly from the liquid-phase synthesis at a relatively high reaction temperature close to the boiling point. The as-prepared CZTS nanoparticles crystallize with a tetragonal wurtzite-type superstructure and exhibit an overall composition of $Cu_{1.35}Zn_{1.11}SnS_{3.96}$ (copper-poor as well as zinc-, tin- and sulfur-rich) and a direct band gap of 1.37 eV. Thin-film solar cells were manufactured after conversion of the as-prepared CZTS nanoparticles to CZTSSe via gas-phase selenization. This procedure supports a densification of the absorber layer due to the volume increase, which fills up the voids and exhibits less interparticulate grain boundaries and defects. Moreover, the band gap of the absorber layer is decreased from 1.37 eV (CZTS) to 1.14 eV (CZTSSe). The best tested solar cell shows an open-circuit voltage of 247.3 mV, a short-circuit current density of 21.3 mA cm^{-2}, a fill factor of 41.1 %, and a promising conversion efficiency of 2.2 %.

While the polyol-mediated synthesis of CZTS nanoparticles and their conversion to a CZTSSe absorber layer turn out successfully, much more efforts and optimization of the experimental conditions (particle size and overall composition of CZTS, thickness of CZTS/CZTSe thin-films, duration and temperature of the selenization process) are required to further improve the absorber-layer morphology and to increase the overall solar-cell performance.

In addition, Se@CuSe core@shell nanoparticles with adjustable diameters were synthesized via a hydrazine-driven reduction of selenious acid in DEG. Via the variation of the $N_2H_4 : H_2SeO_3$ ratio and the duration of the reaction, the size of the as-prepared Se@CuSe core@shell nanoparticles can be controlled from 85 nm to 410 nm in diameter. The Se@CuSe core@shell nanoparticles show a significantly higher phase stability as well as a higher colloidal stability as-compared to non-capped Se nanoparticles. The well-known red a-Se to crystalline grey t-Se phase transition at or even below room temperature was overcome by the Se@CuSe core@shell nanostructure (phase transition at 31 ℃ for bulk-Se and even below room temperature for nano-/micro-sized Se). The as-prepared Se@CuSe core@shell nanoparticles with an inner core of pure selenium (340 nm in diameter) and a CuSe shell (20 nm in thickness) show the onset of the phase transition at a temperature as high as 107 ℃. These core@shell nanoparticles do neither show any merging nor any formation of crystalline t-Se needles. Based on the increased phase and colloidal stability, the Se@CuSe core@shell nanoparticles can be dispersed as a stable Se ink for thin-film deposition and manufacturing of CISe thin-film solar cells. First lab-scale CISe solar cells in a conceptual study using the stable Se inks show promising performances with conversion efficiencies of currently up to 3%. In addition to CISe solar cells, the concept of stabilizing Se nano-/mesoscaled particles by metal selenide cappings could be useful for other areas of application, such as the use of Se particles in mechanical sensors, electrical rectifiers, xerography, or tumour therapy.

Te@Bi_2Te_3 core@shell nanorods of low aspect ratio (<5) were prepared via a hydrazine-driven reduction of telluric acid in DEG. By variation of the N_2H_4 H_2O to H_2TeO_4 $2H_2O$ ratio, the size can be controlled, resulting in nanorods with a mean diameter of 19(2) nm and a mean length of 55(12) nm as well as nanorods with a mean diameter of 14(1) nm and a mean length of 28(4) nm. Such small sizes and low aspect ratios are rare till now since Te nanoparticles show fast agglomeration and merging. The colloidal stability was increased by a Bi_2Te_3 capping. For the Te@Bi_2Te_3 core@shell nanorods, the Te core is highly crystalline, while the Bi_2Te_3 shell remains amorphous. HRTEM and HAADF-STEM images as well as high-resolution line-scan EDX analysis validate the presence of a pure Te nanorod core with a diameter of 13 nm and a Bi_2Te_3 shell with a thickness of 6 nm. The resulting colloidally stable Te nanorods can be interesting precursors for thin-film solar cells, thermoelectrics and topological insulators, especially, in terms of layer deposition and printing.

118

In this thesis, thermal decomposition of zinc glycerolate (Zn(gly)) gives access to ZnO at temperatures of 500-600 ℃. Interestingly, the platelet-like morphology of the as-prepared pure Zn(gly) can be preserved during the formation of ZnO, which also exhibits a platelet-like morphology with diameters of 10-15 μm and a thickness of 100-300 nm. Depending on different dopants, different morphologies and shapes of doped Zn(gly) and corresponding doped ZnO via moderate thermal decomposition of Zn(gly) can be obtained. Controlled thermal decomposition of pure Zn(gly), moreover, allows adjusting a certain porosity of the now granulated ZnO platelets with the specific surface areas (BET) of 5-18 $m^2\,g^{-1}$. Since an initial growth of platelet-like ZnO is less observed, thermal decomposition of Zn(gly) could be an useful alternative. Such porous ZnO platelets with a large aspect ratio (~100) are highly interesting for applications like UV-protection, sun-blocking and catalysis. The doped ZnO can be relevant to the transparent conducting oxides.

Finally, the photoluminescence of heated polyols has been confirmed, which shows blue emission under UV excitation. All heated polyol samples show different luminescent emissions with a dependence on the excitation wavelengths. Types of polyols and metal salts only influence the intensity of the emission. The heated polyol samples have relatively high quantum yields. When heating with rare-earth metal salts and typical fluorophors, the heated polyols can behave as a good enhancer, which enhance the luminescent properties of the resulting samples. Significant advantages of heated polyol samples lie in the low-cost, non-toxic and easily-obtained precursors, the simple and fast synthesis, and excellent sample performances like multicolor emission capabilities, which should enable them to have wide-ranging applications in biological labeling and imaging.

6 References

[1]   BP, *BP Statistical Review of World Energy 2013*,
        http://www.bp.com/statisticalreview, **2013**.

[2]   IEA, *Electricity Information 2010*, OECD Publishing, **2010**.

[3]   A. Feltrin, A. Freundlich, *Renewable Energy* **2008**, *33*, 180-185.

[4]   M. I. Hoffert, K. Caldeira, A. K. Jain, E. F. Haites, L. D. D. Harvey, S. D.
        Potter, M. E. Schlesinger, S. H. Schneider, R. G. Watts, T. M. L. Wigley, D. J.
        Wuebbles, *Nature* **1998**, *395*, 881-884.

[5]   N. S. Lewis, *MRS Bulletin* **2007**, *32*, 808-820.

[6]   BP, *BP Statistical Review of World Energy 2012*,
        http://www.bp.com/statisticalreview, **2012**.

[7]   A. JAEGER-WALDAU, *PV Status Report 2012*, Office for Official
        Publications of the European Union, **2012**.

[8]   J. M. Woodcock, H. Schade, H. Maurus, B. Dimmler, in *14th, European
        photovoltaic solar energy conference, Vol. 1*, H.S. Stephens & Associates,
        1997, pp. 857-860.

[9]   Powalla M, Dimmler B, G. K-H., in *20th European Photovoltaic Solar Energy
        Conference* (Eds.: Palz W, Ossenbrink HA, H. P), Barcelona, Spain, **2005**, p.
        1689.

[10]   S. Niki, M. Contreras, I. Repins, M. Powalla, K. Kushiya, S. Ishizuka, K.
        Matsubara, *Progress in Photovoltaics: Research and Applications* **2010**, *18*,
        453-466.

[11]   D. Aldakov, A. Lefrançois, P. Reiss, *Journal of Materials Chemistry C* **2013**,
        1, 3756-3776.

[12]   M. A. Green, K. Emery, Y. Hishikawa, W. Warta, E. D. Dunlop, *Progress in
        Photovoltaics: Research and Applications* **2013**, *21*, 1-11.

[13]   P. Jackson, D. Hariskos, E. Lotter, S. Paetel, R. Wuerz, R. Menner, W.
        Wischmann, M. Powalla, *Progress in Photovoltaics: Research and
        Applications* **2011**, *19*, 894-897.

[14]   O. Schultz, S. W. Glunz, G. P. Willeke, *Progress in Photovoltaics: Research
        and Applications* **2004**, *12*, 553-558.

[15]   S. Chen, A. Walsh, X.-G. Gong, S.-H. Wei, *Adv. Mater.* **2013**, *25*, 1522-1539.

[16]   S. Siebentritt, S. Schorr, *Progress in Photovoltaics: Research and
        Applications* **2012**, *20*, 512-519.

[17]   D. B. Mitzi, O. Gunawan, T. K. Todorov, K. Wang, S. Guha, *Sol. Energy
        Mater. Sol. Cells* **2011**, *95*, 1421-1436.

[18]   D. R. Lide, *CRC Handbook of Chemistry and Physics*, 86 ed., CRC Press,
        2005.

[19]   Y. S. Avadhut, J. Weber, E. Hammarberg, C. Feldmann, I. Schellenberg, R.
        Pöttgen, J. Schmedt auf der Günne, *Chem. Mater.* **2011**, *23*, 1526-1538.

[20]   F. Fievet, F. Fievet-Vincent, J.-P. Lagier, B. Dumont, M. Figlarz, *J. Mater.
        Chem.* **1993**, *3*, 627-632.

[21]   F. Fievet, J. P. Lagier, B. Blin, B. Beaudoin, M. Figlarz, *Solid State Ionics* **1989**, *32–33, Part 1*, 198-205.

[22]   C. Feldmann, *Adv. Funct. Mater.* **2003**, *13*, 101-107.

[23]   C. Feldmann, H.-O. Jungk, *Angew. Chem. Int. Ed.* **2001**, *40*, 359-362.

[24]   C. Feldmann, *Solid State Sci.* **2005**, *7*, 868-873.

[25]   C. Feldmann, H. O. Jungk, *J. Mater. Sci.* **2002**, *37*, 3251-3254.

[26]   C. Feldmann, C. Metzmacher, *J. Mater. Chem.* **2001**, *11*, 2603-2606.

[27]   V. K. LaMer, R. H. Dinegar, *J. Am. Chem. Soc.* **1950**, *72*, 4847-4854.

[28]   J. Park, J. Joo, S. G. Kwon, Y. Jang, T. Hyeon, *Angew. Chem. Int. Ed.* **2007**, *46*, 4630-4660.

[29]   C. B. Murray, D. J. Norris, M. G. Bawendi, *J. Am. Chem. Soc.* **1993**, *115*, 8706-8715.

[30]   D. V. Talapin, A. L. Rogach, A. Kornowski, M. Haase, H. Weller, *Nano Lett.* **2001**, *1*, 207-211.

[31]   J. Hambrock, R. Becker, A. Birkner, Wei, R. A. Fischer, *Chem. Commun.* **2002**, 68-69.

[32]   N. R. Jana, X. Peng, *J. Am. Chem. Soc.* **2003**, *125*, 14280-14281.

[33]   X. Peng, J. Wickham, A. P. Alivisatos, *J. Am. Chem. Soc.* **1998**, *120*, 5343-5344.

[34]   Z. A. Peng, X. Peng, *J. Am. Chem. Soc.* **2002**, *124*, 3343-3353.

[35]   G. Bühler, C. Feldmann, *Angew. Chem. Int. Ed.* **2006**, *45*, 4864-4867.

[36]   G. Bühler, D. Thölmann, C. Feldmann, *Adv. Mater.* **2007**, *19*, 2224-2227.

[37]   W. Massa, *Crystal Structure Determination*, Springer, **2004**.

[38]   B. Fultz, J. Howe, *Transmission Electron Microscopy and Diffractometry of Materials*, Springer, **2008**.

[39]   P. J. Goodhew, J. Humphreys, R. Beanland, *Electron Microscopy and Analysis, Third Edition*, Taylor & Francis, **2000**.

[40]   E. Abbe, *Archiv f. mikrosk. Anatomie* **1873**, *9*, 413-418.

[41]   D. B. Williams, C. B. Carter, *Transmission Electron Microscopy: A Textbook for Materials Science*, Springer, **2009**.

[42]   L. Reimer, *Scanning Electron Microscopy: Physics of Image Formation and Microanalysis*, Springer, **1998**.

[43]   A. S. Douglas, *Fundamentals of Analytical Chemistry*, Thomson-Brooks/Cole, **2004**.

[44]   D. A. Skoog, F. J. Holler, S. R. Crouch, *Principles of Instrumental Analysis*, Thomson Brooks/Cole, **2007**.

[45]   D. A. Skoog, D. M. West, F. J. Holler, *Analytical chemistry: an introduction*, Saunders College Pub., **2000**.

[46]   H. Günzler, H. U. Gremlich, *IR Spectroscopy: An Introduction*, Wiley, **2002**.

[47]   H.-U. Gremlich, in *Handbook of Analytical Techniques*, Wiley-VCH Verlag GmbH, **2001**, pp. 465-507.

[48]   T. Owen, *Fundamentals of Modern UV-visible Spectroscopy: Primer*, Agilent Technologies, **2000**.

[49]   J. Tauc, R. Grigorovici, A. Vancu, *Phys. Status Solidi* **1966**, *15*, 627.

[50]   M. Gr ä zel, *Heterogeneous Photochemical Electron Transfer*, CRC Press, **1989**.

[51]   A. Hagfeldt, M. Graetzel, *Chemical Reviews* **1995**, *95*, 49-68.

[52]   J. R. Lakowicz, *Principles of Fluorescence Spectroscopy*, Springer, **2006**.

[53]   B. J. Berne, R. Pecora, *Dynamic Light Scattering: With Applications to Chemistry, Biology, and Physics*, Dover Publications, **2000**.

[54]   H. C. Hulst, H. C. van de Hulst, *Light Scattering by Small Particles*, Dover Publications, **1957**.

[55]   P. J. Haines, *Principles of Thermal Analysis and Calorimetry*, Royal Society of Chemistry, **2002**.

[56]   K. S. W. Sing, Engineering Foundation, Bavaria, West Ger, **1984**, pp. 567-583.

[57]   S. Brunauer, P. H. Emmett, E. Teller, *J. Am. Chem. Soc.* **1938**, *60*, 309-319.

[58]   V. Probst, W. Stetter, W. Riedl, H. Vogt, M. Wendl, H. Calwer, S. Zweigart, K. D. Ufert, B. Freienstein, H. Cerva, F. H. Karg, *Thin Solid Films* **2001**, *387*, 262-267.

[59]   K. Ramasamy, M. A. Malik, P. O'Brien, *Chem. Commun.* **2012**, *48*, 5703-5714.

[60]   T. K. Todorov, J. Tang, S. Bag, O. Gunawan, T. Gokmen, Y. Zhu, D. B. Mitzi, *Adv. Energy Mater.* **2013**, *3*, 34-38.

[61]   D. J. Milliron, D. B. Mitzi, M. Copel, C. E. Murray, *Chem. Mater.* **2006**, *18*, 581-590.

[62]   W. Yang, H. S. Duan, B. Bob, H. Zhou, B. Lei, C. H. Chung, S. H. Li, W. W. Hou, Y. Yang, *Adv. Mater.* **2012**, *24*, 6323-6329.

[63]   S. Bag, O. Gunawan, T. Gokmen, Y. Zhu, T. K. Todorov, D. B. Mitzi, *Energy and Environmental Science* **2012**, *5*, 7060-7065.

[64]   V. A. Akhavan, B. W. Goodfellow, M. G. Panthani, C. Steinhagen, T. B. Harvey, C. J. Stolle, B. A. Korgel, *J. Solid State Chem.* **2012**, *189*, 2-12.

[65]   Q. Guo, G. M. Ford, W. C. Yang, B. C. Walker, E. A. Stach, H. W. Hillhouse, R. Agrawal, *J. Am. Chem. Soc.* **2010**, *132*, 17384-17386.

[66]   X. Lu, Z. Zhuang, Q. Peng, Y. Li, *Chem. Commun.* **2011**, *47*, 3141-3143.

[67]   Y. L. Zhou, W. H. Zhou, Y. F. Du, M. Li, S. X. Wu, *Mater. Lett.* **2011**, *65*, 1535-1537.

[68]   S. W. Shin, J. H. Han, C. Y. Park, S. R. Kim, Y. C. Park, G. L. Agawane, A. V. Moholkar, J. H. Yun, C. H. Jeong, J. Y. Lee, J. H. Kim, *J. Alloys Compd.* **2012**, *541*, 192-197.

[69]   K. L. Ou, J. C. Fan, J. K. Chen, C. C. Huang, L. Y. Chen, J. H. Ho, J. Y. Chang, *J. Mater. Chem.* **2012**, *22*, 14667-14673.

[70]   A. Singh, H. Geaney, F. Laffir, K. M. Ryan, *J. Am. Chem. Soc.* **2012**, *134*, 2910-2913.

[71]   C. A. Cattley, C. Cheng, S. M. Fairclough, L. M. Droessler, N. P. Young, J. H. Warner, J. M. Smith, H. E. Assender, A. A. R. Watt, *Chem. Commun.* **2013**, *49*, 3745-3747.

[72]   P. K. Sarswat, M. L. Free, *J. Cryst. Growth* **2013**, *372*, 87-94.

[73]   I. Repins, M. A. Contreras, B. Egaas, C. DeHart, J. Scharf, C. L. Perkins, B. To, R. Noufi, *Progress in Photovoltaics: Research and Applications* **2008**, *16*, 235-239.

[74]   C. J. Hibberd, E. Chassaing, W. Liu, D. B. Mitzi, D. Lincot, A. N. Tiwari, *Progress in Photovoltaics: Research and Applications* **2010**, *18*, 434-452.

[75]   M. Kaelin, D. Rudmann, F. Kurdesau, H. Zogg, T. Meyer, A. N. Tiwari, *Thin Solid Films* **2005**, *480-481*, 486-490.

[76]   M. Kaelin, D. Rudmann, A. N. Tiwari, *Solar Energy* **2004**, *77*, 749-756.

[77]   T. Todorov, D. B. Mitzi, *Eur. J. Inorg. Chem.* **2010**, 17-28.

[78]   J. Ungelenk, V. Haug, A. Quintilla, E. Ahlswede, *Physica Status Solidi - Rapid Research Letters* **2010**, *4*, 58-60.

[79]   F. S. Chen, J. S. Ma, C. H. Lu, *Ceram. Int.* **2012**, *38*, 5319-5323.

[80]   C. Kind, C. Feldmann, A. Quintilla, E. Ahlswede, *Chem. Mater.* **2011**, *23*, 5269-5274.

[81]   V. K. Kapur, A. Bansal, P. Le, O. I. Asensio, *Thin Solid Films* **2003**, *431-432*, 53-57.

[82]   V. A. Akhavan, B. W. Goodfellow, M. G. Panthani, D. K. Reid, D. J. Hellebusch, T. Adachi, B. A. Korgel, *Energy and Environmental Science* **2010**, *3*, 1600-1606.

[83]   Q. Guo, S. J. Kim, M. Kar, W. N. Shafarman, R. W. Birkmire, E. A. Stach, R. Agrawal, H. W. Hillhouse, *Nano Lett.* **2008**, *8*, 2982-2987.

[84]   A. Cho, S. Ahn, J. H. Yun, Y. J. Eo, H. Song, K. Yoon, *Sol. Energy Mater. Sol. Cells* **2013**, *110*, 126-132.

[85]   K. Kim, Y. J. Eo, A. Cho, J. Gwak, J. H. Yun, K. Shin, S. K. Ahn, S. H. Park, K. Yoon, S. Ahn, *J. Mater. Chem.* **2012**, *22*, 8444-8448.

[86]   A. M. Hermann, L. Fabick, *J. Cryst. Growth* **1983**, *61*, 658-664.

[87]   M. Al, A. B. M. O. Islam, A. H. Bhuiyan, *J. Mater. Sci.: Mater. Electron.* **2005**, *16*, 263-268.

[88]   M. Al, A. B. M. O. Islam, *Appl. Surf. Sci.* **2004**, *238*, 184-188.

[89]   S. K. Haram, K. S. V. Santhanam, *Thin Solid Films* **1994**, *238*, 21-26.

[90]   A. Jagminas, R. Juškenas, I. Gailiute, G. Statkute, R. Tomašiunas, *J. Cryst. Growth* **2006**, *294*, 343-348.

[91]   P. O'Brien, D. J. Otway, J. R. Walsh, *Chem. Vap. Deposition* **1997**, *3*, 227-229.

[92]   S. L. Seung, W. S. Kook, I. W. Shim, *Bull. Korean Chem. Soc.* **2006**, *27*, 147-149.

[93]   C. Julien, A. Chevy, D. Siapkas, *Physica Status Solidi (A) Applied Research* **1990**, *118*, 553-559.

[94]   M. Powalla, B. Dimmler, *Thin Solid Films* **2001**, *387*, 251-256.

[95]   A. Weber, R. Mainz, H. W. Schock, *J. Appl. Phys.* **2010**, *107*.

[96]   A. Redinger, D. M. Berg, P. J. Dale, S. Siebentritt, *J. Am. Chem. Soc.* **2011**, *133*, 3320-3323.

[97]   H. Dong, T. Schnabel, E. Ahlswede, C. Feldmann, *Solid State Sci.*, *Submitted*.

[98]   V. V. Ivanov, Y. A. Pyatenko, *Zap. Vses. Mineral.* **1959**, *88*, .

[99]   H. Matsushita, T. Maeda, A. Katsui, T. Takizawa, *J. Cryst. Growth* **2000**, *208*, 416-422.

[100]   A. Fairbrother, X. Fontané, V. Izquierdo-Roca, M. Espindola-Rodriguez, S. López-Marino, M. Placidi, J. López-García, A. Pérez-Rodríguez, E. Saucedo, *ChemPhysChem* **2013**, *14*, 1836-1843.

[101]   C. M. Fella, Y. E. Romanyuk, A. N. Tiwari, *Sol. Energy Mater. Sol. Cells* **2013**, *119*, 276-277.

[102]   F. Rauscher, C. Feldmann, C. Kind, L. Mleczko, H. Lu, K. Köhler, Patent application, WO 2012152740, **2012**.

[103]   C. Feldmann, A. Karpov, H. Hibst, Patent application, WO 2009007369, **2009**.

[104]   R. A. Zingaro, W. C. Cooper, *Selenium*, Van Nostrand Reinhold, **1974**.

[105]   L. Liu, Q. Peng, Y. Li, *Nano Res.* **2008**, *1*, 403-411.

[106]   B. Zhang, W. Dai, X. Ye, F. Zuo, Y. Xie, *Angewandte Chemie - International Edition* **2006**, *45*, 2571-2574.

[107]   Z. Quan, P. Yang, C. Li, X. Zhang, J. Yang, J. Lin, *Crystal Growth and Design* **2008**, *8*, 3834-3839.

[108]   U. Lee, J. Choi, N. Myung, I. H. Kim, C. R. N. Chenthamarakshan, N. R. De Tacconi, K. Rajeshwar, *Bull. Korean Chem. Soc.* **2008**, *29*, 689-692.

[109]   J. L. Li, X. Y. Liu, *J. Nanosci. Nanotechnol.* **2008**, *8*, 2488-2491.

[110]   U. Jeong, Y. Xia, *Adv. Mater.* **2005**, *17*, 102-106.

[111]   X. Cao, Y. Xie, L. Li, *Adv. Mater.* **2003**, *15*, 1914-1918.

[112]   H. Dong, A. Quintilla, M. Cemernjak, R. Popescu, D. Gerthsen, E. Ahlswede, C. Feldmann, *J. Colloid Interface Sci.* **2014**, *415*, 103-110.

[113]   T. W. Smith, R. A. Cheatham, *Macromolecules* **1980**, *13*, 1203-1207.

[114]   C. Kind, R. Popescu, R. Schneider, E. Müller, D. Gerthsen, C. Feldmann, *RSC Advances* **2012**, *2*, 9473-9487.

[115]   X. Wu, *Solar Energy* **2004**, *77*, 803-814.

[116]   D. Kong, Y. Cui, *Nature Chemistry* **2011**, *3*, 845-849.

[117]   M. S. Dresselhaus, G. Chen, M. Y. Tang, R. Yang, H. Lee, D. Wang, Z. Ren, J. P. Fleurial, P. Gogna, *Adv. Mater.* **2007**, *19*, 1043-1053.

[118]   L. Müchler, H. Zhang, S. Chadov, B. Yan, F. Casper, J. Kübler, S. C. Zhang, C. Felser, *Angewandte Chemie - International Edition* **2012**, *51*, 7221-7225.

[119]   D. Milliron, S. M. Hughes, Y. Cui, L. Manna, J. Li, L. W. Wang, A. P. Alivisatos, *Nature* **2004**, *430*, 190-195.

[120]   Z. H. Lin, Z. Yang, H. T. Chang, *Crystal Growth and Design* **2008**, *8*, 351-357.

[121]   B. Mayers, Y. Xia, *J. Mater. Chem.* **2002**, *12*, 1875-1881.

[122]   H. Zhu, H. Zhang, J. Liang, G. Rao, J. Li, G. Liu, Z. Du, H. Fan, J. Luo, *J. Phys. Chem. C* **2011**, *115*, 6375-6380.

[123]   H. S. Qian, S. H. Yu, J. Y. Gong, L. B. Luo, L. F. Fei, *Langmuir* **2006**, *22*, 3830-3835.

[124]   Y. J. Zhu, X. L. Hu, W. W. Wang, *Nanotechnology* **2006**, *17*, 645-650.

[125]   Q. Lu, F. Gao, S. Komarneni, *Langmuir* **2005**, *21*, 6002-6005.

[126] G. S. Cao, X. J. Zhang, L. Su, Y. Y. Ruan, *J. Exp. Nanosci.* **2011**, *6*, 121-126.

[127] Y. J. Zhu, W. W. Wang, R. J. Qi, X. L. Hu, *Angewandte Chemie - International Edition* **2004**, *43*, 1410-1414.

[128] Z. Liu, Z. Hu, J. Liang, S. Li, Y. Yang, S. Peng, Y. Qian, *Langmuir* **2004**, *20*, 214-218.

[129] Z. Liu, Z. Hu, Q. Xie, B. Yang, J. Wu, Y. Qian, *J. Mater. Chem.* **2003**, *13*, 159-162.

[130] N. Watanabe, N. Toshima, *Bull. Chem. Soc. Jpn.* **2007**, *80*, 208-214.

[131] X. Liu, Y. Shen, R. Yang, S. Zou, X. Ji, L. Shi, Y. Zhang, D. Liu, L. Xiao, X. Zheng, S. Li, J. Fan, G. D. Stucky, *Nano Lett.* **2012**, *12*, 5733-5739.

[132] H. Goesmann, C. Feldmann, *Angewandte Chemie - International Edition* **2010**, *49*, 1362-1395.

[133] D. Vollath, *Nanomaterials: An Introduction to Synthesis, Properties and Applications*, Wiley, **2008**.

[134] G. Zhang, Q. Yu, W. Wang, X. Li, *Adv. Mater.* **2010**, *22*, 1959-1962.

[135] G. J. Snyder, E. S. Toberer, *Nat. Mater.* **2008**, *7*, 105-114.

[136] G. Zhang, W. Wang, X. Li, *Adv. Mater.* **2008**, *20*, 3654-3656.

[137] H. Dong, R. Popescu, D. Gerthsen, C. Feldmann, *Zeitschrift fur Anorganische und Allgemeine Chemie* **2013**, *639*, 2406-2410.

[138] A. J. Bradley, *Philosophical Magazine Series 6* **1924**, *48*, 477-496.

[139] M. C. M. H. E. Swanson, E. H. Evans, L. Ulmer, *Standard X-ray Diffraction Powder Patterns, Vol. 3*, U.S. Government Printing Office, **1964**.

[140] S. Schnittger, M. Sinha, *MRS Bulletin* **2007**, *32*, 760-769.

[141] Q. Zhang, C. S. Dandeneau, X. Zhou, C. Cao, *Adv. Mater.* **2009**, *21*, 4087-4108.

[142] T. Minami, *Semicond. Sci. Technol.* **2005**, *20*, S35-S44.

[143] D. Lincot, *MRS Bulletin* **2010**, *35*, 778-789.

[144] A. V. Narlikar, Y. Y. Fu, *Oxford Handbook of Nanoscience and Technology: Volume 2: Materials: Structures, Properties and Characterization Techniques*, OUP Oxford, **2010**.

[145] W. Gao, Z. Li, *International Journal of Nanotechnology* **2009**, *6*, 245-257.

[146] F. Weiss, M. Audier, A. Bartasyte, D. Bellet, C. Girardot, C. Jimenez, J. Kreisel, S. Pignard, M. Salaun, C. Ternon, *Pure Appl. Chem.* **2009**, *81*, 1523-1534.

[147] S. C. Abrahams, J. L. Bernstein, *Acta Crystallographica Section B* **1969**, *25*, 1233-1236.

[148] C. Pacholski, A. Kornowski, H. Weller, *Angewandte Chemie - International Edition* **2002**, *41*, 1188-1191.

[149] C. Klingshirn, *Physica Status Solidi (B) Basic Research* **2007**, *244*, 3027-3073.

[150] X. Lü, X. Zou, J. Cheng, G. Teng, X. Meng, Z. Sun, G. Yang, C. Wei, H. Feng, Y. Yang, *Vol. 123-125*, **2010**, pp. 284-287.

[151] J. Y. Ye, Z. Y. Huang, C. Min, S. R. Pan, D. H. Chen, *Biomedical Materials* **2009**, *4*.

126

[152] M. T. Htay, Y. Hashimoto, K. Ito, *Japanese Journal of Applied Physics, Part 1: Regular Papers and Short Notes and Review Papers* **2007**, *46*, 440-448.

[153] H. Tang, J. C. Chang, Y. Shan, S. T. Lee, *J. Phys. Chem. B* **2008**, *112*, 4016-4021.

[154] G. Han, A. Shibukawa, M. Okada, Y. Neo, T. Aoki, H. Mimura, *Journal of Vacuum Science and Technology B: Microelectronics and Nanometer Structures* **2010**, *28*, C2C16-C12C19.

[155] P. D. Burton, E. J. Peterson, T. J. Boyle, A. K. Datye, *Catal. Lett.* **2010**, *139*, 26-32.

[156] J. Merikhi, C. Feldmann, *J. Colloid Interface Sci.* **2000**, *228*, 121-126.

[157] D. Jezequel, J. Guenot, N. Jouini, F. Fievet, *Mater. Sci. Forum* **1994**, *152-5*, 339-342.

[158] P. Toneguzzo, G. Viau, O. Acher, F. Guillet, E. Bruneton, F. Fievet-Vincent, F. Fievet, *J. Mater. Sci.* **2000**, *35*, 3767-3784.

[159] E. W. Radoslovich, M. R. Raupach, P. G. Slade, R. M. Taylor, *Aust. J. Chem.* **1970**, *23*, 1963-1971.

[160] R. Moleski, E. Leontidis, F. Krumeich, *J. Colloid Interface Sci.* **2006**, *302*, 246-253.

[161] O. A. Yildirim, C. Durucan, *J. Alloys Compd.* **2010**, *506*, 944-949.

[162] J. Das, D. Khushalani, *J. Phys. Chem. C* **2010**, *114*, 2544-2550.

[163] H. Dong, C. Feldmann, *J. Alloys Compd.* **2012**, *513*, 125-129.

[164] T. W. Hambley, M. R. Snow, *Aust. J. Chem.* **1983**, *36*, 1249-1253.

[165] X. Su, Z. Zhang, M. Zhu, *Appl. Phys. Lett.* **2006**, *88*.

[166] M. Roming, C. Feldmann, Y. S. Avadhut, J. S. Auf Der Günne, *Chem. Mater.* **2008**, *20*, 5787-5795.

[167] C. Feldmann, T. Jüstel, C. R. Ronda, P. J. Schmidt, *Adv. Funct. Mater.* **2003**, *13*, 511-516.

[168] J. Dexpert-Ghys, R. Mauricot, M. D. Faucher, *J. Lumin.* **1996**, *69*, 203-215.

[169] G. Bühler, C. Feldmann, *Angewandte Chemie - International Edition* **2006**, *45*, 4864-4867.

[170] M. Yu, J. Lin, J. Fu, H. J. Zhang, Y. C. Han, *J. Mater. Chem.* **2003**, *13*, 1413-1419.

[171] K. Riwotzki, H. Meyssamy, A. Kornowski, M. Haase, *J. Phys. Chem. B* **2000**, *104*, 2824-2828.

[172] K. Riwotzki, H. Meyssamy, H. Schnablegger, A. Kornowski, M. Haase, *Angewandte Chemie - International Edition* **2001**, *40*, 573-576.

[173] Y. P. Fang, A. W. Xu, R. Q. Song, H. X. Zhang, L. P. You, J. C. Yu, H. Q. Liu, *J. Am. Chem. Soc.* **2003**, *125*, 16025-16034.

[174] H. Meyssamy, K. Riwotzki, A. Kornowski, S. Naused, M. Haase, *Adv. Mater.* **1999**, *11*, 840-844.

[175] K. Kömpe, H. Borchert, J. Storz, A. Lobo, S. Adam, T. Möller, M. Haase, *Angewandte Chemie - International Edition* **2003**, *42*, 5513-5516.

[176] C. Calvo, *J. Phys. Chem. Solids* **1963**, *24*, 141-149.

[177] A. L. Smith, *J. Electrochem. Soc.* **1951**, *98*, 363-368.

[178] U. Caldiño, J. L. Hernández-Pozos, C. Flores, A. Speghini, M. Bettinelli, *Journal of Physics Condensed Matter* **2005**, *17*, 7297-7305.

[179] J. Wang, S. Wang, Q. Su, *J. Solid State Chem.* **2004**, *177*, 895-900.

[180] J. Wang, S. Wang, Q. Su, *J. Mater. Chem.* **2004**, *14*, 2569-2574.

[181] G. Blasse, B. C. Grabmaier, *Luminescent materials*, Springer-Verlag, **1994**.

[182] S. Shionoya, W. M. Yen, *Phosphor Handbook*, Taylor & Francis, **1998**.

[183] M. A. Tshabalala, B. F. Dejene, H. C. Swart, *Physica B: Condensed Matter* **2012**, *407*, 1668-1671.

[184] T. Thongtem, S. Jattukul, A. Phuruangrat, S. Thongtem, *J. Alloys Compd.* **2010**, *491*, 654-657.

[185] Y. Kaihatsu, W. N. Wang, F. Iskandar, K. Okuyama, *Mater. Lett.* **2010**, *64*, 836-839.

[186] X. Wang, J. Zhu, Y. Zhang, J. Jiang, S. Wei, *Applied Physics A: Materials Science and Processing* **2010**, *99*, 651-656.

[187] S. Kaci, A. Keffous, M. Trari, O. Fellahi, H. Menari, A. Manseri, L. Guerbous, *J. Lumin.* **2010**, *130*, 1849-1856.

[188] H. Gu, Z. Hu, Y. Hu, Y. Yuan, J. You, W. Zou, *Colloids and Surfaces A: Physicochemical and Engineering Aspects* **2008**, *315*, 294-298.

[189] Y. P. Sun, B. Zhou, Y. Lin, W. Wang, K. A. S. Fernando, P. Pathak, M. J. Meziani, B. A. Harruff, X. Wang, H. Wang, P. G. Luo, H. Yang, M. E. Kose, B. Chen, L. M. Veca, S. Y. Xie, *J. Am. Chem. Soc.* **2006**, *128*, 7756-7757.

[190] R. Liu, D. Wu, S. Liu, K. Koynov, W. Knoll, Q. Li, *Angewandte Chemie - International Edition* **2009**, *48*, 4598-4601.

[191] J. Zhang, W. Shen, D. Pan, Z. Zhang, Y. Fang, M. Wu, *New J. Chem.* **2010**, *34*, 591-593.

[192] H. Peng, J. Travas-Sejdic, *Chem. Mater.* **2009**, *21*, 5563-5565.

[193] S. L. Hu, K. Y. Niu, J. Sun, J. Yang, N. Q. Zhao, X. W. Du, *J. Mater. Chem.* **2009**, *19*, 484-488.

[194] A. S. Karakoti, S. Das, S. Thevuthasan, S. Seal, *Angewandte Chemie - International Edition* **2011**, *50*, 1980-1994.

[195] http://en.wikipedia.org/wiki/Fluorescein.

7 Appendix

7.1 List of Abbreviations

AE	Auger electrons
AES	atomic emission spectroscopy
a-Se	amorphous selenium
BET	Brunauer-Emmett-Teller
BF	bright-field
BJH	Barret-Joyner-Halenda
BSE	backscattered electrons
CAGR	compound annual growth rate
CBD	chemical bath deposition
CCD	charge-coupled-device
CIGS/Se	copper indium gallium sulfide/selenide)
CIS/Se	copper indium sulfide/selenide
CL	cathode luminescence
CZTS/Se	copper zinc tin sulfide/selenide
DF	dark-field
DLS	dynamic light scattering
DSC	differential scanning calorimetry
DTA	differential thermal analysis
EDS	energy-dispersive spectroscopy
EDX	energy dispersive X-ray analysis
EQE	external quantum efficiency
FE	field-emission
FT-IR	Fourier transform infrared
HAADF	high-angle annular dark-field
HOMO	highest occupied molecular orbital
HRTEM	high-resolution transmission electron microscopy
ICDD	international center for diffraction data
IR	infrared
LUMO	lowest unoccupied molecular orbital
Mtoe	million tonnes oil equivalent
MW	megawatt
PMT	photomultiplier tubes
PSD	position-sensitive detectors
PV	photovoltaic
PVP	polyvinylpyrrolidone
SAED	selected area electron diffraction
SE	secondary electrons
Se@CuSe	selenium@copper selenide

SEM	scanning electron microscopy
STEM	scanning transmission electron microscopy
Te@Bi2Te3	tellurium@bismuth telluride
TEM	transmission electron microscopy
TGA	thermogravimetric analysis
TW y	terawatt year
t-Se	trigonal selenium
UV-Vis	ultraviolet-visible
VPSE	variable pressure second electron
XFA	X-ray fluorescence analysis
XRD	X-ray powder diffraction
Zn(gly)	zinc glycerolate
ZnO:Al	aluminium doped zinc oxide
ZSW	Zentrum für Sonnenenergie- und Wasserstoffforschung

7.2 List of Tables

7.3 List of Figures

8 Curriculum Vitae

Personal data:

Name: Hailong Dong
Nationality: Chinese

Education:

2010.01—Now:	**PhD candidate in Inorganic Chemistry at Karlsruher Institut für Technologie, Germany** **Topic**: Polyol-mediated Synthesis of Chalcogenide Nanoparticles for Thin-film Solar Cells
2006.09—2009.03:	**M.Sc. in Biomaterials at Ulm University, Germany** **Topic**: FePt Nanorods and Nanowires for Novel Ferrofluids
2006.09—2007.08:	Starting to study advanced materials at Ulm University as an exchange student from Shandong University of China on a scholarship from DAAD
2003.09—2006.07:	**B.Eng. Chemical Engineering at Shandong University, China**
2000.09—2003.07:	**High school education at Dalian No. 23 high school, China**

List of Publications:

H. Dong, A. Kuzmanoski, D. M. Gößl, R. Popescu, D. Gerthsen, C. Feldmann, *Chem. Commun.*, **2014**, *50*, 7503-7506.

H. Dong, T. Schnabel, E. Ahlswede, C. Feldmann, *Solid State Sci.*, **2014**, *29*, 52-57.

H. Dong, A. Quintilla, M. Cemernjak, R. Popescu, D. Gerthsen, E. Ahlswede, C. Feldmann, *J. Colloid Interface Sci.*, **2014**, *415*, 103-110.

H. Dong, R. Popescu, D. Gerthsen, C. Feldmann, *Z. Anorg. Allg. Chem.*, **2013**, *639*, 2406-2410.

H. Dong, C. Feldmann, *J. Alloys Compd.,* **2012**, *513*, 125-129.

Z. Wu, H. Dong, A. Chuvilin, U. Wiedwald, L. Han, C. Krill III, *Solid State Phenom.*, **2009**, *154*, 89-94.

9 Acknowledgements

Kalam Munshi and Frank Riess, I thank them for the good cooperation and good working atmosphere they create in the institute.

Lots of my friends in Karlsruhe and Ulm, I would like to thank them for having fun together, cooking, eating and drinking together, organizing activities together and helping with each other, especially to Yan Bi, Luyan Dong, Xiaoxin Sun, Lei Zhang, Wenhua Liu, Ming Lin, Qiang Shi, Quan Li, Qibai Zhu, Jieqiong Xia, Li Yu, Yijie Sun, Yan Xie, Biao Xue, Zhenhao Zhang and Xiaomeng Ding in Karlsruhe; Beate Braun, Norbert Rückgauer, Jimin He, Zhenyu Wu, Xiaofeng Wang, Ziyao Gao, Peng Liu, Tong Zhang, Xu Tain, Min Zhang, Junjun Wang, Chong Gao and Ruiju Dong in Ulm.

I also take this opportunity to thank my fiancé Qian Liu who takes care of me very well. Without her support and understanding, everything would be a mess. All that she has done for me will be imprinted in my mind for ever.

Finally, I would like to express my deepest gratitude to my grandmother, my parents and all my relatives for their constant support, patience, understanding and love in my whole life.

140